INSTITUT POLYTECHNIQUE DE PARIS

NNT : 2023IPPAX040

Thèse de doctorat

Search for high mass resonances with multi-lepton channels and study of timing performance of the CMS High Granularity Calorimeter

Thèse de doctorat de l'Institut Polytechnique de Paris
préparée à l'École Polytechnique

École doctorale n°626 Institut Polytechnique de Paris (ED IP Paris)
Spécialité de doctorat : Physique des particules

Thèse présentée et soutenue à Palaiseau, le 27/04/2023, par

AXEL BUCHOT PERRAGUIN

Composition du Jury :

Yves Sirois Directeur de recherche, LLR (CNRS/École Polytechnique)	Président
Djamel Boumediene Directeur de recherche, LPC (CNRS)	Rapporteur
Emmanuel Monnier Directeur de recherche, CPPM (CNRS)	Rapporteur
Anne-Catherine Le Bihan Directrice de recherche, IPHC (CNRS)	Examinatrice
Julie Malclès Directrice de recherche, IRFU (CEA)	Examinatrice
Christophe Ochando Directeur de recherche, LLR (CNRS/École Polytechnique)	Directeur de thèse

Résumé

Cette thèse prend place à un moment charnière où l'ensemble des données collectées par l'expérience CMS lors du Run-2 du LHC (2015 à 2018) sont disponibles et où la nouvelle génération de détecteurs visant à sonder encore plus loin nos connaissances de la physique sont en train d'être élaborés.

Dans cet esprit, cette thèse s'articule autour de deux problématiques, dont la première porte sur l'étude des performances d'un prototype du High Granular Calorimeter (HGCAL) de CMS. Celui-ci s'inscrit dans une vaste campagne d'améliorations à l'horizon de la future phase de vie du LHC, aussi appelée High-Luminosity LHC (HL-LHC) et qui devrait être mise en place en 2029. Son objectif est de générer dix fois plus de données que pendant l'ensemble de la première phase du LHC, et ceci dans le but de mesurer encore plus précisément les prédictions du Modèle Standard (MS) de la physique des particules, ainsi que d'étudier des phénomènes rares qui ne sont pas observables à l'heure actuelle. L'augmentation de la luminosité sera aussi associée à une importante hausse du nombre d'événements simultanés et de la dose de radiation que vont recevoir les détecteurs. Ceux actuellement en place ne sont pas prévus pour fonctionner dans un tel environnement, et c'est pourquoi les actuels calorimètres aux extrémités seront remplacés par HGCAL Celui-ci sera le tout premier calorimètre imageur à base de capteurs en silicium à être utilisé. Pour déterminer sa faisabilité, un premier prototype a été construit et utilisé lors de tests sous faisceaux utilisant des positons et des pions ayant une énergie allant de 20 à 300 GeV. Dans cette thèse, l'accent sera mis sur l'étude des performances temporelles du prototype, en passant par les différentes étapes de la calibration et jusqu'au calcul de la résolution temporelle pour une unique cellule de HGCAL et pour l'ensemble d'une gerbe électromagnétique ou hadronique. Les résultats obtenus lors de cette thèse sont comparés à ceux issus de simulations Monte Carlo et le très bon accord entre les deux confirme la conception finale de HGCAL.

La seconde problématique sur laquelle se penche cette thèse est la recherche de résonances à haute masse en utilisant les canaux de désintégration multileptoniques. Une telle recherche s'explique par le fait que le MS ne permet pas de décrire certains phénomènes, mais d'autres théories leur proposent une explication avec notamment l'ajout de nouveaux bosons. L'objectif de cette analyse est de regarder s'il existe une résonance ayant une masse comprise entre 200 GeV et 3 TeV pouvant correspondre à un nouveau type de boson scalaire. Pour cela, les 138 fb^{-1} de données collectées par l'expérience CMS lors du Run-2 sont utilisées dans le canal de désintégration $H \to ZZ \to 4l$. L'intérêt d'utiliser ce canal en particulier est qu'il correspond à l'un des modes de production dominant à haute masse et

qu'il possède un état final pleinement reconstruit avec une excellente résolution et un bon rapport signal sur bruit. Cette thèse va tout d'abord présenter comment les différents objets constituants les événements d'intérêts sont reconstruits et sélectionnés. Ensuite, la construction d'un modèle de signal est faite de telle sorte que n'importe laquelle des combinaisons de paramètres de la résonance puissent être comparées aux données. Pour cela, cette modélisation comprend une partie décrivant le signal théorique et une autre qui prend en considération tous les effets du détecteur. Afin de savoir si les données expérimentales peuvent être décrites par le signal construit dans cette thèse, un test statistique est réalisé en maximisant une fonction de vraisemblance prenant en compte le signal, ainsi que les bruits de fond et les interférences entre les deux. En guise de résultats sur cette recherche, les limites sur la vraisemblance du signal attendu sont présentées et permettent d'exclure ou non une région de masse dans laquelle peut se trouver une résonance de haute masse.

Abstract

This thesis takes place at a critical moment when all the data collected by the CMS experiment during the LHC Run-2 are available and when the new generation of detectors aiming to probe even further our knowledge of physics are being developed.

In this context, this thesis is structured around two problematics, the first one concerns the study of the performance of a prototype of the CMS High Granularity Calorimeter (HGCAL). It is part of a vast campaign of upgrades for the future life phase of the LHC, also known as the High-Luminosity LHC, which should be in service by 2029. It aims to generate ten times more data than during the entire first phase of the LHC, in order to measure even more accurately the predictions of the Standard Model (SM) of particle physics, as well as to study rare phenomena that are not observable currently. The higher luminosity will also be associated with a significant increase in the number of simultaneous events and the radiation dose that the detectors will receive. The current detectors are not designed to operate in such an environment, so the endcap calorimeters of CMS will be replaced by HGCAL. It will be the first imaging calorimeter based on silicon sensors to be used. To determine its feasibility, a first prototype has been built and used in beam tests using positrons and pions with energies ranging from 20 to 300 GeV. In this thesis, the focus will be on the study of the temporal performance of the prototype, through the various stages of calibration and up to the calculation of the temporal resolution for a single HGCAL cell and for the whole electromagnetic or hadronic showers. The results obtained in this thesis are compared with those obtained from Monte Carlo simulations and the very good agreement between both confirms the viability of the HGCAL concept.

The second problematic addressed in this thesis is about the search for high mass resonances using the multi-leptonic decay channel. Such a search is explained by the fact that the SM does not describe some phenomena, but other theories propose an explanation with the addition of new bosons. The aim of such an analysis is to see if there is a resonance with a mass between 200 GeV and 3 TeV that could correspond to a new type of scalar boson. For this purpose, the 138 fb^{-1} of data collected by the CMS experiment during Run-2 are used in the $H \to ZZ \to 4l$ decay channel. The interest in using this particular channel is that it corresponds to one of the dominant high-mass production modes and has a fully reconstructed final state with excellent resolution and good signal-to-noise ratio. Firstly, this thesis presents how the different objects constituting the events of interest are reconstructed and selected. Secondly, the construction of a signal model is done in such a way that any combination of the resonance parameters

can be compared to the data. For this purpose, this modelling consists of a part describing the theoretical signal and another part that takes into account all the effects of the detector. In order to find out whether the experimental data can be described by the signal constructed in this thesis, a statistical test is performed by maximizing a likelihood function taking into account the signal, as well as the background and interference between both. As a result, limits on the expected signal cross-section are calculated and allow excluding or not a region of mass in which a high mass resonance can be found.

Acknowledgments

This thesis is the result of work I have been doing for over three years, and this period hasn't necessarily been a pleasant one, but fortunately I have been able to count on a number of people to help me through these challenges. That is why I would like to thank all of those without whom this thesis would not have been what it is.

First, I would like to deeply thank Christophe, who has given me so much throughout this adventure, starting by believing in me from the very beginning and giving me the chance to do a PhD thesis with him. I am very grateful for everything he taught me over the years, for his patience in explaining everything to me, and rereading my reports, presentations and this thesis. I would like to thank him for guiding me along the proper path all along the thesis, despite the ups and downs, and for sharing his passion for physics with me. Likewise, I would also like to thank him for his compassion, as he was understanding when I made a mistake, and was reassuring and attentive during difficult moments. In short, I thank him enormously for everything.

Next, I would like to thank my entire jury, starting with Djamel Boumediene and Emmanuel Monnier, who agreed to be the referees for my thesis and to review my manuscript, so helping to improve it. Next, I would like to thank Yves Sirois for agreeing to preside over the jury, and finally Anne-Catherine Le Bihan and Julie Malclès. Their comments and the discussions we had were very helpful in improving certain aspects of the thesis.

During my time at Laboratoire Leprince-Ringuet, but also on my travels to CERN, I met some brilliant and wonderful people, both researchers and engineers, working on CMS and other experiments, whom I met for work or during breaks. All these people helped me to share and open up my mind to the different aspects of what can be done in physics. Among them, I would particularly like to thank Claude, Florian, Roberto and Jean-Baptiste, with whom I have had very enriching discussions on the Higgs boson, HGCAL, new accelerators, travel, politics, gastronomy and many other things. I would also like to thank them for their help and advice during my various studies and the preparation of my thesis defence.

I would also like to thank all the people who worked with me on the HGCAL beam tests. In particular, I would like to thank Artur, who trained me from the very start of my thesis in the analysis methods used to study data from the HGCAL prototype, as well as Arabella, Thorben and Shilpi, with whom I had a great time working on the timing performance of HGCAL, and who gave me a lot of help and advice.

Moreover, I would like to thank all the people in the CJLST team and those

involved in the HZZ analyses with whom I was able to collaborate to carry out the high-mass resonance research. In particular, I would like to thank Nicola and Toni for helping me to understand where the problems of selecting high energy muons came from, Meng for taking the time to answer all my questions and for explaining the basics of modelling a high mass resonance, Savvas, Andrei and Giacomo for their advice and help, and finally Alessandra and Clara with whom I worked and shared a lot.

I am also very grateful for the opportunity to teach at École Polytechnique under the supervision of Alex. These two years of teaching were very interesting and allowed me to get out of my routine, while having a great time on Fridays with Alex, Matteo, Jona and Elena. Above all, I would never have eaten so much sushi and drunk so much Spritz without this opportunity.

In addition, I would like to thank all the postdocs and PhD students in the laboratory, with whom I had some very good times of sharing and captivating discussions around the coffee machine, at the Magnan, and even outside of work. First, I thank Matteo, Alessandro, and Alessandra for taking me to Italy from my office, and Ana and Isaac for saving me from the Italian invasion. Then, I would like to thank Alexandre, Andrès, Bruno, Duje, Geliang, Jona, Louis, Marco, Shamik and Uttiya for all the good times spent in and out of the laboratory, in a serious but also festive atmosphere. And let's not forget Elena for all those shared beers, for speaking so much French with me and for making my journeys on the mighty RER B more interesting and quicker.

Of course, I can't forget to thank all my friends from Chalon with whom I have a great complicity, and most of whom I know since I was a child. Thanks to Clément and Théo for all our adventures and for supporting a former student of the Ecole du Centre, which isn't an easy thing to do. Thanks to Maxime for taking me on as his model, because now I have someone who understands what I'm saying, even if he didn't choose the right collaboration. Thanks to Tim and Noé for reinforcing the Burgundian presence in the capital and for their support during difficult times. Thank you to Raphaël, the first of them, with whom our friendship last for over two decades. Thanks to Hugo for his wacky spirit and for being my reference in terms of "pince". Thanks to Jérémi for his frankness and his passion for snails. I thank them all for their unfailing friendship, support and invaluable help.

I extend my thanks to all my friends in Strasbourg, with whom I have continued to spend some of the best times I have had in engineering school. Not only that, but I would especially like to thank my former roommates Tristan and Julien, as well as Anthony, Kévin, Louis, Nicolas, Thibault, Théophile, Richard and all the others. Thanks to them, I was able to discover new cities and recharge my batteries to relieve the pressure of work.

Furthermore, I would like to sincerely thank my entire family, and in particular my mother Caroline, my father Olivier, my brother Austin, my sister Azalys, my grandmother Michelle, my grandfather Claude, my aunt Stéphanie and my uncle David, who were there at an important moment in my life. I would also like to thank my parents and grandparents for the education they gave me, which made me the curious and persevering man I have become. I would also like to thank my

whole family for the breaths of fresh air and nature they gave me when I returned to Chalon, far from the greyness of Paris. Finally, I would like to thank them enormously for their unfailing support, their encouragement, and the fact that I could always count on them.

I would also like to thank Delphine's family for their support, especially Philippe, Nathalie, Julie, and Camille.

And the best for the end, I would especially like to thank Delphine who has been my greatest ally on this journey. These years were not easy, but she was always there to support me, even though we were both doing a PhD at the same time. Without her, those long months of confinement, curfews, and other restrictions would have been much harder to endure. Furthermore, she knew how to reinvigorate me when my motivation dropped and cheer me up. I am enormously grateful for her patience and strength in enduring me, even though it was very complicated for her too. In short, if there is one person I have to thank, it is her, and I'm still infinitely grateful to her for everything she did from the beginning to the very end of this thesis. And finally, I'm joining her in the doctors' club.

Table of contents

Résumé i

Abstract iii

Acknowledgments v

Table of figures xiii

Introduction 1

1 Introduction to the Standard Model of Particle Physics and beyond 5
1.1 The Standard Model of Particle Physics 6
1.1.1 Elementary particles 6
1.1.2 Fundamental interactions and gauge theory 8
1.1.3 Spontaneous symmetry breaking and the Higgs mechanism 14
1.2 Limits of the Standard Model and new theories 17
1.2.1 The limits of the Standard Model 17
1.2.2 The world beyond the Standard Model 19
1.3 Phenomenology of the Higgs boson 20
1.3.1 Production mechanisms 20
1.3.2 Decay modes 24
1.3.3 Higgs boson properties 25
1.4 Focus on the Golden Channel and its possibilities 28
1.4.1 Interests of the Golden Channel 29
1.4.2 Status of the search of high mass resonance 30

2 The Large Hadron Collider and the CMS experiment 35
2.1 The Large Hadron Collider 35
2.1.1 The birth of the Large Hadron Collider at CERN 36
2.1.2 Design of the apparatus 37
2.1.3 The physics experiments 42
2.1.4 The Large Hadron Collider during operation 44
2.2 The Compact Muon Solenoid detector 47
2.2.1 General overview of CMS 48
2.2.2 The subdetectors and equipments 50
2.3 Reconstruction of particles 66
2.3.1 The particle flow algorithm 67

2.3.2 Identification and reconstruction of particles 69

3 The High Granularity Calorimeter and its prototype 77
3.1 The CMS detector during the High Luminosity LHC 78
3.2 Reminder of calorimetry and interaction of particles with matter . . 80
3.2.1 Interaction of particles with matter 81
3.2.2 Electromagnetic showers 85
3.2.3 Hadronic showers 86
3.2.4 Concepts of calorimetry 88
3.3 The High Granularity Calorimeter 91
3.3.1 HGCAL design 91
3.3.2 Focus on HGCAL silicon sensors 95
3.4 HGCAL prototypes and test beams 99
3.4.1 Silicon module prototype 99
3.4.2 Assembly of the detector prototype and test beams 100
3.4.3 Signal reconstruction 103
3.4.4 Timing information from the prototype 107
3.4.5 Simulation of the test beam with Geant4 111

4 Performance of the High Granularity Calorimeter prototype 113
4.1 Energy and spatial performance of EM shower detection 114
4.1.1 Information selection 114
4.1.2 Energy resolution 115
4.1.3 Spatial reconstruction characteristics 117
4.2 Energy and spatial performance of hadronic shower detection . . . 120
4.2.1 Information selection 121
4.2.2 Energy resolution 122
4.2.3 Spatial reconstruction characteristics 123
4.3 Timing performance 125
4.3.1 Reconstruction of the timing information and selection . . . 125
4.3.2 Impact of the geometry on the timing performance 136
4.3.3 Single channel timing performance 139
4.3.4 Full shower performance 144
4.4 Conclusion on the HGCAL prototype performance 151

5 The Golden Channel for the search of high mass resonance 155
5.1 Object selection 156
5.1.1 Electrons 156
5.1.2 Muons 162
5.1.3 Photons 167
5.1.4 Jets 168
5.1.5 Summary of the object selection 171
5.2 Event selection 172
5.2.1 Trigger selection 172
5.2.2 Z boson reconstruction 173
5.2.3 ZZ candidate selection 175
5.2.4 Optimization of the selection 176

5.3 Event categorization . . . 188
5.3.1 Observables and discriminants . . . 188
5.3.2 Categories at high mass . . . 191

6 Modelling of signal process and background 195
6.1 Signal and background simulation . . . 196
6.1.1 Signal simulation samples . . . 197
6.1.2 Background simulation samples . . . 197
6.2 Background modelling . . . 198
6.2.1 Irreducible background . . . 198
6.2.2 Reducible background . . . 202
6.2.3 Summary of the background modelling . . . 210
6.3 Signal modelling . . . 211
6.3.1 Analytical line shape of the signal . . . 212
6.3.2 Signal efficiency . . . 213
6.3.3 Signal resolution . . . 216
6.3.4 Validation of the signal model . . . 219

7 Statistical analysis and results on the high mass resonance search 221
7.1 Statistical analysis strategy . . . 222
7.1.1 Method of the maximum likelihood . . . 222
7.1.2 The signal and background template parametrization . . . 224
7.1.3 Interferences contribution to the model . . . 226
7.2 Systematic uncertainties . . . 227
7.2.1 Experimental uncertainties . . . 228
7.2.2 Theoretical uncertainties . . . 229
7.2.3 Summary on the uncertainties . . . 230
7.3 Results on the search of high mass resonance . . . 231

Conclusion 237

Appendix 241

Acronyms List 245

Bibliography 249

Table of figures

1.1 Classification of the Standard Model of Particle Physics. The graviton on the right is a hypothetical particle propagating the gravitational force, which is still not explained with the Standard Model. Particle masses are from [1] 7
1.2 Representation of the Higgs potential $V(\phi)$ 15
1.3 Standard Model Higgs boson production cross-sections at $\sqrt{s} = 13$ TeV as a function of the centre of mass energy [2] 21
1.4 Feynman diagrams of the principal Higgs boson production modes: (a) the gluon fusion (ggH), (b) the vector boson fusion (VBF), (c) the associated production with a vector boson (VH), and (d) the associated production with a pair of quarks ($t\bar{t}$H) or ($b\bar{b}$H). 21
1.5 Standard Model Higgs boson production cross-sections at $\sqrt{s} = 13TeV$ as a function of m_H [2]. On the left, a zoom around 125 GeV, and on the right over the wide mass range. 23
1.6 Cross-sections for ggH, VBF, WH, ZH and $t\bar{t}H + tH$ normalized to their theoretical predictions. The black error bars correspond to the total, blue boxes are the systematic uncertainties and yellow boxes show statistical uncertainties. The grey bands indicate the theoretical uncertainties in SM [3] 23
1.7 Principal decay modes of the Higgs boson: (a) the decay in two photons by the way of t quarks triangle, (b) the decay in two vector bosons, (c) the decay in a pair $b\bar{b}$ or $c\bar{c}$, and (d) the decay in a pair $\tau^-\tau^+$ or $\mu^-\mu^+$. 24
1.8 Standard Model Higgs boson decay branching ratios as a function of m_H [2]. On the left, a zoom around 125 GeV, and on the right over the wide mass range. 25
1.9 Mass of four leptons distribution obtained using $H \to ZZ \to 4l$ events from full Run II data. The figure on the left was made by the ATLAS Collaboration [4] and the figure on the right was made by the CMS Collaboration [5] 26
1.10 The likelihood scan of the measured Higgs boson mass in the decay channels $H \to \gamma\gamma$ (blue) and $H \to ZZ \to 4l$ (red). The combination (black) was done with 2016 data only. The solid lines are for the full likelihood scan including all uncertainties, while the dashed lines show the likelihood scan with the statistical uncertainty only [6] . . 26

1.11 Relation between the width Γ_H and the mass m_H of the Higgs boson [7] 27
1.12 Higgs boson couplings to other particles as a function of mass. The predictions by the SM is indicated by the dashed line, and the ratios between measured couplings and SM predictions are shown in the lower panel [8] 28
1.13 Feynman diagram of the "Golden Channel": $H \to ZZ \to 4l$ 29
1.14 Expected and observed upper limits at the 95% CL on the $pp \to X \to ZZ$ cross-section as a function of m_X and for $\Gamma_X = 4$ MeV. The ggF category is represented on the left, and VBF on the right. The results are shown for $4l$ in red, $2l2q$ in black, and $2l2\nu$ in purple. They are also combined and with the $\pm 1\sigma$ in green and $\pm 2\sigma$ in yellow. These results using CMS 2016 data are taken from [9]. . . . 31
1.15 Expected and observed upper limits at the 95% CL on the $pp \to X \to ZZ$ cross-section as a function of m_X and for $\Gamma_X = 100$ GeV. The ggF category is represented on the left, and VBF on the right. The results are shown for $4l$ in red, $2l2q$ in black, and $2l2\nu$ in purple. They are also combined and with the $\pm 1\sigma$ in green and $\pm 2\sigma$ in yellow. These results using CMS 2016 data are taken from [9]. . . . 31
1.16 Expected and observed upper limits at the 95% CL on the $pp \to X \to ZZ$ cross-section as a function of m_X and for $\Gamma_X = 4$ MeV. The ggF category is represented on the left, and VBF on the right. The results are shown for $4l$ in blue, and $2l2\nu$ in red. They are also combined and with the $\pm 1\sigma$ in green and $\pm 2\sigma$ in yellow. These results using ATLAS Run-2 data are taken from [10]. 32

2.1 Schematic representation of the CERN accelerator complex [11]. . . 36
2.2 QCD representation of a proton. Three valence quarks in green, are at the middle of the sea of quarks, anti-quarks in orange, and gluons represented by springs. The figure is taken from [12]. 38
2.3 Schematic representation of a transverse slice of a cryo-dipole of the LHC (lengths are in mm) [13]. 40
2.4 LHC and High Luminosity LHC schedule [14]. 45
2.5 Peak luminosity (on top) and integrated luminosity (on bottom) measured by CMS over time, the three runs are represented: full Run 1 from 2010 to 2012, full Run 2 from 2015 to 2018, and the start of Run 3 in 2022 [15]. 46
2.6 Interactions per bunch crossing, each year of Run 1 and Run 2 are stacked [15]. 47
2.7 View of a longitudinal slice of the CMS detector [16]. 48
2.8 CMS coordinate system in regard to the LHC on the left, and internally with the cylinder representation of CMS on the right. 49
2.9 Relation between the θ of the CMS coordinate system and the pseudorapidity η. 50
2.10 View of the CMS detector partially open [16]. 51
2.11 Schematic representation of a slice of the inner tracker of CMS [17]. 52

2.12 Pixel detector of the inner tracker of CMS. Perspective view on the left and side view on the right [18]. 52
2.13 Simulated material budget expressed as the tracker thickness t over the radiation length X_0, and described as a function of the pseudorapidity. The contribution of each sub-system of the tracker, the beam pipe, and the support tube are described η [17]. 54
2.14 Schematic views of the Electromagnetic Calorimeter of CMS [19]. On the left, an illustration in perspective, and on the right, a representation of a longitudinal slice of a quarter of ECAL. In the barrel, the $PbWO_4$ crystal bars organized in modules and super-modules. And on each side of the endcaps, there is a preshower inside and a dee outside. 56
2.15 Relative response to laser light injected in the ECAL $PbWO_4$ crystals depending on the pseudorapidity η and averaged over all the crystals. Data taking periods corresponding to the years 2011, 2012, 2015, 2016 and 2017 are represented, with the corresponding LHC luminosity on the bottom part [20]. 57
2.16 Schematic representation of a longitudinal slice of a quarter of the Hadronic Calorimeter of CMS [21]. 58
2.17 Schematic view of the CMS magnet field [22]. Spatial representation of the magnetic field is obtained from a simulation. 60
2.18 Schematic view of a longitudinal slice of a quarter of the CMS detector [23] 61
2.19 Summary of the cross-section measurements of Standard Model processes produced by the CMS experiment. Measurements are done for $\sqrt{s} = 7$ TeV in red, 8 TeV in blue, and 13 TeV in green. . . 63
2.20 Dataflow for the Level 1 trigger [24]. Information are from the calorimeters and the muon system. 64
2.21 View of a transverse slice of the CMS detector with detected particles [25]. 66
2.22 Event display of a jet made of five particles only in the (x, y) view in the upper plot, in the (η, ϕ) view of the ECAL surface in the lower left plot and the HCAL surface in the lower right [26]. 68
2.23 Efficiency of PF muon identification from a Z boson decay as a function of p_T on the left, and as a function of η on the right [26]. . 70
2.24 Schematic workflow of electron reconstruction [27]. 72
2.25 Reconstructed electron with photons coming from bremsstrahlung effect [26]. The recorded tracks are represented with the black points and the energy deposits are shown in the ECAL. 72
2.26 Electron seeding efficiency for electrons (triangles) and pions (circles) as a function of p_T. Both the efficiencies for ECAL seeding only (empty symbols) and with the tracker seeding added (full symbols) are displayed [26]. 73
2.27 Schematic procedure of jet energy correction for data and simulation [28]. RC corresponds to random cone, and MJB stands for multiple jets' events. 74

2.28 Jet energy resolution corresponding to the Gaussian width of the ratio between the corrected and reference jet energies, on the left. Jet energy response, corresponding to the mean ratio of the reconstructed jet energy to the reference jet energy, on the right. Both are a function of the reference jet p_T. Results are shown for jets in the barrel ($\eta < 1.3$) with the anti-k_T algorithm with $R = 0.4$ following the PF and calorimeter approaches [26]. 75
2.29 Relative missing transverse energy resolution as a function of expected missing transverse energy [26], from the calorimeters approach in blue and from the PF algorithm in red. 76

3.1 Open view of the CMS detector with the indication of the foreseen upgrades for the HL-LHC [29]. 79
3.2 Evolution of the cross-sections of photon interactions with atoms as a function of the photon energy [30]. Carbon is considered on the left, and lead on the right. There are different photon interactions, which are the Rayleigh scattering $\sigma_{Rayleigh}$, the Compton scattering $\sigma_{Compton}$, the photoelectric effect $\sigma_{p.e.}$, pair production by nuclear fields κ_{nuc}, the pair production by electron fields κ_e, and the photonuclear absorption $\sigma_{g.d.r.}$. 82
3.3 The energy loss fraction per radiation length X_0 of electrons and positrons in lead as a function of particle energy [30]. The ionization is represented by a light blue line for electrons and in an orange dashed line for positrons, Bremsstrahlung is in red, the Møller scattering in burgundy, the Bhabha scattering in green, and the positron annihilation is dark blue. 83
3.4 The evolution of the mean energy loss of anti muons in copper as a function of the muon momentum [30]. The total energy loss is represented with the solid curves. The large vertical lines are boundaries between different approximations, and for instance the Bethe-Bloch equation is used between $0.1 < \beta\gamma < 1000$. 85
3.5 Representation of the development of an electromagnetic shower, initiated by a photon passing through an absorber material. The scheme is obtained from [31]. 86
3.6 Representation of the development of a hadronic shower, initiated by a neutron passing through an absorber material. The decay products are constituted by an electromagnetic shower, a heavy fragment, and other light hadrons such as pions or neutrons. The scheme is obtained from [31]. 87
3.7 On the left, the spatial distribution of the accumulated dose of ionizing radiation, and on the right, the accumulated fluence parametrized with 1 MeV equivalent neutrons. Both are in HGCAL after an integrated luminosity of 3000 fb^{-1}, simulated using the FLUKA program, and shown as a two-dimensional map in the radial and longitudinal coordinates [32]. 92

3.8 View of a section of the HGCAL. The CE-E and CE-H compartments comprise silicon sensor modules, represented in green. The SiPM scintillator tiles are employed in the back of the hadronic compartment and are drawn in blue, the figure is taken from [33]. The expected HGCAL coverage is shown with orange dashed lines, ranging from $\eta = 1.5$ up to $\eta = 3.0$. 93
3.9 Illustration of a layer of the electromagnetic compartment on the left, and of the hadronic compartment on the right [32]. The yellow and green hexagons are the silicon modules, and the scintillating tiles are represented in red. On the left, the colour intensity corresponds to the different sensor thickness of 120, 200, or 300 μm. 94
3.10 Comparison of modules with two different cells' size, the 1.0 cm^2 active area is represented on the left and the 0.5 cm^2 on the right [32]. 94
3.11 Electromagnetic shower containment, expressed as the radii ρ of the cylinder containing 68% and 90% of the energy deposited in a single silicon layer. The colour corresponds to the proportion of the total shower energy detected in the layer [32]. The red dashed line represents the Molière radius. 95
3.12 A PN junction where the electron concentration is reported with a blue lines, and hole one in red. The grey regions have a neutral charge. The pink zone is positively charged, while the light blue zone is negatively charged. Plots under the junction illustration stand for the evolution along the x axis of the charge density, the electric field and the voltage. 96
3.13 Composition of a silicon module and their placement in the copper plate. Each module is a stack of different layers, starting with a baseplate at the bottom, covered with a gold plated Kapton foil on which stands the silicon sensor. A protected PCB with read-out chip is placed on top [32]. 98
3.14 Prototype HGCAL hexaboard, based on a silicon sensor module covered with PCB and electronic readout chips. 99
3.15 Schematic of the H2 beam line. The length of the beam line from the SPS to the test area PPE172 is $\sim$600 m. It comprises the T2 target made of beryllium, collimators, dipole, and quadrupole magnets whose operating parameters can be modified depending on the beam requirements. The NA61 experiment is located in front of PPE172 and adds some amount of passive material to the beam line. 100
3.16 The HGCAL prototype experimental setup used during the 2018 test beam. The electromagnetic section that is the subject of this analysis is denoted as CE-E. It is preceded (to the left) by multiple ancillary beam instrumentation detectors, and is followed by detector prototypes dedicated to the study of hadron showers. . . . 102
3.17 The HGCAL prototype during the 2018 test beam. The electromagnetic section is denoted as CE-E, it is followed by the hadronic part composed of silicon sensors in CE-H and AHCAL scintillating tiles. 103

3.18 Simplified block diagram of HGCROC chip [32]. The preamplifier block is circled in orange, the section computing the ToA is circled in red, and the part responsible for the ToT in blue. In green, there is the entire block in charge of the hit energy calculation. 104
3.19 Two example waveforms for low gain on the left, and high gain on the right. Both due to a signal of about 10 MIP from a 280 GeV/c electromagnetic shower [34]. The fits are shown with the red lines. 104
3.20 High and low gain amplitudes represented with the ToT as a function of the input signal, expressed in MIP ($\sim$3 fC) [34]. The vertical lines stand for the maximum input signals, where the high-gain and low-gain shaper outputs were linear. 106
3.21 Event reconstruction procedure of the HGCAL prototype data. Raw data are given by the EUDAQ input file are coloured in green. This data is merged with reconstructed information from beam characterizing detectors. Reconstructed data are stored in the EDM file format for analysis with CMSSW, or as ntuples. 106
3.22 Diagram of the ToA computation blocks in the Skiroc2-CMS ASIC [35]. 107
3.23 Illustration of the ToA ramp operation in the Skiroc2-CMS for two different cases: a ToA trigger signal after the rising clock edge and before the falling clock edge on the left, and vice versa on the right [35]. 108
3.24 The routing of the 40 MHz clock on the hexaboard PCB is illustrated on the left. The clock is routed sequentially through the chips, starting from the clock buffer at the top of the image. The mapping of the traces connecting the silicon bonding pads and the read-out chip inputs on the right. 109
3.25 Single MCP time resolution estimated as $\sigma/\sqrt{2}$, where σ comes from a Gaussian fit to the distribution of time differences between the two MCPs operated in front of the HGC prototype calorimeter. Given their identical structure, the timing resolution of the two MCP detectors was assumed identical. 110

4.1 Positron shower energy distribution for different beam energy. Data are represented on the top plot and MC simulation on the bottom plot. Each distribution is fitted with a Gaussian function, shown in green dashed line, and for data the range is $[\mu - \sigma, \mu + 2.5\sigma]$. 116
4.2 Mean measured energy as a function of the beam energy on the left. Measured energy resolution on the right [36]. Results obtained for data are represented in black, and in red for MC simulation. 117
4.3 Longitudinal shower profiles for different nominal positron beam energies given by the average number of hits on the left, and the median measured energy on the right [36]. Results obtained for data are represented in black, and in red for MC simulation. 118

4.4 Shower maximum as a function of the beam energy. The shower maximum is determined from the longitudinal profile fit [36]. Results obtained for data are represented in black, and in red for MC simulation. 118
4.5 The transverse profile of electromagnetic showers from positron beams with a nominal energy of 300 GeV is represented on the left. Results are computed in layers 3, 9 and 22. The shapes correspond to the energy deposited in a ring of cells, depending on its radial distance r from the seed channel. The energy normalization of the seed pad is performed for the layer under consideration [36]. On the right, the ratio of the mean energy contained in a cylinder of radius r over the overall event energy. R is the Molière radius evaluated from the fit using Equation 3.9. For both, the results obtained for data are represented in black, and in red for MC simulation. 120
4.6 Energy response of hadronic showers on the left and energy resolution on the right, both depending on the beam energy [37]. All pions are represented in black, only CE-E pions in blue, and only CE-H pions in red. 122
4.7 Longitudinal profiles of hadronic showers induced by pions with different energy [37]. The vertical dashed lines separate the different parts of the prototype. On the left, the shower is initiated in the CE-E, while on the right it starts in the CE-H. 123
4.8 Fraction of energy contained in a cylinder with a varying radius [37]. Data and both MC simulation samples are presented. On the left, the shower is initiated in the CE-E, while on the right it starts in the CE-H. 124
4.9 Timing measurements used in the calibration of the calorimeter hit timestamps. CPD denotes an arbitrary, but constant, clock-phase-difference between a given readout channel and the reference clock. 126
4.10 Location of the calibrated channel of the HGCAL prototype. 126
4.11 The three ToA calibration steps (ToA-rise in this case) of a representative channel, centrally located inside the HGCAL prototype: (a) Linearization of the normalised ToA, (b) assessment of the signal-induced time-walk correction, and (c) assessment of the residual correction, a smaller time-walk that depends on the total energy in the module of the given channel. The magnitude of the time-walk corrections is about one and two orders of magnitude smaller than the calibrated time range, respectively. 129
4.12 ToA_{fall} - MCP distribution depending on the normalized ToA. On the left, the clock correction is not applied, but it is the case on the right. 130
4.13 Normalized ToA distribution. ToA_{rise} is represented in blue and ToA_{fall} in red. The standard ToA distributions are on the left, and the cumulative ones on the right. 130
4.14 Normalized ToA cumulative distribution for different layers on the left, and their associated inverted curves on the left. 131

4.15 ToA non linearity correction function. Black points correspond to the average non linearity over all the channels. The blue and orange curves are the fits. 131
4.16 TW depending on the normalized ToA. Each colour corresponds to a specific cell energy range. The ToA_{fall} is on the left, and the ToA_{rise} is on the right. 132
4.17 Average of the TW depending on the normalized ToA and represented for different cell energy ranges, each colour corresponds to an energy range. ToA_{rise} is represented on the right and ToA_{fall} on the left. 133
4.18 Average of the $TW - TW_{ref}$ depending on the normalized ToA, where TW_{ref} is the TW for specific energy range taken as a reference. Each colour corresponds to a specific cell energy range. The ToA_{fall} is on the left, and the ToA_{rise} is on the right. 133
4.19 Average of the $TW - TW_{ref}$ depending on the normalized cell energy, where TW_{ref} is the TW for specific energy range taken as a reference. The ToA_{fall} is on the left, and the ToA_{rise} is on the right. . 134
4.20 Time-evolution (a–c) of a 250 GeV electron-induced shower (d) in the HGCAL prototype. Data are shown for 81 hits with reconstructed timestamps. If both ToA variants are within their linear region, timestamps are computed from an average of both. Otherwise, the variant in or closest to its linear region is taken. The size and colour of the markers both correspond to the reconstructed hit energy. 135
4.21 ToA distribution of layer 6 from 100 GeV positron beam. On the left, the raw distribution is shown, while on the right only the smallest interval with 68% of the ToA per event is kept. 136
4.22 ToA distribution over all the layers for 20, 150, and 300 GeV. A Gaussian fit is performed and illustrated in orange. 137
4.23 Smeared ToA distribution over all the layers for 20, 150, and 300 GeV. A Gaussian fit is performed and illustrated in orange. 137
4.24 Smeared ToA distribution over all the cells of a single layer for 100 GeV. From left to right, layers 1, 10, and 20 are shown. A Gaussian fit is performed and illustrated in orange. 138
4.25 Standard deviation of the Gaussian fit done on ToA distribution for each beam energy and as a function of the layer. On the left, 7 cells are used, then 19 cells in the middle, and all the cells on the right. . 139
4.26 Mean time of the Gaussian fit done on ToA distribution for each beam energy and as a function of the layer. On the left, 7 cells are used, then 19 cells in the middle, and all the cells on the right. . . . 140
4.27 Standard deviation (on the left) and mean time (on the right) of the Gaussian fit done on ToA distributions as a function of the beam energy. In red 7 cells are used, in blue 19 cells, and all the cells in green. 141

4.28 *ToA* distribution from data for a given positron beam energy. The blue distribution corresponds to the smallest interval containing 68% of the total *ToA* distribution represented in light red. From left to right, the positron beam energy is respectively equal to 30, 150, and 300 GeV. 141
4.29 Experimental *ToA* distribution for a given range of cell energy. These distributions are fitted with a Gaussian function represented by the red line. From left to right, the cell energy range is respectively equal to [50,64] MIP, [107,138] MIP, and [384,496] MIP. 142
4.30 Comparison of the HGCAL prototype timing resolution for electron showers in data and simulated samples. For data, the resolution is measured for all layers using the MCP as a reference (black squares) as well as using only half the layers with respect to the other half and assuming they have identical resolution (purple triangles). Other measurements in the plot allow cross-checking and confirm the hypothesis that a global jitter between the MCP and HGCAL systems was present in the data. 142
4.31 Single channel resolution as a function of the channel energy, using an other channel as timing reference chosen to be in a different module modules (orange) or on the same module (blue). 143
4.32 *ToA* distribution from simulation for a given positron beam energy. Blue distribution correspond to the smallest interval containing 68% of the total *ToA* distribution represented in light red. From left to right, the positron beam energy is respectively equal to 30, 150, and 300 GeV. 144
4.33 Smeared *ToA* distribution from simulation for a given positron beam energy. The blue distribution corresponds to the smallest interval containing 68% of the total smeared *ToA* distribution represented in light red. From left to right, the positron beam energy is respectively equal to 30, 150, and 300 GeV. 145
4.34 2D *ToA* distribution as a function of the cell energy. Blue points correspond to the median value of each energy bin. The *ToA* distribution is on the left, and the smeared *ToA* distribution is on the right. 145
4.35 Time resolution constant term as a function of the hit energy threshold, only a single electron energy is considered. The resolution is measured for full layers, firstly using the MCP as reference and with a jitter subtraction (black circles linked with blue dashed lines), and secondly the intrinsic HGCAL resolution (black triangles linked with orange dashed lines). 146
4.36 Smeared *ToA* distribution from simulation for a given positron beam energy. These distributions are fitted with a Gaussian function represented by the red line. From left to right, the positron beam energy is respectively equal to 30, 150, and 300 GeV. 146

4.37 Correlation matrices between two channels, where they can be from different modules and connected to different chips. Correlation of the mean value on the left, and the resolution on the right. 148
4.38 For electron showers contained in the HGCAL prototype, their average time on the left, and their timing resolution as a function of the beam energy on the right, for both beam data and simulated MC data. 148
4.39 For pion showers contained in the HGCAL prototype, their average time on the left, and their timing resolution as a function of the beam energy on the right, for both beam data and simulated MC data. 149
4.40 Resolution of the event-by-event difference between the time of electron half-showers computed with only even layers and only odd layers separately, as obtained for beam data (blue) and simulated Monte Carlo data (red). Results using positron beams are given on the left, and with pion beams on the right. The green markers correspond to beam data resolutions divided by $\sqrt{2}$, and are an estimate of the performance expected if all the layers were used for the shower time estimation. These measurements are not affected by the jitter between MCP and HGCAL. 150
4.41 Time resolution of the reconstructed electron showers as a function of the energy sum on the left, and of the number of hits on the right. 150
4.42 For the hits used in the reconstruction of the same 300 GeV electron showers, the time distribution of the fraction of hits on the left, and the energy distribution of the hits as a function of their calibrated time on the right. Beam data in full markers and simulated data in empty markers. 151
4.43 Time resolution of the reconstructed hadronic showers induced by pions as a function of the energy sum on the left, and of the number of hits on the right. 152
4.44 Comparison of the HGCAL prototype timing resolution for electron showers in data and simulated samples. For data, the resolution is measured for all layers using the MCP as a reference (black squares) as well as using only half the layers with respect to the other half and assuming they have identical resolution (purple triangles). Other measurements in the plot allow cross-checking and confirm the hypothesis that a global jitter between the MCP and HGCAL systems was present in the data. 153

5.1 The ROC curves of the MVA developed for the electron identification in 2018 data. The training was performed on the 2018 MC simulation samples. Performance are shown for electrons with $5 < p_T^e < 10$ GeV on the left, and $p_T^e > 10$ GeV on the right. Both are done for three different η_e regions: $|\eta_e| < 0.8$ on the top, $0.8 < |\eta_e| < 1.479$ in the middle, and $|\eta_e| > 1.479$ on the bottom. . . 159

5.2 The BDT score distribution for the signal is re presented in blue, and for the background in red. BDT scores for electrons are obtained from the training on the 2018 dataset in the high p_T^e and $|\eta_e|$ bin, corresponding to the region $5 < p_T^e < 10$ GeV and $|\eta_e| > 1.479$. . . 160
5.3 Electron pair energy distribution using $Z \to e^+e^-$ events. Data are represented with black points, while Drell-Yan background is represented in yellow and $t\bar{t}$ in green. Data corresponding to the 2016 period is shown on the top left, 2017 on the top right, and 2018 on the bottom. Electron energy scale correspond to the Double Crystal Ball fit mean and the resolution to the standard deviation. . 161
5.4 Muon pair energy distribution using $Z \to e^+e^-$ events. Data are represented with black points, while Drell-Yan background is represented in yellow and $t\bar{t}$ in green. Data corresponding to the 2016 period is shown on the top left, 2017 in the top right, and 2018 on the bottom. Muon energy scale correspond to the Double Crystal Ball fit mean and the resolution to the standard deviation. 165
5.5 Muon reconstruction and identification efficiency at low p_T for the 2018 dataset using the tag and probe method.It is represented as a function of p_T in the barrel on the left and in the endcap regions in the middle, and as a function of η for $p_T > 5$ GeV on the right. Data and MC agreement is represented in the lower panel. 166
5.6 Loose muon reconstruction and identification efficiency at low p_T for the 2018 dataset using the tag and probe method.It is represented as a function of p_T in the barrel on the left and in the endcap regions in the middle, and as a function of η for $p_T > 5$ GeV on the right. Data and MC agreement is represented in the lower panel. 167
5.7 The PU jet ID efficiency on $Z \to \mu^+\mu^-$+ jets is shown for the loose working point of the BDT model. The efficiencies for data and MC simulation are shown as a function of the jet η on the upper left, as a function of p_T for central jets on the upper right, and forward jets on the bottom. The figures are taken from [38]. 169
5.8 The effect of the L1 prefiring weights on 2017 MC samples for the ggH on the left, and VBF on the right. The samples without the L1 prefiring weight applied are depicted in the red histograms, while the blue histograms show the effect of the application of these weights. The plots are taken from [38]. 170
5.9 Distribution of m_{Z_1} using the full Run-2 statistic. Black points represent data, H signal in pink, and the backgrounds are $q\bar{q} \to ZZ$ in light blue, $gg \to ZZ$ in blue, EW in dark blue, and $Z + X$ in green. The plot on top left corresponds to 4μ, on top right to $4e$, on bottom left to $2\mu 2e$, and on bottom right to $4l$. 174
5.10 Distribution of m_{Z_2} using the full Run-2 statistic. Black points represent data, H signal in pink, and the backgrounds are $q\bar{q} \to ZZ$ in light blue, $gg \to ZZ$ in blue, EW in dark blue, and $Z + X$ in green. The plot on top left corresponds to 4μ, on top right to $4e$, on bottom left to $2\mu 2e$, and on bottom right to $4l$. 175

5.11 Distribution of m_{4l} using the full Run-2 statistic. Black points represent data, H signal in pink, and the backgrounds are $q\bar{q} \to ZZ$ in light blue, $gg \to ZZ$ in blue, EW in dark blue, and $Z + X$ in green. The plot on top left corresponds to 4μ, on top right to $4e$, on bottom left to $2\mu 2e$, and on bottom right to $4l$. Data are blinded after 200 GeV.176
5.12 Selection efficiency depending on m_H from 2018 MC simulation. ggH is represented on the left, while VBF is represented on the right. 4μ channel is coloured in blue, $2\mu 2e$ in red, and $4e$ in green. 177
5.13 Selection efficiency depending on m_H from 2018 MC simulation of ggH. From left to right, 4μ channel is shown, followed by $2\mu 2e$, and then $4e$. In black all the cuts are applied, in red SIP is removed, in green ISO is removed, in light blue ID is removed, in brown the OC is removed, in yellow SIP + ISO + ID are removed, and in blue SIP + ISO + ID + OC are removed. 178
5.14 Selection efficiency depending on m_H from 2018 MC simulation of VBF. From left to right, 4μ channel is shown, followed by $2\mu 2e$, and then $4e$. In black all the cuts are applied, in red SIP is removed, in green ISO is removed, in light blue ID is removed, in brown the OC is removed, in yellow SIP + ISO + ID are removed, and in blue SIP + ISO + ID + OC are removed. 179
5.15 Selection efficiency depending on m_H from MC simulation of VBF. Curves coloured in blue are related to 4μ, those in red to $2\mu 2e$, and those in green to $4e$. Intermediate colours are related to 2016, dark ones to 2017, and light ones to 2018. 180
5.16 On the left, the distribution of the minimal ΔR between a generated and a reconstructed muon from events failing the selection. On the left, the number of matching muons per event. 181
5.17 Distributions of the ratio of $p_{T_{\text{reco}}} / p_{T_{\text{gen}}}$. Each muon of an event is represented in a single plot. 182
5.18 Distributions of the number of muons per event, respecting $|p_{T_{\text{reco}}} / p_{T_{\text{gen}}} - 1| < k$. From left to right, k is equal to 0.05, 0.10, 0.15, and 0.20. . . . 183
5.19 Distribution of $p_{T_{\text{gen}}}$ in blue and $p_{T_{\text{reco}}}$ in red. Z_1 is represented on the left, Z_2 in the middle, and ZZ on the right. 183
5.20 Distributions of the ratio of $p_{T_{\text{reco}}} / p_{T_{\text{gen}}}$. Z_1 is represented on the left, Z_2 in the middle, and ZZ on the right. 184
5.21 Selection efficiency depending on m_H from 2018 MC simulation of VBF. 4μ channel is on the left and $2\mu 2e$ on the right. In black all the cuts are applied, in red SIP is removed, in green ISO is removed, in light blue ID is removed, in brown the OC is removed, in yellow SIP + ISO + ID are removed, in blue SIP + ISO + ID + OC are removed, and in grey SIP + ISO + ID + OC + Ghost Cleaner are removed. . . 184

5.22 ZZ mass distribution from VBF in 4μ at 3 TeV. On the left, the green distribution correspond to the events passing the standard selection, in red only the ghost muon cleaner module is activated only for muon with $p_T < 500$ GeV, and in blue it is deactivated. On the right, in green the fraction of shared segment should be lower than 25%, in red it is 50%, and 75% in blue. 185
5.23 ZZ mass distribution from $qq \to ZZ \to 4\mu$. On the left, the green distribution correspond to the events passing the standard selection, in red only the ghost muon cleaner module is activated only for muon with $p_T < 500$ GeV, and in blue it is deactivated. On the right, in green the fraction of shared segment should be lower than 25%, in red it is 50%, and 75% in blue. 186
5.24 ZZ mass distribution from 4μ events taken from data. The green distributions correspond to the events passing the standard selection, and in blue the ghost muon cleaner module is deactivated. A linear scale is used on the left and a logarithmic on the right. 187
5.25 Selection efficiency depending on m_H from 2018 MC simulation. 4μ decay channel is represented in blue and $2\mu 2e$ in red. The light colours correspond to the efficiency calculated with the standard selection, while the ghost muon cleaner is removed for the more intense colours. ggH is represented on the left and VBF on the right. 187
5.26 Illustrations of H boson production from ggH $gg \to H \to ZZ \to l^+l^-l^+l^-$ on the left, and from VBF $qq' \to qq'H \to qq'ZZ$ on the right. The five angles θ^*, θ_1, θ_2, Φ, and Φ_1 are shown in blue. The primary gluons and quarks are in brown. For ggH, the H boson is in red, while both Z bosons and the four leptons are in green. For VBF, in red are the H and Z bosons, in green are the two merging vector bosons. 189
5.27 Distribution of $\mathcal{D}_{bkg}^{kin}$ using $4l$ events from 2018 MC simulation. VBF signal is represented in red and ggH in blue, $q\bar{q} \to ZZ$ and $gg \to ZZ$ backgrounds are coloured in yellow and green respectively. From left to right the signal mass is 125, 1000, and 3000 GeV. 190
5.28 Distribution of $\mathcal{D}_{bkg}^{kin}$ using the full Run-2 statistic. Black points represent data, H signal in pink, and the backgrounds are $q\bar{q} \to ZZ$ in light blue, $gg \to ZZ$ in blue, EW in dark blue, and $Z + X$ in green. The plot on top left corresponds to 4μ, on top right to $4e$, on bottom left to $2\mu 2e$, and on bottom right to $4l$. 191
5.29 Distribution of $\mathcal{D}_{2jets}^{VBF}$ using $4l$ events from 2018 MC simulation. VBF signal is represented in red and ggH in blue. From left to right the signal mass is 125, 1000, and 3000 GeV. 192
5.30 Distribution of $\mathcal{D}_{2jets}^{VBF}$ using $4l$ events from the full Run-2. Black points represent data, H signal in pink for VBF and in light pink for ggH. The backgrounds are $q\bar{q} \to ZZ$ in light blue, $gg \to ZZ$ in blue, EW in dark blue, and $Z + X$ in green. Dashed lines corresponds to the selection cut used in the high mass analysis. 193

6.1 Distribution of $gg \to ZZ \to 4l$ background obtained from 2018 MC simulation. Black points represent the simulated data and the blue curve is the fit using Equation 6.3. On the upper left, the decay channel 4μ is represented, $2e2\mu$ on the upper right, and $4e$ on the bottom. 200
6.2 Distribution of $q\bar{q} \to ZZ \to 4l$ background obtained from 2018 MC simulation. Black points represent the simulated data and the blue curve is the fit using Equation 6.4. On the upper left, the decay channel 4μ is represented, $2e2\mu$ on the upper right, and $4e$ on the bottom. 201
6.3 Fake rates from the OS method as a function of the probe p_T and using 2018 data. The barrel selection is represented in blue and the endcaps in red. The solid lines correspond to fake rates before the correction of WZ contribution from MC and after with the dashed lines. Muons are represented on the left and electrons on the right. 204
6.4 Distribution of the invariant mass of $Z + X$ background estimated with the OS method from 2018 samples. Data in black are compared to MC simulation of WZ in pink, $Z\gamma$ or ZZ in turquoise, $Z+$ jets in green, and $t\bar{t}+$ jets in blue. On top left, the 4μ final state is represented at the side of $4e$, and the bottom, the $2e2\mu$ and $2\mu2e$ are represented. 206
6.5 Fake rates from the SS method as a function of the probe p_T and using 2018 data. The barrel selection is represented in blue and the endcaps in red. The solid lines correspond to fake rates before the correction of WZ contribution from MC and after with the dashed lines. Muons are represented on the left and electrons on the right. 207
6.6 Distribution of the invariant mass of $Z + X$ background estimated with the SS method from 2018 samples. Data in black are compared to MC simulation of WZ in pink, $Z\gamma$ or ZZ in turquoise, $Z+$ jets in green, and $t\bar{t}+$ jets in blue. On top left, the 4μ final state is represented at the side of $4e$, and the bottom, the $2e2\mu$ and $2\mu2e$ are represented. 208
6.7 Distribution of $Z + X$ background obtained from 2018 data represented in black. The blue curve is the fit using Equation 6.8. On the upper left, the decay channel 4μ is represented, $2e2\mu$ on the upper right, and $4e$ on the bottom. 210
6.8 Distributions of the main backgrounds for $X \to ZZ \to 4l$. $qqZZ$ in blue and $ggZZ$ in red are obtained from 2018 MC simulation, while $Z + X$ in green is estimated from 2018 data. The fit performed on each background is represented in the same colour. On the upper left, the decay channel 4μ is represented, $2e2\mu$ on the upper right, and $4e$ on the bottom. 211
6.9 Examples of signal analytical line shapes as a function of the generated four lepton mass m_{4l}^{gen}. Each curve corresponds to a specific combination of resonance mass m_X and width Γ_X. 213

6.10 Selection efficiency $\mathcal{E}(m_{4l}^{gen})$ as a function of the generated mass of the four leptons m_{4l}^{gen}, and calculated from MC signal samples. Full colours corresponds to ggH, and light colours to VBF. The 4μ final state is represented in blue, $2\mu 2e$ in red, and $4e$ in green. The fit performed on the six different decay channels are represented in the same colour. 214
6.11 Selection efficiency $\mathcal{E}(m_{4l}^{gen})$ taking into account the lepton acceptance as a function of the generated mass of the four leptons m_{4l}^{gen}, calculated from ggF MC signal samples on the left, and from VBF on the right. Full colours corresponds to the ggH category, light colours to VBF + 2 jets, and dark colours to the inclusive category. The 4μ final state is represented in blue, $2\mu 2e$ in red, and $4e$ in green. The fit performed on the six different decay channels are represented in the same colour. 215
6.12 Distributions of $m_{4l}^{\text{reco}} - m_{4l}^{\text{gen}}$ coming from ggH events shown with the black points and the DCB fits performed simultaneously over all the mass points are drawn in blue. The top plots correspond to 4μ final state, those in the middle to $2e2\mu$, and those on the bottom to $4e$. From left to right, three mass points are represented for all the final states: 300, 600, and 900 GeV. 216
6.13 Distributions of $m_{4l}^{\text{reco}} - m_{4l}^{\text{gen}}$ coming from VBF events shown with the black points and the DCB fits performed simultaneously over all the mass points are drawn in blue. The top plots correspond to 4μ final state, those in the middle to $2e2\mu$, and those on the bottom to $4e$. From left to right, three mass points are represented for all the final states: 300, 600, and 900 GeV. 217
6.14 Double Crystal Ball parameters obtained from $m_{4l}^{\text{reco}} - m_{4l}^{\text{gen}}$ distribution fit as a function of m_{4l}^{reco}. The parameters and their corresponding fits are plotted in the same colour with α_L in blue, α_R in light blue, μ in red, σ in black, n_L in yellow, and n_R in green. On the left ggH events are considered, and VBF on the right. From top to bottom, the final states 4μ, $2\mu 2e$, and $4e$ are represented. 218
6.15 Illustration of the signal model as a function of m_{4l}^{reco}. In blue, the signal corresponds to a resonance with $m_X = 200$ GeV and $\Gamma_X = 10$ GeV. In red, the resonance is defined by $m_X = 450$ GeV and $\Gamma_X = 20$ GeV, and multiplied by a factor 2. In green, the resonance is defined by $m_X = 1000$ GeV and $\Gamma_X = 30$ GeV, and multiplied by a factor 50. 219
6.16 Closure test of the signal model on ggH at 200 GeV on the left and VBF at 200 GeV on the right. The model is compared to the reweighted four leptons invariant mass distribution from MC simulation samples. 220

7.1 Conditional templates of $\mathcal{D}_{bkg}^{kin}$ depending on m_{4l}^{reco} calculated from MC signal samples. The upper row corresponds to ggH process and VBF is on the lower one. The first column corresponds to the 4μ channel, $2e2\mu$ for the second one, and $4e$ for the third one. On the colour scale, the more the bin is blue, the more the value is close to one. Inversely, the more the bin is yellow, the more the value is close to one. For each m_{4l} bin, the $\mathcal{D}_{bkg}^{kin}$ distribution is normalized to 1.225

7.2 Conditional templates of $\mathcal{D}_{bkg}^{kin}$ depending on m_{4l}^{reco}. The upper row corresponds to $ggZZ$ process, $qqZZ$ in the middle, and $Z + X$ on the lower one. The first column corresponds to the 4μ channel, $2e2\mu$ for the second one, and $4e$ for the third one. On the colour scale, the more the bin is blue, the more the value is close to one. Inversely, the more the bin is yellow, the more the value is close to one. For each m_{4l} bin, the $\mathcal{D}_{bkg}^{kin}$ distribution is normalized to 1. 226

7.3 Expected upper limits at 95% CL on the product of the X boson cross-section and the $X \to ZZ$ branching ratio as a function of the resonance mass m_X and with a fixed width $\Gamma_X = 1$ GeV. The limits are calculated from 2018 samples only and with $4l$ events from an inclusive category. f_{VBF} is set to 0 on the left, and to 1 on the right. 231

7.4 Expected upper limits at 95% CL on the product of the X boson cross-section and the $X \to ZZ$ branching ratio as a function of the resonance mass m_X. The resonance width is set to $\Gamma_X = 0.1$ GeV on the left and $\Gamma_X = 100$ GeV on the right. The limits are calculated with $4l$ events from 2018 samples, an inclusive category was used, and f_{VBF} is set to 0. 232

7.5 Expected upper limits at 95% CL on the product of the X boson cross-section and the $X \to ZZ$ branching ratio as a function of the resonance mass m_X. The four plots correspond to different resonance width $\Gamma_X = 0.1$, 1, 10, and 100 GeV. The limits are calculated from 2018 samples, with $4l$ events from an inclusive category, and f_{VBF} is set to 0. The blue curves represent the limits using a model without interference and with in red. 233

7.6 Expected upper limits at 95% CL on the product of the X boson cross-section and the $X \to ZZ$ branching ratio as a function of the resonance mass m_X. The limits are calculated from 2018 samples, with a resonance width $\Gamma_X = 0.1$ GeV, and f_{VBF} is set to 0. The black curve represents the limits of $4l$, 4μ in red, $2e2\mu$ in green, and $4e$ in blue. 234

7.7 Distribution of m_{4l} from high mass events using the full Run-2 statistic. Black points represent data, H signal in pink, and the backgrounds are $q\bar{q} \to ZZ$ in light blue, $gg \to ZZ$ in blue, EW in dark blue, and $Z + X$ in green. 234

7.8 Observed and expected upper limits at 95% CL on the product of the X boson cross-section and the $X \to ZZ$ branching ratio as a function of the resonance mass m_X. The resonance width is set to $\Gamma_X = 0.1$ GeV on the left and $\Gamma_X = 1.0$ GeV on the right. The limits are calculated with $4l$ events from 2018 samples, the two categories were used, and f_{VBF} is set to 0. 235
7.9 Observed and expected upper limits at 95% CL on the product of the X boson cross-section and the $X \to ZZ$ branching ratio as a function of the resonance mass m_X. The resonance width is set to $\Gamma_X = 1.0$ GeV. The limits are calculated with $4l$ events from 2018 samples, the two categories were used, f_{VBF} is set to 0 on the left and to 1 on the right. 235
7.10 Observed and expected upper limits at 95% CL on the product of the X boson cross-section and the $X \to ZZ$ branching ratio as a function of the resonance mass m_X. The resonance width is set to $\Gamma_X = 0.1$ GeV on the left and $\Gamma_X = 1.0$ GeV on the right. The limits are calculated with $4l$ events from 2018 samples, the two categories were used, and f_{VBF} is floating. 236
11 Distribution of the invariant mass of $Z + X$ background calculated in the 2P2F CR from 2018 samples. Data in black are compared to MC simulation of WZ in pink, $Z\gamma$ or ZZ in turquoise, $Z+$ jets in green, and $t\bar{t}+$ jets in blue. On top left, the 4μ final state is represented at the side of $4e$, and the bottom, the $2e2\mu$ and $2\mu2e$ are represented. 242
12 Distribution of the invariant mass of $Z + X$ background calculated in the 3P1F CR from 2018 samples. Data in black are compared to MC simulation of WZ in pink, $Z\gamma$ or ZZ in turquoise, $Z+$ jets in green, and $t\bar{t}+$ jets in blue. On top left, the 4μ final state is represented at the side of $4e$, and the bottom, the $2e2\mu$ and $2\mu2e$ are represented. 2P2F contribution is plotted with a red curve. 243

Introduction

The thesis you are about to read can be seen as an additional stone of the great edifice that is science. Its foundations were laid at the dawn of time, long before modern history, because it's in human nature to seek to understand and explain the things and phenomena that surround us. It's a characteristic that drives us to constantly ask ourselves questions, particularly about what we're made of. The first written traces of this thinking take us back to Ancient Greece in the 5^{th} century BC. It was at this time that the Greek philosopher Leucippus postulated the theory of atomism, which is the idea that the universe is made up of just two things: on the one hand, atoms, the indivisible elements that make up matter, and on the other, the void, which is the space in which the atoms are located.

However, it took more than two millennia before we knew exactly what atoms were. Indeed, it wasn't until the 19^{th} century that it was demonstrated that matter is composed of atoms, all with the same properties. Later in the same century, the indivisible nature of the atom was questioned with the discovery of electrons. This led to the idea of understanding the exact nature of atoms, and at the beginning of the 20^{th} century, experiments led to the discovery of the atomic nucleus and, later, to protons. Later during the 20^{th} century, technological advances enabled scientists to design and build the first particle accelerators, providing high energy particles for more detailed studies of the structure of atomic nuclei. Year after year, accelerators became more and more powerful, and the energy that particles could reach increased significantly. Experiments operating at this moment demonstrated that nucleons themselves are not fundamental particles, but are composed of quarks. Added to this the development of sophisticated particle detection techniques resulted in experiments that led to the discovery of many fundamental particles. At the same time, important theoretical works established the framework of quantum mechanics and special relativity. These theories laid the foundations for the definition of the Standard Model (SM) of particle physics, a quantum field theory with gauge symmetries formalized introducing the concept of spontaneous symmetry breaking across the physical vacuum was incorporated. Nowadays, this theory is still the best description of the subatomic world.

Despite the success of the SM in predicting experimental observations, it has serious limitations. For instance, it does not include a description of gravity, nor it does not explain the origin of dark matter, and the observed asymmetry between matter and antimatter. Even if the SM has helped to discover many of the secrets of the subatomic world and the laws that govern it, the quest for the fundamental constituents of the universe is not yet complete. This is why many new theories go beyond the SM and attempt to answer these questions. The aim of collider

based experiments, such as those at the Large Hadron Collider (LHC), is to test the limits of SM physics and look for signatures of new physics. The LHC at CERN is nowadays the world's most powerful particle collider. It collides proton beams at the centre of mass energy of 13 TeV at four points along its 27 km long ring. At each collision point, a detector is placed to detect the particles resulting from the high energy collisions. The Compact Muon Solenoid (CMS) is one such detector. The ultimate success of the SM came in 2012, when both the ATLAS and CMS collaborations announced the observation of a scalar particle compatible with the SM elementary Higgs boson. The existence of a physical H boson is presumed to be a consequence of the spontaneous breaking of electroweak symmetry. The discovery was made possible by the analysis of all the data collected by the experiments during the LHC Run-1 period. This was followed by LHC Run-2, lasting from 2015 until 2018, and giving access to a larger number of candidate Higgs bosons to study. This allowed to study the H boson with more precision and also to prove that the Higgs field is at the origin of fermion masses. Based on these data, it is already possible to undertake research into new physics. One promising area is the study of high mass events. Indeed, many BSM theories introduce new particles to explain phenomena not yet explained by the SM. The particles that are supposed to be the easiest to detect are scalar bosons with masses greater than the H boson.

Another solution would be to have more data to make precise measurements of various SM processes with smaller cross-sections, such as the self-coupling of the Higgs boson, and to discover particles predicted by many BSM theories. The future life phase of the LHC, also known as the High Luminosity LHC (HL-LHC), is designed to achieve this goal. The HL-LHC operation phase is scheduled to start in 2029 and last at least ten years. It will provide ten times more data than the LHC's operating phase, opening up many new physics perspectives. However, this poses several challenges for the detectors. As the HL-LHC collision rate increases, the detectors will suffer intense radiation damage and be confronted with large numbers of particles from additional proton-proton collisions.

But there is an issue, the current CMS detector is not designed to operate in such harsh conditions, indeed the higher radiation rate could damage the sensors and decrease the physics performance. Among the many improvements planned for the HL-LHC, the CMS collaboration will replace the current end calorimeters with the High Granularity Calorimeter (HGCAL). This will be a 5D detector, as it will be able to measure with a great precision the energy of particles, as well as their position in space and their time of arrival. Moreover, it will be the first high granularity silicon based calorimeter to be used in a high energy physics experiment, so a great effort is needed to validate its performances. For this reason, the first large scale prototype of the HGCAL was exposed to pion and positron beams with energies ranging from 20 to 300 GeV in October 2018.

This thesis has allowed me to address both these aspects, working first on a performance study of the HGCAL prototype used during the October 2018 beam tests. Initially, I carried out preliminary studies on the reconstruction of electromagnetic and hadronic showers. But the core of my work is based on the study of the timing performance of HGCAL cells and of full showers. The second

aspect was approached from the angle of a search for high mass scalar resonance using multi-lepton decay channels, with the aim of establishing limits on the production cross-section of such a resonance.

The first two chapters are intended to set the theoretical and experimental context of this thesis and introduce key concepts. To this purpose, Chapter 1 will review the fundamental elements of the Standard Model of particle physics, from the description of elementary particles and interactions to the presentation of its limitations. In addition, the latest results on the study of the Higgs boson and the search for high mass resonance are given. Chapter 2 describes all the experimental equipment, starting with the LHC and then focusing on the CMS experiment as a whole. Furthermore, explanations are given of the methods used to reconstruct the particles passing through the detector.

The next two chapters deal with the HGCAL project. Chapter 3 begins with a reminder of calorimetry, before explaining what the HGCAL project is and detailing what the future calorimeter will consist of. This chapter also introduces the HGCAL prototype and all the equipment used for the beam tests. Chapter 4 then focuses on the prototype's performance. Firstly, the work on characterizing the reconstruction performance of electromagnetic and hadronic sheaves. Secondly, the timing performance of prototype cells is studied, followed by those of full showers.

Finally, the last three chapters focus on high mass resonance research. Chapter 5 corresponds to the reconstruction, selection, and categorization of the objects and events of interest for the analysis. Chapter 6 then describes the modelling of background and the high-mass resonance signal. Finally, Chapter 7 presents the statistical test used, and the results obtained, corresponding to the limits on the production cross-section of a high mass scalar resonance.

Chapter 1

Introduction to the Standard Model of Particle Physics and beyond

Table of contents

1.1 The Standard Model of Particle Physics 6
1.1.1 Elementary particles 6
1.1.2 Fundamental interactions and gauge theory 8
1.1.3 Spontaneous symmetry breaking and the Higgs mechanism 14
1.2 Limits of the Standard Model and new theories 17
1.2.1 The limits of the Standard Model 17
1.2.2 The world beyond the Standard Model 19
1.3 Phenomenology of the Higgs boson 20
1.3.1 Production mechanisms 20
1.3.2 Decay modes 24
1.3.3 Higgs boson properties 25
1.4 Focus on the Golden Channel and its possibilities 28
1.4.1 Interests of the Golden Channel 29
1.4.2 Status of the search of high mass resonance 30

To begin our journey into the wonderful world of the infinitely small, let's start with a quick reminder of the different theories involved at this scale.

At our current level of understanding, the subatomic world is described by a set of physics theories grouped together in the so-called the Standard Model (SM) of Particle Physics. This model was born during the last century to offer a description of the interactions occurring at a subatomic scale. The SM is based on the Quantum Field Theory (QFT) making the link between the quantum mechanics and the special relativity. In this formalism, fields and particles are associated, fundamental particles are represented as a field fluctuation and the interactions as the exchange of a virtual particle. This model is a construction mixing theoretical and experimental advances, and it has been developed gradually. Indeed, at the beginning, the number and the nature of the particles were unknown, and they were added one after the other. The last one was the discovery of the Higgs boson

made in July 2012 by the collaborations A Toroidal LHC ApparatuS (ATLAS) and Compact Muon Solenoid (CMS) [39, 40], which are both working on the eponym experiments and both taking place in the Large Hadron Collider (LHC).

More details about the SM will be given in the Figure 1.1, with a synthesized presentation of the particles, interactions, and physics theories constituting it. As its name indicates it, it is just a model, and like all the models it has its own imperfections and limits. In order to have a better accurate prediction or to have an explanation of phenomena not described by the SM, other theories were postulated and will be discussed in Section 1.2. But let's get back to the matter at hand, most of the work done and on going in the CMS Collaboration is about the Higgs boson, and in Section 1.3 the last results about its characteristics will be given. And this chapter will be closed with the description of "Golden Channel", corresponding to the decay channel of the Higgs boson into four leptons. This channel used in the physics analysis at the end of this thesis will be explained in Section 1.4.

1.1 The Standard Model of Particle Physics

For a better understanding of the SM, it is necessary to start by knowing the elements that compose it. First, the elementary particles, corresponding to the smallest building blocks of matter. And secondly, the fundamental interactions acting like cement and giving the shape of the matter.

1.1.1 Elementary particles

The elementary particles mentioned in this thesis correspond to an isolated physical system representing a unit of matter. They are fundamental objects which are impossible to subdivide. All the known particles of the SM are shown on Figure 1.1

Particles can be arranged into two major groups: the fermions having a half integer spin ($s = \frac{1}{2}$) and respecting the Pauli exclusion principle. They are described by the Fermi-Dirac statistics, hence their name. Moreover, they are divided in two subgroups which will be described later: the leptons and the quarks, which are both matter particles. All the fermions are associated to anti-particles. The bosons having an integer spin ($s = 1$) and they are called like that because they follow the Bose-Einstein statistics. According to the QFT, they are the carriers of interactions.

Bosons

- **Gluons g:** There are eight gluons, which are massless particles, and they are the mediators of the strong interaction.
- **Photon γ:** It is the mediator of the electromagnetic force. The photon is a massless particle in the SM.
- **$W^{\pm}$ and Z bosons:** They are the vectors of the weak interaction, $W^{\pm}$ correspond to the charged weak current and Z to the neutral weak current.

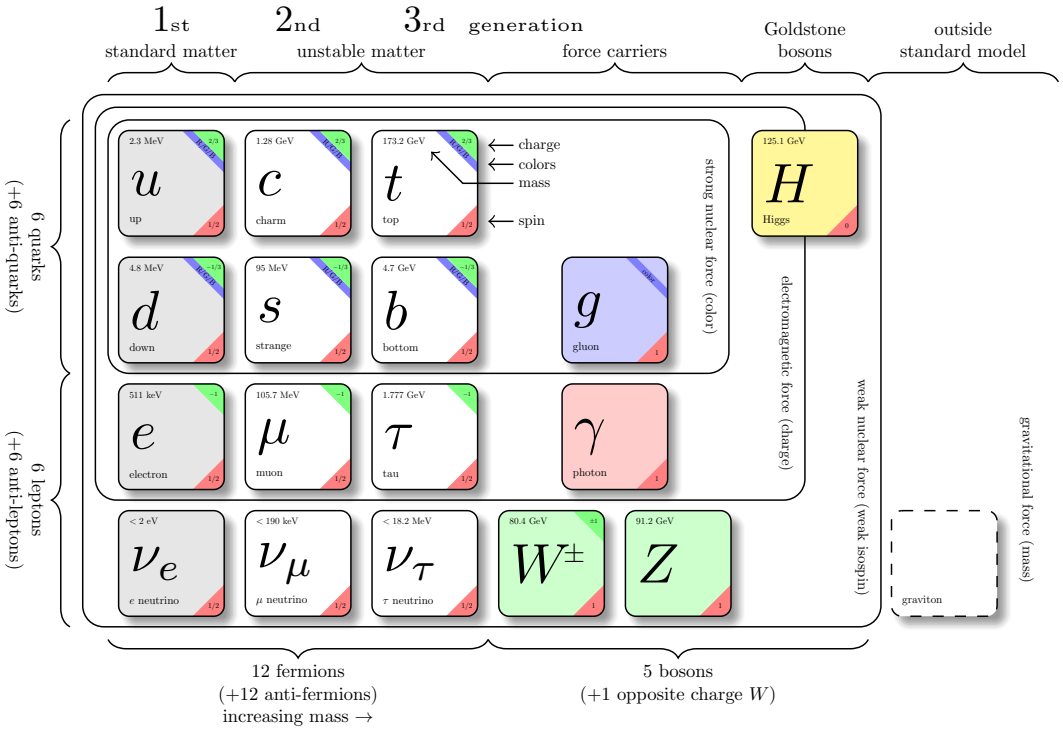

Figure 1.1: Classification of the Standard Model of Particle Physics. The graviton on the right is a hypothetical particle propagating the gravitational force, which is still not explained with the Standard Model. Particle masses are from [1]

- **Higgs boson** H**:** This boson gives a mass to all the other particles (except photons and gluons) and also to itself, this property comes from the electroweak symmetry breaking (EWSB). Finally, it is the only spin $s = 0$ boson, all the others have a spin $s = 1$.

Fermions

- **Quarks:** There are six quarks, divided into three doublets and each one corresponding to a generation. The first one is composed of the quark up (u) and the quark down (d). They are the two valence quarks composing the protons (uud) and the neutrons (udd). Indeed, they are the only stable quarks due to their low masses. The second doublet is composed of the quark charm (c) and the quark strange (s). Finally, in the third one, there is the top quark (t) and the bottom quark (b). The three doublets are :

$$\begin{pmatrix} u \\ d \end{pmatrix} \begin{pmatrix} c \\ s \end{pmatrix} \begin{pmatrix} t \\ b \end{pmatrix} \tag{1.1}$$

The first quark of each doublet has an electric charge $q = +\frac{2}{3}$ and the second quark has one equal to $q = -\frac{1}{3}$. Because of their non-null electric charge, they are sensitive to the electromagnetism. But, also to the weak and strong

nuclear forces. Due to this, they also have quantum numbers corresponding to their sensitivity to these three interactions. First, quarks have a colour, giving the name of Quantum Chromodynamic (QCD), and which control the possible action that they can have with the strong interaction. This phenomenon is called colour confinement in QCD, and it leads to the quarks to be observed bounded together, forming bigger structures called hadrons. A hadron, made with three quarks like protons or neutron, is a baryon. When a quark and an anti-quark are bounded together, the structure is called a meson. The anti-quark have the same properties as "normal" quark, but their quantum numbers will be the opposite. For instance, let's consider the quark up (u), it has an electric charge equals to $q = +\frac{2}{3}$, thus the one of the anti-quark up, noted $(\bar{u})$, is equal to $q = -\frac{2}{3}$. Quarks also interact with the weak force, introducing the flavour as a new quantum number proper to each quark. This number is conserved with the electromagnetic and strong nuclear force, but not with the weak one. This possible change of flavour with the weak interaction is described with the Cabibbo-Kobayashi-Maskawa (CKM) matrix [41], and to some extent, it corresponds to the violation of the charge and parity symmetries (CP) presented in Section 1.1.2.

- **Leptons:** Similarly to the quarks, the leptons are divided into three doublets composed of a charged lepton, with $Q = -1$, and a neutrino. By order of mass, there is the electron (e), followed by the muon (μ) and finally the tauon (τ). On the other hand, neutrinos, as their name suggests, have an electric charge $Q = 0$. Each neutrino is associated to a charged lepton and their name come from them. Thus, they are called electron neutrino (ν_e), electron neutrino (ν_μ), and electron neutrino (ν_τ).

$$\begin{pmatrix} e \\ \nu_e \end{pmatrix} \begin{pmatrix} \mu \\ \nu_\mu \end{pmatrix} \begin{pmatrix} \tau \\ \nu_\tau \end{pmatrix} \tag{1.2}$$

  From these leptons, the electron is the most stable one, thanks to is low mass compared to both other charged leptons. Furthermore, with the quarks up and down, it is part of the constituents of ordinary matter. In addition, concerning the forces which can be applied on leptons, charged leptons and neutrinos must be considered separately because the neutrinos are not sensitive to electromagnetic interaction due to their lacks of electric charge. But in contrast, the weak forces interact with both groups and like quarks, the lepton's flavour is not conserved with this interaction. The relations between leptons are described with the Pontecorvo-Maki-Nakagawa-Sakata (PMNS) matrix [42] and it explains the neutrino's oscillations.

1.1.2 Fundamental interactions and gauge theory

Four fundamental forces describe the interactions in the universe, but only three of them are described in the SM: the electromagnetic force, the weak and strong nuclear forces. The fourth one is the gravitation, which is well understood at large scale thanks to the general relativity. It does not have a satisfactory

formulation at subatomic scale, and it does not have its place inside the SM due to the fact that it is still not well understood and mainly because its propagator is unknown. According to the QFT, the fundamental components of matter are highly correlated to symmetry principles. In a mathematical point of view, a symmetry corresponds to the property of a system to be invariant when a specific transformation is applied to it. The principle of invariance is one of the basis of SM theories and is related to the gauge field theories. Moreover, the SM is one of the quantum field theories, and in addition to the gauge symmetries, it must respect the Poincaré symmetries. Thus, it is formalized in a flat 4-dimensional space-time.

As presented previously, the SM is mainly described by three theories which are the Quantum Electrodynamics (QED) for the electrodynamic interaction, the Quantum Chromodynamics (QCD) for the strong nuclear force, and the Electroweak Theory (EWT) introducing the electroweak interaction. This new force corresponds to the unification of electromagnetic and weak interactions.

The gauge principle of local invariance is used in order to introduce the symmetry group of the SM :

$$SU(3)_C \otimes SU(2)_L \otimes U(1)_Y \tag{1.3}$$

This formula can be explained by taking the terms one by one:

- $SU(3)_C$ is a Lie group of 3×3 unitary matrices, meaning that their determinant is equal to 1. The group generators are Gell-Mann matrices, and it controls the strong interaction of quarks and gluons. Then, the QCD explains the gathering of quarks into hadrons and the stability of the nucleus of an atom, dealing with the repulsive forces originating from the positive charges.
- $SU(2)_L$ is a Lie group of 2×2 unitary matrices, ruling the weak nuclear force of leptons and quarks.
- $U(1)_Y$ is a unitary group governing the electromagnetic interaction.

From this point, it is possible to build the Lagrangian of the strong and electroweak interactions. The electromagnetic and weak forces are taken together according to the theories of S. Glashow, S. Weinberg, and A. Salam [43, 44, 45] who demonstrated the unification of both forces in the symmetry group $SU(2)_L \otimes U(1)_Y$.

Strong interaction

To understand what is the strong interaction and where it comes from, let's build its associated Lagrangian, which is gauge invariant. The construction of SM Lagrangian is explained by M. Thomson in his book [46] and by M. Herrero in his lecture material [47]. Considering a field ψ associated to a fermion of spin $s = \frac{1}{2}$. The Dirac Lagrangian is written:

$$\mathcal{L}_{Dirac} = \overline{\psi}(x)(i\gamma^\mu \partial_\mu - m)\psi(x) \tag{1.4}$$

Where γ corresponds to the Dirac matrices.

In the case of QCD, the Lagrangian must be invariant with respect to the transformations from the $SU(3)_C$ symmetry group. In terms of equation, this is written as:

$$\psi'(x) = e^{ig_s\alpha^a(x)\frac{\lambda_a}{2}}\psi(x) \tag{1.5}$$

And when considering the space-time derivative of this in order to have a global invariance:

$$\mathcal{D}_\mu = \partial_\mu + ig_s\frac{\lambda_a}{2}G^a_\mu \tag{1.6}$$

Where $\frac{\lambda_a}{2}$ refers to the eight Gell-Mann matrices corresponding to the eight massless gluons. They have three degrees of freedom, one per each colour (blue, green, and red) and a self interaction. The coupling g_s is a constant, referring to the strength of the strong interaction. At the end, eight gauge fields G^a_μ represent the gluons, and they respect the gauge invariance given by:

$$G'^a_\mu = G^a_\mu + \alpha^b(x)f^{abc}G^c_\mu + \frac{1}{g_s}\partial_\mu\alpha^a(x) \tag{1.7}$$

Where f^{abc} represents the structure constants of the symmetry group $SU(3)_C$ and it satisfies the commutation rules defined by:

$$\left[\frac{\lambda^a}{2};\frac{\lambda^b}{2}\right] = if^{abc}\frac{\lambda^c}{2} \tag{1.8}$$

The last ingredient for the QCD Lagrangian is the field strength tensor. It will introduce trilinear and quadrilinear terms in the Lagrangian.

$$G^{\mu\nu}_a = \partial_\mu G^a_\nu - \partial_\nu G^a_\mu + g_s f^{abc}G^b_\mu G^c_\nu \tag{1.9}$$

Finally, the QCD Lagrangian is obtained by considering a summation of all the different quark fields, and by replacing these terms into the Dirac Lagrangian presented in the Equation 1.4:

$$\mathcal{L}_{QCD} = \overline{\psi}(i\not{\partial} - m)\psi - g_s\psi\gamma^\mu\frac{\lambda_a}{2}\psi G^a_\mu - \frac{1}{2}G^{\mu\nu}_a G^a_{\mu\nu} \tag{1.10}$$

The new operator $\not{\partial} = \gamma^\mu\partial_\mu$ is introduced in the Lagrangian, thanks to that, the first term corresponds to the former Dirac Lagrangian. The second term represents the interaction between quarks and gluons, and the last one refers to the self interaction of the gluon fields.

Electroweak interaction

The electroweak interaction (EW) was introduced in order to get the unification of the electromagnetic and weak interactions. It is described by the symmetry groups $SU(2)_L \otimes U(1)_Y$, which describe the EW interaction but not the electromagnetic one. It corresponds to the interaction existing before the symmetry

breaking. But, before diving in the details of EW, explanations about QED will be helpful.

QED explains the electromagnetic interaction, more precisely it corresponds to the phenomenon of electrical charged particles interacting with an exchange of photons. The symmetry group $U(1)_{em}$ describes this interaction and the construction of the QED Lagrangian is analogous to the QCD one, which gives this formula:

$$\mathcal{L}_{QED} = \overline{\psi}(i \not{D} - m)\psi - \frac{1}{4}F^{\mu\nu}F_{\mu\nu} \tag{1.11}$$

Where $F^{\mu\nu} = \partial^\mu A^\nu - \partial^\nu A^\mu$ and $\not{D} = \partial - ieA^\mu$. Similarly to the QCD, this Lagrangian is composed of two term s, the first one corresponding to the interaction term introduced by $\not{D}$, and the second one is a kinematic term corresponding to the propagation of the photon.

Some problems start when dealing with the weak interaction. Indeed, the parity violation must be taken into account. To do that, left and right-handed fermion fields are considered, and different interaction terms will be applied to them. This differentiation will be performed with a projection operator in which the gamma matrix is used $\gamma^5 \equiv i\gamma^0\gamma^1\gamma^2\gamma^3$:

$$P_L = \frac{1-\gamma^5}{2}\,, \quad P_R = \frac{1+\gamma^5}{2} \tag{1.12}$$

In $SU(2)_L$, the left-handed fermions are represented by a doublet and the right-handed by two singlets, represented below:

$$\Psi_L = \begin{pmatrix}\psi_L \\ \psi'_L\end{pmatrix} = \frac{1-\gamma^5}{2}\begin{pmatrix}\psi \\ \psi'\end{pmatrix}\,, \quad \psi_R = \frac{1+\gamma^5}{2}\psi\,, \quad \psi'_R = \frac{1+\gamma^5}{2}\psi' \tag{1.13}$$

Concerning the quantum numbers, the weak interaction is related to the weak isospin I_3 and the hypercharge Y. The first one is the quantum number associated to the symmetry group $SU(2)_L$. In fact, it corresponds to the three group generator $I_i = \frac{\sigma_i}{2}$ where σ_i is a Pauli's matrix. Moreover, three gauge fields W^i_μ, are needed to satisfy the gauge invariance. The choice of two singlets for the right-handed particles is justified by the fact that they do not interact with the W^i_μ fields. The hypercharge is associated to the $U(1)_Y$ group, and the gauge invariance is due to the gauge field B_μ.

The relation between the two quantum numbers and the electric charge is given by the Gell-Mann-Nishijima formula 1.14:

$$Q = I_3 + \frac{1}{2}Y \tag{1.14}$$

The value of these quantum numbers are given for all quarks and leptons in the following table.

Knowing that, let's build the EW Lagrangian. Following the same method to create those of QCD and QED, it can be written as:

Table 1.1: Summary table of the electroweak quantum numbers for the different generations of quarks and leptons. The three quantum numbers the weak isospin I_3, the hypercharge Y, and the electric charge Q are given for the different chirality.

Fermions	Chirality	1^{st} gen.	2^{nd} gen.	3^{rd} gen.	I_3	Y	Q
Quarks	Left-handed	$\binom{u_L}{d_L}$	$\binom{c_L}{s_L}$	$\binom{t_L}{b_L}$	$\binom{+1/2}{-1/2}$	$\binom{+1/3}{+1/3}$	$\binom{+2/3}{-1/3}$
	Right-handed	u_R d_R	c_R s_R	t_R b_R	0 0	$+4/3$ $-2/3$	$+2/3$ $-1/3$
Leptons	Left-handed	$\binom{e_L}{\nu_{e,L}}$	$\binom{\mu_L}{\nu_{\mu,L}}$	$\binom{\tau_L}{\nu_{\tau,L}}$	$\binom{-1/2}{+1/2}$	$\binom{-1}{-1}$	$\binom{-1}{0}$
	Right-handed	e_R $\nu_{e,R}$	μ_R $\nu_{\mu,R}$	τ_R $\nu_{\tau,R}$	0 0	-2 0	$+1$ 0

$$\mathcal{L} = \overline{\Psi}_L(i\not{D})\Psi_L + \overline{\psi}_R(i\not{D})\psi_R + \overline{\psi}'_R(i\not{D})\psi'_R \tag{1.15}$$

However, to preserve the $SU(2)_L$ invariance, the mass terms were not considered. To ensure the local $SU(2)_L \otimes U(1)_Y$ symmetry, the covariant derivative D^μ is defined:

$$D^\mu = \partial^\mu - ig\vec{T}\vec{W}^\mu - i\frac{g'}{2}YB^\mu \tag{1.16}$$

Where g and g' are parameters controlling the interaction strength.

The Lagrangian 1.15 can be also seen as the sum of three terms: a kinematic term, a term responsible for the charged current, a last one in charge of the neutral current.

$$\mathcal{L} = \mathcal{L}_{kinematic} + \mathcal{L}_{CC} + \mathcal{L}_{NC} \tag{1.17}$$

Before explaining the different terms, we need to introduce the operator $W^\pm_\mu$. It represents the $W^\pm$ bosons which are formulated under the form of a linear combination.

$$W^\pm_\mu = \frac{1}{\sqrt{2}}(W^1_\mu \mp iW^2_\mu) \tag{1.18}$$

In the same manner, the Pauli's matrix mentioned previously is given by:

$$\sigma^\pm = \frac{1}{\sqrt{2}}(\sigma^1 \mp i\sigma^2) \tag{1.19}$$

Now, the three terms of the Lagrangian 1.17 are given by the following formulas:

$$\mathcal{L}_{kinematic} = \overline{\Psi}_L(i\not{\partial})\Psi_L + \overline{\psi}_R(i\not{\partial})\psi_R + \overline{\psi}'_R(i\not{\partial})\psi'_R \tag{1.20}$$

$$\mathcal{L}_{CC} = \frac{g}{\sqrt{2}}W^+_\mu\overline{\psi}_L\gamma^\mu\psi'_L + \frac{g}{\sqrt{2}}W^-_\mu\overline{\psi}'_L\gamma^\mu\psi_L \tag{1.21}$$

$$\mathcal{L}_{NC} = \frac{g'}{\sqrt{2}}_{\mu} Y[\overline{\psi}_L \gamma^\mu \psi_L + \overline{\psi}'_L \gamma^\mu \psi'_L + \overline{\psi}_R \gamma^\mu \psi_R + \overline{\psi}'_R \gamma^\mu \psi'_R] + \frac{g}{\sqrt{2}} W^3_\mu [\overline{\psi}_L \gamma^\mu \psi_L - \overline{\psi}'_L \gamma^\mu \psi'_L] \tag{1.22}$$

There is still a problem concerning the neutral current. Indeed, it is defined as a function of W^3_μ and B_μ, but they do not have a physical interpretation, they cannot be interpreted as real neutral boson. In order to solve this issue, let's introduce the new fields using the Weinberg's angle θ_w, A_μ and Z_μ which represent the photon and the Z boson respectively.

$$\begin{pmatrix} A_\mu \\ Z_\mu \end{pmatrix} = \begin{pmatrix} \cos\theta_w & \sin\theta_w \\ -\sin\theta_w & \cos\theta_w \end{pmatrix} \begin{pmatrix} B_\mu \\ W_\mu \end{pmatrix} \tag{1.23}$$

Thanks to these new fields, the Lagrangian 1.22 can be written in two different manners, one for the Z boson and one for the photon:

$$\mathcal{L}^Z_{NC} = \overline{\psi}_L \gamma^\mu Z_\mu \left(g \frac{\sigma_3}{2} \cos\theta_w - g' \frac{Y}{2} \sin\theta_w \right) \psi_L \tag{1.24}$$

$$\mathcal{L}^\gamma_{NC} = \overline{\psi}_L \gamma^\mu A_\mu \left(g \frac{\sigma_3}{2} \sin\theta_w + g' \frac{Y}{2} \cos\theta_w \right) \psi_L \tag{1.25}$$

Furthermore, from these two equations we will define the fundamental electric charge e using the Weinberg's angle θ_w and the couplings g and g':

$$e = g' \sin\theta_w = g \cos\theta_w \tag{1.26}$$

Before writing again the EW Lagrangian, we need to define two fields strength tensors given by 1.27 and 1.28:

$$B_{\mu\nu} = \partial_\nu B_\mu - \partial_\mu B_\nu \tag{1.27}$$

$$W^{\mu\nu}_i = \partial_\mu W^i_\nu - \partial_\nu W^i_\mu + g e^{ijk} W^j_\mu W^k_\nu \tag{1.28}$$

Where e^{ijk} is the Levi-Civita tensor. This last term with the tensor indicates that generators W_μ do not commute together because of the nature of the symmetry group $SU(2)_L$. It is at the root of the self interaction of gauge bosons. For instance, this includes the cubic self-couplings (ZW^+W^-, γW^+W^-) and also the quadrilinear ones (ZZW^+W^-, $\gamma\gamma W^+W^-$, $Z\gamma W^+W^-$, $W^+W^-W^+W^-$).

Finally, the full EW Lagrangian is given by:

$$\mathcal{L}_{EW} = \overline{\Psi}_L (i \not{D}) \Psi_L + \overline{\psi}_R (i \not{D}) \psi_R + \overline{\psi}'_R (i \not{D}) \psi'_R - \frac{1}{4} W^{\mu\nu}_i W^i_{\mu\nu} - \frac{1}{4} B^{\mu\nu} B_{\mu\nu} \tag{1.29}$$

And from this equation, the first part corresponds to the impact of the EW interaction on fermions. And the second refers to the impact on gauge bosons.

$$\mathcal{L}_{fermions} = \overline{\Psi}_L(i\not{D})\Psi_L + \overline{\psi}_R(i\not{D})\psi_R + \overline{\psi}'_R(i\not{D})\psi'_R \tag{1.30}$$

$$\mathcal{L}_{gauge} = -\frac{1}{4}W_i^{\mu\nu}W^i_{\mu\nu} - \frac{1}{4}B^{\mu\nu}B_{\mu\nu} \tag{1.31}$$

In a nutshell, the strong and electroweak interactions are represented through $\mathcal{L}_{QCD}$ and $\mathcal{L}_{EW}$ respectively. Both are the resultants of the gauge theory with the symmetry group presented in Equation 1.3. Nevertheless, to satisfy the gauge invariance, there is no mass term of the gauge boson or fermion fields. It remains correct for photons or gluons, but it is not the case for Z and $W^{\pm}$ bosons, and fermions. Indeed, many experimental observations proved the massive nature of these particles. Since the weak interactions are experimentally observed to play a role at small distances, their mediators are expected to be massive, which is not the case. If considering the addition of mass terms for fermions is not a problem with the $SU(3)_C$ symmetry invariance, this will break the $SU(2)_L$ symmetry. And trying to add a mass term for gauge bosons will lead to a non local invariance of $SU(2)_L \otimes U(1)_Y$ symmetry and prevent the theory from being renormalizable.

In order to have massive gauge bosons and fermions, and to keep the gauge invariance, a mechanism was proposed to spontaneously break the EW symmetry. This phenomenon also called Brout-Englert-Higgs (BEH) mechanism was postulated in 1964 independently by P. Higgs [48], by F. Englert and R. Brout [49], and by G. Guralnik, C. Hagen and T. Kibble [50]. It will be discussed in the next section.

1.1.3 Spontaneous symmetry breaking and the Higgs mechanism

The BEH mechanism, or just Higgs mechanism, proposes a new SM Lagrangian in order to solve the massless particles issue. This theory is based on the introduction in the Lagrangian of a complex scalar field $\phi(x)$. This field is linked to a potential $V(x)$ which is invariant under the full symmetry group of Equation 1.3. Despite the fact, that when a specific state is chosen, among a continuum of possible ground states, it happens a spontaneous symmetry breaking. This occurs, when the scalar field corresponds to a massless boson with a spin $s = 0$, also called Goldstone boson. It is introduced as the consequence of the Goldstone theorem [51] proposing this new field in the Lagrangian density for each generator of the group associated to the symmetry breaking. The complex scalar field is defined as a doublet having a hypercharge $Y_\phi = 1$. It is defined as:

$$\phi = \begin{pmatrix}\phi^+ \\ \phi^0\end{pmatrix} = \frac{1}{\sqrt{2}}\begin{pmatrix}\phi^1 + i\phi^2 \\ \phi^3 + i\phi^4\end{pmatrix} \tag{1.32}$$

In addition, the potential field mentioned before is:

$$V(\phi^\dagger\phi) = -\mu^2\phi^\dagger\phi + \lambda(\phi^\dagger\phi)^2, \quad (\mu^2, \lambda > 0) \tag{1.33}$$

This potential field is shaped like the bottom of a bottle of Burgundy wine, represented in Figure 1.2. It is made in a such way to have an unstable local

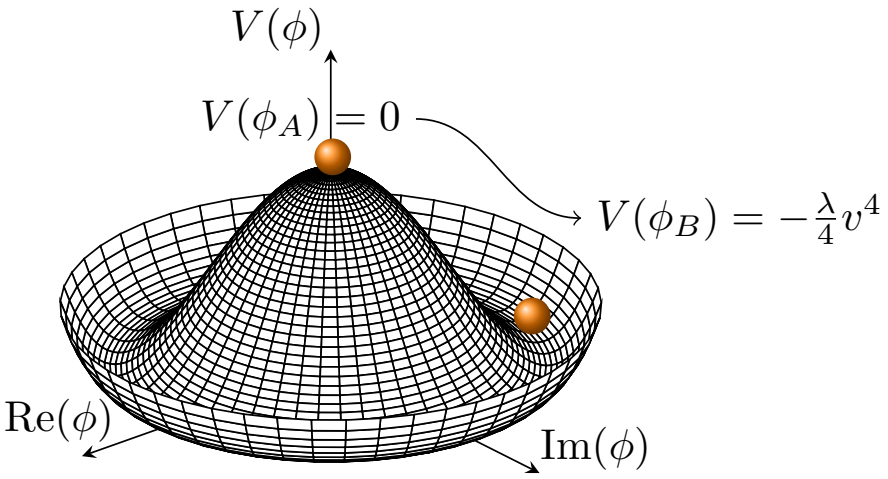

Figure 1.2: Representation of the Higgs potential $V(\phi)$

maximum when $\phi = 0$, and if considering that the ground states continuum corresponds to:

$$|\phi^\dagger \phi| = \frac{\mu^2}{2\lambda} \equiv \frac{v^2}{2} \tag{1.34}$$

Where v is the vacuum expectation value.

A such ground state allow the symmetry to be broken spontaneously and keep the gauge invariance of the Lagrangian. Both $SU(2)_L$ and $U(1)_Y$ symmetry groups are broken. However, $U(1)_Y$ symmetry is preserved when the ground state is chosen parallel to the doublet component ϕ^0 from the definition of the complex field doublet 1.32. This specific ground state is given by:

$$\phi_g = \frac{1}{\sqrt{2}} \begin{pmatrix} 0 \\ v \end{pmatrix} \tag{1.35}$$

Thanks to this potential, we can create the BEH term of the SM Lagrangian, which is written as:

$$\mathcal{L}_{Higgs} = (D_\mu \phi)^\dagger (D^\mu \phi) - V(\phi^\dagger \phi)^2 \tag{1.36}$$

Where D_μ is the same as the covariant derivative defined in the Equation 1.16.

The potential is not always at its minimal value. Indeed, it can endure small fluctuations around the minimum. These perturbations are parametrized as:

$$\phi(x) = \frac{1}{\sqrt{2}} e^{i\sigma^i \theta^i(x)} \begin{pmatrix} 0 \\ v + H(x) \end{pmatrix} \tag{1.37}$$

Where $\theta^i(x)$ is the massless spin $s = 0$ boson field and $H(x)$ is the massive one. $\theta^i(x)$ corresponds to an unphysical Goldstone boson and $H(x)$ can be associated to the Higgs boson. It is possible to remove the Goldstone boson in the equation by using a $SU(2)_L$ transformation. Indeed, the Lagrangian is gauge invariant, but the Goldstone boson will disappear with a unitary gauge transformation. The transformation is shown with the Equation 1.38:

$$\phi(x) = e^{-i\sigma\theta^i(x)}\phi'(x) = \frac{1}{\sqrt{2}}\begin{pmatrix} 0 \\ v + H(x) \end{pmatrix} \tag{1.38}$$

Finally, the field is only depending on $H(x)$ and the Higgs Lagrangian can possibly be written as:

$$\begin{aligned}\mathcal{L}_{Higgs} = \frac{1}{2}\partial_\mu H \partial^\mu H + \mu^2 H^2 + \frac{g^2 v^2}{4} W_\mu^+ W^{-\mu} + \frac{g^2 + g'^2}{6} v^2 Z_\mu Z^\mu \\ + \frac{g^2 v}{2} H W_\mu^+ W^{-\mu} n + \frac{g^2}{4} H^2 W_\mu^+ W^{-\mu} + \frac{g'^2}{2} v^2 H Z_\mu Z^\mu \\ + \frac{g^2}{4} H^2 Z_\mu Z^\mu + \frac{\mu^2}{v} H^3 + \frac{\mu^2}{4v^2} H^4\end{aligned} \tag{1.39}$$

From this formula, it is possible to identify the different mass terms. The first two elements of the sum correspond to the Higgs field. From them, the Higgs mass can be extrapolated:

$$m_H = v\sqrt{2\lambda} = \sqrt{2}\mu \tag{1.40}$$

The next two are respectively the propagator of $W_\mu^\pm$ and Z_μ. And similarly as m_H, the masses of the Z and $W^\pm$ and bosons can be defined as:

$$m_Z = \frac{\sqrt{g^2 + g'^2}}{2} v \tag{1.41}$$

$$m_{W^\pm} = \frac{gv}{2} = m_Z \cos\theta_w \tag{1.42}$$

The last two parts of the equation describe the trilinear and quadrilinear self-couplings of the Higgs boson. In this case, the potential field is given by:

$$V(\phi) = \mu^2 H^2 + \frac{\mu^2}{v} H^3 + \frac{\mu^2}{4v^2} H^4 = \frac{1}{2} m_H^2 H^2 + \lambda_{HHH} v H^3 + \lambda_{HHHH} H^4 \tag{1.43}$$

Where the Higgs boson self-couplings are:

$$\lambda_{HHH} = \lambda_{HHHH} = \frac{m_H^2}{v^2} \tag{1.44}$$

Finally, the four other terms refer to trilinear and quadrilinear couplings between H and the propagators of the weak interaction: Z and $W^\pm$. The trilinear couplings are (HZZ, HW^+W^-) and the quadrilinear ones are ($HHZZ$, HHW^+W^-). The coupling HZZ will be particularly important for the latter, because it corresponds to the Higgs decay process analysed in this thesis.

After the demonstration of the mass of the vector and scalar bosons, it remains to explain how the fermion mass is obtained.

The fermionic mass is also resulting from the BEH mechanism. But, the mass term is from another Lagrangian. Indeed, the interaction between the H field and

the left and right-handed fields of the fermions is described using the Lagrangian of the Yukawa interaction.

Before building it, the Yukawa couplings must be defined. There are two of them, y_f and $y_{f'}$ where f corresponds to the upper fermions in the doublets defined in the Equations 1.1 and 1.2, and f' corresponds to the lower fermions. Furthermore, the charge conjugate of the Higgs fields is defined as $\phi^c = i\sigma^2\phi^*$. Thus, the Yukawa Lagrangian is given by:

$$\mathcal{L}_{Yukawa} = -y_{f'}(\overline{\Psi_L}\phi\psi'_R + \overline{\psi'_R}\phi^\dagger\Psi_L) - iy_f(\overline{\Psi_L}\phi^c\psi_R + \overline{\psi_R}\phi^{c\dagger}\Psi_L) \tag{1.45}$$

If a symmetry breaking is applied, this Lagrangian becomes:

$$\mathcal{L}_{Yukawa} = -\sum_f \frac{y_f}{\sqrt{2}}\overline{\psi}\psi(v+H) - \sum_{f'} \frac{y_{f'}}{\sqrt{2}}\overline{\psi}\psi(v+H) \tag{1.46}$$

The equation is composed of two parts, the first one for the upper fermions and the second one for the lower ones. Each part has a mass term and a term corresponding to the coupling between fermions and the Higgs field. Eventually, the mass terms of the fermions are obtained from this formula, and they are equal to:

$$m_f = \frac{y_f v}{\sqrt{2}} \quad , \quad m_{f'} = \frac{y_{f'} v}{\sqrt{2}} \tag{1.47}$$

At the end, the full SM Lagrangian correspond to the combination of the four main Lagrangian developed in this chapter. It can be written as:

$$\mathcal{L}_{SM} = \mathcal{L}_{QCD} + \mathcal{L}_{EW} + \mathcal{L}_{Higgs} + \mathcal{L}_{Yukawa} \tag{1.48}$$

To summarize, this chapter gave an overview of the constituents of the universe and the physical description of the fundamental interaction using a single formula: the SM Lagrangian. But, even if this definition is the most powerful currently, there are still some problems with it that will be developed in the following chapter.

1.2 Limits of the Standard Model and new theories

1.2.1 The limits of the Standard Model

The SM proposes a description of all the elementary particles and the fundamental interactions at the subatomic scale. However, it is not a universal model considering also the gravitation, and it is currently facing some problems which some of them are explained below:

- **The neutrino oscillation** has been observed from atmospheric neutrinos in 1998 by the Super-Kamiokande Collaboration [52] and confirmed later with other experiments [53] using reactor's neutrinos. The oscillation of the neutrino flavour needs the neutrinos to be massive particles, and constraints on the difference of the square of their and upper limits were measured using

different methods. Among them, there are experiences such as KATRIN [54], observations of cosmic events like supernovas, or cosmological constraints. The problem is that they do not have a mass according to the SM theory. It is still possible to add to the SM, but the theory does not predict them. However, there are some theories proposing the mechanism from which the neutrino's mass comes from.

- **The asymmetry between matter and anti-matter** is not addressed in the SM. A. Sakharov [55] proposed that this phenomenon could be explained by the CP symmetry violation, the baryon number violation, and the fact that the rate of baryon-asymmetry generation is less than the universe expansion rate. But it is even not enough to explain the magnitude of the baryonic imbalance.

- **The gravitational interaction** is not taken into account in the SM. Its most accurate description is made in the general relativity. However, the quantum form of this theory cannot be renormalized using a perturbative method, making impossible the unification with the SM. Its very low strength at particle scale makes it no problem that it is not involved in particle physics. There should be a quantum description for some phenomena, such as the early universe, where it was infinitely small but also infinitely dense. The graviton is the hypothetical particle serving as vector of the gravitational forces, according to the theory it should be a massless boson with a spin $s = 2$. It has not been observed so far.

- **Dark matter and dark energy** were introduced to explain some cosmological observations. The unexpected rotation speed of galaxies [56] suggests that the matter described in the SM represents only 5% of the total mass of the universe. On the other hand, dark matter should correspond to 26%, and the remaining 69% is dark energy. Dark matter should behave like "normal matter", but interacting very poorly with the SM fields. Dark energy should be a repulsive force acting against gravity, and explaining the acceleration of the universe expansion [57]. Currently, there is no potential candidate for the dark matter among the SM particles.

- **The hierarchy problem** of the Higgs boson mass comes from the high sensitivity that the boson has with loop corrections. Meaning that it get important quantum corrections because of the virtual particles forming the loop (like virtual t quarks) [58]. In this way, these corrections should highly increase the Higgs boson mass compared to the current one and leading to quadratic divergences. This problem can be described with the following formula:

$$\delta m_H^2 = \frac{3G_F\Lambda^2}{8\sqrt{2}\pi^2}\left(2m_W^2 + m_Z^2 + m_H^2 - 4m_t^2\right) \tag{1.49}$$

  Where Λ is a cut-off scale which has an arbitrary value, and in order to keep the mass as it is, it must be fine-tuned. At the end, the hierarchy problem derives from this a posteriori fine-tuned parameter, which comes from bias.

- **The number of parameters in the SM** is quite important. Indeed, there are 19 free parameters which were determined experimentally, but their theoretical origins are still missing.

This list is non-exhaustive, some other experimental divergences or theoretical misunderstandings can be missing. Currently, the SM can be applied only to describe interaction at the electroweak scale. Nonetheless, theories beyond the Standard Model (BSM) are addressing these problems, or at least part of them.

1.2.2 The world beyond the Standard Model

There are many BSM theories which propose to solve the above-mentioned problems while keeping the validity of the SM. They would be in some way extensions of the SM. Among those, we can quote an enlargement of the gauge group with the addition of new gauge bosons, a relation of quarks and leptons called leptoquarks, an increase of the number of dimensions, the addition of a new electroweak breaking mechanism, or the extension of the Poincaré group including the supersymmetry theories, with in particular the Minimal Supersymmetry Standard Model (MSSM) proposed by C. Csaki [59].

When talking about supersymmetry, it refers to a set of theories introducing new symmetry groups and adding them to those of the SM. The supersymmetry is designed as an extension of the SM that should complete it by explaining with still not described properly by the SM. It predicts a partner particle for each of the SM particles. These new particles would determine the mass of the Higgs boson, thus solving an important problem of the Standard Model. In this section, only the Minimal Supersymmetric Standard Model (MSSM) will be explained.

According to this theory, each particle of the SM get his own superpartner. Taking the case of the electron e, its superpartner is the selectron $\tilde{e}$. The new super fermions will be named by adding a "s" at the beginning of their names and a tilde over their symbols, so it gives the squarks and the sleptons. However, for the bosons, "ino" is added at the end of their name, giving for instance the higgsino and the photino. There is also an inversion of spin, the superpartners of fermions are bosons and vice versa.

The mass of these new particles should be the same in an unbroken symmetry scenario, but it can differ if going into a symmetry breaking. This supposition can solve the hierarchy problem. The proposed solution is to reduce the quantum corrections by ensuring that the interaction terms that the Higgs boson has with fermions cancel out with that of the interaction with bosons. This happens at the electroweak scale, at Planck-scale it is the cancellation between particles and super-particles.

Another motivation for the MSSM comes from grand unification, the idea that the gauge symmetry groups should unify at high-energy. In the Standard Model, however, the weak, strong and electromagnetic gauge couplings fail to unify at high energy. Indeed, there is no energy where the three coupling constants can meet together.

The MSSM proposes a superpartner to the Higgs boson, the higgsino $\tilde{H}$. Searches of this particle have been performed by both the ATLAS and CMS

experiments at the Large Hadron Collider at CERN, but currently no higgsino has been observed [60, 61].

Nevertheless, there are also a dark matter candidates in MSSM [62] with the neutralino (super particle composed of $\tilde{H}$, $\tilde{g}$ and $\tilde{\gamma}$). It is considered as a promising candidate because it should be a weakly interacting massive particle (WIMP).

Such as a graviton, these particles theorized in MSSM could be at the root of high mass resonances, which are at the centre of the preoccupations of the physics analysis presented in this thesis.

1.3 Phenomenology of the Higgs boson

The 4^{th} of July, is not only the US Independence Day, but more importantly, the birthday of the first observation of the Higgs boson. Indeed, the ATLAS and CMS Collaborations announced in July 4^{th} 2012 this observation of a new boson looking like the Higgs boson [39, 40]. This particle had a mass around 125 GeV, and it was discovered using proton-proton collision in the LHC with an energy in the centre of mass equals to $\sqrt{s} = 7$ TeV in 2011 and $\sqrt{s} = 8$ TeV in 2012. Both collaborations chose different decay channels to perform the analysis at this time. Among them, they chose for instance the channel $H \to ZZ \to 4l$, or $H \to W^+W^-$, and some channels composed of a doublet of particles in the final state such as $H \to \gamma\gamma$, $H \to b\bar{b}$, or $H \to \tau^+\tau^-$.

The discovery was claimed in 2012, when the statistics were high enough to reach 5σ. Then, in 2013 all the Run-1 data were analysed and the Higgs boson candidate was definitively considered as the Higgs boson. At this moment, both collaborations came with a more precise measurement of the Higgs boson mass coming from the combined results of their channels of predilection. This new value of the mass was $m_H = 125.09 \pm 0.21(\text{stat.}) \pm 0.11(\text{syst.})$ GeV [63]. Right after that, the first measurements of the other properties of this boson were carried out. But, before going deeper in the presentation of the Higgs boson characteristics, it could be interesting to understand how they are produced at LHC.

1.3.1 Production mechanisms

At LHC, the analyses regarding the Higgs boson are using data from proton-proton collisions. The production cross-section is dependent on the collision energy, but this probability is also calculated for a given value of m_H. Taking only the mass of 125 GeV, the cross-sections for the different production process occurring at LHC are given in Figure 1.3.

In the context of proton-proton collisions at LHC, Higgs bosons can be produced mainly via four processes, which are represented in Figure 1.4.

It is possible to make the link between these diagrams and the curves from Figure 1.3. The blue one correspond the gluon fusion (ggH), the red one to the vector boson fusion (VBF), the green and brown ones to the associated production with a vector boson (VH), and the pink and purple one to the associated production with a pair of quarks ($t\bar{t}$H) or ($b\bar{b}$H) respectively. There is also the mallow curve

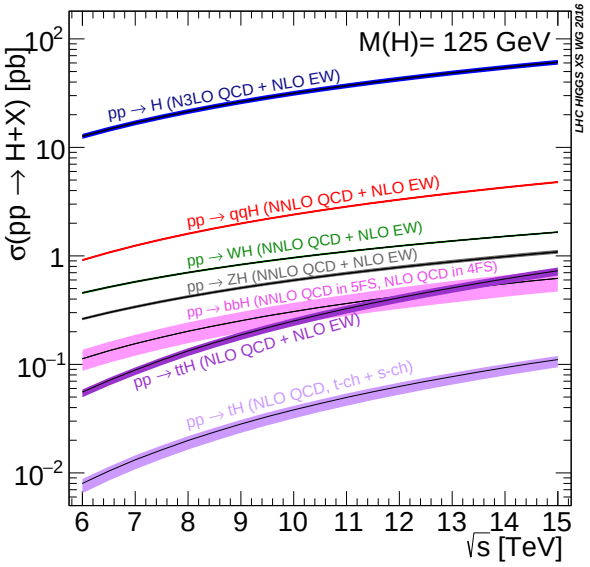

Figure 1.3: Standard Model Higgs boson production cross-sections at $\sqrt{s} = 13$ TeV as a function of the centre of mass energy [2]

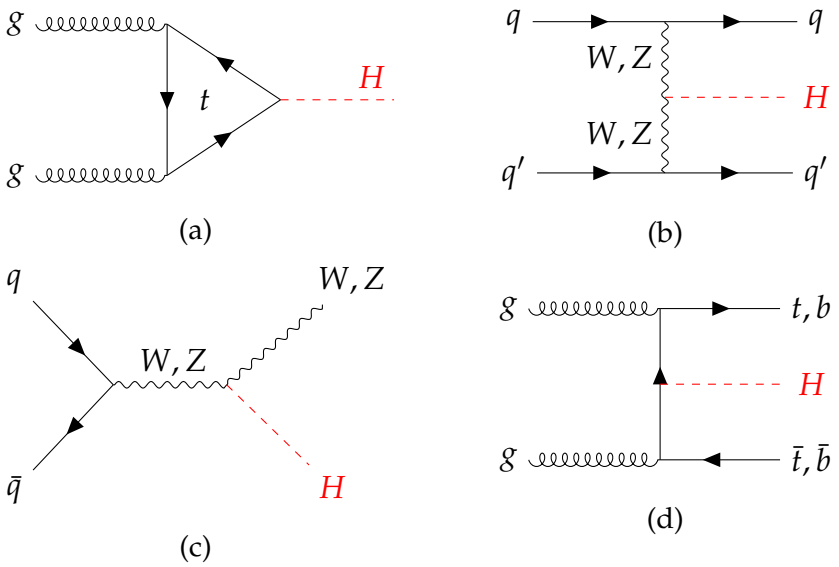

Figure 1.4: Feynman diagrams of the principal Higgs boson production modes: (a) the gluon fusion (ggH), (b) the vector boson fusion (VBF), (c) the associated production with a vector boson (VH), and (d) the associated production with a pair of quarks ($t\bar{t}$H) or ($b\bar{b}$H).

corresponding to the associated production with a t quark. This one will not be treated in particular in this chapter due to its low probability to occur compared to the others.

- **ggH** is the major production mode, with a cross-section of 49 pb visible in Figure 1.5. Its predominance comes from the high Parton Density Function (PDF) for gluons. Gluons cannot produce directly a Higgs boson, indeed

there is no coupling between them in Equation 1.39 which can be understood through the fact that gluons are massless. However, they will generate a heavy quark loop, and the Higgs boson will come from it. The coupling with fermions, written in Equation 1.47, is proportional to the fermion mass, and more probably leading to a t quarks loop. ggH is a process representing almost 87% of the total Higgs bosons production.

- **VBF** process is the second most important, even if its cross-section of 3.8 pb is more than ten times lower than ggH. This phenomenon comes from the radiation of two vector bosons from quarks, forming the accelerated protons. Higgs boson cones from the fusion of these two vector bosons. The two quarks in the final in Figure 1.4 (b). But, there is a higher chance to have jets coming from the participated quarks. Hopefully, they can be easily tagged due to the characteristics, such as a trajectory close to the beam line and with a rapidity gap between both.

- **VH** process, also known as Higgs-Strahlung is the third dominant process, with a cross-section of 2.3 pb. It comes from the fusion of a quark and an anti-quark into a vector boson. And at its turn, the produced boson will radiate a Higgs boson. The analogy in the name can be understood because Bremsstrahlung is the phenomenon of electrons radiating photons when their trajectories are curved. Contrary to ggH and VBF, this process is more difficult to reconstruct properly. Indeed, in addition to the Higgs boson, the produced vector boson is still here.

- **The associated production with 3^{rd} generation quarks** is the fourth main production mode. It gathers the processes $t\bar{t}$H, $b\bar{b}$H and even tH. For the first two, the two gluons will be converted in two pairs of heavy $q\bar{q}$. One of them will remain, instead of the other, will fuse in a Higgs boson. In the case of tH, the production starts with the exchange of a $W^{\pm}$ boson between a b quark and a quark from the protons. The Higgs boson is radiated from the $W^{\pm}$ boson, and it will be accompanied by a t quark. This process is not as clean as ggH or VBF, and has a smaller cross-section.

Furthermore, the production mode can also be considered depending on m_H at a given centre of mass energy. In the case of the last runs of the LHC, it is $\sqrt{s} = 13$ TeV as represented in Figure 1.5.

This parametrization has an interest for the work presented in this thesis. Indeed, the analysis performed aims to search for high mass resonances. And according to the right part of Figure 1.5, the dominant production modes are ggH and VBF. Moreover, for $m_H > 1$ TeV, VBF passes in front of ggH.

Until now, the cross-sections mentioned were the theoretical ones. For instance, an experimental measurement of their values was performed by ATLAS [3]. It was found that the four principal processes are in agreement with the SM predictions, as shown by Figure 1.6. A recapitulation of the cross-section measurements is given in Table 1.2. The different values are calculated for the main production modes and using all the Run-2 data with a centre of mass energy of $\sqrt{s} = 13$ TeV.

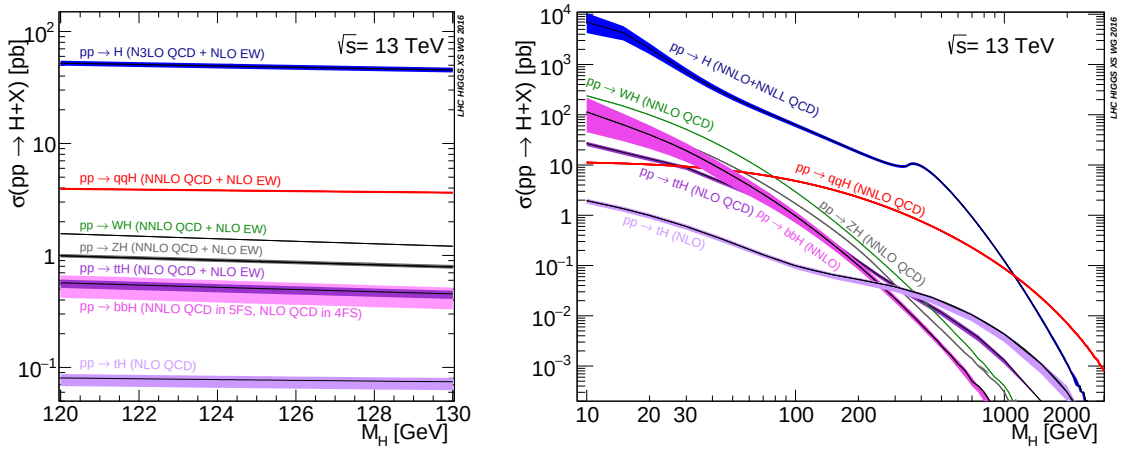

Figure 1.5: Standard Model Higgs boson production cross-sections at $\sqrt{s} = 13TeV$ as a function of m_H [2]. On the left, a zoom around 125 GeV, and on the right over the wide mass range.

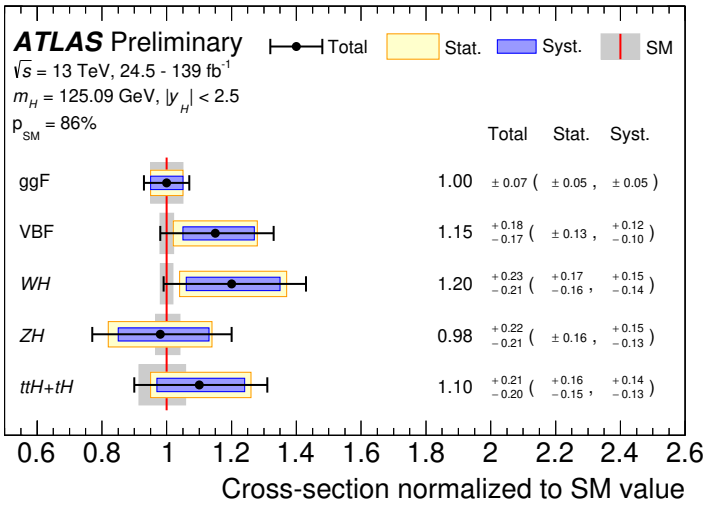

Figure 1.6: Cross-sections for ggH, VBF, WH, ZH and $t\bar{t}H + tH$ normalized to their theoretical predictions. The black error bars correspond to the total, blue boxes are the systematic uncertainties and yellow boxes show statistical uncertainties. The grey bands indicate the theoretical uncertainties in SM [3]

Table 1.2: Cross-section of the Higgs boson main production modes for a centre of mass energy of $\sqrt{s} = 13$ TeV [3].

Production mode	Cross-section (pb)
ggH	44.7 ± 3.1
VBF	4.0 ± 0.6
WH	$1.45^{+0.28}_{-0.25}$
ZH	$0.78^{+0.18}_{-0.17}$
$t\bar{t}H + tH$	0.64 ± 0.12

1.3.2 Decay modes

The theoretical prediction of the Higgs boson lifetime is $1.56 \times 10^{-22} s$. With a such short lifetime, a direct detection is impossible. The only way to have access to it is through its decay products.

Table 1.3: Branching ratios associated to the principal decay modes at $m_H = 125.09$ GeV [1]

Decay mode	Branching ratio (%)
$H \to b\bar{b}$	$58.09^{+0.72}_{-0.73}$
$H \to W^+W^-$	21.52 ± 0.33
$H \to gg$	8.18 ± 0.42
$H \to \tau^+\tau^-$	6.27 ± 0.10
$H \to c\bar{c}$	$2.88^{+0.16}_{-0.06}$
$H \to ZZ$	2.641 ± 0.040
$H \to \gamma\gamma$	0.2270 ± 0.0047
$H \to Z\gamma$	0.1541 ± 0.0090
$H \to \mu^+\mu^-$	$0.02171^{+0.00036}_{-0.00037}$

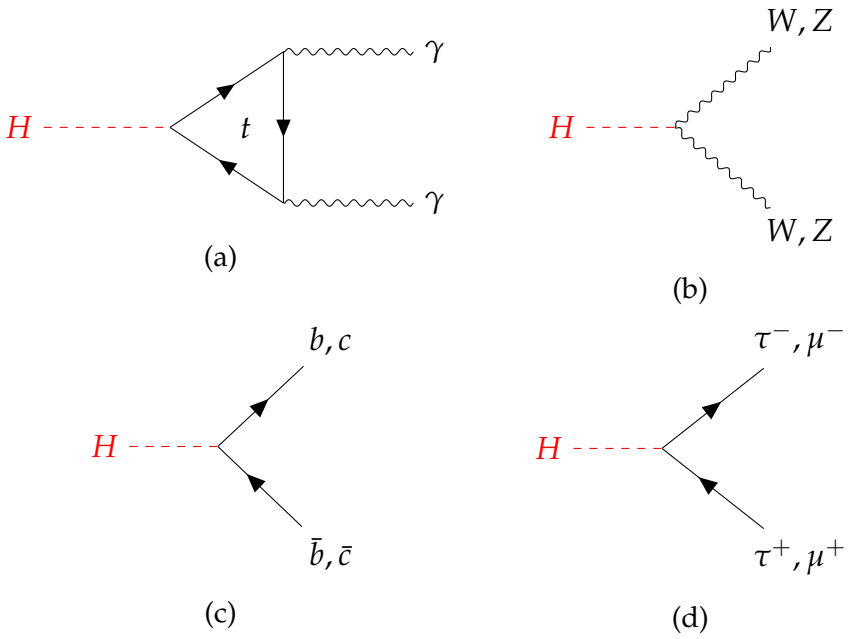

Figure 1.7: Principal decay modes of the Higgs boson: (a) the decay in two photons by the way of t quarks triangle, (b) the decay in two vector bosons, (c) the decay in a pair $b\bar{b}$ or $c\bar{c}$, and (d) the decay in a pair $\tau^-\tau^+$ or $\mu^-\mu^+$.

The principal decay channels at $m_H = 125.09$ GeV are given with their corresponding branching ratios (BR) in Table 1.3. Some correspond to the Higgs boson coupling with fermions ($H \to b\bar{b}$, $H \to c\bar{c}$, $H \to \tau^+\tau^-$, and $H \to \mu^+\mu^-$) represented in Figure 1.7 (c) and (d), some others with vector bosons ($H \to W^+W^-$ and $H \to ZZ$) represented in Figure 1.7 (b), and the other cases are less trivial. Indeed,

the remaining decay modes are not direct, they involve a triangle loop of other particles like in represented in Figure 1.7 (a) ($H \to gg$, $H \to \gamma\gamma$, and $H \to Z\gamma$).

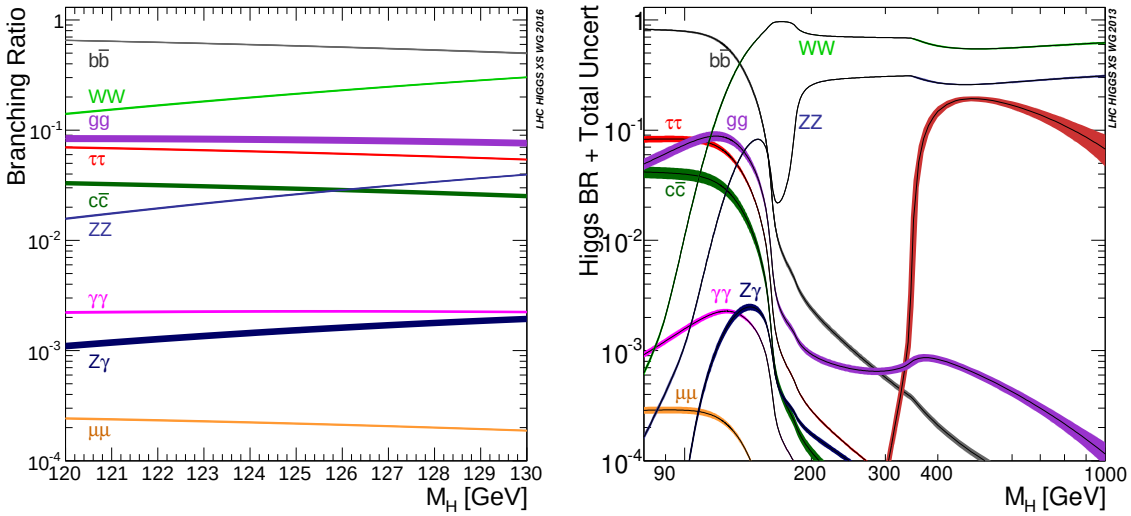

Figure 1.8: Standard Model Higgs boson decay branching ratios as a function of m_H [2]. On the left, a zoom around 125 GeV, and on the right over the wide mass range.

As well as production methods, the branching ratios of the decay channels also have a m_H dependency. The values presented in Table 1.3 correspond to the values given by the curves when $m_H = 125.09$ GeV. In the high mass region, the channels $H \to W^+W^-$ and $H \to ZZ$ are dominant. Justifying the use of $H \to ZZ \to 4l$ for the search of high mass resonances.

1.3.3 Higgs boson properties

The first parameter of the Higgs boson to be properly studied, and the first one to be treated in this section, is its mass m_H. In order to calculate it, analyses based on the study of the $H \to ZZ \to 4l$ and $H \to \gamma\gamma$ decay channels are carried out, in both ATLAS and CMS. This measurement needs precision, which induces to use data from decay mode with a high ratio of signal over background, such as the first one quoted. This means that the decay products can be easily reconstructed and identify as coming from a Higgs boson decay. Moreover, in this way the background should be also easily rejected without causing a loss of signal. For instance, $H \to ZZ \to 4l$ corresponds to only 2.641% ($H \to b\bar{b}$ BR is around twenty times higher) of the decays when $m_H = 125.09$ GeV, but its signal is quite different to the background, allowing the good separation of the mass excess. This example is represented on Figure 1.9.

The measurement with the best precision was performed by the CMS Collaboration in 2020 [6]. The mass resulting from this study is $m_H = 125.38 \pm 0.14$ GeV. It was obtained by combining the mass measured from the decay channel $H \to \gamma\gamma$ with the mass from $H \to ZZ \to 4l$, represented with the black curve in Figure 1.10.

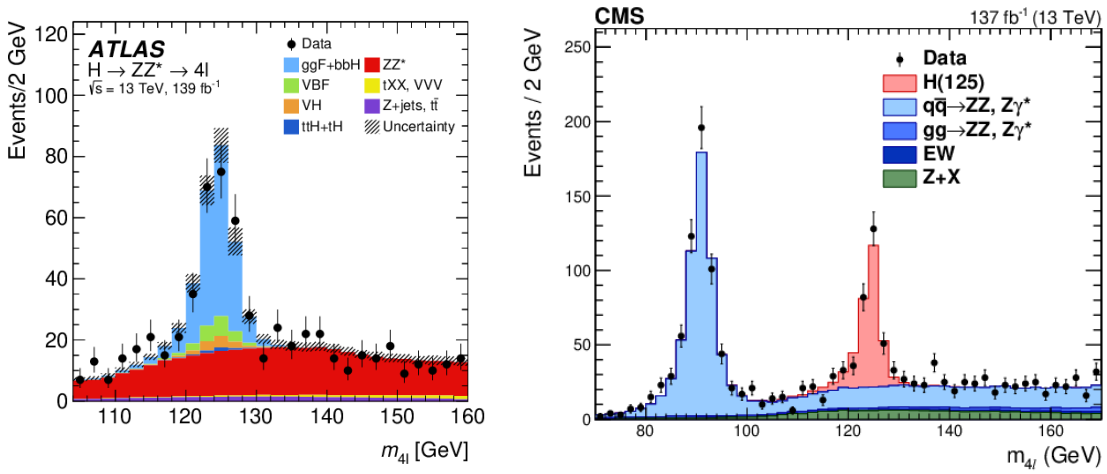

Figure 1.9: Mass of four leptons distribution obtained using $H \to ZZ \to 4l$ events from full Run II data. The figure on the left was made by the ATLAS Collaboration [4] and the figure on the right was made by the CMS Collaboration [5]

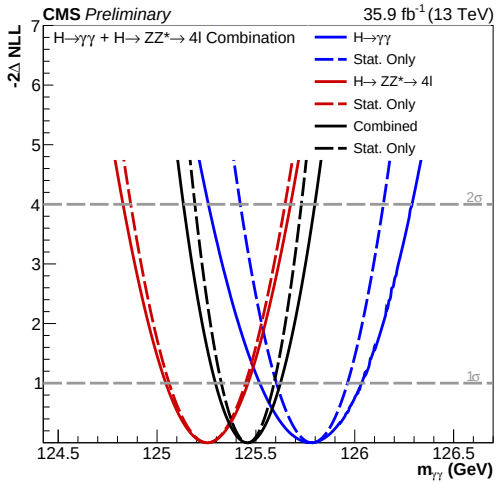

Figure 1.10: The likelihood scan of the measured Higgs boson mass in the decay channels $H \to \gamma\gamma$ (blue) and $H \to ZZ \to 4l$ (red). The combination (black) was done with 2016 data only. The solid lines are for the full likelihood scan including all uncertainties, while the dashed lines show the likelihood scan with the statistical uncertainty only [6]

Another parameter of interest is the width of the Higgs boson, written Γ_H, depends on m_H. The width of a signal is in general determined directly from the distribution. In this case, considering the mass distributions in Figure 1.9, it should be the width of the blue peak on the left, or the pink on the right. However, the experimental resolution of the mass measurement is more important to the expected width.

By chance, it is possible to measure the Higgs boson width with a method consists of studying the high mass tail of the distribution. More precisely, the

measurement is done by computing the ratio of the on-shell cross-section over the off-shell one. If considering the channel $H \to ZZ$, the main background will be two Z bosons not coming from a Higgs, and both will interfere because they share the same final state. This interference makes the measurement even more difficult to realize.

The most precise measurement at this date was performed by the CMS Collaboration using the Higgs boson decay channel in two vector bosons [64]. The method detailed in the previous paragraph was used, and the width was measured at $\Gamma_H = 3.2^{+2.8}_{-2.2}$ MeV, which is a promising result even if the expected value is $\Gamma_H = 4.1^{+5.0}_{-4.0}$ MeV.

The width and the mass of the signal are correlated. It is shown with the blue curve in Figure 1.11. This mass dependency makes possible to extrapolate the expected width directly from the mass of the interesting distribution.

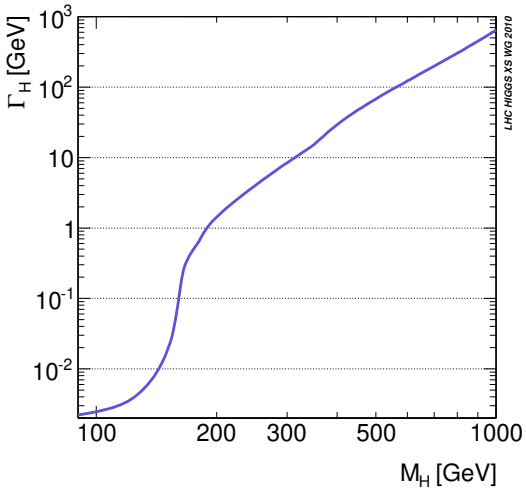

Figure 1.11: Relation between the width Γ_H and the mass m_H of the Higgs boson [7]

Some studies were performed to get precision measurement of the Higgs coupling with the fundamental fields. These studies aimed to confirm experimentally the SM prediction of the couplings. Actually, if a divergence was obtained, it could have been a sign of a new physic. The Figure 1.12 represents the Higgs boson couplings to some other particles, depending on m_H. It shows that the Higgs boson is proportionally coupled to the mass, this feature is a fundamental prediction of the SM. As it is shown, experimental results are consistent with the theoretical expectations.

Currently, only a part of the couplings were measured experimentally. First, there are the couplings with the vector bosons $W^{\pm}$ and Z [65]. Next, the couplings with the 3^{rd} generation fermions: the t quarks [66], the b quarks [67], and the tau lepton τ [68]. The coupling with muons μ [69] is not yet measured. Although, limits were obtained and show an evidence of 3σ, in this case the decay channel studied was $H \to \mu^+\mu^-$. Most of the coupling are measured with a precision of 10%, except the ones with μ and b quarks, which are closer to 20%.

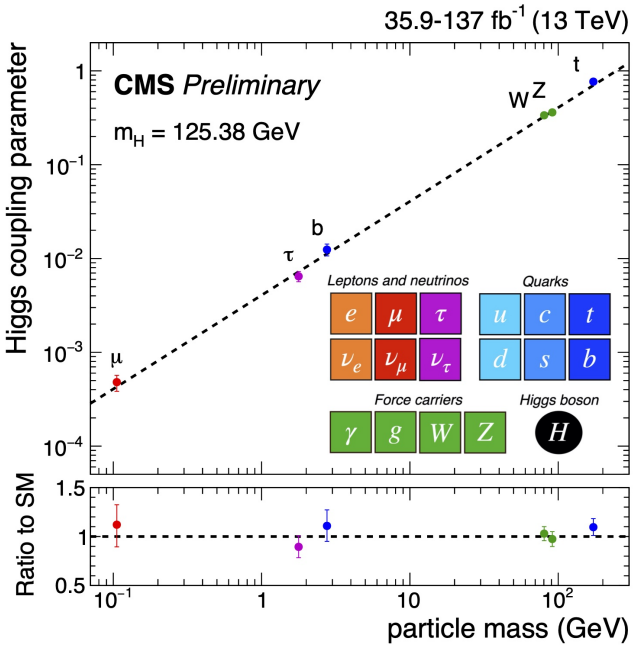

Figure 1.12: Higgs boson couplings to other particles as a function of mass. The predictions by the SM is indicated by the dashed line, and the ratios between measured couplings and SM predictions are shown in the lower panel [8]

Among the missing couplings which are not in this picture, there are the ones with some 2^{nd} generation particles (c and s quarks), all the 1^{st} generation particles, and also the self-coupling of the Higgs boson. Currently, there are only limits measured for c quarks using the decay channel $VH \rightarrow c\bar{c}$ [70]. Actually, there is a chance to measure these remaining couplings with fermions, using Higgs pair production [71]. But, it is not for tomorrow, because the production of such events will be done probably with collision at a higher centre of mass energy. Thus, new LHC runs are required and new colliders allowing a higher energy as well as higher integrated luminosity.

The Higgs self-coupling, not shown on the figure as well, can be calculated with the Equation 1.44 thanks to the precise measure of m_H. Until now, experimental limits for this coupling, using direct single and double Higgs direct constraints, were calculated by both collaborations [72, 73]. More recently, theoretical methods have proposed to constrain the Higgs self-coupling using only the single Higgs decay channels [74]. Using EW corrections on loops of virtual particles linked to the production and decay processes of the Higgs boson. This approach is quite promising for the future, but currently it is very limited by the statistics.

1.4 Focus on the Golden Channel and its possibilities

In this thesis, a specific decay channel will be studied. It is about the $H \rightarrow ZZ \rightarrow 4l$ where the four leptons at the end refer to pairs of e^+e^- or $\mu^+\mu^-$, and with its Feynman diagram represented in Figure 1.13. The description of the characteristics of $H \rightarrow ZZ \rightarrow 4l$ is addressed in this thesis, as the search for high

mass resonance $X \to ZZ \to 4l$ is built on the Golden Channel analysis.

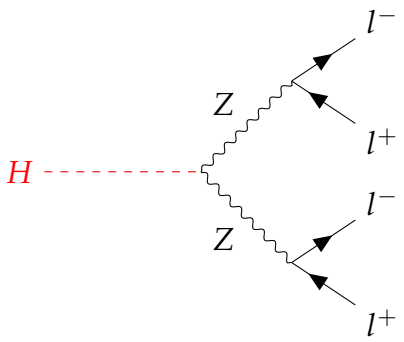

Figure 1.13: Feynman diagram of the "Golden Channel": $H \to ZZ \to 4l$

Moreover, this decay channel has also a more poetic name: the golden channel. This surname is explained by the fact that this process is characterized by a rare final state composed of two pairs of leptons, which makes its identification easier to do. In contrast, there is also the direct production of two Z bosons acting as an important source of background. But fortunately, the ratio of the signal over background is quite high. That's why the CMS Collaboration focused its effort on this channel to allow the discovery of the Higgs boson in July 2012. Apart from that, this channel is interesting for many reasons which are listed after and which can be a great benefit for a high mass study.

1.4.1 Interests of the Golden Channel

The golden channel has many advantages. For instance, it has a very good signal over background ratio, as it can be observed with the distinct peak of the Higgs boson on the plots of Figure 1.9. The two lepton pairs forming the final state correspond to a very specific decay, where the main background is the direct production of two Z bosons. Indeed, the four leptons are originating from the primary vertex and are well isolated and identified. Moreover, the CMS subdetectors are optimized to measure their energy and momentum with a high precision. Thus, the separation between signal and background is quite easy to realize due to the large difference of their shapes: the golden channel shape is represented by an important peak, while the background shape is rather flat.

Even if, its branching ratio is not the most important, but it is still enough to have good statistics. It is especially true at the Higgs mass, where the ratio of $2.88^{+0.16}_{-0.06}$ % is quite small compared to the one of $H \to b\bar{b}$, and which is almost twenty times higher with $58.09^{+0.72}_{-0.73}$ %. Because of this, an important work must be done in order to maximize the signal selection efficiency. Conversely, things become more interesting at high mass, indeed, from 200 GeV a Higgs boson has more than 20% of the probability to decay in two Z. There is just the W^+W^- channel, which is always more important, as demonstrated on Figure 1.8. But this decay channel does not have a signal over background ratio as good as the one of the golden channel. Indeed, W bosons are more likely to decay in leptons and neutrinos, leading to a missing part of energy in the final state. Although, there

are still some non-negligible backgrounds such as $qq \to ZZ$, $gg \to ZZ$, or $Z + X$. Some rare backgrounds could be also considered at high mass even if their impact is lower, it is possible to quote the tri-bosons processes or also those associating t quarks and vector bosons such as $t + V$ and $t\bar{t} + VV$.

Besides, the good separation between signal and background allow realizing high precision measurements. For instance, the last measurement of the Higgs mass with the best precision was done using the golden channel. Thanks to the high resolution of the CMS detector, the characteristics of electrons and muons can be precisely measured, giving a sharp peak well distinct. From this, it is possible to get the experimental value of m_H and Γ_H with an unsurpassed precision [6, 64].

In addition, this channel corresponds to very well studied final state. Starting with the first Higgs boson observation, different tools were created and enhanced over time to analyse the golden channel in the best possible way. With the detector at the beginning, with a high resolution electromagnetic calorimeter and a dedicated muon detection system (which was at the root of the Compact Muon Solenoid), the four leptons of the final state can be well detected. After that there are all the software environments allowing to reconstruct and identify electrons and muons. At the end, the analysis framework of the golden channel can precisely reconstruct the two Z bosons and ultimately the Higgs boson. The software packages uses selection criteria and discriminants which are now optimized to improve the background rejection.

Finally, the fact that this decay channel is said to be golden can be interpreted as the fact that it has a totally reconstructed final state with a high precision, and thus it allows performing a lot of measurements. For instance, it is used to measure the Higgs boson mass, width, cross-sections, parity, spin, and also it is used to search additional resonances. To sum up, the golden channel is a well understood process, allowing a lot of opportunities to measure physical properties of the Higgs boson. Indeed, since the announcement of the first observation and later for the discovery [40, 63], a lot of other measurements using it came to corroborate the SM predictions. Among that there are the mass and width measurements [6, 64].

However, there is actually a limitation to further improvements or new studies, which are the limited statistics. That is why, a new campaign of collisions started this year at LHC and the ongoing development of its next life phase aims to increase the statistics by a factor ten.

1.4.2 Status of the search of high mass resonance

More specifically, two studies were carried out on the search of high mass resonance using the golden channel, one made by the CMS Collaboration [9] and the other one made by the ATLAS Collaboration [10].

CMS high mass resonance study

A search for high mass resonance was performed by CMS and published in 2018. It was gathering three decay channels and involving the golden channel ($H \to ZZ \to 4l$, $H \to ZZ \to 2l2\nu$, and $H \to ZZ \to 2l2q$). It was done using only the data collected by the CMS experiment in 2016, corresponding to an integrated

luminosity of 35.9 fb^{-1} produced at LHC with a centre of mass energy of 13 TeV. Moreover, only the events coming from ggH and VBF production modes were considered. In addition, this analysis was performed over a Z boson pair mass range starting from 130 GeV to 3 TeV. In this case, different width values were used to search a new scalar resonance.

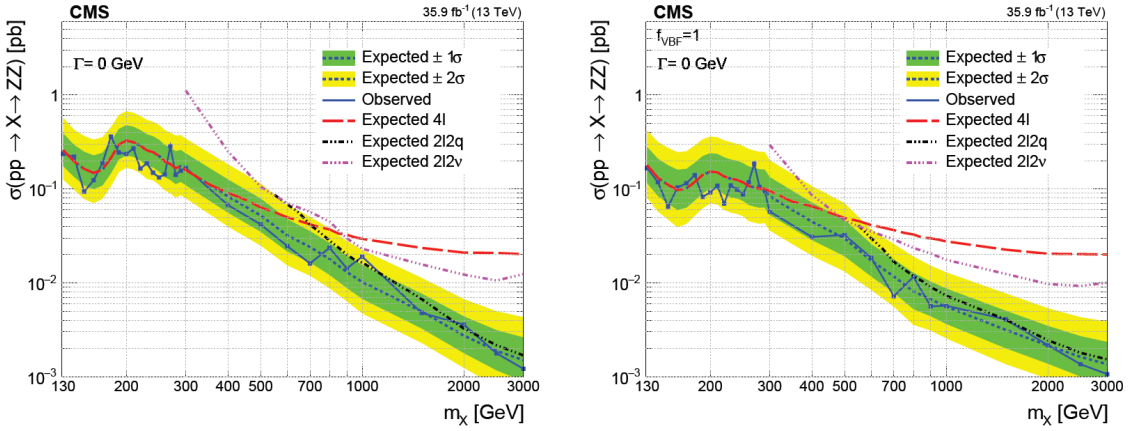

Figure 1.14: Expected and observed upper limits at the 95% CL on the $pp \to X \to ZZ$ cross-section as a function of m_X and for $\Gamma_X = 4$ MeV. The ggF category is represented on the left, and VBF on the right. The results are shown for $4l$ in red, $2l2q$ in black, and $2l2\nu$ in purple. They are also combined and with the $\pm 1\sigma$ in green and $\pm 2\sigma$ in yellow. These results using CMS 2016 data are taken from [9].

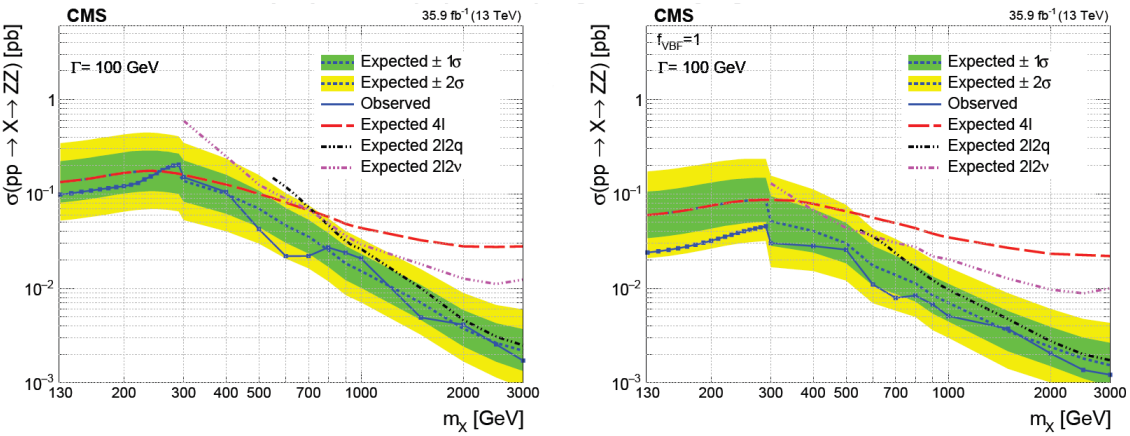

Figure 1.15: Expected and observed upper limits at the 95% CL on the $pp \to X \to ZZ$ cross-section as a function of m_X and for $\Gamma_X = 100$ GeV. The ggF category is represented on the left, and VBF on the right. The results are shown for $4l$ in red, $2l2q$ in black, and $2l2\nu$ in purple. They are also combined and with the $\pm 1\sigma$ in green and $\pm 2\sigma$ in yellow. These results using CMS 2016 data are taken from [9].

As a result, this study calculated expected and observed limits for high mass resonances. For instance, limits represented in Figure 1.14 were computed for the three decay channels over all the mass range and for a narrow width of 4 MeV. On

the left, the limits were computed for a ggF category, and on the right for a VBF category.

Moreover, other signal configurations were considered. In this study, the resonance width is a free parameter. As represented in Figure 1.15, the width can also wider, even have the same order of magnitude of the signal mass. This example shows the expected and observed limits for $\Gamma_X = 100$ GeV.

But, this search did not conclude to the observation of a new resonance. There was no significant excess of events compared to the SM prediction, and this for all the different possibilities.

ATLAS high mass resonance study

This analysis, performed by ATLAS and publish in 2022, used all the data from the second run of LHC, meaning all the data from 2015 until now. This corresponds to an integrated luminosity of 139 fb^{-1} recorded by the ATLAS experiment, from collisions produced at a centre of mass energy of 13 TeV. Furthermore, two decay channels were considered ($H \to ZZ \to 4l$ and $H \to ZZ \to 2l2\nu$), both coming from ggH and VBF production modes. The mass range started at 200 GeV up to 2 TeV.

Similar to the CMS study, this one proposes expected and observed limits for high mass resonances. For example, limits represented in Figure 1.16 were computed for the two decay channels over all the mass range and for a narrow width. On the left, the ggF production mode was used to compute the limits were computed for, and on the right the VBF was used.

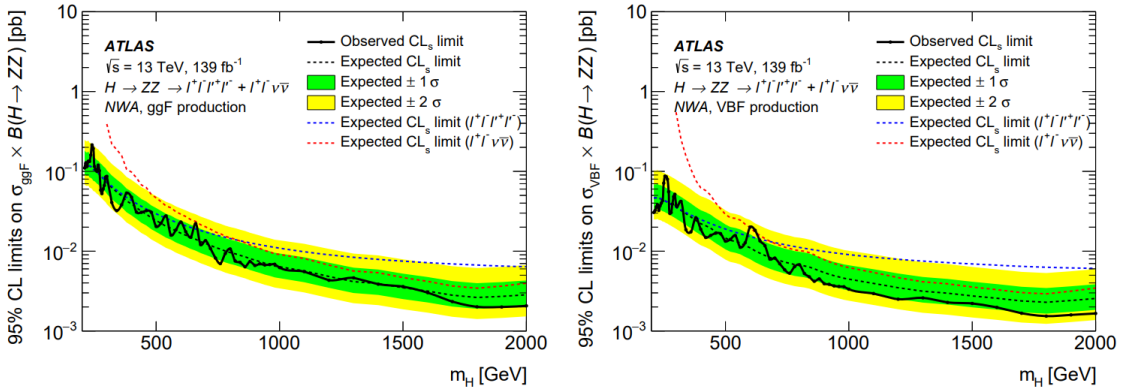

Figure 1.16: Expected and observed upper limits at the 95% CL on the $pp \to X \to ZZ$ cross-section as a function of m_X and for $\Gamma_X = 4$ MeV. The ggF category is represented on the left, and VBF on the right. The results are shown for $4l$ in blue, and $2l2\nu$ in red. They are also combined and with the $\pm 1\sigma$ in green and $\pm 2\sigma$ in yellow. These results using ATLAS Run-2 data are taken from [10].

Also in this case, no significant excess of events over the SM expectation was observed. Other limits were computed for other width values, not only narrow, but the conclusion is still the same.

Motivation for a new search of high mass resonance

These studies show many points which can improved, and which are sources of motivation for another search of high mass resonance. First, the CMS studies only used 2016 data and now 2017 and 2018 data are available with a new set of calibration. More statistics can be a huge benefit for this kind of study because at high mass the production cross-section is quite, as shown on Figure 1.5, and events in this mass region are rare. Next, considering the ATLAS study, the data used are also coming from the full second run of LHC, but the upper limit on the mass range is 2 TeV. For CMS, it is possible to go up to 3 TeV which represents a wide extension of the mass range never analysed with all the data. In addition, from the CMS point of view, it may be worthwhile to cross-check ATLAS results. Indeed, both collaborations do not use the same detectors, the same identification and reconstruction algorithms, and the same statistical analysis methods. Thus, discrepancies can come from these differences.

Before going deeper in the explanations of a physics analysis looking at the high mass region of the golden channel. It is worth to explain how the events are produced and reconstructed. For that, the best way is to have a description of the LHC and the CMS detector.

Chapter 2

The Large Hadron Collider and the CMS experiment

Table of contents

2.1 The Large Hadron Collider 35
2.1.1 The birth of the Large Hadron Collider at CERN 36
2.1.2 Design of the apparatus 37
2.1.3 The physics experiments 42
2.1.4 The Large Hadron Collider during operation 44
2.2 The Compact Muon Solenoid detector 47
2.2.1 General overview of CMS 48
2.2.2 The subdetectors and equipments 50
2.3 Reconstruction of particles 66
2.3.1 The particle flow algorithm 67
2.3.2 Identification and reconstruction of particles 69

This chapter aims to give the experimental context of the work presented in this thesis, to describe the impressive technological installations which are at the root of discoveries, and to emphasize their complexity.

To properly begin, it is important to talk about the Large Hadron Collider, as it is the apparatus that creates the collisions, and therefore generates the elementary particles with which physics analyses can be carried out. To continue, it is worth looking at the CMS detector and everything that makes it up. Starting with a look at each of its component parts and ending with the actual detector that allows the reconstruction of particles passing through it.

2.1 The Large Hadron Collider

The Large Hadron Collider, as its name suggests, is the largest particle collider ever built. It is located about 100 metres underground, between the Jura mountains and the city of Geneva. It is the largest facility of the European Organization for Nuclear Research, more commonly designated by its French acronym: CERN

and standing for Conseil Européen pour la Recherche Nucléaire. The LHC is the principal tool of the Higgs boson quest. It will be presented in detail in the following paragraphs of this section.

2.1.1 The birth of the Large Hadron Collider at CERN

In 1949, in a post-war context of European cooperation, the French physicist Louis de Broglie had the idea to create a European nuclear research laboratory. This came true five years later, when twelve European countries ratified the convention establishing CERN on the 29^{th} September 1954. Its location was decided to be on the Franco-Swiss boarder in the Gex county, which is a neutral place at the centre of Europe with a low population density (it changed since 1954). Moreover, at the beginning its purpose was mainly nuclear physics, but with some time and the potential investments from a number of member states in evolution, CERN has moved into particle physics.

At present, 23 countries are CERN's member states. Besides, about 2 500 scientists are working at CERN on a permanent basis, but nearly 15 000 scientists, representing more than 100 nationalities, come to work at CERN during the year.

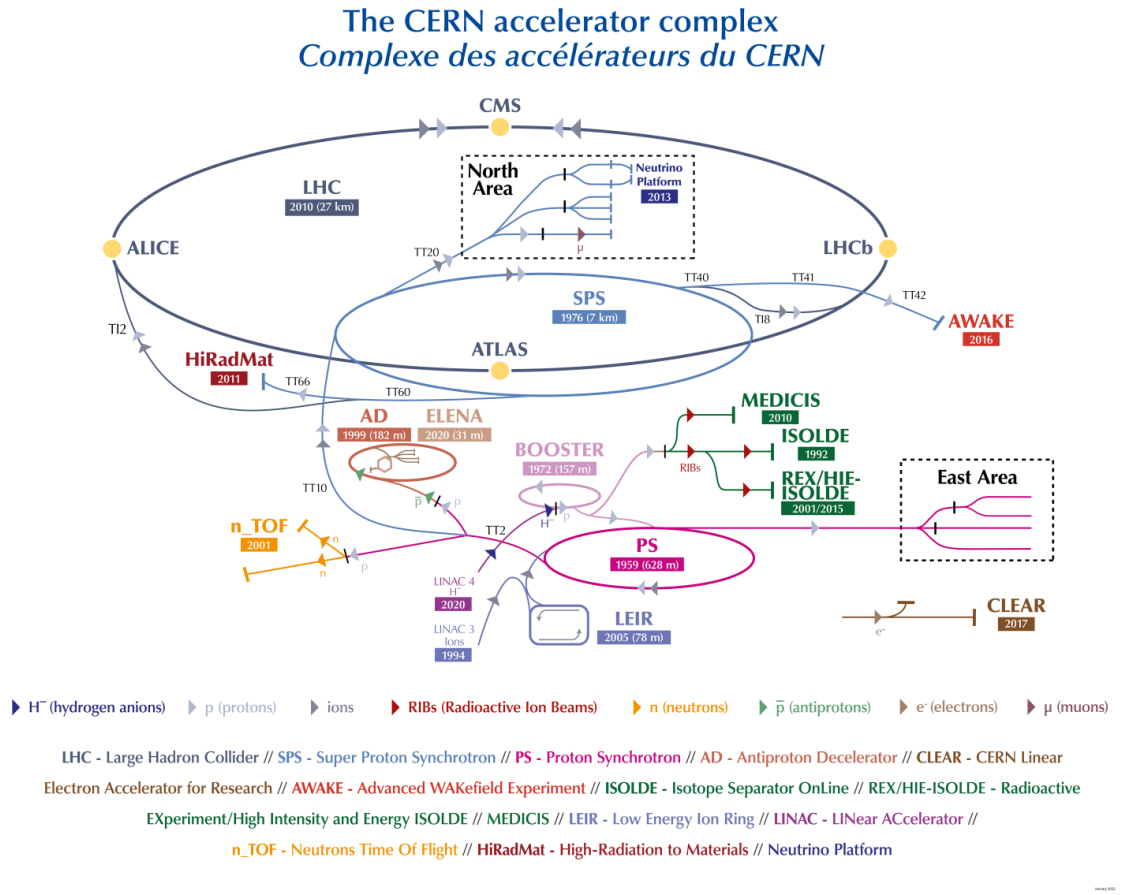

Figure 2.1: Schematic representation of the CERN accelerator complex [11].

In addition to all this, CERN is responsible for other progresses. Notably in the

field of electronics and computing, with the creation of the World Wide Web in 1990.

In 1957, the Synchro-Cyclotron was CERN's first accelerator, and it was accelerating protons. This was followed in 1960 by the Proton Synchrotron (PS) which is still in use today, as shown in fuchsia in Figure 2.1. CERN was extended in 1971 to build the Super Proton Synchrotron (SPS) with its 7 km of circumference. This accelerator was at the root of the discovery of the $W^{\pm}$ [75, 76] and Z bosons [77] in 1983 by the experiments UA1 and UA2. Then, the experiment NA48 measured the direct CP violation in 1999 [78]. The next apparatus is the Large Electron Positron collider (LEP). Its construction started in 1983, but it was only in 1989 that it enters into service. The LEP consists of a tunnel with a circumference of 26.7 km. It was the largest particle accelerator in the world and the most powerful lepton collider. It was dismantled, and its tunnel was used for the LHC, which is in service since 2008.

As it shown in Figure 2.1, the LHC is the last part of the accelerator complex [79]. Before turning inside it, protons must follow a specific acceleration path. All start from a bottle of hydrogen: atoms of this gas are only composed of one electron and one proton. Both are separated thanks to a strong magnetic field, and protons are then extracted to a Radio Frequency Quadrupole (RFQ). The magnetic field of this device form proton bunches and accelerate them up to an energy of 750 keV. Then, the bunches are injected in a Linear Accelerator (LINAC 4) which provides an acceleration up to 50 MeV. The next step occurs in the Booster, which is the first circular accelerator with a length of 150 m, where bunches are accelerated up to 1.4 GeV. Protons are then sent to the 628 m ring of the PS. In it, proton beam's energy can increase until 26 GeV. The last step before entering the LHC is the acceleration in the SPS. There, proton's energy will reach 450 GeV. Finally, when the energy is high enough, the proton beam is separated in two different beam pipes. The first one is injecting the protons in the LHC in the clockwise direction, and the other one in the anti-clockwise direction. Bunches are accelerated up to a design energy of 7 TeV, and proton beams are crossing at some points indicated in yellow in Figure 2.1. Other particles like heavy ions (lead nucleus for instance) can also be injected in the accelerators. The collisions are recorded by four main experiments which are ATLAS, ALICE, CMS, and LHCb. More information about them will be given, but before that more precise elements about LHC must be understood.

2.1.2 Design of the apparatus

The LHC is a proton-proton collider which replaces an e^+e^- collider: the LEP. Compare to electrons, protons have a huge advantage, they are less impacted by the synchrotron radiation effect due to their higher mass. This effect corresponds to the radiation of photons when a charged particle is accelerated radially. This induces an energy loss which limits the nominal energy of a lepton collider. It is one of the reason which led to the construction of a hadron collider to replace the LEP. To understand the requirements needed to build such an apparatus and the characteristics that it must satisfy to reach its goal, the first thing to know is how

works a proton-proton collision.

Proton-proton physics

In general, a proton is described as the assembly of two u quarks and one d quark. But in reality, it is a more complex structure governed by the strong interaction. The QCD describes the proton as a composite system in which the three valence quarks are confined in a sea of quarks and gluons, represented in Figure 2.2. The particles from this sea, as well as the valence quarks, are called partons.

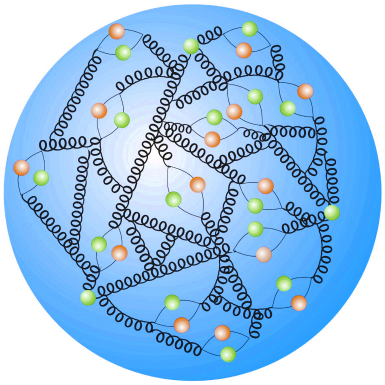

Figure 2.2: QCD representation of a proton. Three valence quarks in green, are at the middle of the sea of quarks, anti-quarks in orange, and gluons represented by springs. The figure is taken from [12].

This proton structure explains all the Higgs boson production modes. For instance, in the case of ggH, the interacting partons are gluons. Moreover, if the protons are amalgams of partons, multiple interaction can append during the same proton-proton collision. In this case, the interaction energy is not equal to the total centre of mass energy. A parton momentum represents only a fraction of the total proton momentum noted x and used in the following formula:

$$p_{parton} = x p_{proton} \tag{2.1}$$

In the same way, when a collision between two partons occurs, the resulting centre of mass energy of this interaction is not $\sqrt{s}$. The momentum fraction $\tilde{s}$ of both parton must be taken into account:

$$\sqrt{\tilde{s}} = x_1 x_2 \sqrt{s} \tag{2.2}$$

This expression can explain that the energy of an event is much lower than $\sqrt{s}$.

When multiple interactions involving partons append at the same time, a lot of particles can be generated by hard scattering processes. This phenomenon is called multi-parton interaction (MPI). The modelling of these extra events is important to correct the background resulting from MPI. The principal source of uncertainties at LHC comes in this modelling, the spatial distribution of partons depending on x, also called parton distribution function (PDF), and the final state of these interactions.

Architecture of the LHC pipes

Actually, the LHC is not a perfect ring, it is more a kind of octagon composed of eight straight sections and eight arcs by way of angles. The straight sections are in average 528 m long. Their size depends on their position in the LHC, for example the size differs if the section is used for the beam injection in the collider. Besides, the acceleration is done by radio frequency (RF) cavities placed in cylindrical refrigerators called cryo-modules, allowing the RF cavities to operate in a superconducting state. Each straight section is equipped with two RF cavities placed in a single cryo-module. The first one accelerate the clockwise beam and the second one the anti-clockwise beam. Furthermore, each arc is 2.45 km long and contains 154 magnetic dipoles to bend the particle trajectory.

Magnetic systems

Powerful magnetic fields are needed to keep the proton beams inside the pipe. One of the challenge of the LHC design was to maintain the pseudo-circular trajectory of the particles. In addition, it is possible to bend two beam trajectories which have opposite directions. To do that, opposite magnetic fields are used. In general, LHC's magnetic fields are not the same depending on the section. Many magnet technologies are used to achieve this. The values given for the different parameters correspond to the nominal ones from the initial design of the LHC.

- **Dipole magnets** are located in the arc sections of the LHC. They are the most numerous and are in total 1232. They provide an 8.3 T magnetic field which is used to curve the trajectory of particles. To reach a such impressively high magnetic field, an 11 000 A current is required. These values correspond to the nominal ones when protons are accelerated at 7 TeV. Figure 2.3 represents a section cut of a LHC's cryo-dipole, where the magnets have a copper colour. The vacuum chambers where the vacuum is created are also indicated.

- **Quadrupole magnets** are 392 in total. Their purpose is to focus vertically and horizontally the beam. They are used to maintain the beam in the pipe and to minimize the beam section. In this way, it is also maximizing the probability to have a collision per bunch crossing.

- **High order multipole magnets** are used as corrector magnets. They are here to correct the imperfect magnetic fields at transition regions. For instance, they can correct the magnetic field around the experiments where their own fields can interfere with the dipoles and quadrupoles.

LHC's superconducting magnets are made of niobium and titanium ($NbTi$) cables. Their superconducting properties are operating with a temperature of 1.9 K reached thanks to a cryogenic system based on the use of superfluid helium. Its high thermal conductivity, is ideal for the refrigeration and stabilization of large superconducting systems. The cooling is a crucial work to increase the performance of $NbTi$ and maximize the strength of the superconducting magnets.

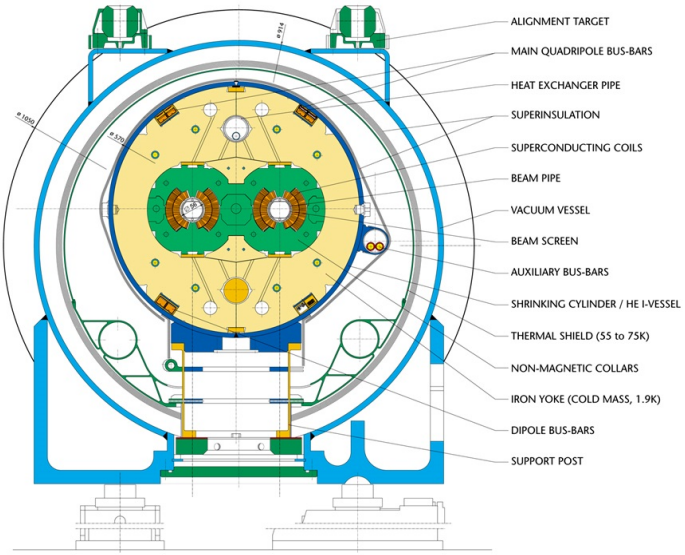

Figure 2.3: Schematic representation of a transverse slice of a cryo-dipole of the LHC (lengths are in mm) [13].

Vacuum

The LHC beam pipes must be as empty as possible to avoid protons to interact with remaining atoms inside the pipes. A three levels vacuum system was put in place to achieve this complex task. First, the main one corresponds to the beam vacuum. It is one of the most impressive feature of the LHC. Indeed, at the interaction points the pressure is lower than 10^{-9} Pa, making this vacuum even more intense than the interstellar vacuum of 10^{-8} Pa. In the other part of the pipe, the vacuum can go up to 10^{-7} Pa, allowing the pipe to stay at the temperature of 5 K. Next, there is an insulation vacuum around the cryo-modules. It is needed to maintain the cryo-modules at 1.9 K when they are cooled with liquid helium. And finally, another insulation vacuum is used for the helium providing system, it has the same purpose as the previous one and act to preserve the liquid helium temperature.

Radio frequency cavities

All along the accelerator complex, the acceleration of protons is made with RF cavities. In the LHC, these apparatus consist of metal chambers grouped by four in a cryo-module. Inside the chambers, a 4.5 T electromagnetic field is used to accelerate protons. During this operation, the protons are spatially concentrated to form compact bunches, which facilitate the collision and insure a high luminosity at the interaction points. Bunches measure a few centimetres in the LHC's ring, but their sizes are not constant, they are permanently squeezed and expanded through the different processes of acceleration and control of the trajectory.

Expected performance of the collider

The LHC was designed in a such way to reach its goal [79]. This implies the definition of nominal parameters which are supposed to be respected. They are listed in Table 2.1.

Table 2.1: Nominal parameters of the LHC in proton-proton collisions [79].

Parameter	Notation	Nominal value
Centre of mass energy	$\sqrt{s}$	14 TeV
Bunch separation	Δt	25 ns
Number of bunches	n_b	2 808
Number of protons per bunch	N_p	1.15×10^{11}
Instantaneous luminosity	$\mathcal{L}$	10^{34} cm^{-2}s^{-1}
Revolution frequency	f_{rev}	11 245 Hz
Transverse bunch RMS at the IP	σ_z	16.7 μm
Longitudinal bunch RMS at the IP	σ_{xy}	7.55 cm
Beta function at the IP	β^*	0.55 m
Crossing angle at the IP	θ_c	285 μrad
Transverse emittance	ϵ_n	3.75 μm

When thinking about LHC, the first parameter which comes in mind is the centre of mass energy of proton-proton collision. It is equal to $\sqrt{s} = 14$ TeV, corresponding to the collision of two protons, each having an energy of 7 TeV. But, the entire proton will not participate in the collision, just some partons having a fraction of the initial momentum will interact. A such value of energy is required to have enough partons with the required energy to produce Higgs bosons and also other heavy particles.

In the LHC's pipes, a total of 2 808 bunches (n_b) composed of approximatively 1.15×10^{11} protons (N_p) are turning in the ring. The bunches are spaced 25 ns (Δt) apart from the closest ones and make 11 245 turns of the 26.7 km ring per second (f_{rev}).

The instantaneous luminosity $\mathcal{L}$ serves as an indicator of the collider performance. It is related to the cross-section σ and the number of events per unit of time $\frac{\partial N}{\partial t}$ via the following equation:

$$\frac{\partial N}{\partial t} = \mathcal{L}\sigma \tag{2.3}$$

A high value of instantaneous luminosity is double edged. On one side, it is the key to produce rare processes such as $t\bar{t}H$, but on the other one it means a lot of background from events originating from pile up that must be discarded. From this parameter, it is possible to get the amount of produced data which corresponds to the integrated luminosity noted L. It is the integration of the instantaneous luminosity over time:

$$L = \int \mathcal{L} dt \tag{2.4}$$

The two beams are not frontally crossing each other, there is a crossing angle called θ_c. In addition, the bunches are not spherical, when the crossings append the cross-section are not the same in function of which parts of the bunches are interacting. For that, the transverse and longitudinal Root Mean Square (RMS) of the bunch sizes (respectively σ_{xy} and σ_z) must be taken into account. Thus, a reduction factor of the instantaneous luminosity F is introduced as:

$$F = \left(1 + \frac{\theta_c \sigma_z}{2\sigma_{xy}}\right)^{-\frac{1}{2}} \tag{2.5}$$

Knowing this factor, the instantaneous luminosity can be written as:

$$L = \frac{N_p^2 n_b f_{rev} \gamma_r}{4\pi \eta_n \beta^*} F \tag{2.6}$$

Where ϵ_n is the emittance of the beam, β^* is the beam focus, and γ_r is a relativistic factor because the proton speed is close to the speed of light.

With the high value of luminosity at the LHC, there is a phenomenon called pileup. It is defined as the number of simultaneous interactions per bunch crossing. Its average value is given by:

$$\langle PU \rangle = \frac{\sigma_{pp} L}{n_b f_{rev}} \tag{2.7}$$

Where σ_{pp} is the inelastic cross-section in proton-proton collision. From the LHC parameters, it should be equal to $\sigma_{pp} = 69$ mb for a centre of mass energy equals to 13 TeV according to the CMS Collaboration [80]. The expected pileup should be 23 interactions per bunch crossing in 2016, and 32 for 2017 and 2018 [81]. In reality, the nominal parameters are quite similar to the real ones, but there are still some differences measured by the experiments. Indeed, it was found experimentally that the pileup values are 28 for 2016, 38 for 2017, and 37 for 2018. Moreover, in some extreme cases this value is much higher, with a value going above 60 interactions per bunch crossing [81].

2.1.3 The physics experiments

As represented in Figure 2.1, there are four experiments working on the LHC. Actually, there are eight, the four main experiments represented in the figure, and four smaller ones. The principal experiments are located at dedicated interactions points and are built around it in order to completely incorporate the collision products. These four experiments are:

A Toroidal LHC Apparatus (ATLAS)

ATLAS [82] is one of the two multi-purpose detectors designed to participate in the Higgs boson quest and to measure its properties. But, it has also the vocation to study QCD effects or to explore possible BSM physics. It is also the biggest detector, with a 25 m diameter and a 46 m length.

The ATLAS detector is located at the first interaction point (IP1). It is a huge cylinder composed of many subdetectors specialized in the detection of specific type of particle. The closest subdetector from the beam line is the inner tracker, where the track sensing is based on gaseous and silicon sensors. Right after that, there is a first 2 T solenoid magnet. Then comes the sampling calorimeter composed of two part: the inner one made of liquid argon with accordion lead absorbers for the electromagnetic calorimeter, and the hadronic one is made of scintillating tiles and iron absorbers for $|\eta| < 1.7$, liquid argon and copper absorbers for $1.7 < |\eta| < 3.2$, and the forward region is made of liquid argon with copper and tungsten absorbers. The muons chambers are in the outer region of ATLAS, the system forming the 4 T toroidal magnet is included in the set of chambers.

Compact Muon Solenoid (CMS)

CMS [83] is the other multi-purpose detector. It can study the same thing as ATLAS. It is located in the fifth interaction point (IPS), which is diametrically opposed to IP1, where the ATLAS detector is. Two similar purpose experiments can allow making complementary studies, some cross-check. It allows validating the results of the other experiment like it was done for the Higgs boson discovery. It is not the biggest one, with only a 14.6 m diameter and a 21.5 m length. But it is the heaviest with its 14 000 tons, which corresponds to one and a half Eiffel Tower.

The CMS detector has a central place in this thesis, the Section 2.2 is entirely dedicated to its detailed presentation.

A Large Ion Collider Experiment (ALICE)

ALICE [84] has the purpose to study the expected matter state at the primordial universe, resulting in a quark-gluon plasma (QGP). For that, it focuses on the detection of heavy ion physics. Some special runs of the LHC are using lead nuclei, which are accelerated in the same way as protons. It is located around the second interaction point (IP2).

The ALICE detector is constituted of an inner tracker close to the beam line, complemented by a time projection chamber used to improve the particle identification and the background rejection. Then there are calorimeters, associated with time of flight and Cherenkov light detectors. Muon chambers are only placed orthogonally to the beam line in the forward region, and they are surrounded by a dipole magnet.

Large Hadron Collider beauty (LHCb)

LHCb [85] as its name indicates, it is an experiment focused on the b quark physics. It aims to understand the CP violation via interactions of hadrons with b quarks. During the studies performed by this experiment, a lot of new hadrons were discovered, like mesons, baryons, and more exotic forms like tetraquarks and pentaquarks [86] (composed of four and five quarks).

The LHCb detector is only built in the forward region after the eighth interaction point (IP8). Close to the primary vertex location there is the tracker, followed

by the electromagnetic and hadronic calorimeters, and the muons chambers at the end. A dipole magnet encloses the tracker, and all of this subdetectors are orthogonal to the beam line.

And the four other experiments are:

Total Elastic and diffractive cross-section Measurement (TOTEM)

TOTEM [87] has its goal directly written in its name, thus the measurements of the total cross-section, the elastic one, and the diffractive one. To do that, it is equipped with a tracker composed of cathode strip chambers, gas electron multipliers, and silicon sensors. They are placed in many places along the beam line and at an average distance of 420 m of IP5. They detect scattered proton coming from collisions at IP5.

Large Hadron Collider forward (LHCf)

LHCf [88] aims at precisely characterizing ultra high energy cosmic rays, by measuring the energy and the number of pions π^0 produced in the forward region at IP1. To do that, it is composed of two detectors situated at 140 m on either side of ATLAS.

Monopole and Exotics Detector At the LHC (MoEDAL)

MoEDAL [89] is trying to measure directly a theoretical particle, called a magnetic monopole [90]. It is a particle with a single magnetic pole: only a North pole or only a south pole. The analogy with normal magnetic objects does not work with it because they have both. It is also looking for other exotic particles. The detector is located at IP8, and it is a kind of giant photograph combining a plastic tracking, a calorimeter, and a timing detector.

Forward Search Experiment (FASER)

FASER [91] is designed to search light particles with a very low interaction probability. These particles are candidates for dark matter or can explain phenomenon such as neutrino oscillation or the asymmetry between matter and anti-matter. It is located at 480 m of IP1, and it is composed of a brand-new neutrino detector, a tracker, and an electromagnetic calorimeter.

2.1.4 The Large Hadron Collider during operation

The LHC follows a precise schedule, presented in Figure 2.4, in which proton collisions are planned for the physics experiments, but also collisions with heavy ions. When the LHC is in operation, this is called a run. So far there have been three: the first from 2010 to the beginning of 2013, a second from 2015 to the end of 2018, and a third that has just started and is expected to finish at the end of 2025. Between two runs, the long shutdowns (LS) take place, which are phases where the LHC is stopped and allow repairing or improve the equipment. At the end of

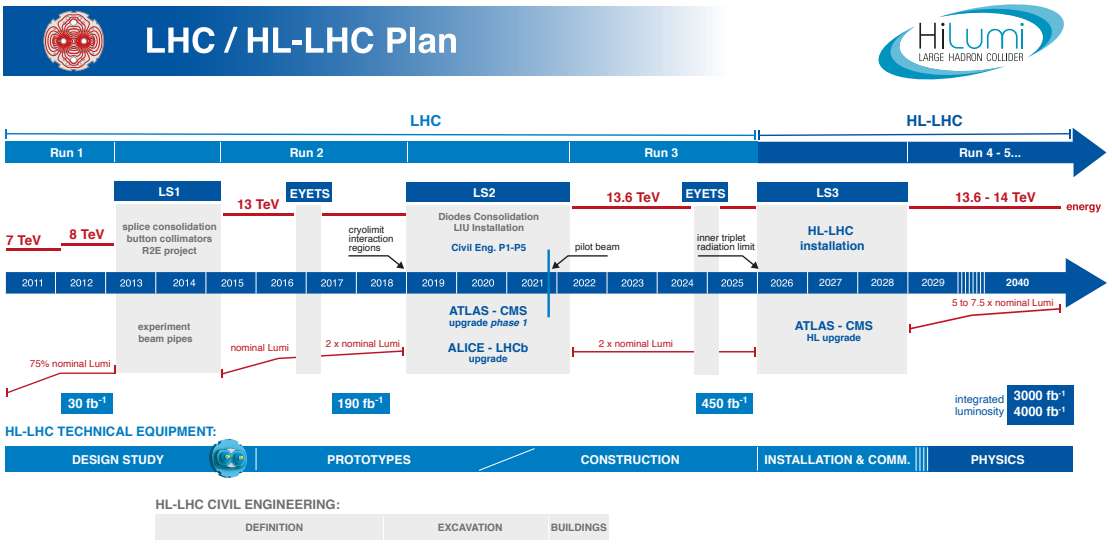

Figure 2.4: LHC and High Luminosity LHC schedule [14].

Run-3, the LHC will enter its final phase and will be the High Luminosity LHC (HL-LHC). This stage of the LHC's life will be covered in a dedicated section.

The different runs do not all have the same characteristics, whether in terms of duration, performance, or even some subdetectors are changed for the different experiments.

Run 1

The first LHC physics run started in 2010. It was the first time that the LHC reached collisions with 7 TeV as centre of mass energy. The next year, the energy was still the same, but in 2012 it went up to 8 TeV. The luminosity was not constant over year, starting from less than 0.05 fb^{-1} in 2010 to 23.3 fb^{-1} in 2012. These results are shown in Figure 2.5. The full Run-1 integrated luminosity was around 30 fb^{-1}, but some analyses started at its beginning when only few picobarns of data were collected, just enough to measure the W and Z bosons cross-sections. Then, the main highlight of the Run-1 is the Higgs boson discovery. Moreover, at this time, the average pile up was 21 simultaneous interactions per bunch crossing. The end of 2012 was the end of the first run, followed by the LS1, lasting more than two years. It was done in order to start the experiment upgrades and to increase the luminosity and essentially to increase the centre of mass energy closer to its nominal value, presented in Table 2.1.

Run 2

The second run started in 2015 and lasted until the end of 2018. At this time, the centre of mass energy of proton-proton collisions increased up to 13 TeV, which is closer to the LHC designed value. This parameter was barely constant over the different periods of this run, only small fluctuations were observed.

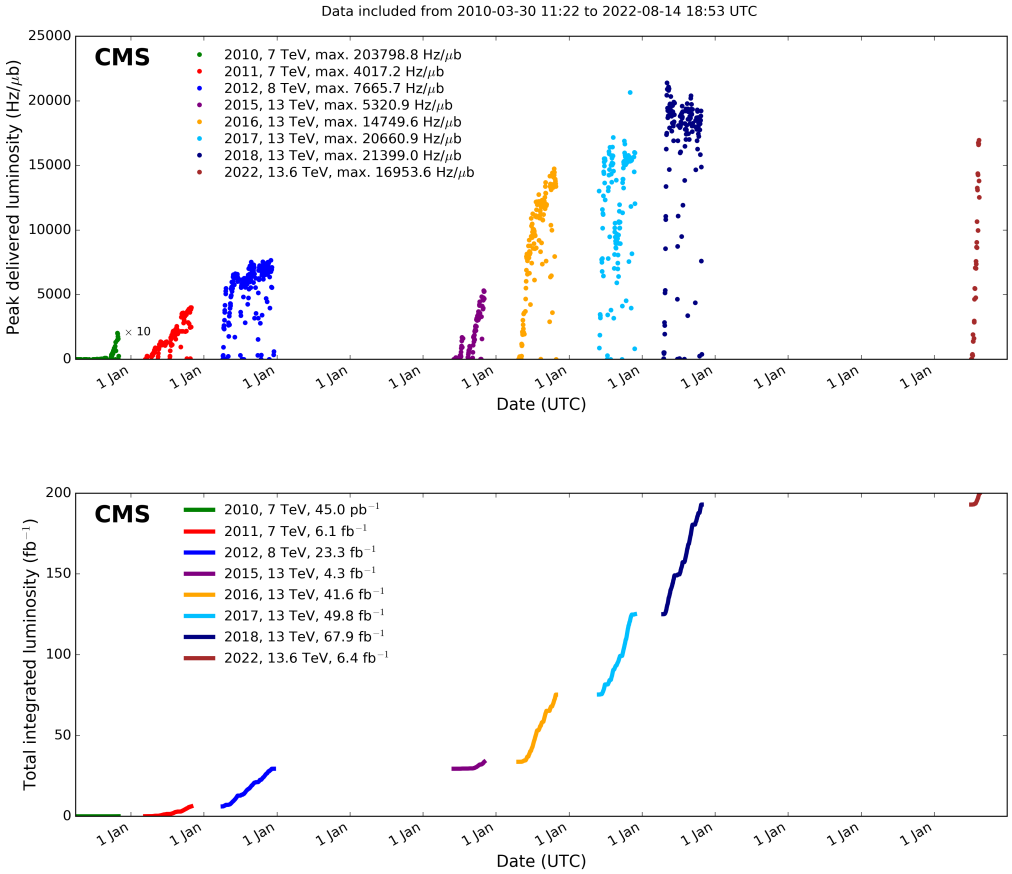

Figure 2.5: Peak luminosity (on top) and integrated luminosity (on bottom) measured by CMS over time, the three runs are represented: full Run 1 from 2010 to 2012, full Run 2 from 2015 to 2018, and the start of Run 3 in 2022 [15].

During the Run-1, the bunch spacing was equal to 50 ns, and it only reached its nominal value of 25 ns in the Run-2. Concerning the luminosity, only at the end of 2016 the full Run-1 luminosity was more than doubled. At the end of 2018, the integrated luminosity for the full Run-2 was higher than 160 fb^{-1}. The instantaneous luminosity finally reached its nominal value in 2016, followed by a peak observed at 2×10^{34} $cm^{-2}s^{-1}$ in 2018, as shown in the upper part of Figure 2.5. Such a value correspond to the record of luminosity which is twice higher than the designed value. The pileup was also higher than during Run-1, its average value was 34 simultaneous interactions per bunch crossing, going up to 38 in 2017, as represented in Figure 2.6. At the end of this run, started the LS2. Its aim was to increase the centre of mass energy and to maintain the detector performance. Some upgrades were provided, like the new gas electron multiplier (GEM) chambers for the muon detection in the CMS detector [92].

Run 3 (Ongoing)

At the moment of the writing of this thesis, the Run-3 has just started recently with promising results in terms of beam performance. The first proton beam was

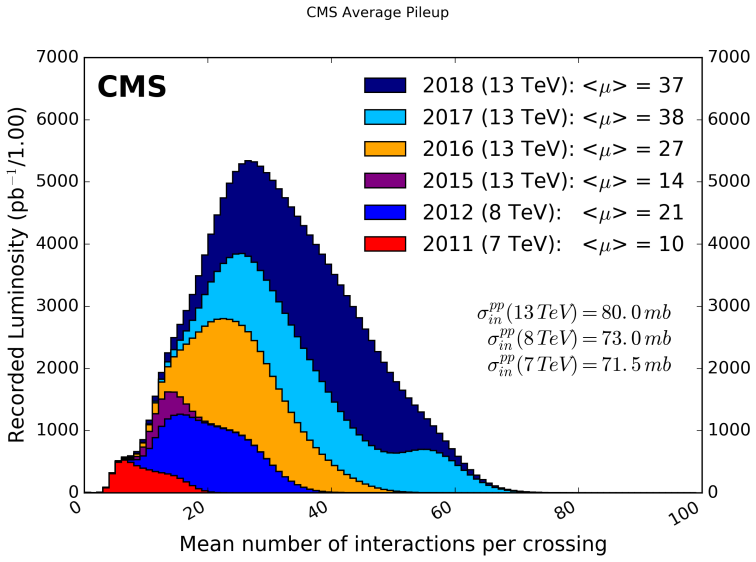

Figure 2.6: Interactions per bunch crossing, each year of Run 1 and Run 2 are stacked [15].

stabilized in the LHC on July 5^{th} 2022, thus the day after the 10^{th} birthday of the Higgs boson first observation. The centre of mass energy is still below its nominal value, but it is higher than during Run-2 with 13.6 TeV. The instantaneous luminosity still does not reach a new record even if it is just a question of time, but it is currently comparable to what was observed in Run-2 and with. Run-3 will last until the end of 2025. During these years, it is expected to reach more than 350 fb^{-1} of total integrated luminosity from proton-proton collisions.

2.2 The Compact Muon Solenoid detector

When talking to people about CMS, the first thing they ask is: what does the acronym means? And answering that it stands for Compact Muon Solenoid is rarely enough to satisfy them. First, why compact? It is always useful to remind them that CMS is a cylinder with a 14.6 m diameter and a 21.5 m length, compared to the 25 m diameter and the 46 m length of ATLAS, it is quite compact for the same purpose. Also, its mass is equal to 14 000 tons, in comparison the Eiffel Tower is 319 m high and 125 m wide for a mass of 10 100 tons. Next, what about muon? The CMS detector was initially designed to precisely measure muons coming from Higgs boson decays. And finally, what is a solenoid? It refers to the shape of the 3.8 T superconductive magnet used in CMS. A solenoid is an electromagnet made with a helical coil of wire.

More seriously, the CMS detector is located 100 m under the small city of Cessy in the Gex county. It corresponds to the IP5 of the LHC, which is totally surrounded by the detector. It is composed of many subdetectors, each having a specific role to play in the detection of particles. First, the tracker is recording the trajectory of the charged particles, it allows determining the position of the primary vertices, and provides a measurement of the particle momentum. Then,

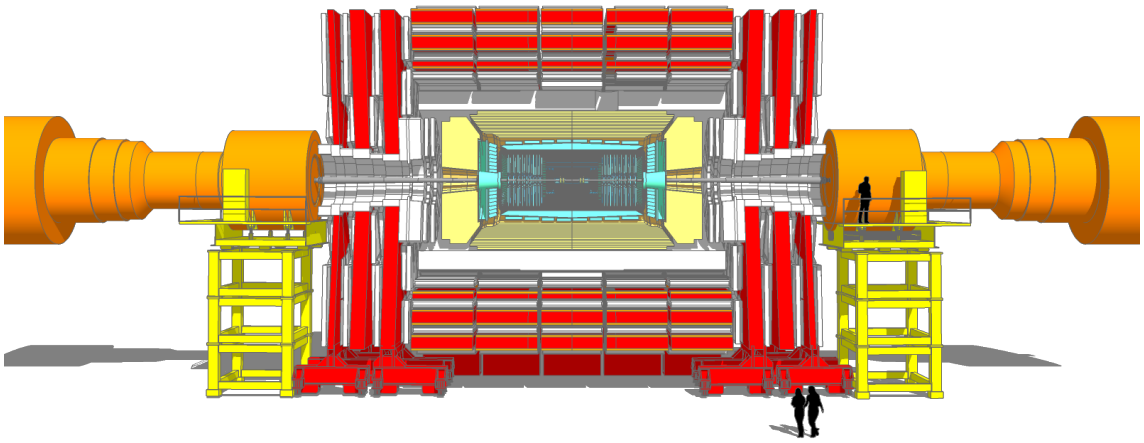

Figure 2.7: View of a longitudinal slice of the CMS detector [16].

there are the electromagnetic and hadronic calorimeters, collecting the energy of photons and charged leptons for the first one, and the energy of hadrons for the second one. After that, there are central elements of CMS: the 3.8 T solenoid magnet used to curve the trajectory of charged particles, and the muon chambers detecting muons as indicated by its name. All these sub-systems will be described with more details in the Subsection 2.2.2.

2.2.1 General overview of CMS

The CMS detector can be described as a cylinder with its centre is the interaction point and its length is tangential to the beam line. In a right-handed Cartesian coordinate system, the cylinder centre corresponds to the origin, while the tangent to the beam line is the z axis oriented in the direction of anti-clockwise proton beam. If talking about geography, this axis points on the direction of the Colomby de Gex, which a nice spot for hikes offering the chance to observe chamois. Apart from that, the transverse plane is described by the x axis which is radial to the centre of the LHC ring, and the y axis pointing upward.

A polar coordinate system is also introduced due to the cylindrical shape of the detector. Considering a vector $\vec{p}$ starting from the origin and going to a point somewhere inside the CMS detector, it is worth introducing its radial coordinate r corresponding to the distance from the z axis to the vector. With that, it is needed to have an azimuthal angle ϕ which is defined on the transverse plane between the vector and x axis. Another polar angle θ is defined between the vector and the z axis. These coordinate systems are represented in Figure 2.8, where on the left it is with respect to the LHC ring, and on the right it is just at the CMS scale where the detector is illustrated by a cylinder.

Both coordinate systems have their advantages. The polar system is more

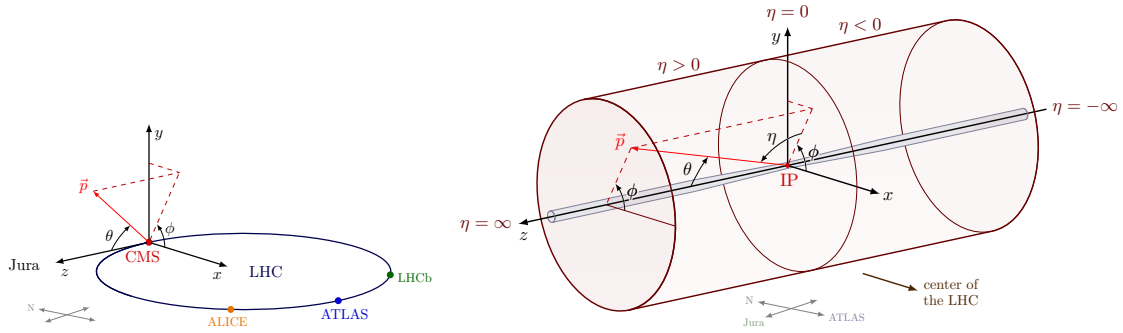

Figure 2.8: CMS coordinate system in regard to the LHC on the left, and internally with the cylinder representation of CMS on the right.

adapted to describe macroscopic observables. For instance, an event will be described in this system where the observables are invariant under a Lorentz boost, corresponding to projections on the transverse plane (x, y). Among these observables, there are the transverse momentum p_T and the transverse mass m_T. These transverse plane variables are used because in proton collisions only a fraction of the momentum is carried by the partons and the rest of the protons usually escape detection in the vacuum tube. Both are kinematic information about the detected particles, and they are defined as:

$$p_T = \sqrt{p_x^2 + p_y^2} \tag{2.8}$$

$$m_T = \sqrt{m^2 + p_x^2 + p_y^2} \tag{2.9}$$

On the other hand, considering the transverse energy E_T, it is also convenient to use the polar coordinates:

$$E_T = E \sin\theta \tag{2.10}$$

Similarly, the transverse mass m_T can also be defined with these coordinates:

$$m_T = \sqrt{E^2 - p_z^2} \tag{2.11}$$

In general, this system is used to describe the orientation and angles of particles relative to the z axis. Observables like the rapidity y or the pseudorapidity η of a particle are expressed using the polar coordinates.

$$y = \frac{1}{2} \ln\left(\frac{E + p_z}{E - p_z}\right) \tag{2.12}$$

For a particle, the pseudorapidity corresponds to its relative angle to the z axis. It can be written in the same way as y or using only *theta* angle, where their relation is illustrated in Figure 2.9:

$$\eta = \frac{1}{2} \ln\left(\frac{p + p_z}{p - p_z}\right) = -\ln\tan\left(\frac{\theta}{2}\right) \tag{2.13}$$

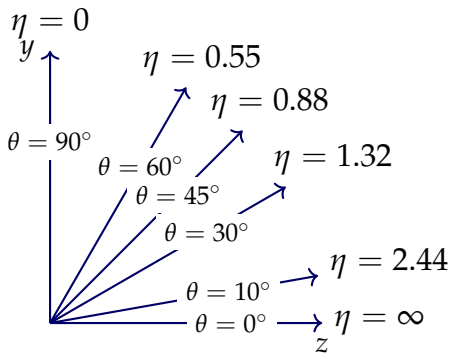

Figure 2.9: Relation between the θ of the CMS coordinate system and the pseudo-rapidity η.

If the particle is only in the transverse plane, this leads to $\eta = 0$ for $\theta = \frac{\pi}{2}$. And the other extreme case is when the particle is moving perfectly parallel to the beam line, thus it gives $\eta = +\infty$ for $\theta = 0$, or $\eta = -\infty$ for $\theta = \pi$.

In the case of the detection of two particles at the same time, another parameter could be a great benefit. It is the spatial separation between two particles called ΔR. It uses the ϕ angle difference and the pseudorapidity η difference, which are both Lorentz boost invariant.

$$\Delta R = \sqrt{\Delta\eta^2 + \Delta\phi^2} \tag{2.14}$$

Setting a condition on ΔR allows to characterize a solid angle around the desired particle, which is often used to know if the particle is isolated from hadronic activity. Indeed, if the ΔR between two particles is higher than the threshold condition, it means that it is possible to spatially separate particles from each other.

2.2.2 The subdetectors and equipments

The CMS detector was designed in a such way to surround the IP5 in order to have the possibility to detect all the particles coming from a collision [83]. Even if the detector's shape is closer to a cylinder, it can be compared to an onion. Indeed, it is composed of concentric layers of subdetectors. The subdetectors are composed of two parts: the barrel, a cylinder around the beam line, and the endcaps, which, as indicated by their names, close the barrel on each side. The separation between both parts can be express with a pseudorapidity value. Each of the subdetectors, pointed in Figure 2.10, has a specific mission in the particle detection.

- **The inner tracker** is in charge of the reconstruction of the charged particle trajectories. Its inner part composed of high precision silicon pixels is dedicated to the reconstruction of vertices and the particle momentum measurement.
- **The electromagnetic calorimeter** is made of $PbWO_4$ crystal bars, collecting the energy coming from photons and electrons.

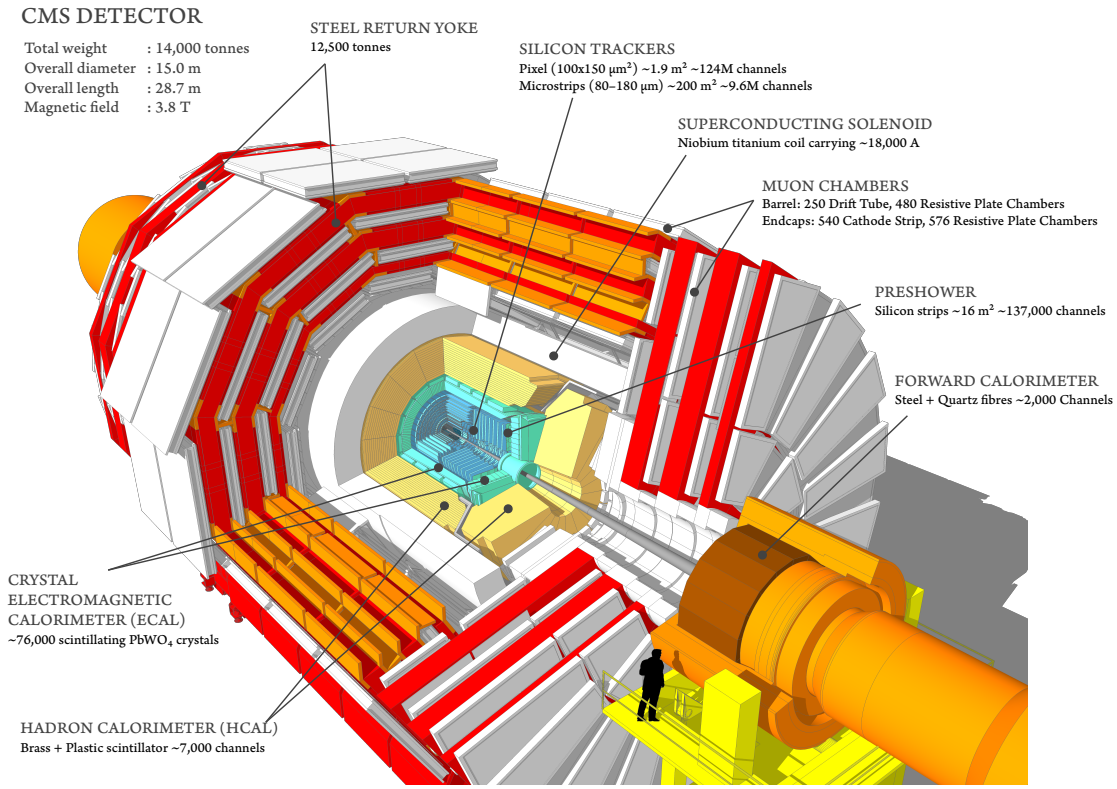

Figure 2.10: View of the CMS detector partially open [16].

- **The hadronic calorimeter** is in charge of the energy collection of hadrons or hadronic jets. It can detect charged hadrons as well as neutral hadrons.
- **The superconducting solenoid** is not a detector, but it is a central part of the detector and important enough to be mentioned. It provides a 3.8 T magnetic field, curving the particle trajectories. Thanks to the curvature, the momentum and the charge of the particles can be deduced.
- **The muon chambers** are focused on the detection of muons. They are the last layer of subdetector due to the fact that muons are weakly interacting with the other subdetectors due to their heavy mass. The chambers measure the muon trajectories and their energies, thanks to 12 500 tons of steel reducing their velocity.

Inner tracker

The inner tracking system of CMS is placed as close as possible to the interaction point [17]. It consists of a cylinder with a 2.4 m diameter and a 5.6 m length, covering entirely the region where $|\eta| < 2.5$. It is composed of a succession of silicon sensor layers, as shown in Figure 2.11, which can detect charged particles originated from the primary vertices. More precisely, the signals recorded by these silicon sensors correspond from a small fraction of charged particle energy. The tracker is under a uniform magnetic field of 3.8 T facilitating the particle

identification, reconstruction, and momentum measurement. Furthermore, the inner tracker has the mission to reconstruct the vertices and then to determine which is the primary vertex, the secondary vertices coming from decay of particles with a certain time, and those from pileup events.

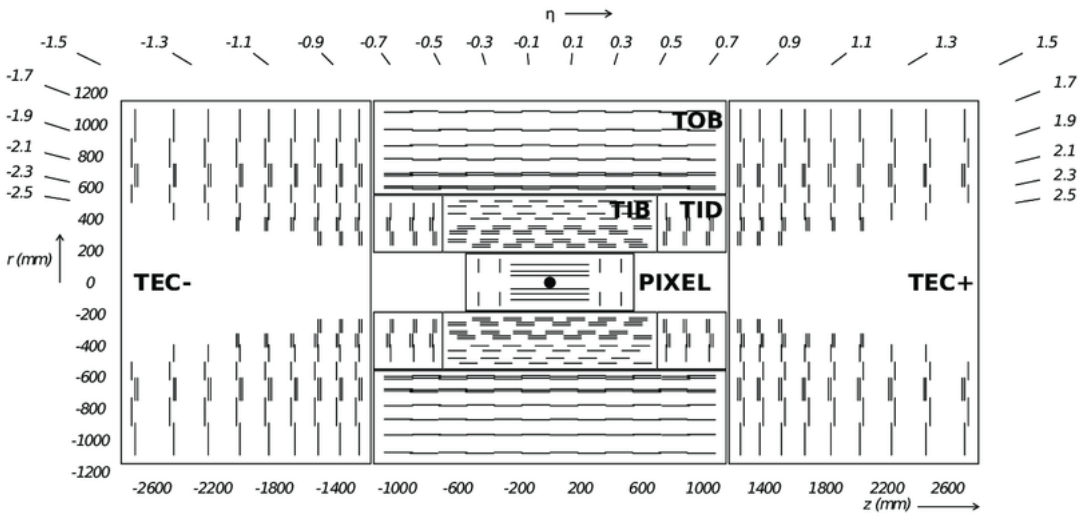

Figure 2.11: Schematic representation of a slice of the inner tracker of CMS [17].

The central part of the tracker is called the pixel detector. Its name comes from the 65 million silicon pixels, each of them measuring 100×150 μm^2. They are arranged in different manners depending on if they are in the barrel or the endcap part. The three barrel layers (BPix) have a cylindrical shape, and the spaces to the beam line are 4.4, 7.3 and 10.2 cm respectively. It is represented with the two different views in Figure 2.12. Each endcaps are made with two disks of pixel (FPix) with an inner radius of 6 cm and 15 cm for the outer one. Each pixel has a 10 μm spatial resolution in the transverse plane, and 20 μm in the longitudinal plane.

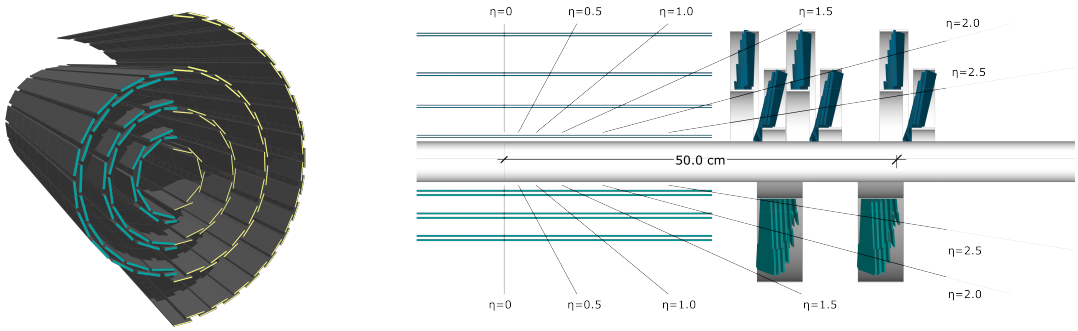

Figure 2.12: Pixel detector of the inner tracker of CMS. Perspective view on the left and side view on the right [18].

One of the drawbacks of this impressive spatial resolution is the large amount of passive material added in the tracker. Firstly, it is a silicon detector which is

discrete in nature, as it is subdivided into modules. It is not a continuous detector like a gas detector. All of these modules are integrated into the detector by means of a mechanical support. Then there is indeed a need for electronics and the various power and readout cables. These electronics need a cooling system to prevent them from overheating and to preserve the silicon, which is cold hard radiation. The cooling is delivered by pipes which together with the rest of the elements mentioned above contribute to the extra material, and thus noise.All these extra components leads to an increase of background noise such as multiple scattering or nuclear interactions. And these parasitic effects can have an impact on the performance of the particle trajectory reconstruction. To counteract this, a new pixel detector was installed between 2016 and 2017 and the improvement consists of the addition of an extra BPix layer and another FPix disk. In addition, the former BPix and FPix were redesigned to reduce significatively the amount of non active material used. At the end, the thickness of the silicon sensors was 285 μm for the BPix and 300 μm for the FPix.

The outer part of the tracker used silicon strip sensors. starting from 20 to 116 cm of radial distance, and going up to 282 cm along the z axis after the interaction point. The motivation of this sensor technology was due to the lower probability to have particles in its geometrical region compared to the pixel detector's one. As visible in Figure 2.11, the micro strip sensors are separated in three categories and for each of them the sensor design is a bit different.

The part surrounded directly the pixel detector is organized in four barrel layers (TIB) and three endcap disks (TID) measuring up to 55 cm of outer radius. The assembly of the two subsystems can provide a precise radial and angular measurement of tracks, thus four measures of the radius r and the angle ϕ are obtained from these. The strip size varies from 80 to 120 μm and with a thickness of 320 μm. Each strip has a spatial resolution comprised between 23 and 25 μm.

The next part is the tracker outer barrel (TOB) which encloses the TIB and TID. In terms of dimension, it has an outer diameter of 232 cm and a length of 236 cm. The TOB is composed of sensors with a thickness of 500 μm and with a size varying from 122 up to 183 μm. Moreover, still in the case of these sensors, six radial and angular measurements can be provided with spatial resolution is ranging from 35 to 53 μm.

The last part is located in the forward region and corresponds to the tracker endcaps (TEC). The disks start from 22.5 cm far from the beam line to 113.5 cm. Their location along the z axis is equivalent to the range 124 cm $< |z| <$ 282 cm. In total, each TEC is formed by nine disks and the more they are far from the interaction point the more they are away from the beam line. Nevertheless, they are covered with radial micro-strip sensors which are 320 to 500 μm thick, with a size ranging from 97 to 184 μm. The TEC part adds up to nine radial measurements.

In order to improve the tracking capacities, the layers are doubled with additional strip sensors oriented with a 100 *mrad* angle. This configuration allow the barrel to make longitudinal measurement and radial ones for the endcaps. In total, the tracker represents a 198 m^2 surface of silicon strip sensors, making it the largest detector using only silicon sensors.

The operational temperature is one of the critical aspects of silicon-based detectors, as it is necessary to reduce the ionizing radiation damage on the sensors.

One of the important parameters which allows the CMS tracker to work perfectly, is its operating temperature. It was designed to be cooled at $-20°C$. However, this temperature has never been reach during the LHC runs. Indeed, during the run 1, the entire tracker worked at a $4°C$ temperature. Thanks to the upgrades made in the context of LS1, the working temperature of the run 2 was improved: going to $-10°C$ for the pixel detector to $-15°C$ for the rest of the tracker.

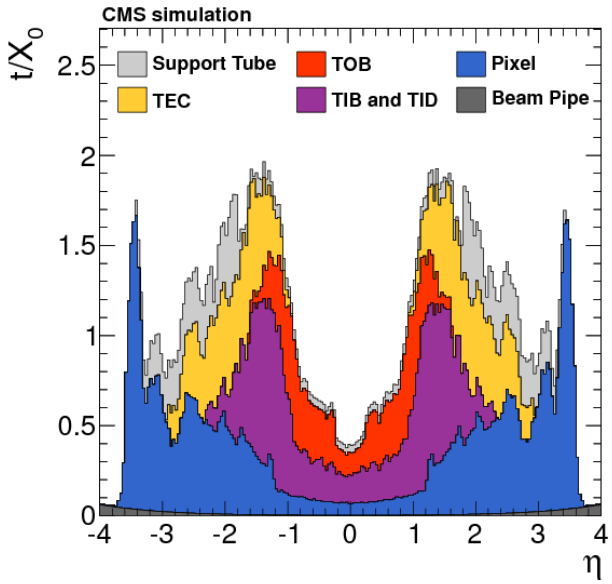

Figure 2.13: Simulated material budget expressed as the tracker thickness t over the radiation length X_0, and described as a function of the pseudorapidity. The contribution of each sub-system of the tracker, the beam pipe, and the support tube are described η [17].

The purpose of the inner tracker of CMS is only to detect tracks of the particle trajectories to reconstruct the vertices and to measure particle momentum. The energy measurement is performed right after by the calorimeters. Thus, the design of the tracker was made in a such way to reduce at the maximum the amount of particle energy loss in its material. Moreover, to have a good trajectory reconstruction, it is required to reduce the parasitic phenomenons coming from the primary vertices. Most of them are interaction with the material used for the detector, like multiple scattering, bremsstrahlung, matter and anti-matter annihilation, or photon conversion. These two arguments lead to search the best compromise, allowing to have the best detector performance and a dead material budget as low as possible.

A simulation of material budget of the tracker, shown in Figure 2.13, was made to understand which part of the tracker is absorbing the most particle energy. Thanks to this, energy corrections can be done at a given pseudorapidity. Besides, the pixel upgrade mentioned before allowed a reduction of 10% of the material

budget in the barrel and 40% in the endcaps.

In definitive, the tracker is the subdetector dealing with the most constraining requirements in terms of design, detection efficiency, and radiation hardness.

Electromagnetic calorimeter

The Electromagnetic Calorimeter of CMS (ECAL) [93] is the next subdetector surrounding the inner tracker. It aims at providing a precise measurement of the energy of electrons and photons. It is composed of approximatively 70 000 crystal blocks of lead tungstate $PbWO_4$. The choice of the material was motivated to have a dense calorimeter with an excellent energy resolution and radiation hard. Moreover, this ensures the detection of all the particle energy and to have a fast response. The electrons and photons are responsible for electromagnetic showers happening in the crystals, and they must be fully contained in the calorimeter. A detailed explanation of this phenomenon will be presented in Chapter 3. The lead tungstate crystal was chosen because of three of its properties: a high density $\rho = 8.29$ g/cm^3, a small radiation length $X_0 = 0.89$ cm, and a short Molière radius $R_M = 2.2$ cm for the transverse containment of the showers. These parameters are detailed in Section 3.2.4. Moreover, with $PbWO_4$ crystals, the collection of more than 80% of the scintillating light during 25 ns is possible.

The structure of ECAL is described in Figure 2.14, and it is divided in two parts: the ECAL Barrel (EB) and the two ECAL Endcaps (EE). The EB is made of two half cylinders, each consisting of 18 super-modules. A single super-module gathers 1 700 crystal bars, forming a rectangle of 20 bars in ϕ and 85 in η. Each weights around 1.5 ton and covers 20° in ϕ and $|\eta| < 1.479$. The EB groups 62 000 crystals, each with a front face measuring 22×22 mm^2, corresponding to a coverage of 0.0174×0.0174 in $\phi \times \eta$. The crystal groups composing the EE disks are called the super-crystals, which are squares of 25 crystals, and the EE coverage is $1.479 < |\eta| < 3.0$. However, some gaps between the different modules exist, especially in the transition region between EB and EE. In order to improve the coverage, the $PbWO_4$ crystals are oriented with a 3° tilt.

An electromagnetic preshower (ES) is placed just in front of the EE. The purpose of the ES is to make the discrimination between $\gamma\gamma$ pairs coming from the decay of a neutral pion π^0 and single photons with high forward energies. It is used to increase the spatial resolution in the endcap region with a pseudorapidity $1.65 < |\eta| < 2.6$. It is a sampling calorimeter made of two lead absorbers, each followed by a silicon sensor plate. Each silicon sensor has an active area of 61×61 mm^2, and it is divided into 32 strips. The silicon plate is 320 μm thick and lead absorbers have a radiation length of 2 X_0 and 1 X_0 respectively [94]. The small depth ensures to have single photons starting an electromagnetic shower in the sensor. The motivation to choose silicon sensors was due to its high radiation hardness. Like most of the detectors using a silicon sensor technology, the optimal performance is reached when the material is cold enough. The ES working temperature is comprised between $-15°C$ and $-10°C$. The ES can be beneficial for the reconstruction, but it collects only 8% of the particle energy. Indeed, the material budget is important in the endcaps, so the showers start to occur in the tracker and eventually the preshower does not help a lot.

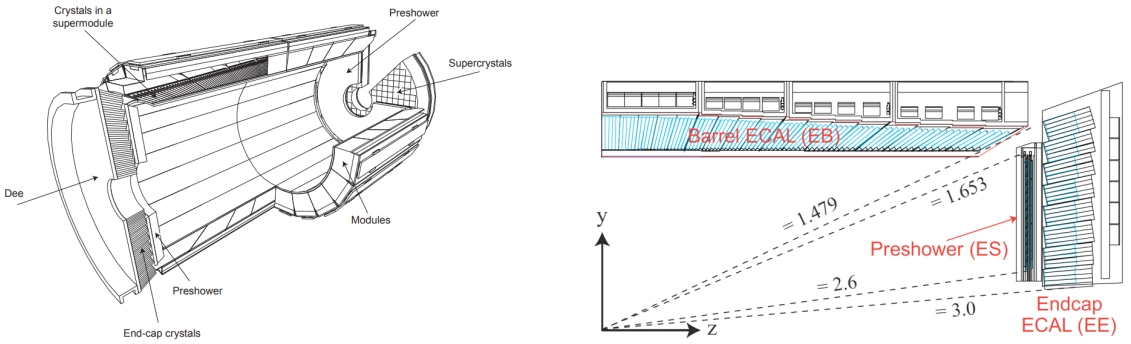

Figure 2.14: Schematic views of the Electromagnetic Calorimeter of CMS [19]. On the left, an illustration in perspective, and on the right, a representation of a longitudinal slice of a quarter of ECAL. In the barrel, the $PbWO_4$ crystal bars organized in modules and super-modules. And on each side of the endcaps, there is a preshower inside and a dee outside.

The energy resolution of ECAL was measured with a 3×3 crystals square [19] and it is parametrized with the following formula:

$$\left(\frac{\sigma_E}{E}\right)^2 = \left(\frac{f_s}{\sqrt{E}}\right)^2 + \left(\frac{f_n}{E}\right)^2 + f_c^2 \tag{2.15}$$

Where the first term corresponds to the statistical fluctuations coming from the physical development of an electromagnetic shower, it is designated as the stochastic term with $f_s = 2.8\%$ for ECAL. The second term represents all the noise induced by the electronic chain and the pileup, its factor is $f_n = 12\%$. At low energy, it may be the dominant term because it is inversely proportional to the energy, and it only depends on the data acquisition system. The third and last one, is the constant term with $f_c = 0.3\%$. It does not depend on the shower energy and refers to the intrinsic calorimeter properties, such as energy leakage of the crystals, non-uniformity of the light collection, and a non-perfect calibration. All these values were calculated using test beam data.

The CMS ECAL is a homogeneous calorimeter. On one hand, it has the benefit to provide a higher measurement precision and better shower energy reconstruction than using a sampling detector. On the other hand, it does not provide precise spatial measurements of the showers. Indeed, only the transverse profile of the showers is well defined due to the small Molière radius, but there is no information about their longitudinal profile. In the same way, it cannot provide additional tracking points in order to enhance the trajectory reconstruction made by the inner tracker at lower radial distance.

Furthermore, it was expected that the crystal response decreases with time, as shown in Figure 2.15. Because of that, a laser monitoring was put in place and shows that from April 2011 until May 2017, the ECAL response decreased of 10% in the region where $|\eta| < 1.4$ and more than 80% where $|\eta| > 2.7$. This phenomenon is explained by the fact that ECAL was conceived to sustain such luminosities, and the crystals are losing their transparency. Since the CMS detector is expected to collect about 350 fb^{-1} by the end of the Run-3, the radiation damages

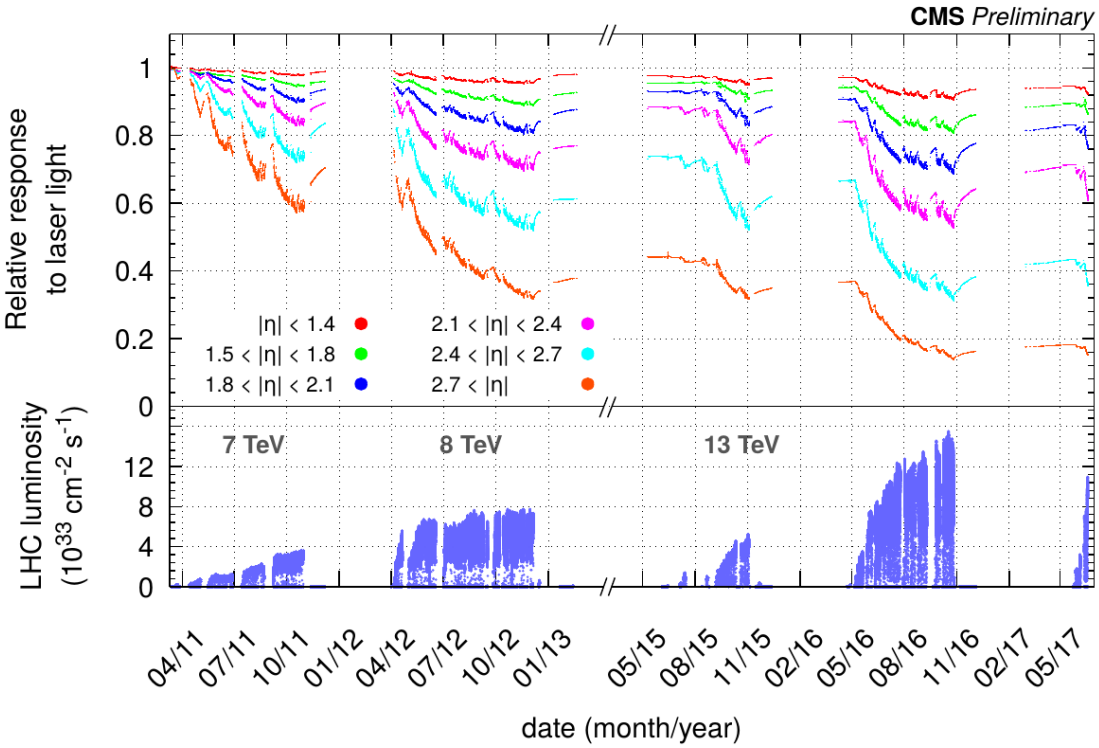

Figure 2.15: Relative response to laser light injected in the ECAL $PbWO_4$ crystals depending on the pseudorapidity η and averaged over all the crystals. Data taking periods corresponding to the years 2011, 2012, 2015, 2016 and 2017 are represented, with the corresponding LHC luminosity on the bottom part [20].

will be too important to continue to use the current crystals. That is why, ECAL will be upgraded during the LS3, in view of the HL-LHC. Especially the endcaps, where the loss of transparency is the most important, will be replaced by the High Granularity Calorimeter (HGCAL), described in Chapter 3.

Hadronic calorimeter

The Hadronic Calorimeter of CMS (HCAL) [95] aims at collecting the energy of the hadrons passing through the detector. Actually, hadrons may start interacting in the ECAL crystals, where they deposit approximatively 30% of their energy. But ECAL is not designed to contain entirely the hadronic showers, which require a more important amount of dense material to be fully absorbed. The HCAL is able to measure energy from neutral hadrons, which interact mostly via the strong interaction, and also to determine the energy of particles which are not interacting directly with matter, such as the neutrinos. Moreover, compared to electromagnetic showers, the hadronic ones are more complex. Indeed, they are characterized by large fluctuations of spatial shape development and also of missing energy. At the end, HCAL must be larger than ECAL to achieve its goal.

The HCAL is a sampling calorimeter composed of an alternance of brass layers acting as an absorber, and layers of scintillating plastic tiles. It is placed between the ECAL and the superconducting magnet, its design was highly constrained by

the magnet geometry which was decided earlier by the collaboration. As shown in Figure 2.16, the HCAL is the assembly of four distinct subdetectors: the HCAL Barrel (HB) and the HCAL Endcaps (HE), are the hadronic extension of the EB and the EE respectively. To ensure the containment of the entire hadronic showers, an additional outer hadronic calorimeter (HO) is placed outside the magnet. Thanks to that, the average depth correspond to a hadronic interaction length of 11 λ_i. The last one is the Forward Calorimeters (HF), placed at 11.2 m from the interaction point, meaning outside the main CMS cylinder. They are located at this distance to ensure the coverage of the high η regions.

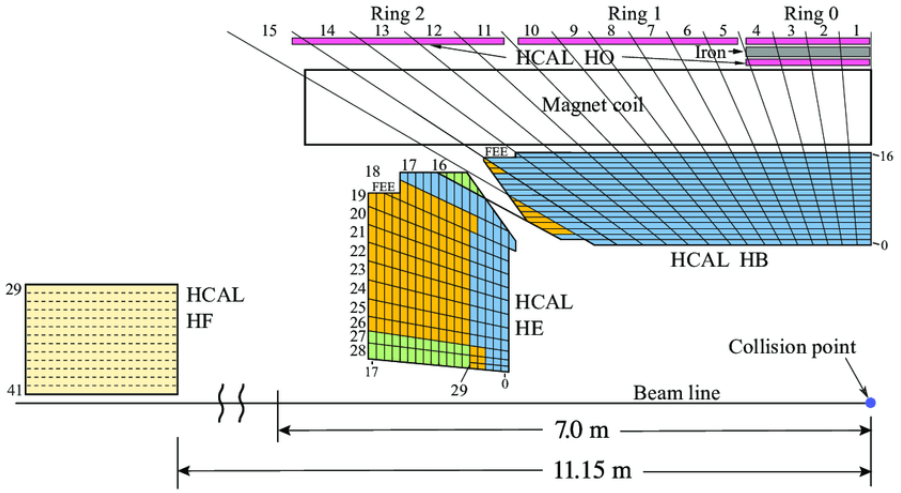

Figure 2.16: Schematic representation of a longitudinal slice of a quarter of the Hadronic Calorimeter of CMS [21].

The HB is a sampling calorimeter made of layers of brass absorbers and layers of scintillating plastic tiles. Like EB, it is divided into two half cylinders, each composed of 18 layers made of absorbers and scintillator tiles. It is divided into 16 sectors depending on η, and 72 sectors in function of ϕ. This sampling calorimeter has a spatial resolution of 0.087×0.087 mm^2 in $\phi \times \eta$. Its depth is equivalent to 7 λ_i, and it covers the $|\eta| < 1.3$ region. The scintillator tiles are grouped with those having the same η and ϕ coordinates, and these tile stacks are called projective towers of HCAL. The light from the scintillator is extracted with thin optical fibres having a 1 mm diameter, and doing a wavelength shifting. The fibres transport the light until the readout electronics containing hybrid photodiodes to read and digitized the signal.

The HE have most of their design in common with the HB. However, they cover the region where $1.3 < |\eta| < 3$ and their depths correspond to a hadronic interaction length of 10 λ_i. Besides, they slightly overlap with the HB to avoid any η gap, and the spatial resolution of each projective tower is equal to 0.17×0.17 mm^2 in $\phi \times \eta$.

The HO is made of plastic scintillators located after the solenoid, and it covers the region where $|\eta| < 1.26$. Two scintillators, spaced with a layer of iron, are used in the $|\eta| < 0.4$ region and only one to cover the $0.4 < |\eta| < 1.26$ region. This additional calorimeter was used to extend the depth to 11 λ_i, thus to fully absorbed

the hadronic showers. Moreover, this depth is reached when considering the magnet coil as a dead material, ensuring the shower containment. The scintillating light was collected with the same readout electronics as the one used for the HB and HE. During LS1 it was decided to replaced them with silicon multipliers (SiPM) [96], in order to get a faster response, and as a result to improve the physics performance.

The HF allow a coverage of the $2.9 < |\eta| < 5.2$ region. Its design is different of the other subdetectors, it is made of an alternance of steel absorber and quartz fibres. The choice of quartz as active material was motivated by its important radiation hardness. In the high η region, along the beam line, the radiation doses are high due to an important flux of neutrons. In the quartz fibres, the scintillating light comes from the Cherenkov effect, and it is collected thanks to photomultiplier tubes (PMT) located just after the absorber.

The imperfect containment of hadronic showers in HCAL lead to a high stochastic factor $f_s = 110\%$, and the constant term factor is equal to $f_c = 9\%$. This resolution was calculated thanks to measurements performed during a test using pion beams [97]. Moreover, the presence of unpredictable events happening during the development of hadronic showers, the production of undetectable particles, and electromagnetic events contained in the shower are limiting the HCAL performance. To improve this energy resolution, it is possible to combine it with the one found for ECAL. The combined resolution for calorimeters has a stochastic term with $f_s = 84.7\%$ and a constant term with $f_c = 7.4\%$.

Finally, to maintain the HCAL performance, certain components were changed at the end of 2017 [98]. The photodetectors used in the HB, HE and HF were replaced, as well as the readout electronics to expand their functionalities. For instance, they are now capable to perform precision timing measurements and longitudinal depth segmentation. The particle recognition is improved, and the background rejection is made easier.

Superconductive magnet

All the CMS subdetectors were designed and built around the superconducting magnet. It is a huge solenoid initially designed to generate a 4 T magnetic field. A such field is used to bend the trajectories of particles passing through the detectors and as it was already discussed before, it is very useful to improve the particle identification and reconstruction performance of the overall CMS detector. If considering a magnetic field $\vec{B}$ and a particle with a charge q and a speed $\vec{v}$, the resulting Lorentz force is $\vec{F_L} = q(\vec{v} \times \vec{B})$. To have an accurate estimation of the charge and momentum of a particle, the magnetic field must be perfectly known inside the detector and especially in the inner tracker, where trajectories are essentially recorded. It is the reason Monte Carlo simulation and precise measurement were done as shown in Figure 2.17.

In definitive, the solenoid is 12.5 m long and with a 6 m diameter. It is the largest magnet of this kind and its 220 tons weight is due to the alloy of niobium-titanium ($NbTi$) which constitutes it. This material is specifically used for its superconducting properties when cooled to a very low temperature. That is why a

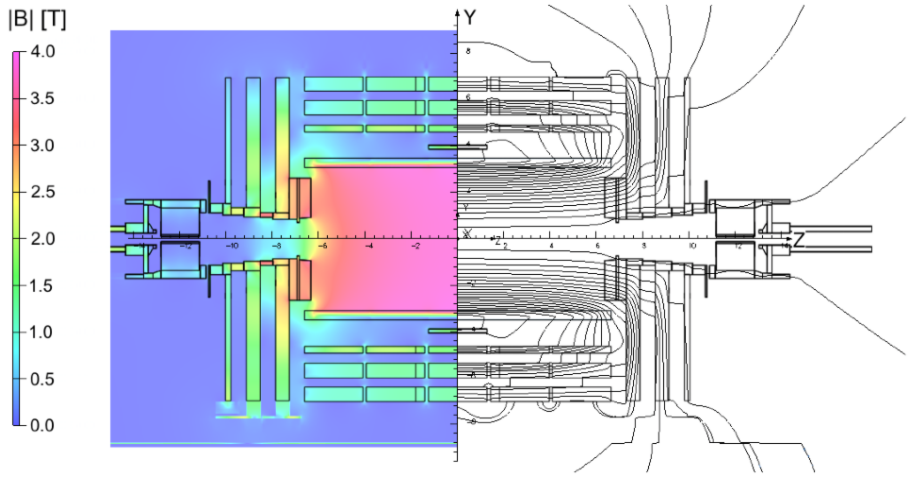

Figure 2.17: Schematic view of the CMS magnet field [22]. Spatial representation of the magnetic field is obtained from a simulation.

cryostat system working with liquid helium is used to lower down the temperature to 4.7 K.

Finally, even if it was designed to reach 4 T, the magnetic field inside the CMS' solenoid goes up to 3.8 T, and it is mostly uniform is this region. The steel return yoke of the muon system surrounding the magnet serves to return the flux of the magnetic field and to reduce it to 2 T inside the muon system [99].

Muon detectors

The muon detection system [100] is a key element of the CMS detector. It is the last subdetector placed in the outermost region of the detector and surrounding the superconducting magnet. It is designed to precisely detect muons which are weakly interacting with the tracker and the ECAL. The identification and the precise measurement of muon momentum are crucial to reconstruct events where Higgs and vector bosons are involved. In the barrel as well as in the endcaps, the muon detection system is divided into four stations separated with iron yokes, also called wheels, which are immersed in a 2 T magnetic field inferring muon momenta from their curvature. As represented in Figure 2.18, this subdetector is composed of more than 1 400 muon chambers separated in four groups corresponding to a different detector technology. The choice of different technologies was motivated by the non-uniformity of the magnetic field and the difference of background event density depending on η. Each of them has advantages to operate in a specific situation. In the barrel part defined by $|\eta| < 1.2$, Drift Tubes (DT) are used, while in the endcaps, Cathode Strip Chambers (CSC) operate in $0.9 < |\eta| < 2.4$ and Gas Electron Multipliers are used only close to the beam line where $1.6 < |\eta| < 2.4$. DT and CSC are supported by Resistive Plate Chambers (RPC).

The Drift Tubes [101] are 2.4 m long rectangular cells with a section surface varying from 1.3 to 4.2 cm^2. The cells are filled with a gas composed of 85% of Ar and 15% of CO_2, in which there are two cathode strips and one anode wire. The tube are arranged in rectangular plate detectors, each having a surface comprised

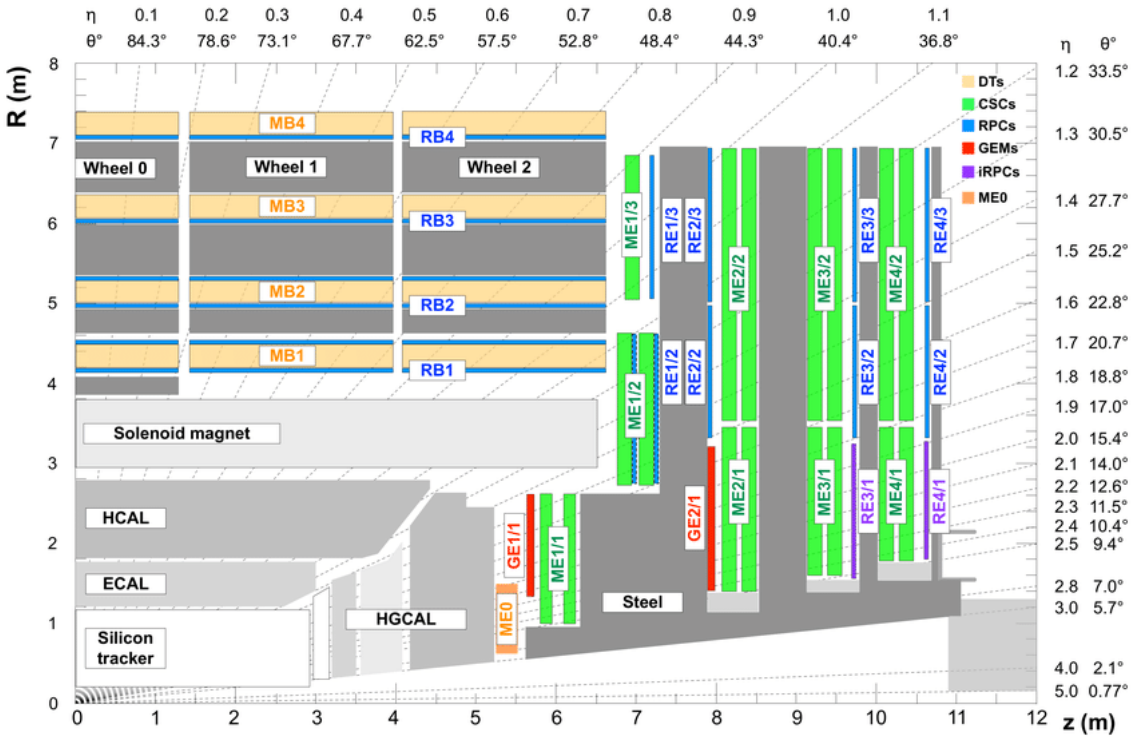

Figure 2.18: Schematic view of a longitudinal slice of a quarter of the CMS detector [23]

between 2 and 2.5 m. In total, there are 250 DT grouped by four and distributed into the five wheels forming the barrel. Besides, the measurement of the position of incoming muons is derived from the drift time of electrons to the anode wire. Each DT has an efficiency of 99.8% and a spatial resolution close to 180 μm. Moreover, the superposition of DT layers allows improving the spatial resolution, and for the overall it is comprised between 80 and 120 μm. The DT layout results in a timing resolution lower than 3 ns. DT technology was chosen for this region due to the low muon rate and good uniformity of the magnetic field, as represented in Figure 2.17, allowing the DT to have good detection performance.

The Cathode Strip Chambers [102] are placed in the endcaps and have a trapezoid shape. They cover an angle of 10° or 20° and, like for the DT, they are arranged into the four stations which are between the steel yoke. Each chamber is filled with a gas mixture composed of 50% of CO_2, 40% of Ar, and 10% of CF_4. Inside the gas there are six alternances of anode wires enclosed between a continuous copper cathode providing η measurements, and cathode stripes providing radial and ϕ measurements. In total, the CSC represent a surface of 5 000 m^2 approximatively, and a volume of 50 m^3. The distance between two layers is of the order of 2 cm. Furthermore, the efficiency of the CSC is above 99%, with a spatial resolution comprised in the range of 47 to 243 μm, and a timing resolution per layer lower than 5 ns. In the endcaps, where the parasitic event rate is higher and the magnetic field is non-uniform. The motivation to use such technology was mainly driven by its radiation hardness and its fast timing capabilities.

The Resistive Plate Chambers [103] are coupled with the DT as well as with

the CSC. Hence, they are placed both in the barrel and in the endcaps. Each RPC provides an additional measurement similar to those done by the other subdetectors. This redundancy allows the optimization of the muon tracking by removing the ambiguities caused by multiple hits in a single cell. In the first two barrel layers, the RPC are mounted on both sides of the DT, and only on the inner side for the two other layers. In the endcaps, the RPC are placed on each of the four stations. Precisely, RPC are double-gap resistive plate chambers filled with a gas mixture composed of 95.2% of $C_2H_2F_4$, 4.5% of iC_4H_{10} (isobutane), and 0.3% of SF_6. Each chamber correspond to a 2 mm gas gap formed between two parallel electrodes. When a muon pass through the detector, part of its energy is converted by ionization of the gas and an electron avalanche occurs. In terms of performance, the RPC have in average 94% of efficiency, a spatial resolution of the order of 1 cm, and a timing resolution lower than 3 ns [104]. Even if the spatial resolution worse, the RPC timing resolution is better than the other subdetectors, and it is very benefic for triggering muons in case of high pileup rate. Nevertheless, two layers of new RPC, called improved Resistive Plate Chambers (iRPC), will be added during the shutdown happening at the end of 2022. This project aims to add 18 new chambers per endcap stations, or 144 chambers in total. The principal improvement lies on a better timing resolution of about 2 ns, and a spatial resolution of about 0.3 cm in the transversal direction.

The Gas Electron Multiplier (GEM) [92] are placed in the endcaps, and operating in a region with high radiation rate. Their goal is to provide redundant measurements to enhance the trigger and muon reconstruction capabilities. A chamber consists of three layers of micro holed copper foils enclosed by a drift plane and readout strips. The chamber is filled with a mixture of 70% of Ar and 30% of CO_2, which is ionized by incoming muons. The generated electrons are accelerated through the GEM foil holes, and they produce avalanches which are collected on the readout strips. In 2021, the 72 first GEM super-chambers were installed, each containing two GEM detectors. Finally, other GEM super-chambers are planned to be installed during the LS3.

Trigger and data acquisition systems

The core of the CMS experiment is the set of subdetectors, but what would they be if the information they collect could not be recorded? Indeed, one should not neglect the various electronic systems that are behind them, but taking care of a vital part of the experiment.

During the LHC runs, there is a bunch crossing every 50 ns during the Run-1 or every 25 ns during the Run-2, meaning that 40 million events are produced each seconds. The first challenge with this amount of data is that the acquisition system must be fast enough to save all the interesting information. Moreover, all the information collected from a single event represent in average 1 Mb of disk space. If all the events are saved, the CMS collaboration should fill 40 Tb of permanent storage per second, which is obviously not feasible. Thus, the second challenge of the CMS collaboration, as well as all the other LHC experiments, is the storage capacity and coupled with a strong optimization of the amount of saved information. To answer this problem, a trigger and data acquisition

system (TriDAS) was put in place [105, 106]. Its purpose is to take the decision if an event is interesting or not in a fraction of a second, and in this way a lot of events will be discarded. Indeed, the cross-section of processes interesting for the physics purpose of CMS reach at the maximum for the W production of 10^5 pb for collisions with a 13 TeV energy in the centre of mass, as shown in Figure 2.19. But high centre of mass energy is mainly interesting to study rare processes with a low cross-section. For instance, ZZ events represent have a cross-section around 10 pb, meaning that such events correspond to less than 1% of the total cross-section.

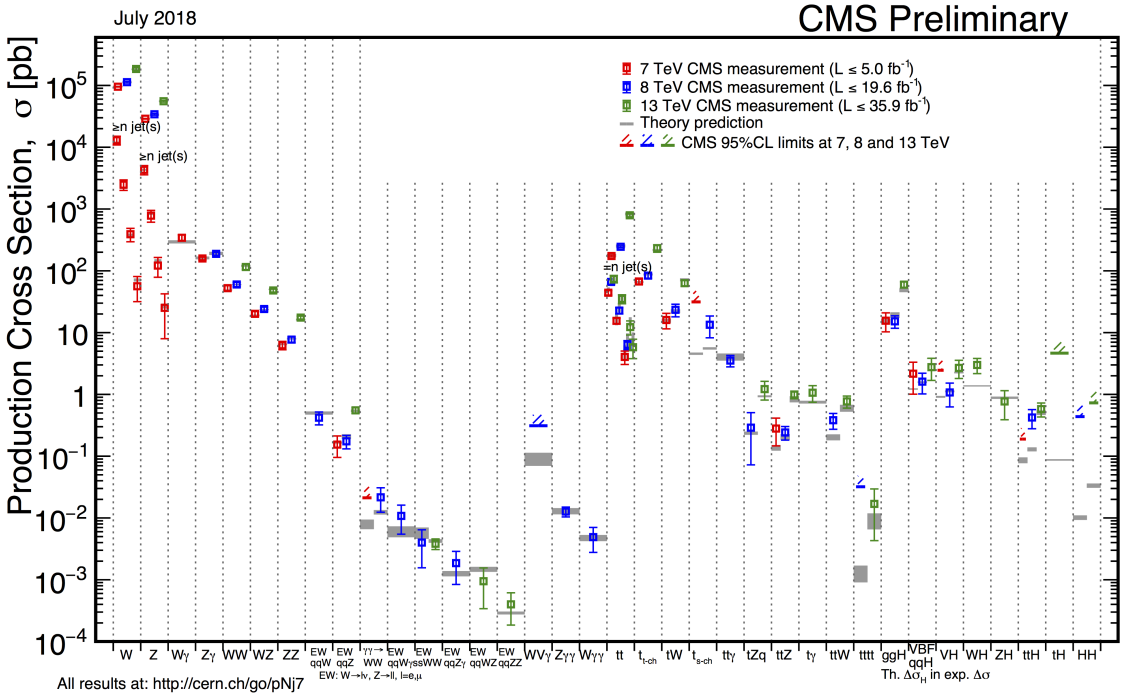

Figure 2.19: Summary of the cross-section measurements of Standard Model processes produced by the CMS experiment. Measurements are done for $\sqrt{s} = 7$ TeV in red, 8 TeV in blue, and 13 TeV in green.

In the same configuration, the proton-proton collisions happening at the LHC have an overall cross-section of the order of 10^{11} fb. At the end, the TriDAS lower by a factor 10^6 the total amount of information. This significative reduction of information is done directly by the trigger systems, it happens before any writing of event information, and it makes possible to save them on hard disk space.

The TriDAS is composed of data acquisition systems (DAQ) and of two level of triggers: the Level 1 Trigger (L1 trigger) and the High Level Trigger (HLT).

The Level 1 trigger is the first to reduce the amount of information. It is a hardware based trigger, allowing to skim the event rate from 40 MHz to 100 kHz. All the subdetectors are not used to trigger an event, since a fast decision is needed. In those which are taken into account, only a part of the available information is used and this come from specific trigger clusters. Indeed, this is done in order to make a compromise between the amount of information used and the complexity of the algorithms on the one hand, and the performances on the other. The L1

trigger is implemented on an assembly of different kinds of electronic circuits, such as Field Programmable Gate Arrays (FPGA) and Application Specific Integrated Circuits (ASIC). They are used to access the information originated from the readout systems mounted on the different subdetectors. Moreover, Programmable Memory look up Tables (LUT) are used for more complex algorithms. The L1 trigger takes a decision within a latency time of 3.8 μs, which is based on the identification of electrons, photons, muons, jets, and missing transverse energy. These objects are determined thanks to information coming from the calorimeters and the muon system. If these objects fulfil some requirements, they can be considered as L1 trigger candidates. The overall L1 trigger is represented in Figure 2.20, where two paths are distinguished: the calorimeter trigger based on information coming from the ECAL and HCAL, and the muon trigger taking into account the outputs of the different muon chambers.

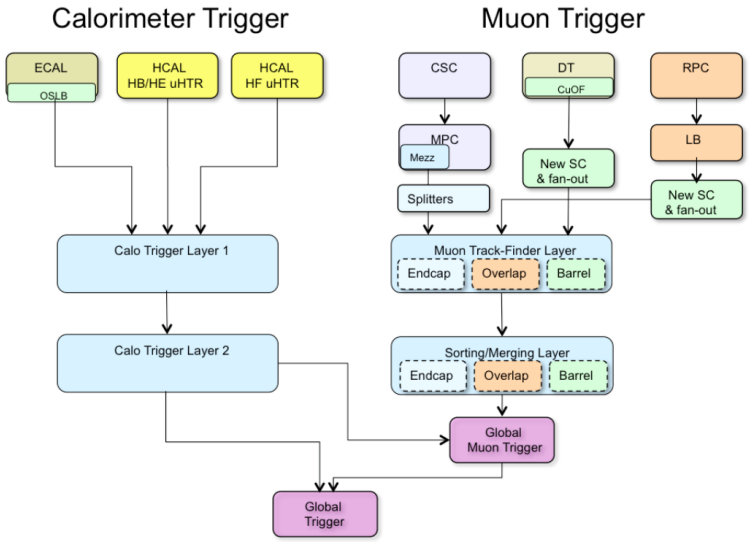

Figure 2.20: Dataflow for the Level 1 trigger [24]. Information are from the calorimeters and the muon system.

For each event, the information determined by the ECAL and HCAL are gathered into energy deposit clusters, also called trigger towers. These clusters represent electrons, photons, or jets. The calorimeter trigger is in charge of filtering the events where electrons, tauons, or photons are identified. The muon trigger is activated when a muon is identified in the DT, CSC, or RPC. Since the Run-3, GEM chambers are also integrated in the muon trigger, reinforcing the measurements done by the CSC. The global muon trigger is enhanced by the addition of information coming from the calorimeter trigger because muons can partially interact within the calorimeters before reaching the chambers. Finally, the overall L1 trigger combines both calorimeter and muon triggers, and its activation follows different scenarios.

The final L1 trigger decision, to accept or reject the event, is mainly determined by the results of the overall trigger. After that, the signal emitted by the L1 trigger is given to the HLT system.

All the events approved by the L1 trigger will then have to go through a second

trigger, called the High Level Trigger [106], performing a stricter selection and thus a higher skimming of the event rate. It consists of a software based trigger which aims at reducing the event rate from 100 kHz after the L1 trigger to only 1 kHz. It is implemented on computing devices having more than 32 000 Central Processing Units (CPU), and located on the surface facility on top of IP5. All the parameters about the detectors such as their spatial resolutions are exploited by the HLT to try to reconstruct the objects from the selected events. The HLT uses a collection of more than 600 algorithms representing combinations of selection criteria and reconstruction processes, called trigger paths. Each of them corresponds to a specific physics signature.

For example, *HLT_Ele17_Ele12_CaloIdL_TrackIdL_IsoVL_DZ_v* is a trigger path that will select a pair of electrons with thresholds of 17 and 12 GeV, calorimetric and tracker isolation requirements.

Many HLT paths are used and some of them change with the increase in luminosity. For this reason, energy thresholds are set at a higher value, as well as more restrictive criteria on identification and isolation.

Furthermore, during the LHC runs, many versions of the HLT trigger algorithms were used. As a key element of the experiment and on the physics analysis, the HLT has to be updated each time that a subdetector undergoes a modification to keep it in agreement with the embedded material. Besides, new reconstruction strategies were developed to match analysis requirements and then integrated in the HLT. Finally, the main constraint on the HLT is the latency due to the limited number of CPU at disposition, inducing a maximum of event processing time of 320 ms.

The measurement of instantaneous and integrated luminosity carried out by the CMS detector is an important tuning factor of the LHC beam parameters, but also a key point for the trigger and DAQ systems. Indeed, a precise measurement can provide useful information to both systems in order to adapt their rates to the beam intensity. This measurement was made with silicon detector modules placed the closest possible to the beam line and situated at 1.8 m from the interaction point. During the LS1 and continuing with the LS2, the BRIL detector [107] was installed, and it aims at providing a fine measure of the luminosity. It consists of three different types of sensors arranged in four modules along the beam axis. The first sensors are the Beam Condition Monitor Fast (BCM1F) [108] which is a monitoring system used to have fast measurements of the beam properties, and it is placed in the HF. The second ones are the Beam Condition for Losses (BCM1L) [109] used for the measurements of the lost beam fragments. And the third ones are Pixel Luminosity Telescopes (PLT) [110] which is the central part of the BRIL subdetector, providing precise measurements of the LHC luminosity at IP5. Even if the pixel sensors are more accurate, their information cannot be used directly due to their latency, and the two other subsystems are used to give information to the trigger. In definitive, the luminosity observables are studied each year to provide a systematic uncertainty comprised between 2.3 and 2.5%, which is used for the different physics analysis. In the work presented in this thesis, the luminosity measurements considered are those corresponding to the data taking period of 2016 [111], 2017 [112], and 2018 [113].

2.3 Reconstruction of particles

The physics analysis described later in this thesis aims to study a final state constituted of four leptons. However, the different subdetectors do not give directly the nature and the characteristics of the recorded particles. Indeed, when a particle goes through the layers it can activate silicon sensors of the tracker resulting in a signal giving a spatial and temporal information, also called a track. The calorimeters can provide also such information, but with a lower resolution. Electrons and photons, will continue their path into the ECAL and initiate electromagnetic showers. All the resulting particles will deposit their energy in a close group of ECAL cells, also called a cluster. In the case of hadrons, the shower can start in ECAL or in HCAL. Similarly, the hadronic showers will be contained in a cluster of HCAL cells, or even cells coming from both calorimeters. Muons which are weakly interacting with the innermost part of the CMS detector are principally let tracks in the different muon chambers, but also in the tracker layers, and sometimes they can deposit part of their energies in the calorimeters. Finally, emitted neutrinos are most likely to escape the CMS enclosure without interaction within the different subdetectors, leaving no direct clue of their passage. Hence, neutrinos are at the root of a missing part of the transverse energy of the overall event energy. All the particle paths presented in this paragraph are represented in Figure 2.21.

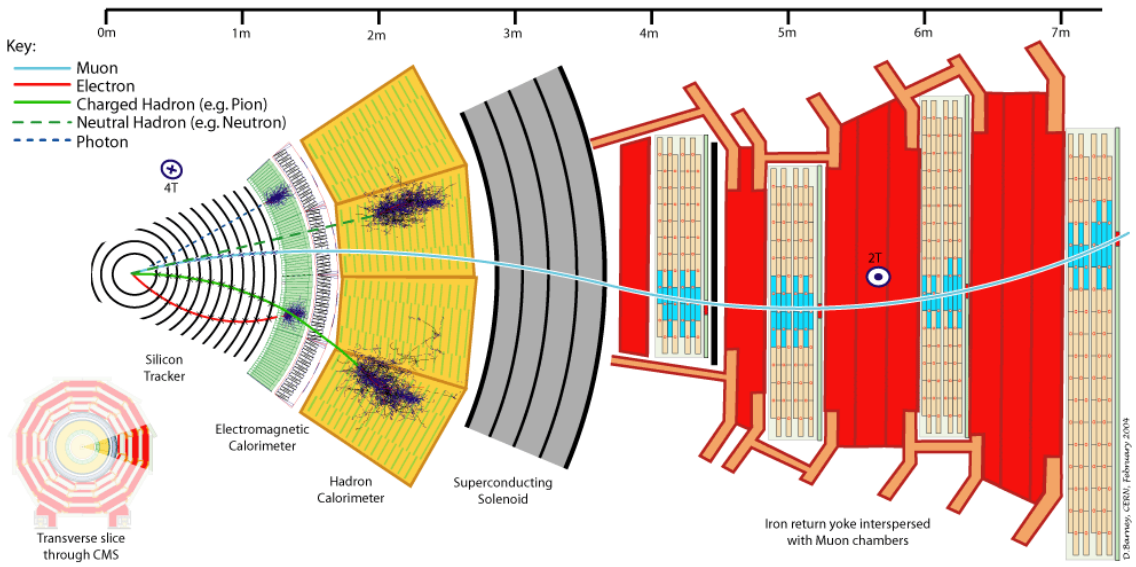

Figure 2.21: View of a transverse slice of the CMS detector with detected particles [25].

All these subdetector information allow reconstructing and identifying the required particles for physics analysis. These operations are performed with a set of algorithms, and the main one is called the Particle Flow (PF) [26]. This algorithm uses the most basic subdetector signals to construct the elementary objects for the reconstruction. They correspond to particle hits in the tracker layers to build the tracks, and energy deposits in the calorimeters to build the clusters. Concerning

the particle reconstruction, the PF starts with the muons, which are determined by matching the tracks from the inner tracker and those of the muon chambers. Next, the electrons are reconstructed by using tracks leading to an ECAL cluster, the correspondence between both takes into account the bremsstrahlung radiation. Then, the photons are built with the remaining electromagnetic clusters, which are not associated to tracks. The hadrons' reconstruction comes after, starting with the neutral hadrons which are characterized only by a HCAL cluster and then the charged hadrons with the remaining HCAL clusters matching tracks. Finally, some reconstructed particles are gathered in more complex structures, such as jets, and are used to estimate the amount of missing transverse energy resulting from the emission of neutrinos during an event.

2.3.1 The particle flow algorithm

The PF algorithm [114] is based on the creation of elementary building blocks for the particle reconstruction, which are the tracks and clusters. They are the key elements of the identification and reconstruction of all the objects observed in all event final states.

The tracks are reconstructed from the hits made by charged particles in the silicon tracker layers. Their reconstruction is operated with the Combinatorial Track Finder (CTF) algorithm, which is based on the Kalman filtering method [115, 116, 117], also known as linear quadratic estimation. In order to assess a high reconstruction efficiency and to minimize the fake rate, an iterative approach is adopted. The first iteration consists of reconstructing only the isolated tracks coming from the primary vertex, and at the end of this step, the selected hits are no longer considered for the next stages. The complexity will be reduced step after step due to the decrease of hits and thus of combination possibilities. This allows the quality criteria applied in successive iterations to be gradually more relaxed. This is very beneficial for not obvious tracks, such as hadrons made of heavy quarks or radiating electrons [118]. In general, a track reconstruction requires a dozen iterations, allowing the algorithm to reconstruct tracks with p_T of at least 0.1 GeV and produced up to 60 cm from the primary vertex [119].

The clusters are formed from the energy deposits in the different calorimeters and the algorithm used runs separately in the preshower, ECAL and HCAL subdetectors. This is to maximize efficiency even at low p_T and to be able to distinguish overlapping showers. It is based on an iterative clustering technique that follows the characteristic lateral profile of the showers. Specifically, the local maxima of energy deposits are identified, and the neighbouring deposited energy are grouped with the maxima. This step requires neighbouring energy deposits to have their signals are greater than twice the standard deviation of the electronic noise. It typically takes less than 5 iterations for the algorithm to converge.

At the end, PF blocks are build by linking tracks and clusters together. A good example of the reconstruction of particles with the PF algorithm is given with the Figure 2.22, representing the reconstruction of a jet with a 65 GeV transverse momentum and made of five particles: a K_L^0, a π^-, a π^+, and the two photons coming from the decay of a π^0. In the first representation, ECAL and HCAL

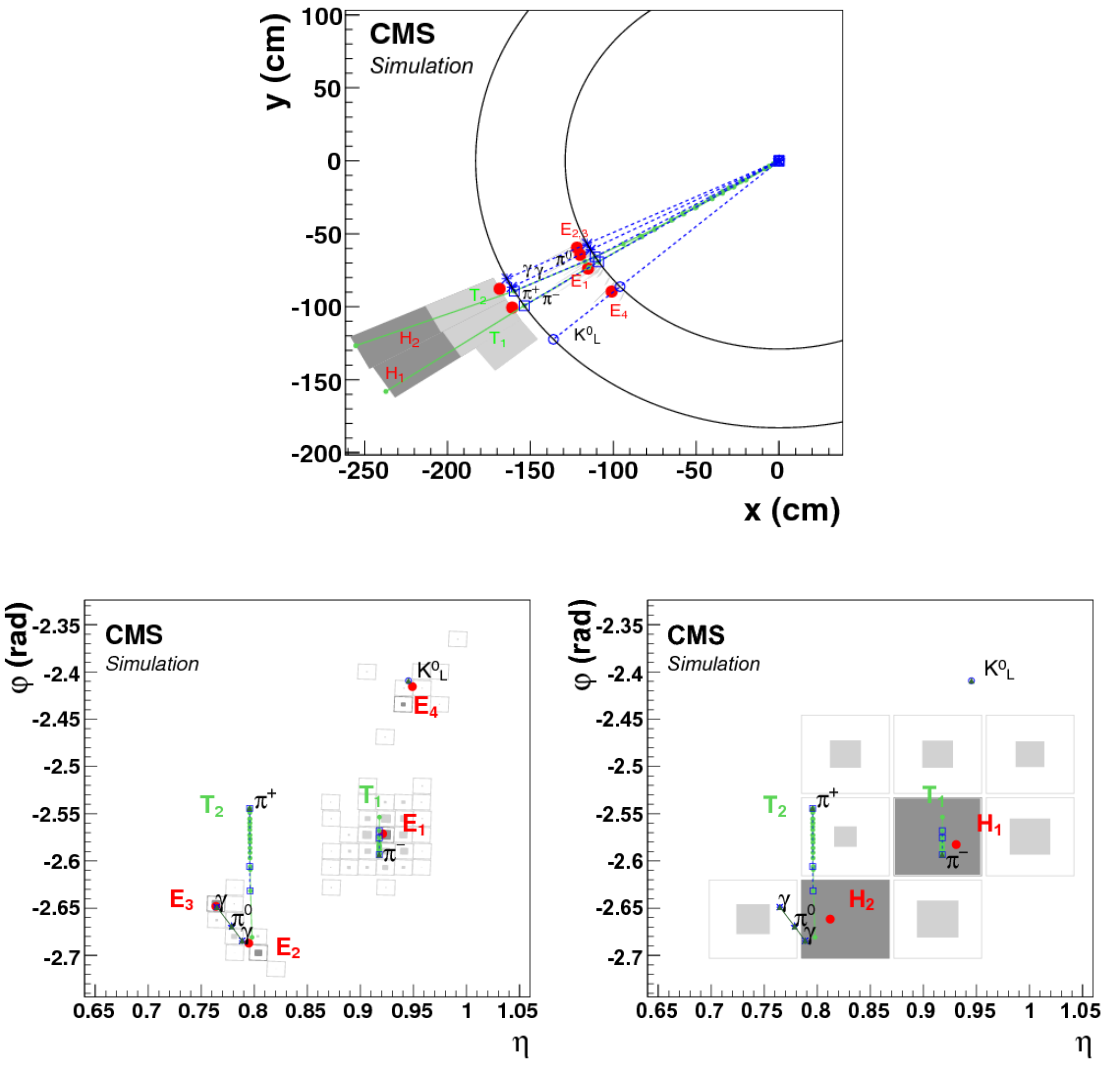

Figure 2.22: Event display of a jet made of five particles only in the (x, y) view in the upper plot, in the (η, ϕ) view of the ECAL surface in the lower left plot and the HCAL surface in the lower right [26].

surfaces are represented by circles centred around the interaction point. The K^0_L, the π^-, and the two photons are detected as four clusters noted $E_{1,2,3,4}$. The π^+ does not create a cluster in the ECAL. The two charged pions are reconstructed as charged-particle tracks $T_{1,2}$, appearing as vertical solid lines in the (η, ϕ) views and circular arcs in the (x, y) view. These tracks point towards two HCAL clusters $H_{1,2}$. In the lower views, the ECAL and HCAL cells are represented by squares, with an area proportional to the cell energy. The local maxima, corresponding to the centres of the clusters, are shown in dark grey. In all the three views, dots represent the cluster positions, dashed lines for the simulated particles, and open markers for the positions of their impacts on the calorimeter surface.

To summarize this example, in each step of the PF algorithm, the following procedure of particle identification and reconstruction is performed:

- Identification and reconstruction of muon candidates with tracks coming

from the muon chambers. Consecutively, these muon associated tracks are removed.

- Identification and reconstruction of electron candidates with information coming from ECAL clusters and tracks. The bremsstrahlung photons are recovered in order to estimate the electron energy.
- Identification and reconstruction of energetic photon candidates satisfying a good isolation.
- Among the tracks associated previously, those without a good χ^2 are removed in order to reduce the number of fake candidates.
- Identified muons are removed and if the track p_T is larger than the energy cluster energy sum, another fake removal is performed to separate the tracks with a $p_T > 1$ GeV. This operation is realized when components of a muon are gathered with fake tracks or jets, leading to PF track p_T is higher than the cluster energy sum.
- Identification and reconstruction of charged hadrons using the remaining tracks.
- Comparison of the cluster energy sum to the track p_T sum. If the difference is smaller than the ECAL energy, thus a photon is identified, and it is a neutral hadron in the other cases.
- Isolated clusters from ECAL which are not linked to any track are used to create photons.
- Isolated clusters from HCAL which are not linked to any track are used to create neutral hadrons.

The following subsections will detail the reconstruction of the main physics objects.

2.3.2 Identification and reconstruction of particles

Muons

Muons are the first particle to be identified in CMS, due to their distinctive signature recorded in the muon chambers and their high identification efficiency. Their tracks are reconstructed independently in the muon chambers [23] and in the silicon tracker [118]. The reconstruction of the former, the so-called standalone muon tracks, is independent of the PF and relies solely on information from the muon systems. In this case, the positions of the impacts in the DT, CSC and RPC sensors are combined and adjusted to form track segments, which give a first estimate of the muon direction and momentum. These are reconstructed following the PF procedure explained in the previous section 2.3.1 and are called tracker tracks. The tracker segments are then combined to reconstruct the muon track, using a Kalman filter technique [115].

The reconstruction of global muons in CMS is done by matching tracker muons to standalone muons or inversely. The tracker muon tracks are constructed from the centre outwards, the tracker tracks with $p_T > 0.5$ GeV and a total momentum $p_T > 2.5$ GeV are propagated to the muon system, and for this at least one muon segment at a compatible position is required. The global muons are reconstructed by matching a standalone muon track to the tracker tracks after checking the compatibility of their parameters. Then the global fit is performed on both tracks together. Due to the large size of the muon chambers, the combined fit improves the momentum resolution compared to the tracker fit alone for muons of $p_T > 200$ GeV. Finally, about 99% of the muons produced in the muon system acceptance are reconstructed with one of these two approaches. Most of the time with both, and in this case they are merged into a single candidate.

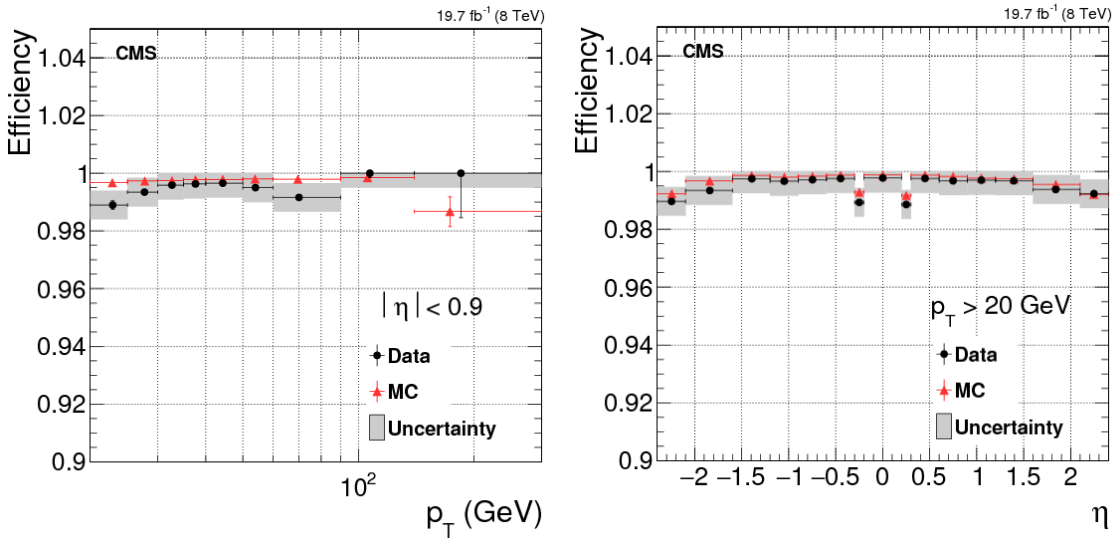

Figure 2.23: Efficiency of PF muon identification from a Z boson decay as a function of p_T on the left, and as a function of η on the right [26].

The reconstructed muons undergo a set of selection criteria based on the quality of the tracks. These observables such as the track fit χ^2, the number of hits per track or the degree of matching between tracker and standalone tracks. Different levels of requirements result in different muon identification working points, with increasing purity and decreasing efficiency, where the most common are defined as loose, medium, and tight. The information of the muon subdetectors is further analysed to compute the isolation of the muon candidate, which serves as a handle to distinguish between prompt muons and those arising from weak decays within jets. The PF relative isolation is defined as the ratio between the sum of p_T of all PF candidates within a cone size $\Delta R < 0.4$ around the muon and the p_T of the muon itself.

The reconstructed muons are subjected to a set of selection parameters, which are based on the quality of track observables. Among them, there is the χ^2 of the track fit, the number of hits per track or the degree of correspondence between the tracker and the standalone tracks. Different levels of selection requirements can be considered for muon identification and the most common being defined as loose,

medium, and tight. The selection difference comes from the increasing purity and decreasing efficiency requirements. The information provided by the muon subdetectors is then analysed to calculate the isolation of the candidate muon, which is used as a handle to distinguish prompt muons from those originating from weak decays within the jets. The relative isolation of the PF is defined as the ratio of the sum of the p_T of all PF candidates in a cone of size $\Delta R < 0.4$ around the muon and the p_T of the muon itself.

Thanks to the upgrade of the muon system and the improvement of the algorithms, the performance between the first two runs remains similar, even with increasing luminosity and pile up. The spatial resolution of the reconstructed hits is between 50 and 300 μm, which leads to a muon selection efficiency of more than 96% [120]. Figure 2.23 shows the efficiency as a function of p_T and η after applying the most restrictive criteria for PF identification and isolation to the reconstructed muons. The CMS magnetic field and the resolution of the muon system are ideal for reconstructing two muon candidates in the 150 GeV mass range. This was a great advantage for the discovery of the Higgs boson, and now also for the search for high-mass resonances.

Electrons

The second particle to be reconstructed at CMS is the electron [121]. In their paths to the ECAL crystals, electrons are losing a non-negligible fraction of their energy in the tracker layers. This loss is mainly due to the bremsstrahlung effect, which is a non-Gaussian phenomenon. At $\eta \simeq 0$, an electron loses an average of 33% of its own energy, and this energy amount can reach $\sim$ 86 % at $\eta \simeq 1.4$, where the tracker material budget is the most important as shown in Figure 2.13. This energy loss does not always happen, indeed the bremsstrahlung energy loss is a stochastic process. That is why some electrons are said to be golden due to their very low amount of radiated energy. This makes their reconstruction more complex and to overcome this, the tracking algorithm has to take into account the energy loss and the clustering algorithm has to collect the energy of bremsstrahlung photons, which may be located very far from the point of interaction of the electrons in the ECAL. The electron reconstruction addresses these challenges with a dedicated tracking algorithm and an advanced energy collection procedure. The full electron reconstruction workflow is illustrated with Figure 2.24.

The electron tracks are reconstructed with the Gaussian-Sum Filter (GSF) algorithm [122], which is independent of the PF iterative procedure. The algorithm modelizes the electron energy loss with a weighted sum of Gaussian PDF to better take into consideration the bremsstrahlung effects, instead of only relying on a Kalman filter procedure of the PF algorithm. The electron energy deposits in the calorimeters are built by regrouping ECAL clusters in the so-called superclusters. The procedure consists in identifying a seed cluster, to which the energy deposits associated to the bremsstrahlung photons are aggregated. These typically spread along the ϕ direction due to the magnetic field, tangent to the electron trajectory, as schematically shown in Figure 2.25.

The global electron is reconstructed by associating GSF tracks to superclusters

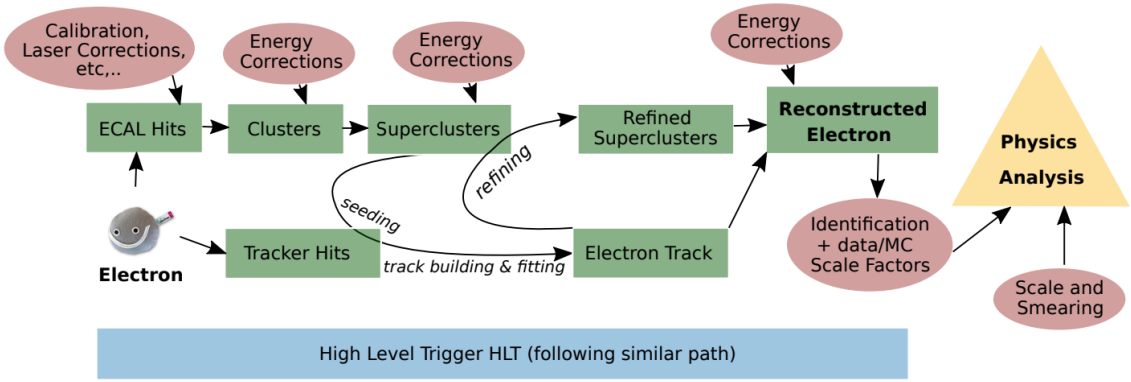

Figure 2.24: Schematic workflow of electron reconstruction [27].

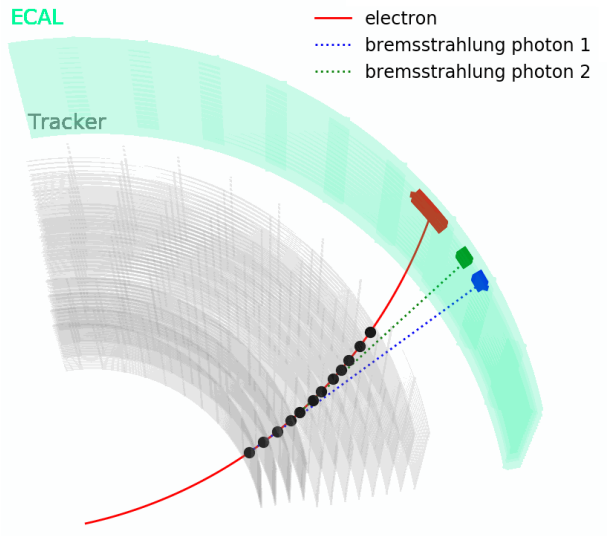

Figure 2.25: Reconstructed electron with photons coming from bremsstrahlung effect [26]. The recorded tracks are represented with the black points and the energy deposits are shown in the ECAL.

using two approaches. The ECAL approach uses superclusters with $p_T > 4$ GeV as seeds for the search of the electron GSF tracks. This procedure is best suited to high p_T and well-isolated electrons, as low p_T superclusters are too small for containing all the bremsstrahlung radiation, as represented in Figure 2.25. In order to recover the soft electrons, a tracking approach is used, which takes the GSF tracks with $p_T > 2$ GeV as seeds for clustering. GSF tracks and PF superclusters are combined into a candidate electron if they respect requirements on the quality of the match. They are used to estimate the charge and momentum of the electron, the latter being derived from the curvature of a GSF track and the energy of the supercluster. Thanks to the high granularity of the tracker and ECAL detectors, the energy resolution of electrons with a p_T of 10 GeV is 0.1 % in the barrel and 0.3 % in the endcaps [27, 123].

The electron candidates are subject to additional identification criteria to distinguish the electrons from the misidentified jets. The identification is based on

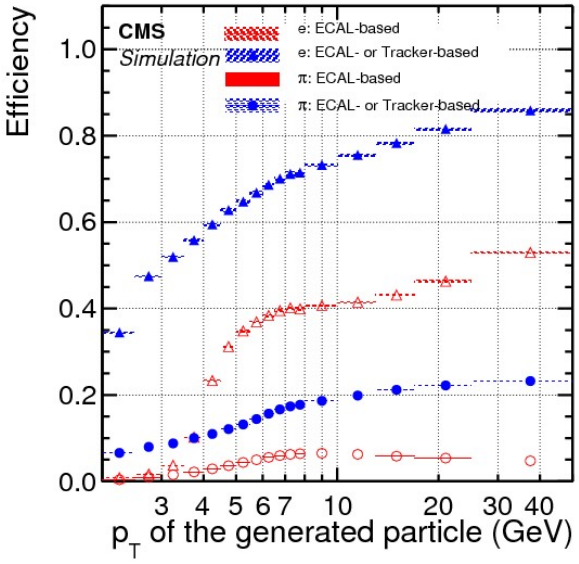

Figure 2.26: Electron seeding efficiency for electrons (triangles) and pions (circles) as a function of p_T. Both the efficiencies for ECAL seeding only (empty symbols) and with the tracker seeding added (full symbols) are displayed [26].

Boosted Decision Trees (BDT) with input variables related to the shower shape, the track quality, the track-cluster matching, the fraction of momentum lost due to bremsstrahlung and the isolation. The output of the BDT, representing the probability of the candidate to be an electron, is used to define three levels of electron identification: loose, medium, and tight. Each time with decreasing selection efficiency and increasing purity.

A specific electron seeds collection is formed by merging the ECAL and tracker seeds, yet saving the information on the origin of the seed. The combination of the two subdetectors brings a substantial improvement to the overall seeding efficiency, as shown in Figure 2.26. The final electron track reconstruction is performed by a fit on the layer hits using a GSF method. The electron loss is modelized with a Bethe-Heitler function, and relaxed requirements on the estimation of the hits' position in each layer are used. The electrons' isolation is used to reject electrons originating from jets, and it is evaluated within a cone with a size of $\Delta R = 0.3$.

Photons

The photon reconstruction procedure is quite similar to the electron's one, but it mainly relies on the ECAL information. Indeed, photons passing through the tracker layers will let linearly aligned tracks, and they deposit most of their energy, around 97% in the ECAL [27]. Where the generated electromagnetic shower can spread into multiple neighbouring ECAL crystals. Hence, the photon reconstruction is seeded from ECAL superclusters with $p_T > 10$ GeV which are not related to any GSF track. These superclusters must be isolated from other ECAL clusters or any track extrapolated from the tracker, and their energy deposit

must present a distribution compatible with a photon shower. In some cases, photons interact with the tracker material and convert into electron-positron pairs before entering the ECAL. Converted photons are identified because the electron and positron leave bent trajectories in the tracking system, with momenta approximately parallel as a result of the photon being massless, and an energy deposit spread in the ϕ direction. The corresponding tracks are either seeded by displaced secondary vertices and extrapolated outward, or by ECAL superclusters and extrapolated inwards. The typical energy resolution for photons with $p_T > 25$ GeV is around 1% in the barrel and 2.5% in the endcaps [27].

The high precision of the photon energy reconstruction enhances the selectivity of signal with photon in the final state, such as $H \rightarrow \gamma\gamma$ which is one of the main channels used for the Higgs boson discovery. Moreover, a precise photon reconstruction is a great benefit to discriminate background such as π^0, one of the most important source of photon misidentification. This meson is decaying into a pair of photons highly collimated, and usually reconstructed as a single one. The contribution of this background is reduced, thanks to the tight isolation of the photon candidate.

Jets

Finally, the jets are the last objects to be reconstructed. The quarks and gluons emitted during the hard interactions in the detector produce large showers of collimated particles, grouped together in jets with conical shape. The procedure for reconstructing the jets is illustrated in Figure 2.27. The momenta of the jets is estimated from the collected hadronic products, which can be charged or neutral, and they are reconstructed with the remaining PF elements after removing electrons, muons, and photons. As they generally deposit energy in both the ECAL and the HCAL, the clusters of the two calorimeters are first connected. If the HCAL cluster is reconstructed in the calorimeter acceptance and is not linked to any other track, it is identified as a neutral hadron when no ECAL cluster is found. Other HCAL clusters are linked to one or more tracks, which may also be linked to ECAL clusters, and they are reconstructed as charged hadrons.

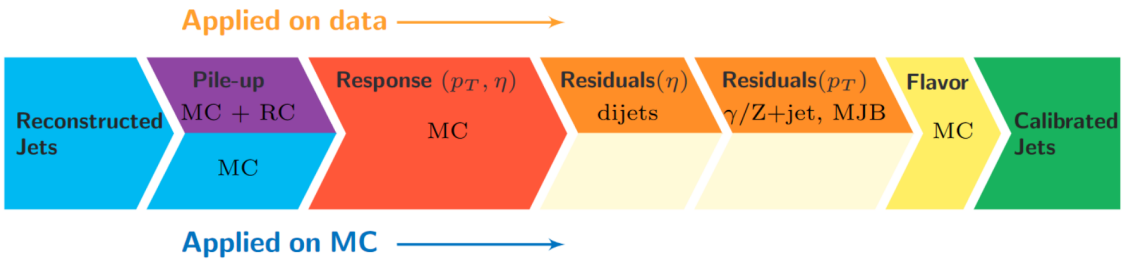

Figure 2.27: Schematic procedure of jet energy correction for data and simulation [28]. RC corresponds to random cone, and MJB stands for multiple jets' events.

The jets are reconstructed by gathering charged and neutral hadrons with the anti-k_T algorithm [124]. The clustering is performed recursively by matching PF candidates that are close to each other, according to a metric defined to produce

conical shaped jets. The size of the cone is determined by the distance parameter R at which the algorithm operates, which can be set to $R = 0.4$ or $R = 0.8$. In both cases, the highest p_T pairs are grouped together first. In this way, the cone is built around the hardest particle in the event and the soft radiation or collinear splitting of partons at the boundaries is suppressed. The momentum of a jet is calculated as the vector sum of the momentum of the grouped PF candidates, it differs from that of the original parton due to theoretical uncertainties in the hadronization process and other experimental effects. A set of jet energy corrections depending on p_T and η is applied to calibrate the jet response taking into account the detector noise and the pile up, as well as the response non-linearity and inhomogeneity of calorimeters. The typical reconstructed jet energy has a response of about 0.9 and a resolution of less than 15% for all p_T ranges [125, 126], as shown in Figure 2.28, where the improvement of the PF approach over the calorimeter-based reconstruction is clearly visible. The jets are then subjected to identification requirements aimed at eliminating those poorly reconstructed or due to instrumental noise in the calorimeters.

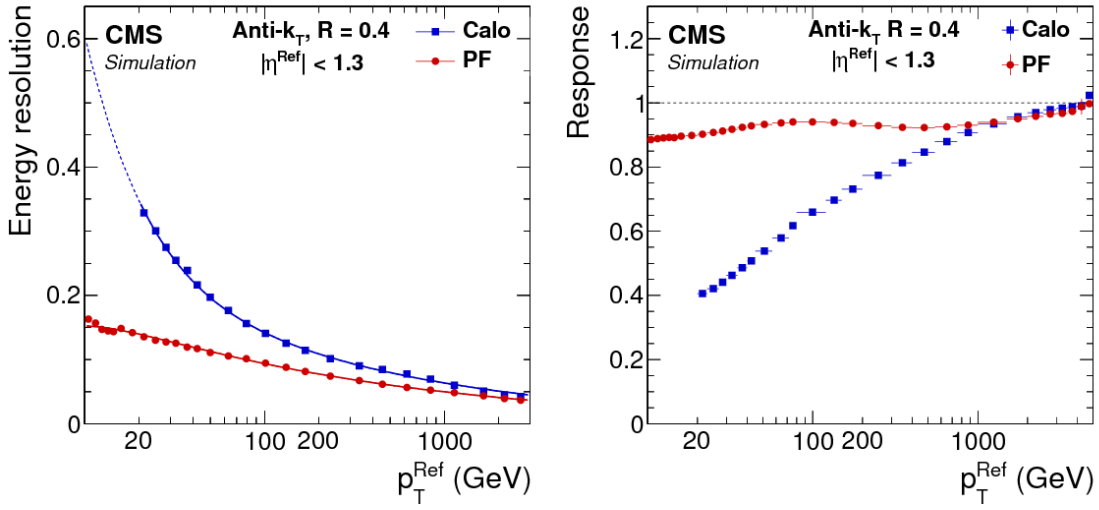

Figure 2.28: Jet energy resolution corresponding to the Gaussian width of the ratio between the corrected and reference jet energies, on the left. Jet energy response, corresponding to the mean ratio of the reconstructed jet energy to the reference jet energy, on the right. Both are a function of the reference jet p_T. Results are shown for jets in the barrel ($\eta < 1.3$) with the anti-k_T algorithm with $R = 0.4$ following the PF and calorimeter approaches [26].

Two increasingly stringent levels of selection are defined (loose, tight) based on the fraction of charged and neutral hadrons in the jet, the charged hadron multiplicity and the fraction of energy deposited in the ECAL. Three working points are defined as loose, medium, tight, similarly to the other particle. Jets induced by quarks or by gluons can be distinguished in CMS with the Quark-Gluon Likelihood algorithm [127]. This technique exploits the fact that jets induced by gluons are wider, with higher particle multiplicities and with a more uniform energy fragmentation than those induced by quarks.

Jets can be created by heavy particle such as τ leptons or b and t quarks. These specific cases will not be treated in this thesis, since they are not interesting for the physics analysis or for the instrumental study.

Missing transverse energy

The last element is not a particle as such, but the missing transverse energy remains important information. The partons colliding inside the protons carry an unknown fraction of the proton momentum in the longitudinal direction.

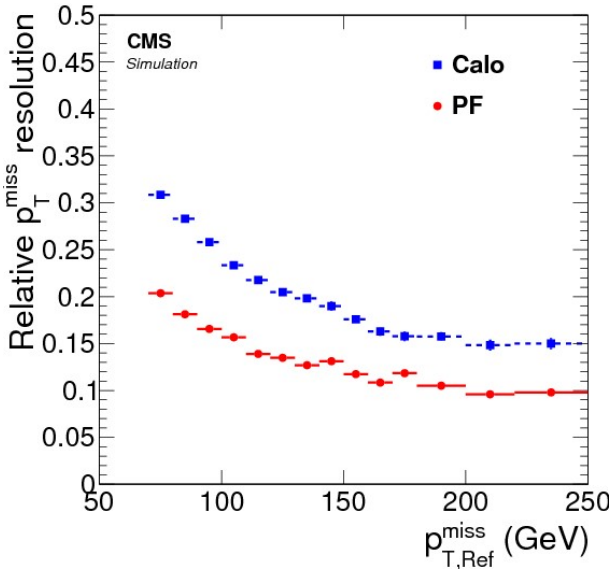

Figure 2.29: Relative missing transverse energy resolution as a function of expected missing transverse energy [26], from the calorimeters approach in blue and from the PF algorithm in red.

However, their momentum is negligible in the transverse plane. Therefore, conservation of momentum can be exploited in the transverse plane to infer the production of undetected particles, such as neutrinos. An instrumental quantity is the missing transverse momentum, defined as the negative of the vector sum of the transverse momenta of all reconstructed PF objects. Inefficiencies arising from tracking or clustering algorithms and non-linearities in the calorimeter response can introduce biases in the determination of the missing energy.

As represented with the Figure 2.29, the missing transverse energy can be calculated using the PF approach as well as the combined calorimeter method. Besides, the energy corrections applied to jets are also propagated to the missing transverse energy computation. After corrections, the relative energy and ϕ angular resolution of the missing transverse energy lies under 20% for all p_T ranges.

Chapter 3

The High Granularity Calorimeter and its prototype

Table of contents

3.1 The CMS detector during the High Luminosity LHC 78
3.2 Reminder of calorimetry and interaction of particles with matter . . 80
3.2.1 Interaction of particles with matter 81
3.2.2 Electromagnetic showers 85
3.2.3 Hadronic showers 86
3.2.4 Concepts of calorimetry 88
3.3 The High Granularity Calorimeter 91
3.3.1 HGCAL design 91
3.3.2 Focus on HGCAL silicon sensors 95
3.4 HGCAL prototypes and test beams 99
3.4.1 Silicon module prototype 99
3.4.2 Assembly of the detector prototype and test beams 100
3.4.3 Signal reconstruction 103
3.4.4 Timing information from the prototype 107
3.4.5 Simulation of the test beam with Geant4 111

After almost fifteen years of good and faithful services, the LHC will be upgraded in order to allow it to start its new life phase. This one should start with a three years shutdown, during which the LHC and its detectors will be upgraded. And the High-Luminosity LHC (HL-LHC) is expected to start its operations by the end of 2029, as shown in Figure 2.4.

Its goal is to increase significatively the amount of collected data. For that, it is designed to deliver a peak instantaneous luminosity of 5×10^{34} cm^{-2}s^{-1}, meaning that is giving access to a total integrated luminosity of 3000 fb^{-1}. Thanks to a such amount of additional data, the discovery potential of the LHC will be highly improved. Moreover, the HL-LHC is designed to allow more precise measurements of the SM properties, and to allow the search of rare processes which were not analysed yet due to the lack of statistics. In general, such analyses

aim to look for the presence of unknown particles which can be explained by BSM theories.

The higher luminosities of the HL-LHC will also result in exceedingly high pile-up rates, with $\mathcal{O}(200)$ events per bunch crossing and unprecedented radiation levels, with fluences of up to 10^{16} n_{eq}/cm^2 and doses of around 2 MGy, thus posing several technical challenges for the operation of the detectors, the computing system, and the entire infrastructure. For example, the LHC tunnel will have to feature the most advanced superconducting magnets, vacuum pipes, cryogenic systems, and superconducting radio frequency cavities.

The CMS Collaboration, as well as the other LHC experiments, are planning a series of major upgrades of the sub-detectors, expected to be commissioned during the second and the third long shutdowns, to maintain the current physics performance in the harsh environment of the HL-LHC.

A brief overview of the CMS upgrade plans is given in Section 3.1, followed by the description of calorimetry physics in Section 3.2. Then, the Section 3.3 focuses on the High Granularity Calorimeter (HGCAL) that will replace the current CMS endcap calorimeters. The HGCAL will feature silicon-based active layers for a total active area of about 600 m^2, and it will be the first large-scale silicon-based imaging calorimeter employed in a high-energy physics experiment. Hence, validating the detector design and assessing its physics performance are cornerstone aspects for the successful realization of this project. For this purpose, a long series of test beams of HGCAL prototypes have been carried out since the end of 2016, leading to the test of the first large scale prototype of the HGCAL in October 2018, presented in Section 3.4. On this occasion, the prototype was exposed to positron and hadron beams with momenta ranging from 20 to 300 GeV at the CERN-SPS beam line, thus allowing a comprehensive characterization of the properties of this innovative detector. The findings of the test beam data analysis are presented in Chapter 4, with a main focus on the timing performance measurement of the HGCAL prototype.

3.1 The CMS detector during the High Luminosity LHC

The final objective of the CMS upgrade programme for the HL-LHC phase, described in [29], consists of two main considerations. Firstly, the fact that many of the current detector components will not be able to withstand the harsh environment expected at the HL-LHC, as the radiation level will be five times higher than today. This will require a complete replacement, meaning an upgrade of the existing sub-systems. On the other hand, the current physics performance must not deteriorate during the high-luminosity research programme, which could be due to the impact of the increased pile up. To achieve this, new detection techniques and improved resolution are required. This would allow new precision measurements, direct searches for rare processes and possible clues to BSM physics. These two aspects can be summarized as the three major challenges for CMS at the HL-LHC:

- The large increase of radiation doses will force replacing the detectors involved in the tracker and in the endcap calorimeters. Moreover, the electronic systems in the barrel calorimeters and the muon detectors will have to be upgraded.
- The high luminosity that will cause a high increase of the data stream, for which significant optimization and improvements must be done at the level of the L1 Trigger primitives. In the same way, the overall TriDAS system upgrade will be fundamental in managing the proceeding of all the events.
- The pile up rate increase will force having subdetectors with better characteristics, such as a high granularity and the introduction of precision timing, in order to discard parasitic particles originating from pile up and to have detector performances at least as good as the ones of Run-2.

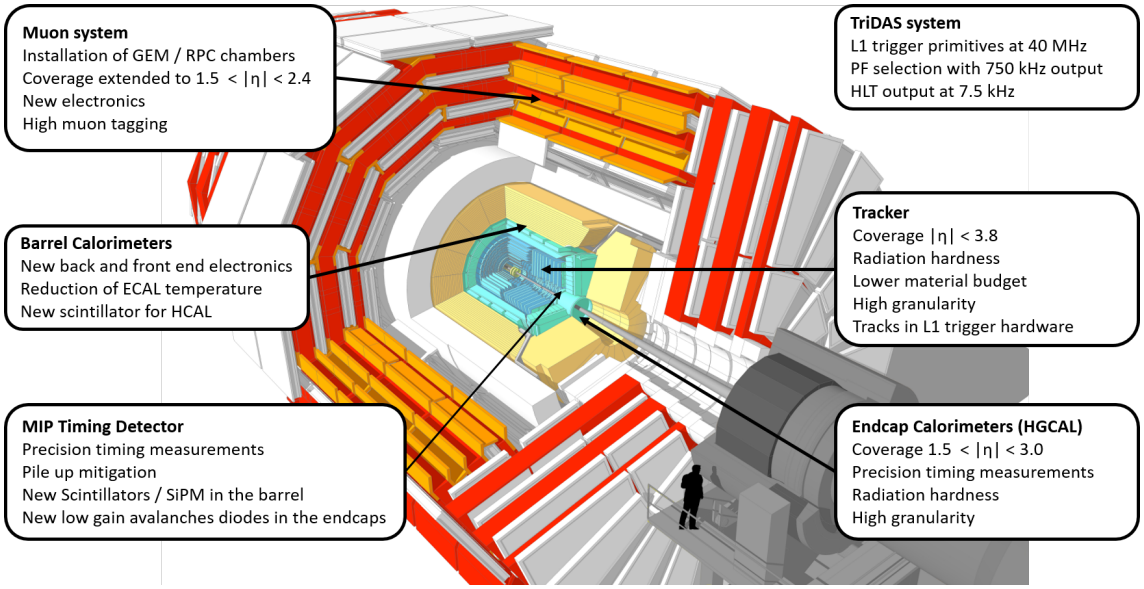

Figure 3.1: Open view of the CMS detector with the indication of the foreseen upgrades for the HL-LHC [29].

Concerning the detector updates which are required, Figure 3.1 gives a short summary of the modifications that will happen. From the innermost to the outermost, there are six main parts of the CMS which must be changed: the tracker, the barrel and endcap calorimeters, the muon system, the TriDAS, and the new MIP timing detector which will be placed in CMS for the first time.

Starting with the tracking system, it will be completely replaced in order to increase the granularity of the detector. Hence, the reconstruction performance will be greatly enhanced, while at the same time the overall material budget will be reduced [128]. Indeed, in the update program for the inner tracking system for Phase-2 [129], it is expected that the current pixel detectors will be replaced by smaller ones. Concerning the outer tracking stations, they will be equipped with strips and macro pixel sensors [130], allowing to extend the coverage up to $|\eta| = 3.8$. This new design will improve both the longitudinal and the transverse

resolution. From these modifications, it is foreseen to have lower fake rates, thus increasing the reconstruction range of L1 trigger tracks [131], which could be done up to $|\eta| = 2.4$.

Then, the brand-new MIP timing detectors (MTD) [132] will be placed in front of the barrel and endcap calorimeters to increase the available timing information on charged particles. These detectors were not installed in CMS during the first and second run, they are designed especially for the Phase-2.

Both endcap calorimeters as well as the preshowers will be replaced with the HGCAL [32]. The high granularity of this new sampling calorimeter enhanced shower's separation and particle identification. In addition, it will have the capability to provide precise timing information, which will be highly beneficial for the particle identification, and principally to discard particles coming from the increased pile up.

As well as the endcaps, the ECAL and HCAL upgrade [133, 134] is focused on increasing the overall granularity and providing additional timing measurements of particles passing through the subdetectors. To be able to withstand the harder operating conditions, an upgrade of the electronic readout is necessary.

Besides, the current muon detection system composed of DT, RPC, and CSC, will be increased with the addition of Gas Electron Multiplier chambers and a new generation of RPC [135]. The coverage will be extended up to $|\eta| = 2.8$ with the GEM and up to $|\eta| = 2.4$ with the RPC.

Finally, the TriDAS systems will be subject to a complete replacement [136], with increased throughput. The HLT will continue to have access to the total detector information, even at the maximum input rate of 750 kHz expected at the top of the HL-LHC operations, to which it will provide a reduction factor of $\sim$100 for a bandwidth output of 7.5 kHz.

3.2 Reminder of calorimetry and interaction of particles with matter

Before diving into the details of the HGCAL detector, it is worth understanding what a calorimeter is and how does it work.

Calorimetry plays a key role in the detection of collision events in modern particle physics. The electromagnetic and hadronic calorimeters are responsible for measuring the energy of charged and neutral particles, as well as for reconstructing jets and measuring their energy. In addition, the calorimeter system is essential for measuring the overall energy flow and for evaluating the missing transverse momentum, signing the presence of invisible particles leaving no signal in the detector system.

Calorimeters are blocks of instrumented material in which particles to be measured are fully or partially absorbed, and their energy transformed into a measurable quantity. The interaction of a high energy particle with the calorimeter matter leads to the development of a particle shower. First, the primary particle produces secondary particles when crossing through the calorimeter. Then, each secondary particle interacts with the calorimeter matter and produces more parti-

cles. As this process continues, the number of particles increases as long as the energy of the secondary particles is sufficient to create new particles.

Any calorimeter consists of active signal generators, the active material that measure the shower energy, and a passive particle absorber, which is the material that causes the particles to initiate showers. The energy deposited in the active part serves as a measurement of the energy of the incident particle. For accurate measurements, the size of a calorimeter should be large enough to contain the entire energy deposit of the particle. The required calorimeter thickness corresponds to the shower depth, which is a logarithmic function of the initial particle energy and which is described later in this section. Thus, detection of particles with high energies does not require extremely thick calorimeters.

The interaction processes that play a role in the shower development depend on the energy and the nature of the primary particle, as well as the nature of the material in which they are interacting, since the cross-section of a process depends on the atomic number Z. Electrons, positrons, and photons will undergo electromagnetic interactions with the atomic fields, generating electromagnetic showers, detailed in Section 3.2.2. As for hadrons, a range of strong interactions with the nuclei will take place, producing hadronic showers presented in Section 3.2.3.

The designs differ by the materials, the read-out method and the geometry implemented in each calorimeter. Typically, calorimeters are classified by their construction into homogeneous and sampling calorimeters, as well as by their use for electromagnetic or hadronic interactions. The expected performance of calorimeters for both types of showers is discussed in Section 3.2.4.

3.2.1 Interaction of particles with matter

In this section, the focus will be put on the interaction of particles passing through matter. Among all of them, the highlight is put on the photons, the electrons, and the heavy particles such as muons or hadrons in general. This choice is motivated by the nature of particles which should pass through the HGCAL detector and the interactions happening in it.

When a photon passes through matter, different processes can intervene due to the complex atom structure. The possible interactions involving photons and matter are the following:

- **The Rayleigh scattering** consists in the interaction of photons with the atomic nuclear charge, thus this effect happens with a polarized particle. This leads to a cross-section dependency on the particle size and polarity, as well as the light wavelength. In this process, the photon does not lose energy, leading to no contribution to the shower development.

- **The Thomson scattering** is the interaction of photons with atomic electrons, thus it happens with a not polarized charged particle. Similarly to the previous effect, the photon does not lose energy, therefore there is no contribution to the shower development. These first two effects are also called coherent elastic scattering.

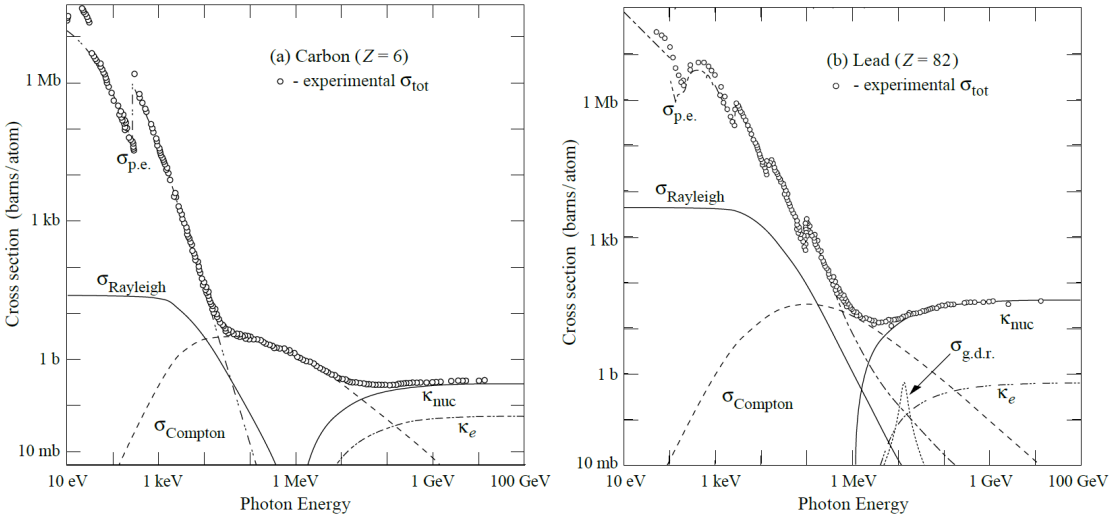

Figure 3.2: Evolution of the cross-sections of photon interactions with atoms as a function of the photon energy [30]. Carbon is considered on the left, and lead on the right. There are different photon interactions, which are the Rayleigh scattering $\sigma_{Rayleigh}$, the Compton scattering $\sigma_{Compton}$, the photoelectric effect $\sigma_{p.e.}$, pair production by nuclear fields κ_{nuc}, the pair production by electron fields κ_e, and the photo-nuclear absorption $\sigma_{g.d.r.}$.

- **The Compton scattering** corresponds to a photon interaction with an atomic electron and transferring some of its energy to the struck electron. In general, the electron acquires enough energy to leave the atom.
- **The photoelectric effect** happens when a photon having an energy larger than the electron binding energy is absorbed by atomic interaction. As a result, an electron is ejected with a kinetic energy corresponding to the energy difference of the photon energy and the electron binding energy. The term photo-electron is employed to refer to this emitted electron.
- **The e^+e^- pair production** occurs when the photon energy is greater than twice the electron rest mass. This phenomenon is induced by the fact that when a photon passes through a Coulomb field, it can result in the creation of a pair of electron and positron. The atom's nucleus or the electrons do not have the same contribution, indeed in more than 99% of the case it is due to the nuclear electromagnetic fields, whereas less than 1% is originated from the electron fields.
- **The photo-nuclear absorption**, as indicated by its name, corresponds to the absorption of a photon with an energy above 10 MeV. A such energy corresponds to the Giant Dipole Resonance (g.d.r) energy region, where a resonant state in the nuclei can be excited. The decay of these exciting states can emit a neutron, a proton, or another photon.

These effects are dependent on the nature of the interacting atoms and the photon energy. The Figure 3.2 represents most of these processes in a light element

(carbon) as well as in a heavy element (lead). The contributions of each interaction differ with the photon energy. Indeed, the contributions from Compton scattering, Rayleigh scattering and the photoelectric effect are dominant at low energy, whereas the pair production is more probable at high energy.

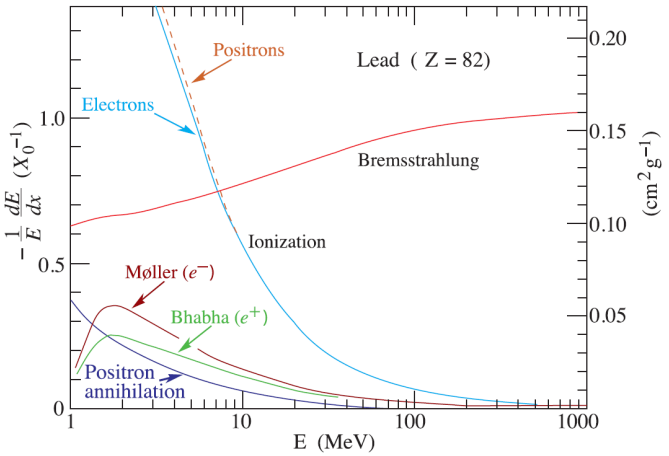

Figure 3.3: The energy loss fraction per radiation length X_0 of electrons and positrons in lead as a function of particle energy [30]. The ionization is represented by a light blue line for electrons and in an orange dashed line for positrons, Bremsstrahlung is in red, the Møller scattering in burgundy, the Bhabha scattering in green, and the positron annihilation is dark blue.

The next category of particles, is constituted of electrons and positrons. When such particles are passing through matter, they lose energy due to the following electromagnetic interactions:

- **The Møller scattering** occurs when a moving energetic electron scatters with an atomic electron of the matter. It is an electron-electron scattering.
- **The Bhabha scattering**, unlike the Møller scattering, stands for positron-electron scattering. In this case, the incident particle is a positron which scatters with an atomic electron of the matter.
- **The positron annihilation** is when a positron collides with an atomic electron, leading to the annihilation of both the electron and the positron. The result of this decay is the creation of two gamma ray photons emitted in opposite directions.
- **The ionization** happens in the context of the development of an electromagnetic shower, this process corresponds to an electron or a positron collision with an atomic electron. The incident particle transfers sufficient energy to put the atomic electron in an unbound state. In the end, the considered atom became an ion due to its missing electron.
- **The Bremsstrahlung effect** corresponds to an electromagnetic radiation produced during acceleration or deceleration of an electron or positron in

the presence of the electromagnetic field of the atoms in the material. This phenomenon was mentioned in Section 2.3.2, where an example was given.

The different contributions to the energy loss of electrons and positrons per radiation length X_0 in lead are shown in Figure 3.3 as a function of the particle energy. A physical definition of X_0 is given with Equation 3.2. At low energies, electrons, and positrons primary lose energy by ionization. Other contributions in this energy range are bremsstrahlung, Møller scattering, Bhabha scattering and positron annihilation. For high energies (approximately larger than 10 MeV), the energy loss is predominantly due to bremsstrahlung.

All these phenomena, involving photons, electrons, and positrons, are at the root of the development of electromagnetic showers happening inside a calorimeter. A detailed description of electromagnetic showers is given in Section 3.2.2.

Heavy charged particles, such as muons and charged hadrons, can undergo ionization and bremsstrahlung when interacting with the atomic fields of matter. The emission of bremsstrahlung scales with the particle mass m and its energy E, as E.m^{-2} and therefore is suppressed in particles with energies lower than a few hundred GeV. The mean rate of energy loss through ionization and atomic excitations for fast particles with speed $v = \beta c$ and charge ze (e being the elementary charge) is well-described by the Bethe-Bloch equation:

$$\left\langle -\frac{dE}{dx} \right\rangle = K\frac{z^2}{\beta^2}\frac{Z}{A}\left[\frac{1}{2}ln\frac{2m_e c^2\beta^2\gamma^2 T_{max}}{I^2} - \beta^2 - \frac{\delta(\beta\gamma)}{2}\right] \tag{3.1}$$

Where T_{max} is the maximum kinetic energy which can be imparted to a free electron in a single collision, K is the proportionality constant, Z and A are the atomic and mass number of the material, respectively, I is the mean excitation energy of the dense material and $\delta(\beta\gamma)$ is the density effect correction function 3.2.1. This equation describes with an accuracy of a few percent the mean rate of energy loss in the region $0.1 < \beta\gamma < 1000$ for intermediate Z materials. The energy loss of positive muons on copper as a function of the momentum is shown in Figure 3.4. In the relevant range, the energy loss is computed with the Bethe-Bloch equation, while outside this range additional corrections are applied. A broad minimum in the energy loss is visible around $\beta\gamma$. A particle with an energy corresponding to this range is referred to as a Minimum Ionizing Particle (MIP).

In thin layers of dense material, fewer interactions occur and therefore fluctuations in the energy loss are expected. These fluctuations, which are referred to as Landau fluctuations, occur due to variations in the number of interactions as well as in the energy transferred in each interaction. The distribution of energy loss in these thin layers, corresponds to a Landau distribution, which is asymmetric and characterized by a narrow peak with a long tail toward large energy losses. The high energy tail comes from a few individual collisions, each with a small probability of transferring a large amount of energy. The large weight of these rare events drives the mean value toward the tail of the distribution.

The energy loss of single particles in thin layers is in general described with the Most Probable Value (MPV) of the energy loss distribution. The MPV is a robust estimator of the energy loss, this choice of observable is and compared to the mean

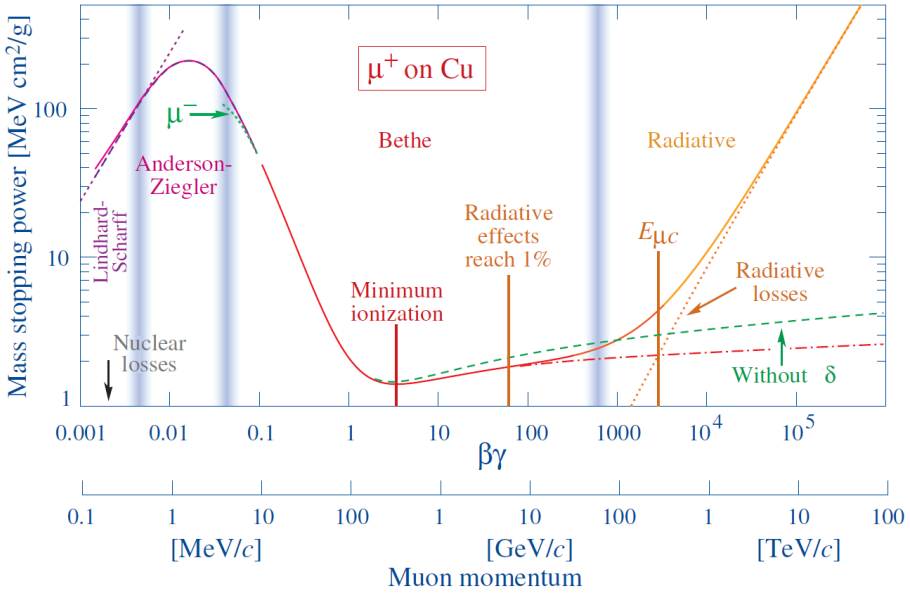

Figure 3.4: The evolution of the mean energy loss of anti muons in copper as a function of the muon momentum [30]. The total energy loss is represented with the solid curves. The large vertical lines are boundaries between different approximations, and for instance the Bethe-Bloch equation is used between $0.1 < \beta\gamma < 1000$.

value which has a higher dependency on the particle energy. In thin layers, the MPV is lower than the mean value, which increases more rapidly with the particle energy.

By definition, a calorimeter aims to measure the energy of the incoming particles. To achieve this goal, it is composed of specific material in which particles will lose all, or most of their energies, and it is at this step that the bestiary of interactions with matter intervenes. Due to the high energy of particles used, this energy loss is accompanying by the generation of secondary particles, which in their turn are decaying in another generation of secondary particles, et cetera until that all the energy is absorbed by the detector. The chain reaction is called a shower, and it exists in two sorts: electromagnetic and hadronic showers. Both are described in the following Section.

3.2.2 Electromagnetic showers

Electromagnetic showers may be initiated by photons, electrons, or positrons entering a material. These showers result from electromagnetic interactions with atomic electromagnetic fields, which give increasingly more particles of lower energy, until the energy carried by individual particles cannot sustain the production processes.

The characteristic length scale for the longitudinal development of an electromagnetic shower in a material is the radiation length X_0, which is usually measured in g.cm^{-2}. The radiation length is defined as the mean length over which an energetic electron has lost ∼63% of its initial energy by bremsstrahlung.

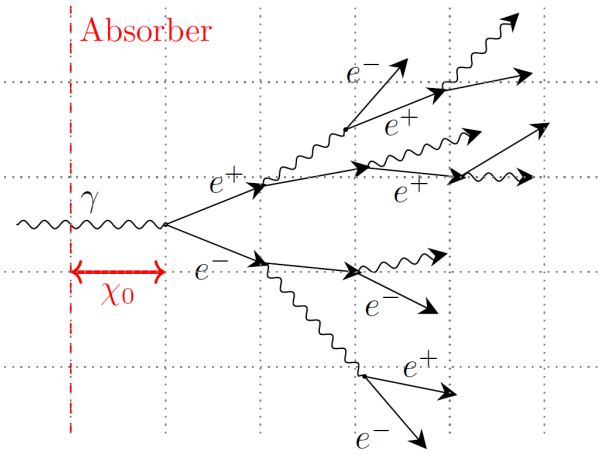

Figure 3.5: Representation of the development of an electromagnetic shower, initiated by a photon passing through an absorber material. The scheme is obtained from [31].

This corresponds to 7/9 of the mean free path of a high energy photon before inducing a e^+e^- pair production. A common parametrization of the radiation length of a material as a function of its atomic number and mass, Z and A, respectively.

$$X_0 = \frac{A \times 716.4 \text{ g.cm}^{-2}}{Z(Z+1)ln(278/\sqrt{Z})} \tag{3.2}$$

The transverse development of an electromagnetic shower in different materials is measured by the Molière radius ρ_M, which stands for the radius of a cylinder containing 90% of the energy of the shower. The Molière radius is given by the following formula:

$$\rho_M = 21.2 \text{ MeV} \times \frac{X_0}{\epsilon_c} \tag{3.3}$$

Where ϵ_c is the critical energy in which the electron ionization loss per radiation length is equal to the electron energy.

3.2.3 Hadronic showers

Hadrons passing through matter undergo electromagnetic interactions in the presence of atomic electromagnetic fields, as well as strong interactions with the nuclei of matter. Of these interactions, inelastic hadronic interactions are those that generate hadronic showers by producing secondary particles, which then lose their energy either by ionization and excitation or by undergoing further inelastic interactions. When particle production is balanced by particle absorption, the number of particles in the shower reaches a maximum, which is followed by a gradual decrease in energy deposition from that point.

Inelastic interactions with nuclei induce meson and baryon production, spallation, excitation of nuclei and nuclear fission. The characteristic length scale for the development of showers with these interactions is the nuclear interaction length

λ_n. This length indicates the average distance that a high-energy hadron must travel within an absorbing medium before a nuclear interaction occurs. Therefore, the probability that the particle will travel a distance x in the medium without causing a nuclear interaction is given by :

$$P = exp\left(-\frac{x}{\lambda_n}\right) \tag{3.4}$$

λ_n value scales with the atomic mass of the material as $A^{\frac{1}{3}}$. Cross-section measurements for interactions of protons and pions with different fixed targets have shown an additional dependence on the projectile's size and result in a correction factor for pion interaction length λ_π, which is a factor $\frac{3}{2}$ larger than the proton interaction length. The nuclear interaction length is typically larger than the radiation length, and therefore hadronic showers are usually larger in extension compared to electromagnetic showers.

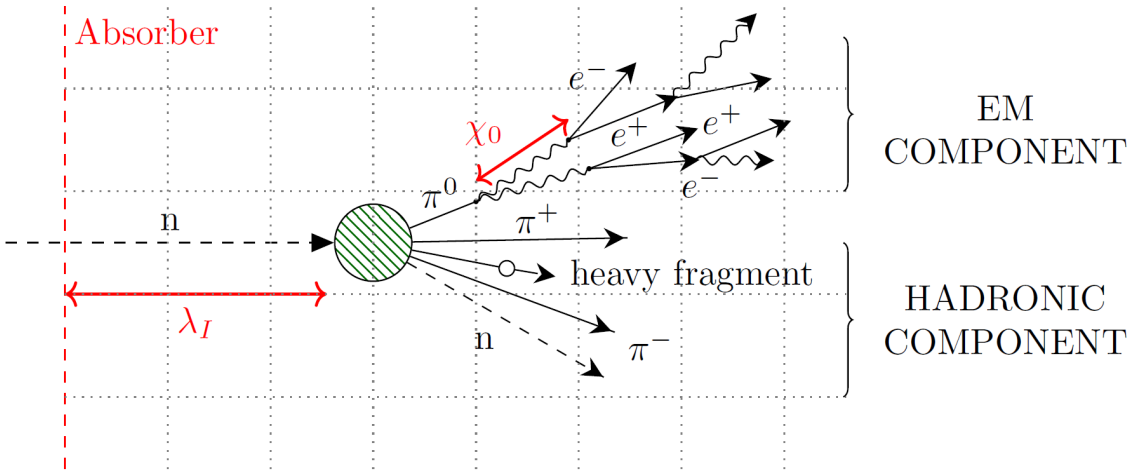

Figure 3.6: Representation of the development of a hadronic shower, initiated by a neutron passing through an absorber material. The decay products are constituted by an electromagnetic shower, a heavy fragment, and other light hadrons such as pions or neutrons. The scheme is obtained from [31].

An example of a hadronic shower is given in Figure 3.6. The complexity of hadronic showers is much higher compared to electromagnetic showers, due to their electromagnetic component and their invisible energy.

Indeed, neutral particles produced in the shower, in particular the decay of π^0 into two photons, initiating an electromagnetic shower inside the hadronic shower. Since $\lambda_n > X_0$ in most materials, this electromagnetic component is typically narrower and spatially more compact than the pure hadronic component. The fraction of the electromagnetic component varies strongly from event to event, depending on particular processes occurring in the early phase of the shower development; however, on average, this electromagnetic component increases with the energy of the initial hadron.

A certain fraction of the deposited energy produced by the strong interactions is undetectable and thus referred to as invisible energy. The main source of this

phenomenon are energy losses in the excitation or recoil of the target nuclei, which often do not result in a signal in the active medium. In addition, the neutrons generated within the shower lose their energy in elastic scattering processes, which reach an end either by the decay of the neutron or by a neutron capture. In the latter case, the excited nucleus releases additional energy by photon emission. Since this process is very slow compared with the shower time scale, usually the energy it contributes is not measured. Additional energy might be lost to neutrinos originating from meson decays.

All the materials have specific values of X_0, λ_n, dE_{min}/dx, and ρ. During the conception of a calorimeter, the choice of the material is highly dependent on the desired values of these parameters. For instance, the main materials used in the design of HGCAL are given in Table 3.1.

Table 3.1: Summary of parameters linked to the energy loss and the evolution of particle showers for materials used in HGCAL. For each atom, there is the density ρ, the minimum energy loss per distance due to ionization dE_{min}/dx, the radiation length X_0, the nuclear interaction length λ_n, the ratio with the pion interaction length λ_π/λ_n, and the Molière radius ρ_M. All values are taken from [1].

Material	ρ [g/cm^3]	dE_{min}/dx [MeV/cm]	X_0 [cm]	λ_n [cm]	λ_π/λ_n	ρ_M [cm]
Carbon $^{12}_{6}$**C**	2.27	3.952	18.85	37.89	1.37	4.894
Silicon $^{28}_{14}$**Si**	2.33	3.876	9.370	46.52	1.27	4.944
Iron $^{30}_{26}$**Fe**	7.87	11.43	1.757	16.77	1.22	1.719
Copper $^{64}_{29}$**Cu**	8.96	12.57	1.434	15.32	1.21	1.568
Tungsten $^{184}_{74}$**W**	19.3	22.10	0.3504	9.946	1.14	0.9327
Lead $^{207}_{82}$**Pb**	11.4	12.74	0.5612	17.59	1.13	1.602

The choice of these different materials is explained in the Section 3.3, where the design of HGCAL is detailed.

3.2.4 Concepts of calorimetry

Calorimeters are classified into two categories according to their read-out implementation: homogeneous calorimeters and sampling calorimeters. In homogeneous calorimeters, the entire detector volume is sensitive to particles, acting simultaneously as the absorbing material and the signal generator. The materials which are usually used for this purpose are dense scintillating crystals, lead doping glass or liquefied noble gases. Typically, measurements of photons produced in the interactions within these materials are used to evaluate the energy of the initial particle. These photons, generated via a process known as scintillation, are then detected by photo-detectors located at the far-end of the material.

Due to the high granularity needed for the HGCAL, the choice of a sampling calorimeter was necessary. Indeed, only this kind of design can allow a precise SD spatial and temporal sampling of the showers induced by the detected particles. Besides, the hadronic part of HGCAL is gathering both technologies: silicon sensors and scintillating tiles, which are described with more details in Section 3.3.1. In sampling calorimeters, the different functions of shower generation and particle detection are exercised by different materials in alternating layers. The passive absorber layers which generate the shower are chosen to have a high density and high atomic number to produce more compact showers. Typically, materials such as iron, copper, lead, steel, tungsten, or uranium are used. The active read-out layers which record the particles inside the shower can be implemented in different ways using a variety of technologies.

The advantage of sampling calorimeters is the possibility to optimally choose the absorber and active material independently. When choosing a very dense absorber material, the calorimeters can be made very compact. Moreover, using sampling calorimeters gives the possibility to study spatial properties of the showers, such as their longitudinal and transverse development. On the other hand, these calorimeters detect only a small fraction of the particles and due to sampling fluctuations, they are characterized by an inferior energy resolution of electromagnetic showers compared to homogeneous calorimeters.

The electromagnetic and the hadronic showers extend to different scales due to the difference between the nuclear interaction length and the radiation length in matter. For that reason, calorimeters are often divided into ECAL, for measuring mainly electromagnetic showers, and HCAL, for measuring mainly hadronic showers. The advantage of this separation is the possibility to perform an independent optimization of both calorimeters for their specific needs, resulting in a better performance, in particular for electromagnetic showers. However, the energy reconstruction of hadrons in such a calorimeter system becomes more complex due to transition effects and inter-calibration corrections between the different detectors.

In the calorimetry technic typically used in high energy physics, the energy of an incoming particle is evaluated with all the signals generated by the showering particles. Ideally, the signal amplitude is proportional to the energy E of the primary particle. The concept of calorimeter linearity refers to the level of which this proportionality is achieved in practice. The precision with which E can be measured is evaluated by the relative width of the signal distribution, which defines the energy resolution of the calorimeter. The calorimeter response for electromagnetic and hadronic showers, evaluated with the linearity and the energy resolution of the calorimeter.

The simple development of electromagnetic showers, and the capability to efficiently detect secondary particles of such showers, allow a high degree of linearity in ECAL. Homogeneous calorimeters are the most efficient in this respect, using the entire kinetic energy of the incoming particle to generate the calorimeter signal. However, due to non-linear effects such as saturation and shower leakage, deviations from linearity may be observed.

The development of an electromagnetic shower is a stochastic process, and

therefore fluctuations from shower to shower are unavoidable. These fluctuations follow the Poisson's statistics. In general, the number of particles that constitute the calorimeter signal, and it is proportional to the total measured signal. Moreover, as the number of particles in the shower grows with the energy, so it is the same for the measured signal. For that reason, for higher energies, a more precise measurement is expected. By extension of this principle, the reconstructed energy of a shower E is linearly related to the energy of the incoming particle noted E_0. The linearity allows determining a factor α, making the link between the average shower energy $\langle E \rangle$ and E_0, and it is given by the following formula:

$$\langle E \rangle = \alpha E_0 \tag{3.5}$$

Then, when the reconstructed energy distribution is known, it is possible to calculate its standard deviation σ_E. The energy resolution of a calorimeter is given by the ratio of the energy standard deviation over the average detected energy, and it is parametrized with the following expression:

$$\frac{\sigma_E}{\langle E \rangle} = \sqrt{\frac{a^2}{E_0^2} + \frac{b^2}{E_0} + c^2} = \frac{a}{E_0} \oplus \frac{b}{\sqrt{E_0}} \oplus c \tag{3.6}$$

All the statistics related contributions to the energy resolution are described by the stochastic component of the energy resolution, given by $\frac{b}{\sqrt{E_0}}$ is called the stochastic term and used commonly with the energy E_0 given in units of GeV. Additional consideration for a full description of the energy resolution of a calorimeter is the energy independent noise contribution arising from electronic noise of the readout chain. This is described with the noise term $\frac{a}{E_0}$. Other influences on the signal distribution are non-uniformities in the detector, such as dead regions or inhomogeneities in the detector material, and the calibration uncertainty. The signal uncertainties introduced by these factors scale with the energy and result in a constant energy resolution, defined with the constant term c. Since all the sources of fluctuations described above are not correlated, their contributions to the energy resolution could be added in quadrature.

Sampling calorimeters also allow the measurement of spatial properties of showers. First, concerning the longitudinal development of a shower, meaning the development along the axis of the particle trajectory, and then the transverse shower profile.

The average longitudinal electromagnetic shower profile for homogeneous media can be described empirically using Longo's parameterization [137]:

$$\left\langle \frac{dE(z)}{dz} \right\rangle = E_0 \frac{(\beta z)^{\alpha - 1} e^{-\beta z}}{\Gamma(\alpha)} \tag{3.7}$$

Where z is the depth in radiation length, E_0 is the mean of the total energy deposited in the calorimeter and α and β are respectively the shape and scaling parameters. The previous equation gives a good first order approximation for sampling calorimeters. The measured energy longitudinal profiles are used to

examine the expected logarithmic energy dependence of the position of the longitudinal shower maximum T given by $\frac{\alpha-1}{\beta}$. The shower maximum as a function of the beam energy is obtained with the following parameterization [1]:

$$T = log(\frac{E}{E_c}) - \frac{1}{2} \tag{3.8}$$

Where E_c is the critical energy of the calorimeter, representing the electron or positron energy for which the ionization and excitation losses are equal to those from radiative processes such as bremsstrahlung and pair creation.

The transverse development of a shower is mainly studied through its radial containment. It corresponds to the ratio of the energy included in a r radius cylinder over the overall energy. It is parametrized as follows:

$$\left\langle \frac{E(r)}{E} \right\rangle = 1 - A \times e^{-Br} \tag{3.9}$$

Where A and B are free parameters.

The Molière radius ρ_M is defined as the radius of a cylinder aligned along the shower axis and containing on average 90% of the total energy deposited by the shower. It corresponds to $\langle E(\rho_M)/E \rangle = 0.9$.

Hadronic calorimetry is much more complex than electromagnetic calorimetry. The reason for this is the complex development of hadronic showers, the presence of two components, electromagnetic and pure hadronic, and invisible energy. The calorimeter response for the total energy deposited by a hadron shower, noted π, can be written as:

$$\pi = f_{em} \times e + (1 - f_{em}) \times h \tag{3.10}$$

Where e and h denote the calorimeter response to the electromagnetic and the pure hadronic components, respectively, and f_{em} represents the electromagnetic fraction. The response π is non linear for two reasons. First, due to the invisible energy, the calorimeter response to the hadronic secondary shower is typically smaller than the electromagnetic response ($\frac{e}{h} > 1$). Second, f_{em} increases on average with the hadron energy.

3.3 The High Granularity Calorimeter

3.3.1 HGCAL design

The endcap calorimeters of the CMS detector which are currently in place have been designed to handle integrated luminosities of up to 500 fb^{-1}, which are expected to be far exceeded by the 3,000 fb^{-1} expected at the end of Phase-2 operations. Furthermore, the scintillating crystals currently used in the endcaps cannot withstand the high radiation doses expected during the HL-LHC operation. Especially, in this peculiar region of the detector, the radiation doses should reach 2 MGy and fluences are expected to go up to 10^{16} n_{eq}/cm^2. Such values

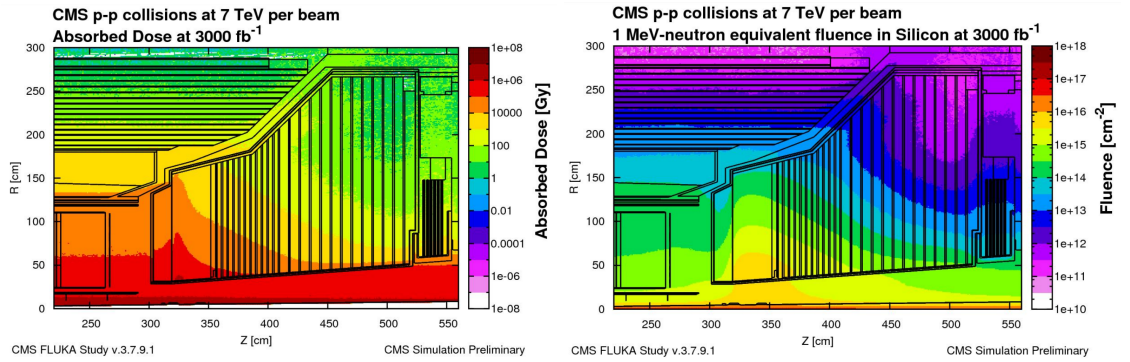

Figure 3.7: On the left, the spatial distribution of the accumulated dose of ionizing radiation, and on the right, the accumulated fluence parametrized with 1 MeV equivalent neutrons. Both are in HGCAL after an integrated luminosity of 3000 fb^{-1}, simulated using the FLUKA program, and shown as a two-dimensional map in the radial and longitudinal coordinates [32].

are represented in Figure 3.7, where the simulated spatial distributions of both quantities are represented.

Accordingly, the CMS Collaboration should replace the current endcap calorimeters with a High Granularity CALorimeter (HGCAL) [32] and the preshower in the context of the Phase-2 upgrades programme [29]. The HGCAL will be composed of an electromagnetic (CE-E) and a hadronic (CE-H) compartment. The first one will be made of a stack of 26 active layers, separated by absorber material layers composed of CuW, Cu, and Pb. While the second one features 21 layers interspersed with layers of stainless steel. The electromagnetic compartment will extend for a total of 27.7 radiation lengths X_0, also equivalent to 1.3 nuclear radiation lengths λ_n. The HGCAL depth results in a total of 10 λ_n when both the CE-E and CE-H compartment are gathered.

To reach the requirements of a radiation resistant detector, the CE-E and the front part of the CE-H will use silicon as active material, for a total area of about 600 m^2 to be covered. Hexagonal silicon sensors will be used to optimize the coverage of such a large surface and reduce the detector's total cost. The design, production, and validation of these hexagonal sensors, also refers to as modules in the rest of this thesis, is one of the most challenging element of the HGCAL project since it is at the root of all the recorded signals which will be used for the reconstruction of particles.

The longitudinal cross-section of the HGCAL is shown in Figure 3.8, along with the difference between the CE-E and CE-H active materials and the lines defining the expected detector coverage of $1.5 < |\eta| < 3.0$. The calibration of the detector will be performed with minimum ionizing particles (MIP). The effects of radiation damage must be limited in order to ensure a reasonable detection of MIP throughout the detector lifetime and to ensure a signal to noise ratio above one. To achieve this, the HGCAL will have to be operated at a constant temperature of -30°C or less. This temperature is obtained with a dedicated CO_2 cooling system directly implemented in the copper base plate. It consists of a small pipe circulated inside the copper and allowing to provide the most uniform cooling to the sensors.

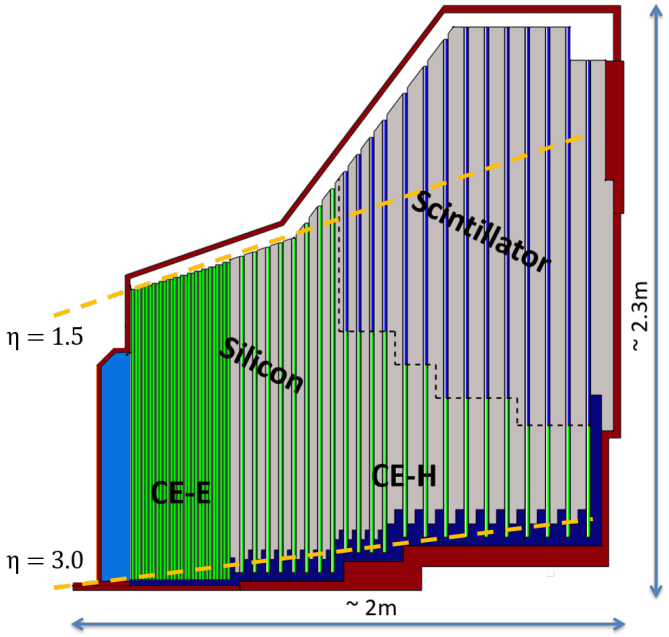

Figure 3.8: View of a section of the HGCAL. The CE-E and CE-H compartments comprise silicon sensor modules, represented in green. The SiPM scintillator tiles are employed in the back of the hadronic compartment and are drawn in blue, the figure is taken from [33]. The expected HGCAL coverage is shown with orange dashed lines, ranging from $\eta = 1.5$ up to $\eta = 3.0$.

Because of its highly granular readout design, the HGCAL is often referred to as a 5D calorimeter, meaning that the high granularity in the three spatial dimensions (its sampling capabilities are in the longitudinal and transverse planes) can be exploited to entirely reconstruct and study electromagnetic and hadronic shower profiles. The two other mentioned dimensions are the energy, obviously, and the timing, which will be a very beneficial for discarding particles coming from pile up event.

It is expected that the radiation doses will be lower in the hadronic part of the endcaps, more precisely at a distance of 4 m from the interaction point. Such doses allow the use of segmented plastic scintillators tiles coupled with silicon photo-multipliers (SiPM) for the readout. In the back part of the CE-H, two calorimetry technologies are involved and using two different active materials. Squared scintillator tiles have a minimum size of 4 cm^2 and ranging up to a maximum of 30 cm^2 will be used. The overall active surface of the scintillators can cover up to more than 400 m^2.

The arrangement of the silicon modules in the CE-E and in the front part of the CE-H, as well as the mixed technology of silicon sensors and scintillator tiles employed in the back part of the CE-H, are shown in the right part of Figure 3.9.

The HGCAL will be composed of 8" sensors with an active thickness of 120, 200, or 300 μm, depending on the detector region. Each module will comprise several single readout diodes, hereafter referred to as cells or pads, with a 0.5 or 1.0 cm^2 active area, for a total of about six million cells read out individually in the

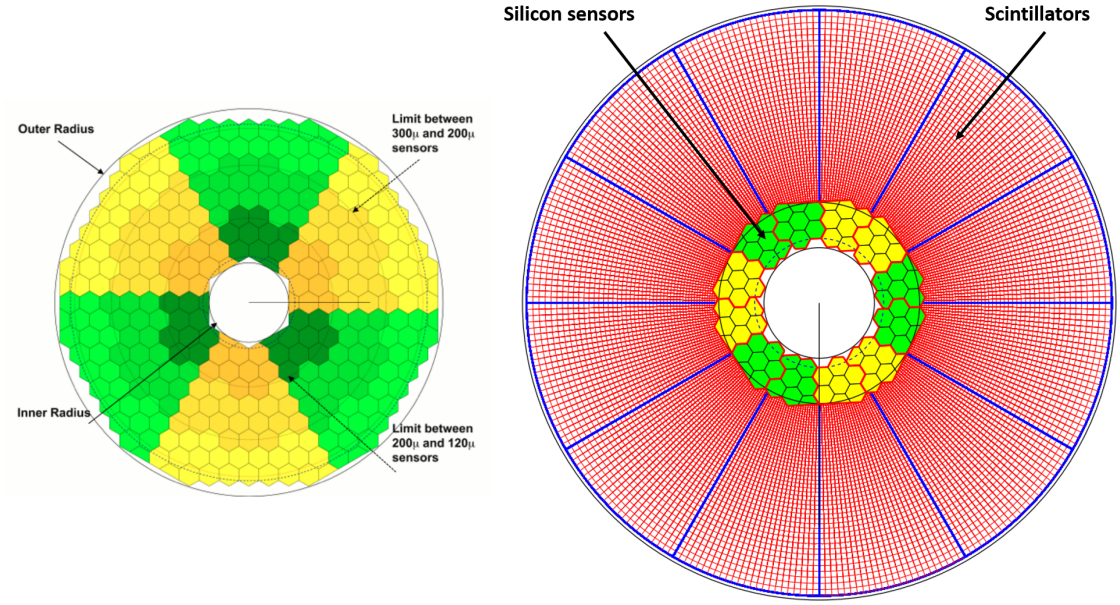

Figure 3.9: Illustration of a layer of the electromagnetic compartment on the left, and of the hadronic compartment on the right [32]. The yellow and green hexagons are the silicon modules, and the scintillating tiles are represented in red. On the left, the colour intensity corresponds to the different sensor thickness of 120, 200, or 300 μm.

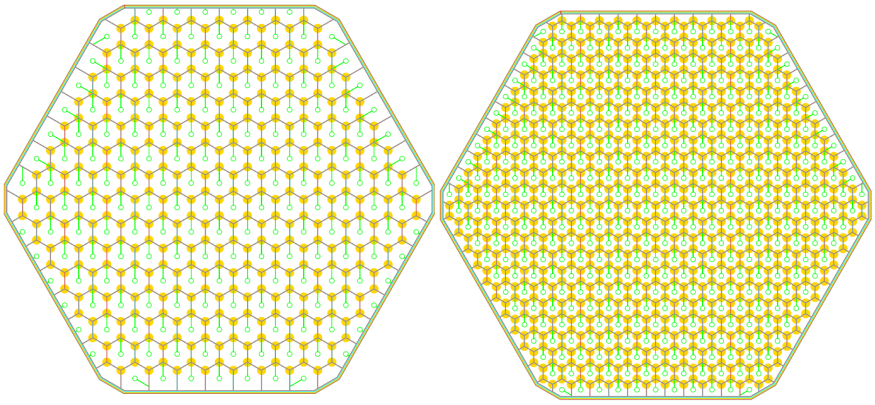

Figure 3.10: Comparison of modules with two different cells' size, the 1.0 cm^2 active area is represented on the left and the 0.5 cm^2 on the right [32].

ultimate detector operation. A schematic representation of the subdivision of a silicon module into its readout units is shown in the left part of Figure 3.10.

The number of layers and the depth of the electromagnetic compartment of the HGCAL has to allow the detection of the full showers, meaning that their energy deposit should be entirely contained in the in it. The design take into account the conclusion of the simulation represented in Figure 3.11. The conclusion of this simulated study validates the design of the width of a module and the depth of the electromagnetic compartment.

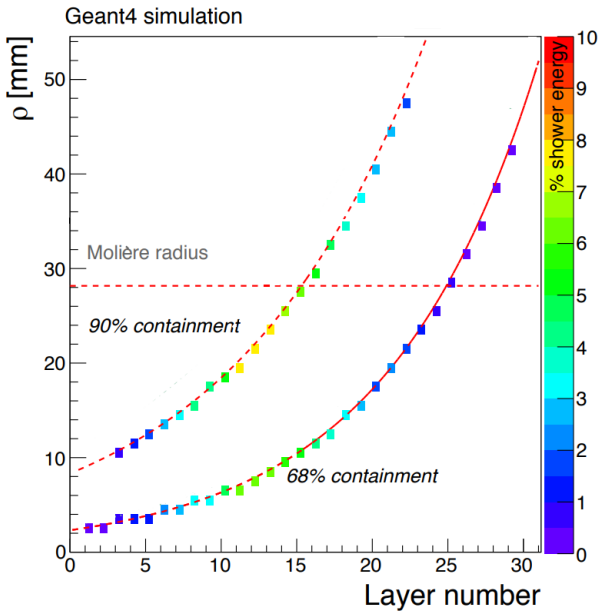

Figure 3.11: Electromagnetic shower containment, expressed as the radii ρ of the cylinder containing 68% and 90% of the energy deposited in a single silicon layer. The colour corresponds to the proportion of the total shower energy detected in the layer [32]. The red dashed line represents the Molière radius.

3.3.2 Focus on HGCAL silicon sensors

The choice of silicon as an active material was led by its semiconducting properties and is used as a sensitive material in many applications in the detection of particles. Although, semiconductors cannot be used alone for the detection of ionizing particles, indeed the addition of dopants is necessary. With the doping, PN junctions can be constructed to yield the equivalent to an ionization chamber, a device that is sensitive to traversing charged particles.

The passage of ionizing particles through the silicon creates pairs of electrons and holes in its bulk that are subsequently collected by an electric field. The energy measurement is based on the collected charge carriers, which cause a detectable signal at the electrodes. In general, the required energy of around 3.6 eV for creating the charge carriers in silicon is relatively low, resulting in good energy resolutions. Figure 3.12 illustrates the main idea of using silicon for particle detection. In the case of HGCAL, silicon is particularly preferred over other sensitive materials as it allows for a compact calorimeter design and provides fast signals. Furthermore, its robustness against radiation is acceptable.

The relevance of using silicon as an active material for particle detection in a calorimeter will be explained in this section. Firstly, by starting with the fundamental properties of semiconductors, then explaining the working principle of the PN junction diode and the energy measurement principle. Finally, the impact of radiation is briefly discussed. This discussion is kept to a minimum because the effects of radiation are not studied in this thesis. Nevertheless, it is necessary to know about them in order to understand some design choices of the HGCAL. The impact of radiation on silicon is caused by many non-trivial effects and is an area

of ongoing research.

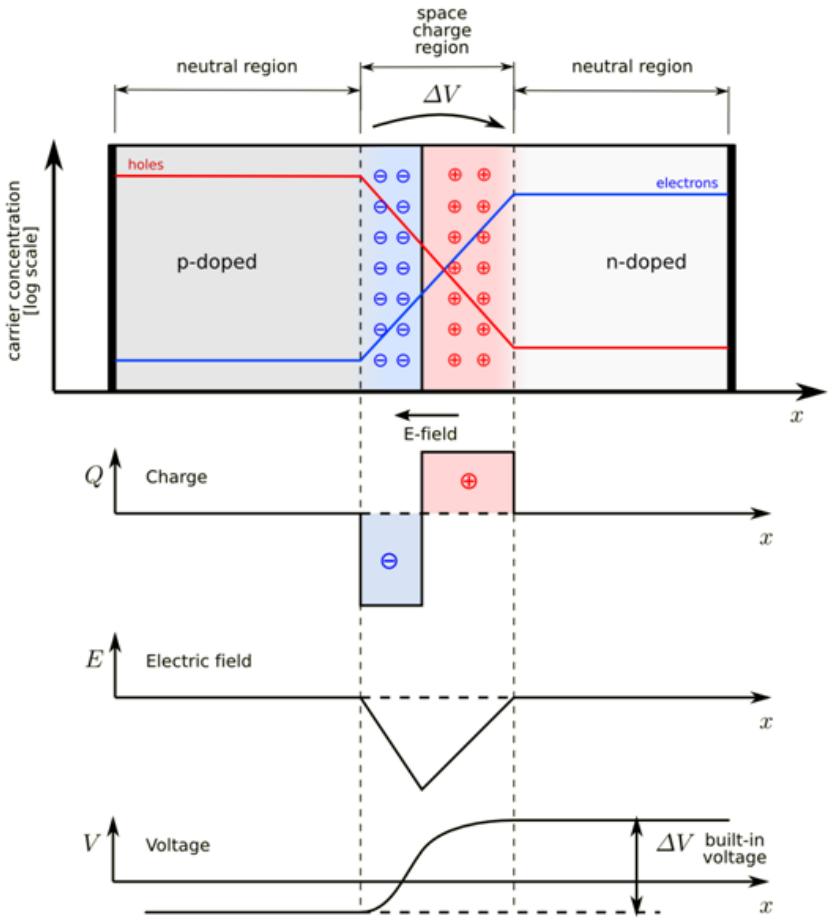

Figure 3.12: A PN junction where the electron concentration is reported with a blue lines, and hole one in red. The grey regions have a neutral charge. The pink zone is positively charged, while the light blue zone is negatively charged. Plots under the junction illustration stand for the evolution along the x axis of the charge density, the electric field and the voltage.

The silicon atoms in a solid state material form a crystal and are therefore arranged in a periodic lattice. Thus, the wave functions of the electrons overlap in such a way that band structures in the allowed energy spectrum are created. The electrons bound to the atom are in the valence band. The free and mobile electrons are in the conduction band. The gap between the two bands is called the band gap and is devoid of any free charge carriers, this band corresponds to a potential gap. While this energy gap is large for insulators and non-existent for conductors, it has an intermediate extent for semiconductors. In silicon, the energy gap between the insulating and conducting regime is approximately E_q = 1.21 eV. Thermal excitation of an electron in the valence band can transfer it to the conduction band, making the semiconductor slightly conductive. Not only electrons but also the absence of electrons, also called holes, in the lattice contribute to the conductivity of the semiconductor. At thermal equilibrium, the conductivity of the semiconductor generally depends on the temperature and the mobility of

the electrons or holes. Pure semiconductors are said to be intrinsic. Only one atom in 10^{12} is usually ionized, and the conductivity is minor. In the case of silicon, it is usually improved by adding impurities to the material. In the case of the sensors used, phosphorus atoms have been added to the silicon lattice to create additional levels in the energy band near the conduction band. This results in an excess of free moving electrons, and the doped silicon is characterized as n-type. Similarly, an excess of holes can be caused by adding levels in the band gap close to the valence band with the addition of boron atoms, which then attracts free electrons and the doping is p-type.

The equivalent to an ionization chamber is created when n and p-type doped silicon volumes are connected to form a PN junction diode. Then, the freely moving electrons from the n-type region are attracted to the p-type region and vice versa for the holes. The region where this happens is called the depletion zone because it is depleted from freely moving charge carriers. Since the volume is initially neutral, this movement results in a distribution of charge densities in the depletion zone. The may be applied to infer the corresponding electric potential $V(x)$ and with it the field strength in this zone. The difference in the electric potential on either side is called the contact potential and amounts to $\mathcal{O}$(1 V) in typical applications with silicon.

$$\frac{d^2V(x)}{dx^2} = -\frac{\rho(x)}{\epsilon_0} \tag{3.11}$$

An illustration of the distribution of charge carriers is shown in Figure 3.12. Using this simplified model, the potential difference ΔV may be related to the capacitance of the junction. The contact potential as well as an externally applied bias voltage contribute to ΔV. Besides the already introduced quantities, A is the junction's cross-section area and r is a junction constant that depends on the concentration of the doping materials and the mobility of the electrons and holes.

The choice of silicon as the active material for the modules is driven by the constraints imposed by the expected physics performance and the environment in which the detector will operate. More precisely, silicon sensors ensure the detection of both minimum ionizing particles (MIP) and the precision measurement of high energetic showers. The former is a key requirement for the operational performance of the HGCAL, as MIP are intended to be used for in situ calibrations of the detector. The latter can be ensured only with full containment of the showers, for which the compactness of the detector, achieved with thin silicon modules and a proper mixture of absorbers, is fundamental to keep under control the Molière radius of the calorimeter.

Silicon sensors meet these requirements and have the advantage of producing fast signals $\mathcal{O}$(10 ns), fundamental to keep up with the 40 MHz rates expected in the busy environment of the HL-LHC. In addition, silicon modules can be produced in a relatively short time scale, profiting from the long standing industrial efforts in the field.

As illustrated in Figure 3.13, each module is made of a stacked structure comprising the printed circuit board (PCB), where the front-end electronics are installed, the silicon sensor, a gold plated Kapton sheet providing high voltage

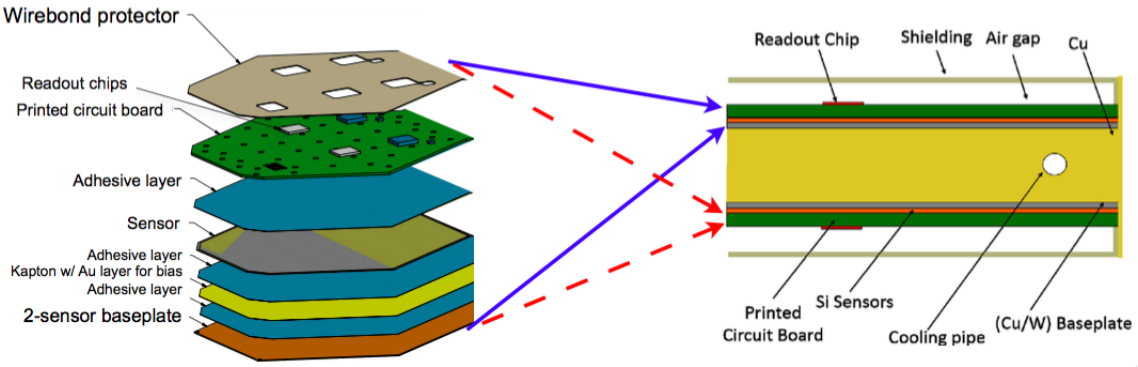

Figure 3.13: Composition of a silicon module and their placement in the copper plate. Each module is a stack of different layers, starting with a baseplate at the bottom, covered with a gold plated Kapton foil on which stands the silicon sensor. A protected PCB with read-out chip is placed on top [32].

connection to the sensor and electrical insulation from the baseplate, made of materials such as CuW or Cu in order to ensure enough rigidity to support the module, whilst minimizing the total radiation length and dissipating the heat via a dedicated cooling system. A schematic view of the structure of a typical HGCAL module is given on the left side of Figure 3.13 and the disposition of the modules on the two faces of the copper plates.

One of the most challenging aspects in the design of this module is the front-end electronics [138]. The readout ASICs foreseen for the final design have to operate over a wide dynamic range starting from 0.2 fC to 10 pC, featuring low noise levels and reduced power consumption, and they should be capable of transmitting the high granularity information of the HGCAL to the L1 trigger. The silicon sensors will require a bias voltage of $\mathcal{O}$(200 V) that is expected to steadily grow up to 800 V to cope with their ageing in the HL-LHC operations. In addition, in order to fully exploit the HGCAL as an imaging calorimeter, the ASIC needs to have an intrinsic single channel resolution of the order of 40 ps for signals above 50 fC, thus achieving an ultimate timing resolution of $\mathcal{O}$(10 ps). These requirements have to be met all together with the additional constraint of the reduced space available for the integration of the ASIC into the active layers, resulting in a HGCAL specific front-end readout electronics. Hence, the Omega Microelectronic Center in École Polytechnique was chosen by the CMS collaboration to design and develop the HGCROC. The ultimate design of the HGCROC is not finalized yet for production, therefore prototypes with preliminary functionalities have been developed for the beam test campaigns. As detailed later in this section, the Skiroc2-CMS ASIC [139] was used for the October 2018 test beam, which was part of the work performed in the context of this thesis. This read-out chip is based on the Skiroc2 design previously proposed for the electromagnetic calorimeter of the International Linear Collider (ILC) [140].

3.4 HGCAL prototypes and test beams

During October 2018, some tests with energetic electrons were performed at CERN's North Area, where fixed target experiments and prototype tests are supplied with primary proton delivered by the SPS and accelerated up to a 450 GeV/c momentum. The PPE172 area at the H2 beam line [141] was the main facility for testing the HGCAL prototype. Besides, the test treated in this thesis corresponds to the largest test of a full scale HGCAL prototype calorimeter equipped with more than 90 prototype modules.

The analyses composing the core of the Chapter 4 were performed with the data collected during October 2018 at the H2 beam line in the EHN1 experimental hall of the CERN-SPS North Area. Full details of the beam line may be found in [36].

3.4.1 Silicon module prototype

The main component of the HGCAL prototype is the hexagonal module hosting the active material. The most important part of it is the silicon layer with a 6" diameter and a 300 μm thickness. It is divided into 135 sensors, in the following they are also called cells or channels. A single channel has a surface of approximatively 1 cm^2. But only 128 of them are read-out, and they are divided into four groups of 32. Each group of channel is read by an ASIC called Skiroc2-CMS and in Figure 3.14 they are noted IC3, IC4, IC5, and IC6. The clock path is represented by a red line starting from the IC1 chip and circulating on the board to connect the other chips.

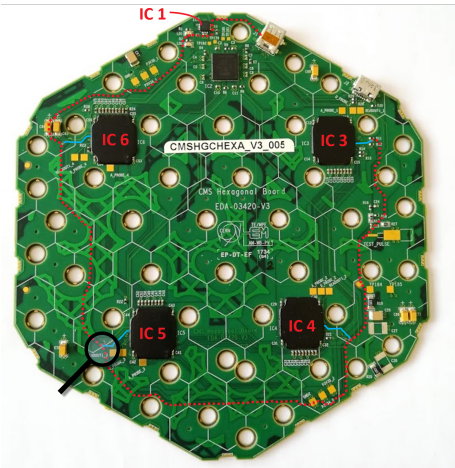

Figure 3.14: Prototype HGCAL hexaboard, based on a silicon sensor module covered with PCB and electronic readout chips.

Each channel connected to an ASIC has low and high gain shapers, and time over threshold (ToT) and time of arrival (ToA) circuits. The shapers have analogue to digital converters (ADC) allowing to sample the pulse shape every 25 ns, time corresponding to a clock period. Then, the information is saved in a 13 switched capacitor array (SCA) rolling array memory.

The general layout of the prototype hexaboard follows the same scheme as described in Figure 3.13. These modules are used for the electromagnetic compartment as well as for the hadronic one.

3.4.2 Assembly of the detector prototype and test beams

The beam generation at the CERN's North Area starts with protons from the Super Proton Synchrotron (SPS). The protons circulating in it can be either injected into the LHC or delivered to the SPS' experiments. Most of the time, the SPS beam is ejected towards the North Area targets T2, T4 and T6. Depending on the SPS cycle, spills occur roughly once or twice per minute, they last approximately 5 s and contain $\mathcal{O}(10^{13})$ protons each. At the three targets, a broad spectrum of secondary particles is created when they are exposed to the proton beam. The beam lines work as magnetic spectrometers that provide specific particle beams with some parameters which can be changed such as: the particle type, the polarity, and the momentum with an uncertainty under 2% [142].

The beam lines H2 is used on the T2 target made of beryllium. This material was chosen for its high melting point and for having a X_0 similar to its λ_n per thickness unit. The high similarity between its two parameters guarantees the fact that the production of electrons and hadrons due to incident protons occurs at a comparable rate. In terms of interactions at the root of the particle production, the hadrons are originating from nuclear interactions of the incident proton with beryllium nuclei, while the electrons are produced by photon conversion into a e^+e^- pair. The photons are coming from the decay of π^0. Hence, the production rates for both hadrons and electrons is a function of the thickness of the beryllium target. In the case of the HGCAL prototype tests in October 2018, a 500 mm thick target has been used in order to ensure a good equilibrium between the hadrons and electrons produced in the secondary beam.

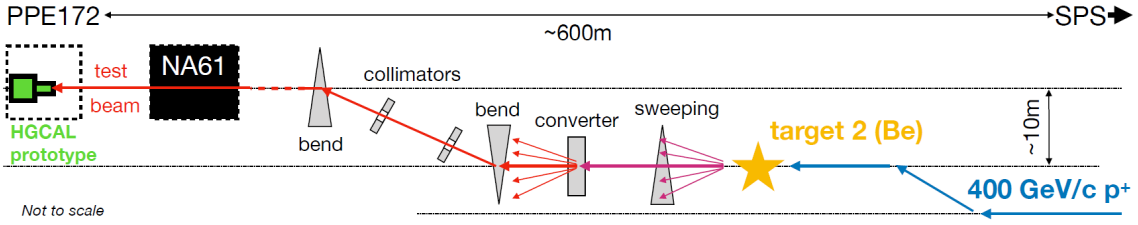

Figure 3.15: Schematic of the H2 beam line. The length of the beam line from the SPS to the test area PPE172 is ∼600 m. It comprises the T2 target made of beryllium, collimators, dipole, and quadrupole magnets whose operating parameters can be modified depending on the beam requirements. The NA61 experiment is located in front of PPE172 and adds some amount of passive material to the beam line.

The hadron beams undergo further purification by inserting in the beam line an additional converter material with a high ratio of X_0/λ_n, such as lead. In this way, the electrons lose a significant amount of momentum and are pushed away from the beam line, while the hadrons pass through this material with a

weak interaction.The electron beam purification that was used in October 2018 is sketched in Figure 3.15.

Behind the T2 target, a magnet is used to bend the trajectories of all charged secondary particles away from the beam path and allow only neutral particles to pass, as explained above.

Next, a converter causes the neutral particle to cascade into e^+e^- pairs. This is followed by sets of dipole magnets and collimators that allow selection of the transverse momentum. Due to the curvature of the magnetic field, the energy loss of synchrotron P-radiation is not negligible for high momentum electrons, while it is practically unimportant for hadrons. The scaling law of P is given by the following equation:

$$P \propto \frac{p^2 B^2}{m^4} \tag{3.12}$$

Where p is the particle momentum, m the mass, and B the perpendicular field strength in which the particle is travelling.

The synchrotron losses have two effects: first, the electron beams can be further purified by tuning the magnet currents to the expected electron energy losses. In this case, the hadrons' momentum would be out of the acceptance requirement of the beam line. Secondly, the configured electron momentum no longer matches that of the incident electrons in the test area. This leads to the loss of energy linearity with the prototype calorimeter. The effect of synchrotron radiation losses is responsible for additional beam momentum dispersion and lower than nominal beam energy values. The final positron beam moments at the entrance to the experimental zone, together with the corresponding spread, are given in the table 3.2.

Table 3.2: Summary table of beam momenta for positron beams provided by the H2 beam line and used during the HGCAL test beam of October 2018. Nominal momenta were measured by the beam operators, then the real values of beam momenta has been measured by a spectrometer placed between the last dipole and the HGCAL prototype. Values are taken from [36].

Nominal beam momentum (GeV/c)	Real beam momentum (GeV/c)	Momentum spread (GeV/c)	Momentum resolution (%)
20	20.00	0.06	0.3
30	30.00	0.08	0.3
50	49.97	0.12	0.3
80	79.81	0.19	0.2
100	99.81	0.22	0.2
120	119.64	0.28	0.2
150	149.16	0.35	0.2
200	197.40	0.47	0.2
250	243.84	0.60	0.2
300	287.65	0.79	0.3

To specify the beam particle momentum and type, most of the magnet and collimator settings along the beam line can be changed. In addition, this allows the transverse beam size to be adjusted and, to some extent, particle rates to be controlled. However, the NA61 experiment [143] is located opposite the PPE172 area, which added a few percent of a radiation length of passive material in the beam line that could not be removed during the HGCAL beam tests. Preliminary simulation studies of the beam transport in the H2 line indicate a systematic shift of the order of 0.5% on the average beam momentum when the relevant parts of NA61 are taken into account.

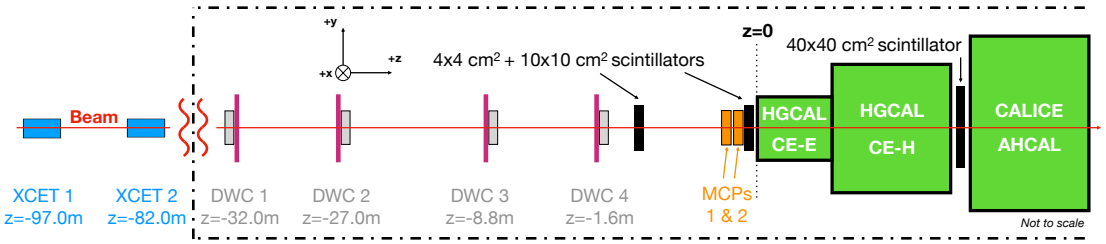

Figure 3.16: The HGCAL prototype experimental setup used during the 2018 test beam. The electromagnetic section that is the subject of this analysis is denoted as CE-E. It is preceded (to the left) by multiple ancillary beam instrumentation detectors, and is followed by detector prototypes dedicated to the study of hadron showers.

The HGCAL prototype calorimeter consists of two compartments, referred to as EE, representing the electromagnetic, and referred to as FH, mimicking the silicon based hadronic parts of the final calorimeter design. A common right-handed coordinate system is defined such that the z dimension coincides with the beam direction and the y axis points away from the hall floor.

The HGCAL prototype, represented in Figure 3.17, was assembled for the 2018 test beam comprises a fully instrumented electromagnetic compartment (CE-E) made of 28 layers, which are each composed of a single hexagonal module. The hadronic part (CE-H) contains 66 modules arranged into twelve layers. The first nine gather seven modules each, they are organized around a central module surrounded by six others, and this gives at the end a six petals' flower structure. Concerning the last three CE-H layers, they are made of a single module. Then, there is the CALICE AHCAL which aims to reproduce the scintillator tiles with SiPM readout. The CE-E prototype has had a total length of $\sim$27.2 X_0 and $\sim$1.3 λ_n to which the CE-H prototype and the AHCAL added 3.5 λ_n and 4 λ_n, respectively, thus reflecting the ultimate design of the HGCAL. A schematic representation of the experimental setup is shown in Figure 3.16 with the correspondence of most of the elements described previously.

The electromagnetic and the hadronic compartments are equipped with 6" silicon modules. All the modules were equipped with four Skiroc2-CMS ASIC [139], developed specifically for the HGCAL project, and they are designed to deliver a high and low gain amplification. They provide a supplementary measurement of

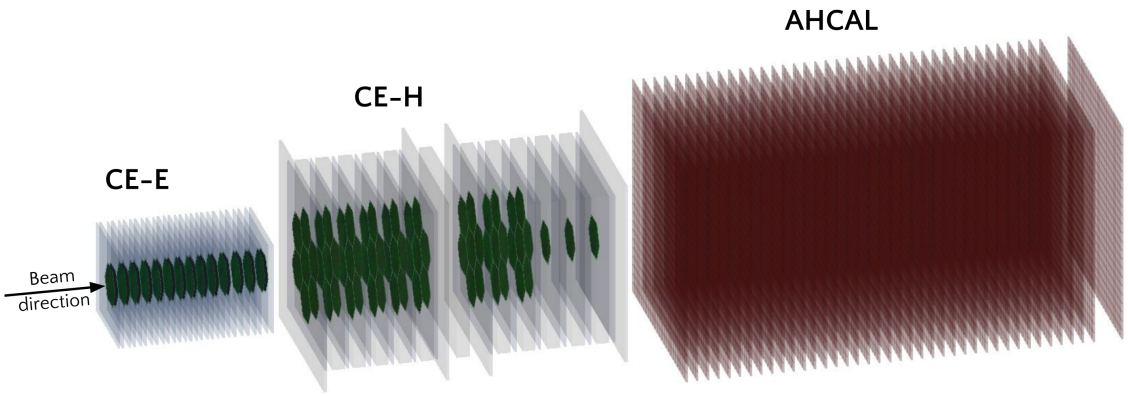

Figure 3.17: The HGCAL prototype during the 2018 test beam. The electromagnetic section is denoted as CE-E, it is followed by the hadronic part composed of silicon sensors in CE-H and AHCAL scintillating tiles.

the time over threshold (ToT) used for final reconstruction of the pulse shape when the channel is in a saturation regime. After a pre-amplification stage, the pulse shape is sampled with a frequency of 40 MHz, given by the system clock, and stored to a 13 channels Switch Capacitor Array (SCA). Finally, the Skiroc2-CMS ASIC provides a measurement of the pulse time of arrival (ToA), used for the assessment of the timing performance of the HGCAL prototype.

3.4.3 Signal reconstruction

The Skiroc2-CMS ASIC features 64 channels connected to the silicon sensors' hexagonal cells and to non-hexagonal cells at the boundaries of the sensors. During the October 2018 test beam, half of the channel were unconnected to facilitate the routing of the channels of such a complex board. The simplified schematic diagram of a Skiroc2-CMS ASIC is similar to the one for HGCROC in Figure 3.18 which was designed initially.

The reconstruction of the HGCAL prototype data consists of converting the raw data extracted from the ASIC, hereafter referred to as calorimetric hits, including the energy E_i and the time t_i of deposition in a given cell, as well as its Cartesian location (x_i, y_i, z_i). The pedestals are determined for each SCA and subtracted. A subsequent common mode noise reduction is performed for each ASIC. Further details on these two steps of the reconstruction workflow are provided in [144]. After the background and common mode noise subtractions, the raw time-ordered SCA values are used to reconstruct the pulse shapes and extract the amplitudes in the low and high gain regimes. The pulse shape data are fitted as a function of time, starting from the analytical expression of a bipolar waveform, with some additional modifications:

$$S(t) = \begin{cases} A_0 \left[\left(\frac{t-t_0}{\tau} \right)^2 - \frac{1}{n+1} \left(\frac{t-t_0}{\tau} \right)^{n+1} \right] e^{-\alpha(t-t_0)/\tau} & \text{if} \quad t > t_0 \\ 0 & \text{if} \quad t \leqslant t_0 \end{cases} \tag{3.13}$$

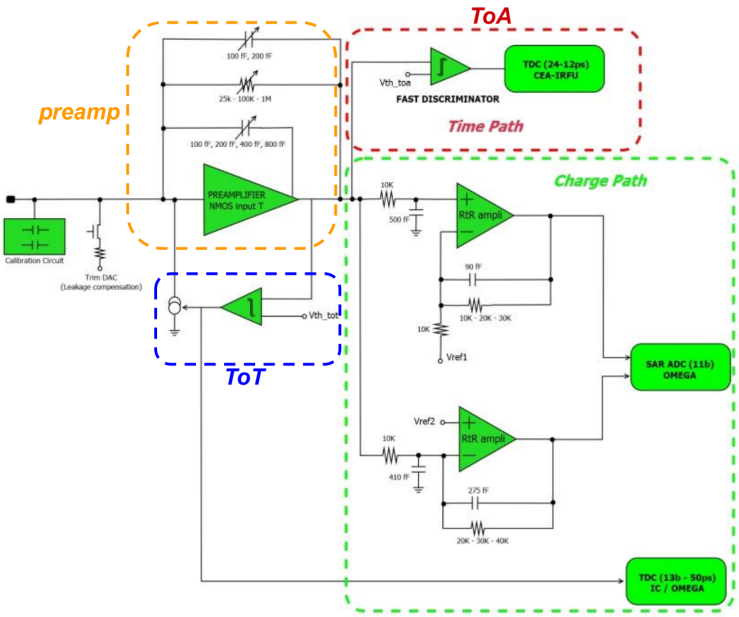

Figure 3.18: Simplified block diagram of HGCROC chip [32]. The preamplifier block is circled in orange, the section computing the ToA is circled in red, and the part responsible for the ToT in blue. In green, there is the entire block in charge of the hit energy calculation.

Where A_0 is the pulse shape amplitude in either the low or high gain regimes, and it is expected to be directly proportional to the charge deposited in the silicon sensors, t_0 is the starting time of the pulse shape, and τ is the time constant of the shapers. The parameter n is left free in the optimization of the fitting function, and an additional parameter α is introduced to properly take into account the Skiroc2-CMS pulse shape. The optimization of the analytical expression of Equation 3.13 was performed in the context of the commissioning of the prototype silicon module in [145].

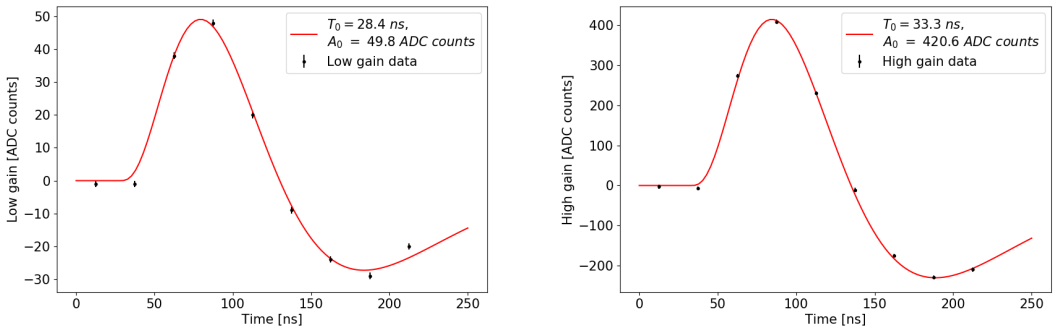

Figure 3.19: Two example waveforms for low gain on the left, and high gain on the right. Both due to a signal of about 10 MIP from a 280 GeV/c electromagnetic shower [34]. The fits are shown with the red lines.

Figure 3.19 illustrates the fit done on the pulse shape coming from one readout

channel. Signals from events are selected to which pulses with considerable amplitude could be fitted. The corresponding time samples are normalized by the reconstructed amplitude A_0 and by the start time t_0 in each event. All fixed parameters therein have previously been optimized by the HGCAL beam test group to yield an almost uniform distribution in t_0, that is consistent with the asynchronous beam with respect to the clock, and to result in a smooth continuity in the hit energy spectrum when the high gain saturates. It reveals that further optimizations of the default settings might be possible because it describes the average undershoot and signal peak better than the default model in this example.

The ASIC operates in the linear region of the gain shapers or of the ToT when both the gains are saturated to ensure a direct proportionality between the reconstructed amplitude A_0 and the collected charge. Figure 3.20 shows an example of high and low gain with the ToT curve for a specific Skiroc2-CMS ASIC channel. Two different slopes are derived for the linear regions for the high gain compared to the low one, and the low gain versus the ToT regime. They are used to retrieve the gain calibrated signal of each cell. More precisely, the reconstruction procedure selects either one of the non-saturated gains or the ToT and converts it to the high gain equivalent A_{HG} according to the following relation:

$$A'_{HG} = \begin{cases} A_{ToT} \times m_{LG/ToT} \times m_{HG/LG} & \text{if} \quad A_{LG} > TP_{LG} \\ A_{LG} \times m_{HG/LG} & \text{if} \quad A_{HG} > TP_{HG} \quad \text{and} \quad A_{LG} < TP_{LG} \\ A_{HG} & \text{if} \quad A_{HG} < TP_{HG} \end{cases} \tag{3.14}$$

Where the $m_{LG/ToT}$ and $m_{HG/LG}$ coefficients are calibration constants determined in the linear region of the low gain versus the ToT, and respectively the high gain versus the low one. The parameters TP_{HG} and TP_{LG} are the values of the transition points between the linear and saturated regimes for the high gain (HG) and low gain (LG), respectively.

The final step of the calorimeter hits reconstruction consists in converting the pulse shape amplitude into the corresponding energy deposit in the active sensors in MIP units. The conversion factor $M^{-1}_{HG/MIP}$ involved in this step corresponds to the MPV of the Landau convoluted to a Gaussian function used to fit the high gain signal distribution. Eventually, the reconstructed energy deposit associated to each hit can be written as:

$$E_{MIP} = A'_{HG} \times M^{-1}_{HG/MIP} \tag{3.15}$$

Most of the sensors involved in the 2018 test beam had an active thickness of 300 μm in which the MIP energy deposit is expected to be 86 keV, but a few module 200 μm modules were installed in some layers and where the expected MIP energy is 57 keV.

During the test beam, data coming from the Skiroc2-CMS was stored inside EUDAQ format files. Then in blue are the different transformation steps which take into account the external information from configuration files. Similarly, information from the beam characterizing detectors is reconstructed and synchronized. Ultimately, the ntuple provides all necessary inputs to the calibration and

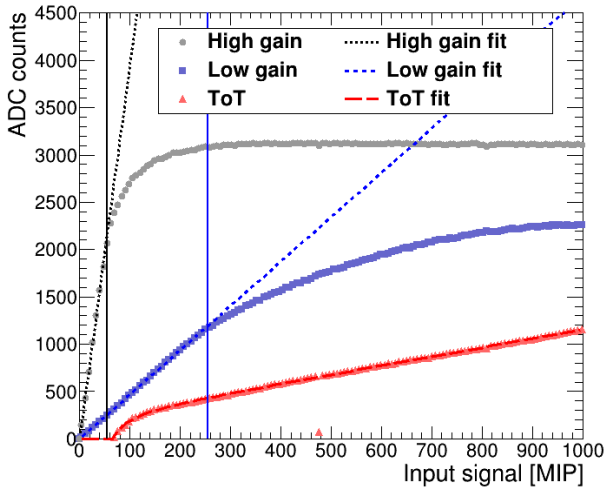

Figure 3.20: High and low gain amplitudes represented with the ToT as a function of the input signal, expressed in MIP (∼3 fC) [34]. The vertical lines stand for the maximum input signals, where the high-gain and low-gain shaper outputs were linear.

analysis of the beam test data. Reconstructed ntuples are used in order to assess the HGCAL prototype's performance with test beam data.

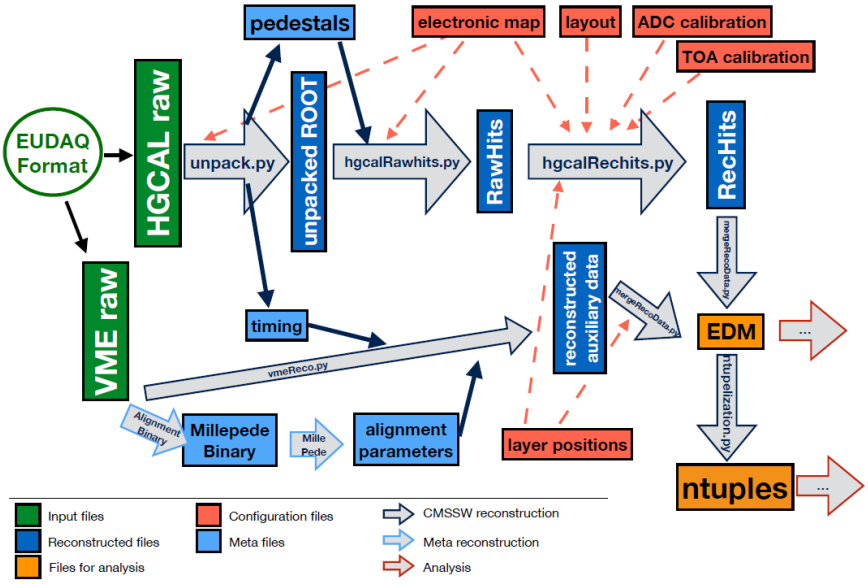

Figure 3.21: Event reconstruction procedure of the HGCAL prototype data. Raw data are given by the EUDAQ input file are coloured in green. This data is merged with reconstructed information from beam characterizing detectors. Reconstructed data are stored in the EDM file format for analysis with CMSSW, or as ntuples.

A series of reconstruction algorithms, bundled into certain steps, are applied. Figure 3.21 illustrates an example progression of these steps that are executed sequentially for the joint reconstruction of HGCAL prototype data in combination

with data from the delay wire chambers.

Each arrow represents a step in the sequence leading to the final file. The code is compiled into either executables or libraries, which in turn are executed directly or interfaced via additional driver files. The algorithms are discussed in detail later in this chapter. It should be noted here that the steps are not self-contained, as they require the presence of the output of their predecessors in the sequence. In addition, other files such as configuration-dependent calibrations, geometry definitions or electronic mappings have to be introduced into the workflow at different stages.

3.4.4 Timing information from the prototype

Since the main study performed during this thesis work was about the timing performance, a highlight on the timing information reconstruction is given in this section. First, the Skiroc2-CMS readout chip is responsible for the ToA computation. Then, the impact of the clock distribution in a module has to be taken into account, as well as the timing reference given by the MPC placed before the prototype.

Time of Arrival in the Skiroc2-CMS readout chip

In order to evaluate the timing performance of an HGCAL prototype in beam tests, the Skiroc2-CMS is equipped with a ToA circuitry for timing measurements of the signals. The principal components of the ToA circuit are shown in Figure 3.22, where a fast shaper is followed by a fast discriminator which starts a voltage ramp, originating that is sampled at the rising and falling edge of the main 40 MHz clock.

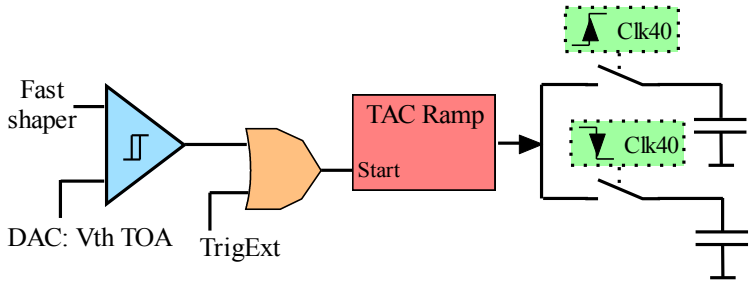

Figure 3.22: Diagram of the ToA computation blocks in the Skiroc2-CMS ASIC [35].

The shaping time of the shaper can be configured by slow control, and was chosen to be 5 ns for the test beam configuration. This allowed for an optimal noise and timing performance, especially because HGCAL is expected to do fast timing. The discriminator threshold is defined by a voltage DAC, which is set by slow control configuration. In order to give unbiased information, an external trigger was selected, and it gives a signal which can be fed into the Time-to-Amplitude Converter (TAC) for calibration purposes. The principle of the TAC used by the ToA is shown in Figure 3.23. On the rising edge of the trigger signal from the ToA

discriminator, an analogue voltage ramp is launched (for the hit channel). The ramp can run until 35 ns, and it is sampled on the second and third clock edge (respectively to the type of ToA measurement). The values of the ramp voltage are stored in the SCA of the Skiroc2-CMS it is linked to the clock edge type: falling or rising.

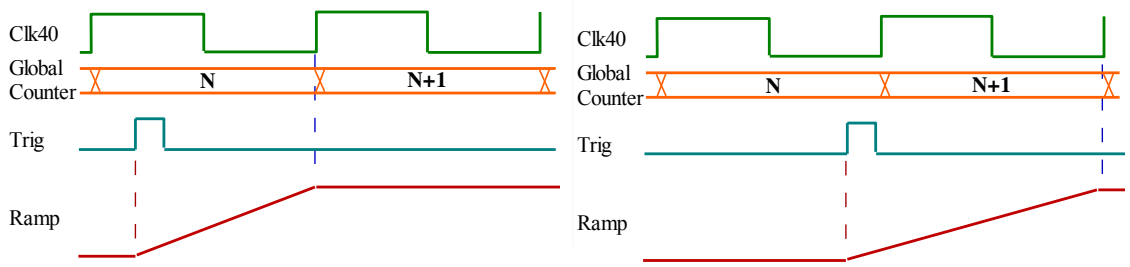

Figure 3.23: Illustration of the ToA ramp operation in the Skiroc2-CMS for two different cases: a ToA trigger signal after the rising clock edge and before the falling clock edge on the left, and vice versa on the right [35].

This way, the effective time measured by the TAC ranges from 12.5 ns to 37.5 ns. The SCA values are digitized with the same 12-bit Wilkinson ADC responsible for the digitization of the gain and ToT values. The binning of the TAC corresponds to approximately 20 ps, with the jitter being 50 ps. It is good to notice that in order to achieve a finer binning the default ToA configuration (TAC parameters defined by external voltage references) leads to a non-linear behaviour of the ToA: the first $\sim$10 ns were linear with $\sim$12.5 ps binning, after which the TAC ramp saturated.

The ToA values stored in the SCA of all channels are reset after 13 clock cycles following the first ToA hit in the chip (the OR of all 64 channels). This resets as well the ToT values of all channels in the chip. This prevents the interference of earlier hits from a previous particle or noise.

Clock distribution

The clock is distributed from a master synch-board (SB) through slave SB and read-out boards to the hexaboards. The jitter from the clock distribution is estimated to be below 7 ps. Differences in the delay of the clock between different chips are mainly due to the clock routing inside the hexaboard. This delay corresponds to a phase offset between the chips.

The left plot of Figure 3.24, shows the routing of the clock within a single hexaboard PCB. The clock trace runs from the clock buffer around the PCB and provides the clock signal to the chips sequentially. Since the trace lengths are considerable and the propagation delay is about 70 ps/cm, the phase offset between the chips becomes significant. The distances and estimates of the corresponding time delays are given in Table 3.3 represents these differences:

In the case of the clock delay correction performed, the time difference between chips is computed with IC6 as reference. The largest distance, corresponding to the one between the first and last chips to get the clock, is about 23.6 cm, representing a time difference of more than 1.6 ns.

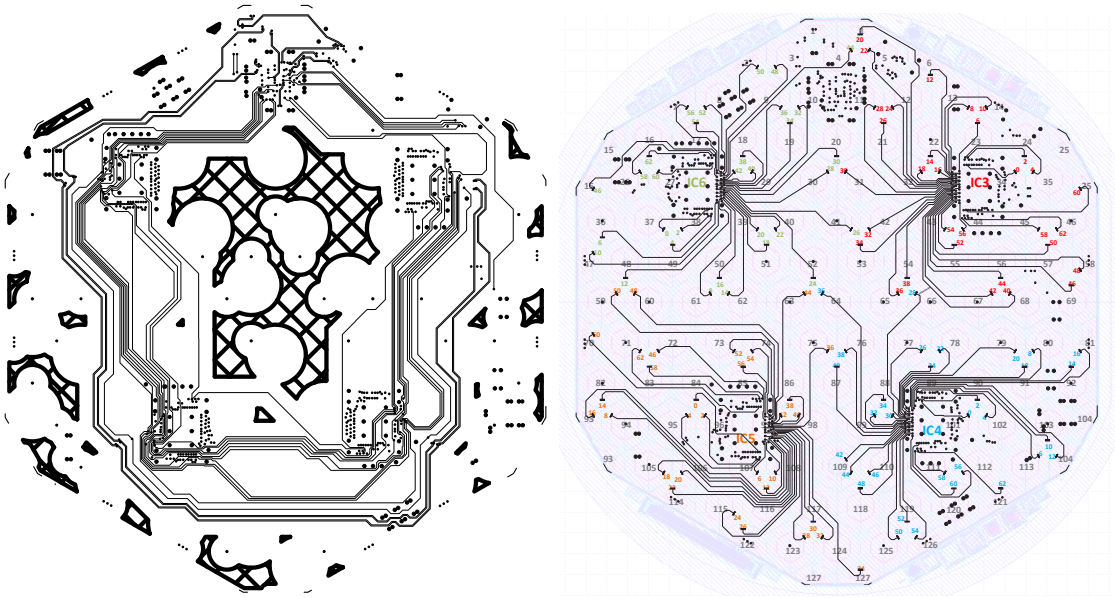

Figure 3.24: The routing of the 40 MHz clock on the hexaboard PCB is illustrated on the left. The clock is routed sequentially through the chips, starting from the clock buffer at the top of the image. The mapping of the traces connecting the silicon bonding pads and the read-out chip inputs on the right.

Table 3.3: Clock trace lengths on 6" hexaboard PCB with the absolute distance measured until the clock buffer. Moreover, the time difference is relative to the distance between the chip and IC6.

ASIC	Clock trace length [mm]	Distance to IC6 [mm]	Time difference [ns]
IC6	86	0	0
IC5	154	68	0.476
IC4	256	170	1.19
IC3	322	236	1.652

Another contribution that has to be taken into account is the difference in the lengths of the traces connecting the silicon wire-bond pads and the chip inputs. The right plot of Figure 3.24 shows the routing of the traces from the ROC inputs. The lengths of the traces vary from 0.5 cm up to 4 cm within individual chips, resulting also in different real arrival times of the signals in the read-out chips.

Time reference reconstruction

The microchannel plates (MCP) devices are well known in literature for their superior time response to single relativistic particles [146]. Prior to the test beam campaign, the MCP has been tested to characterize their time response to the ionizing component of electromagnetic showers.

One of the MCP detectors (MCP 1) was used as a timing reference, while the second was used as a cross-calibration, to obtain the timing resolution as a function

of the signal amplitude, shown in 3.25. The average resolution for an electron crossing MCP 1 was found to be about 25 ps.

Both MCP are operated in the standard PMT-MCP mode, they are exploited as precision timing detectors and their measurements are considered as timing reference for the HGCAL prototype. The MCP photomultipliers were mounted in a light tight box, with the optical window towards the beam and orthogonal to the beam direction. A logic signal, synchronous with the beam gate and the synch-board clock, was used to trigger waveform digitization of the anode signals, over 200 ns, into a 12 bit switched capacitor digitizer.

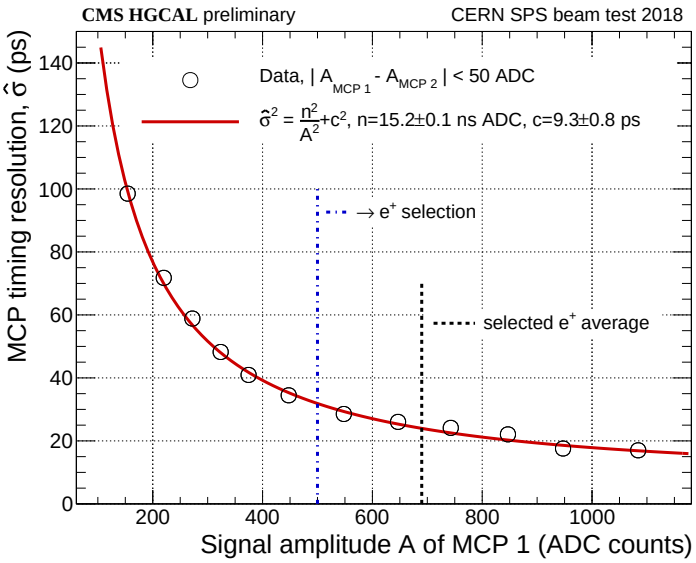

Figure 3.25: Single MCP time resolution estimated as $\sigma/\sqrt{2}$, where σ comes from a Gaussian fit to the distribution of time differences between the two MCPs operated in front of the HGC prototype calorimeter. Given their identical structure, the timing resolution of the two MCP detectors was assumed identical.

The MCP waveforms were analysed using the same technique developed for [146]. The typical MCP waveform has a rise time of 1 ns, and a total amplitude of 5 ns. The time of the MCP signal is extracted from a linear interpolation of the rising edge, evaluated at 50% of the maximum amplitude, in order to provide good performance on the timing resolution. The choice to use a constant fraction helps to minimize the time-walk effect. The maximum amplitude is measured from a parabolic interpolation of the 5 points at the maximum of the waveform, this allows to smooth the shape and provide a more solid estimate.

To use the time measured by the MCP as reference for the prototype modules, the MCP time offset has to be referred to the same zero that is used for the rest of the system. This is represented by the falling edge of the system clock. To improve the precision of the extracted clock reference time, each falling edge is fitted linearly over 4 digitized samples and the time is taken as the value at a fixed threshold of 3200 ADC counts.

The time correlation between the two MCP can be approximated by a linear function after adjusting the MCP time offset with respect to that of the system

clock. The time range covers the time range from 0 to 25 ns, accordingly with the asynchrony of the clock with respect to the beam.

3.4.5 Simulation of the test beam with Geant4

Geant4 [147] is a software framework used to simulate the propagation and interaction of particles passing with matter using the Monte Carlo method. It is the fourth main version of the GEANT software developed by CERN and its name is the acronym for *GEometry ANd Tracking*. Moreover, it is the mostly utilized toolkit for the simulation of particle showers. Hence, it is also the principal tool to simulate calorimeter data. In order to estimate the effects of particle showers in a given material, meaning that the exact geometry needs to be implemented. As well as, all the physics processes must be defined with their initial conditions, and the relevant output information must be computed.

The shower simulation itself proceeds sequentially in the sense that each particle including its interactions with the material is tracked individually. In this context, a track represents the current instant in the simulation and can be understood as a snapshot of a particle. A track is updated in a series of steps. The steps are governed by the involved interaction processes. They occur both along the step, after the step and before the step, the latter only if the associated particle is at rest. Effectively, interactions change the dynamic physics quantities assigned to the track, they may generate secondary tracks from secondary particles, or they may stop the progressing of the track by particle decay or absorption. Inside a volume defined as sensitive, the steps are accessible to obtain various delta information. Among other things, those include information on the energy loss of the associated particle in that volume. Lost energies, in turn, could be used to compute sums of deposited energies in the sensitive volumes, it corresponds to simulated hits.

The Geant4 framework gathers a wide variety of physics processes [148]. The implemented processes can be categorized into different groups, such as the interactions with matter, particle decays, transportations as well as parameterized models. In order to take into account all these processes and to include them properly into a simulation, Geant4 follows an atomistic approach, in which it is possible to select the desired processes for each involved shower particle individually.

Cascade models are optimized for energies in the range of a few MeV to a few GeV. In this energy range, the modelling scale is comparable to the distance between the nucleons, this means that the distance as well as the nucleon structure can be neglected. The interactions are then described through the projectile hadron and the target nucleons. The mean free path between the secondary particle interactions is calculated from the parameterized cross-sections and nucleon densities, which are modelled differently in the different cascade models.

In the Bertini cascade model, which is implemented in Geant4 [149], the nuclear potential is represented by several concentric density spheres. The nucleons contained in each sphere are treated as a Fermi gas, meaning that the nucleons can occupy all possible states of the system, but the Pauli exclusion principle must be taken into consideration because it imposes a minimum energy for the creation of

secondary particles. For each interaction in this model, calculations of the nucleon momentum, the type of reaction taking place and the momentum of the reaction products are performed. The model also includes de-excitation algorithms which take over when all cascade particles have either left the volume or been trapped in a nucleus.

The parton string models used in Geant4 [150] describe the interactions of high-energy hadrons with nuclei, where the energy exceeds 5 GeV. The scale of modelling in this case is rather small, and therefore the quark substructure of the projectile and target nucleons is taken into account. The nucleus is modelled as a collection of protons and neutrons. In a simulation using this model, each interaction is described as a collision between the hadron and a single nucleon. The type of interaction is predicted from the centre of mass energies, the hadron impact parameter and the diffractive and inelastic cross-sections. During the interaction, a chain between a quark of the projectile and a quark of the nucleon is formed, carrying energy and momentum. The string propagates and is excited by other nuclei. Then the excited strings are fragmented into quark and anti-quark pairs and so on as long as there is enough energy. At the end of this process, the remaining secondary particles propagate through the nucleus in a cascade pattern described above. The de-excitation of the nucleus is then simulated by nuclear fragmentation, pre-composition and nuclear de-excitation models.

The Geant4 model used for the HGCAL test beam simulation is based on the Fritiof (FTF) model. The FTF model considers only the momentum exchange between the projectile and the nucleon. This model is described with more details in [151].

In general, this atomistic approach allows adjusting the accuracy of the simulation and to avoid comparison between different simulation results. Geant4 also provides common physics lists with predefined interaction definitions and particle-specific parameters. The recommended physics list for high-energy particle physics experiments is FTFP_BERT. It incorporates a standard set of electromagnetic physics, the Bertini cascade for hadronic interactions below 5 GeV and the Fritiof model for hadronic interactions above 4 GeV. FTFP_BERT and one of its extensions which includes a CMS-specific tuning for electromagnetic interactions, called FTFP_BERT_EMN, and used in the analysis presented in chapter 4.

The HGCAL prototype is modelized with Geant4, and then during an event simulation, the software has direct access to the hits of all the particles in the active layers. The electronic noise in the silicon module is included in the simulation, as well as the non-uniformities in the response. Although, the DWC placed before the HGCAL prototype is not modelled as a sensitive detector. Therefore, an extrapolation of the beam gun position and its direction is done to reconstruct the DWC hits, and they are smeared according to the nominal DWC resolution of 500 μm in both x any y planes. The simulation of the detector is complemented with detailed modelling of the full H2 beam line and of all the detectors located before the prototype.

Chapter 4

Performance of the High Granularity Calorimeter prototype

Table of contents

4.1 Energy and spatial performance of EM shower detection 114
4.1.1 Information selection 114
4.1.2 Energy resolution 115
4.1.3 Spatial reconstruction characteristics 117
4.2 Energy and spatial performance of hadronic shower detection . . . 120
4.2.1 Information selection 121
4.2.2 Energy resolution 122
4.2.3 Spatial reconstruction characteristics 123
4.3 Timing performance 125
4.3.1 Reconstruction of the timing information and selection . . . 125
4.3.2 Impact of the geometry on the timing performance 136
4.3.3 Single channel timing performance 139
4.3.4 Full shower performance 144
4.4 Conclusion on the HGCAL prototype performance 151

The first goal of this thesis is to study the performance of the HGCAL prototype tested in October 2018 at CERN's SPS. A set of preliminary studies was performed to have a first overview on the energy related characteristics of the prototype, such as the linearity relation between the particle energy and the detected one, and the energy resolution. Moreover, spatial energy distributions were used to compute the depth of the maximum of the shower and the containment radius. This work was done firstly for electromagnetic showers generated from positron beams, presented in Section 4.1, and secondly for hadronic showers originating from pions, described in Section 4.2. Since my results were just preliminary and were done just at the beginning of the study campaign of data collected during the test beam, other people continued to work on it and studied the same parameters with better calibrations. The results presented in both sections mentioned above are taken from [36] and [37] respectively, and their inclusion is motivated by the will

to stay coherent with the channel energy calibration used, since all the presented HGCAL test beam studies are using the same. Last but not least, the main HGCAL study made in the context of this thesis consists in the determination of the timing performance of the prototype. It is an original work, detailed in Section 4.3, and which is also presented in an article still in a journal reviewing process.

4.1 Energy and spatial performance of EM shower detection

Data and simulation described in Chapter 3 are used to carry out the characterization and performance of the electromagnetic showers within the prototype. But, before describing this, a selection of the information must be applied to get a good compromise between the purity and the amount of statistic of positron induced events.

4.1.1 Information selection

A first set of selection was used to keep positrons with high purity and hence a high quality dataset. At the beginning, the selection concerns the calorimeter hit level, and then it is applied at the event level. It is applied to data as well as simulation. Concerning the hits' selection, it is composed of two requirements:

1. Hits need to have their corresponding energy higher than 0.5 MIP. This threshold was selected to be above the typical noise, calculated to be $\sim$0.15 MIP. This noise level stands for the high gain chain in the CE-E section, and it was measured in the silicon module commissioning [145].

2. Hits need to come from valid channels. Indeed, 1.6% of channels are abnormally noisy, and for instance it is induced by a defective chip in the first layer. All the hits coming from these problematic channels are just discarded.

Since the hits are selected individually, the next step consists of the full selection happening at the event level. This final selection requires three criteria, which are defined as:

1. Events need to have a single track reconstructed in all the DWC installed just the calorimeter prototype. This requirement allows rejecting the events with a shower start happening upstream to the prototype.

2. Events need to have less than 50 selected hits in the hadronic section, or they are rejected. Similarly, events should have more than 95% of the measured energy in the electromagnetic compartment. This criterium efficiently removes events with shower coming from hadrons, in general protons and pions in the context of the test beam.

3. Events need to have an extrapolated track from DWC at the entrance of the CE-E compartment, contained in an acceptance window with a size of 2×2 cm^2. The position of the acceptance window was chosen to discard events with a shower axis distant from the module centre and where the shower maximum could happen in a region with a defective amplifier. Thus, this selection limits the lateral losses in case of impact far from the centre of the prototype, and the differences in beam profile between the data and the MC.

Now that the hits and events have been selected using the above criteria, it is finally possible to begin the performance study.

4.1.2 Energy resolution

In order to perform properly the analysis of the energy reconstruction capability of the HGCAL prototype, it is important to study the distribution of the event energy. All the individual hit energies coming from CE-E are summed per event and for a given positron beam energy. These distributions are realized for data as well as for the MC simulation, and are illustrated in Figure 4.1. The comparison between both shows that data are a bit lower due to a higher energy spread. To compensate for this effect, and mainly to improve the comparison, a 1.035 factor is applied to the data.

For each positron beam energy listed in Table 3.2, both data and MC distributions are fitted with a Gaussian function, where the formula is given in Equation 4.1:

$$f(x) = \frac{1}{\sigma\sqrt{2\pi}} e^{-\frac{1}{2}\left(\frac{x-\mu}{\sigma}\right)^2} \tag{4.1}$$

The fits are performed within the range $[\mu - \sigma, \mu + 2.5\sigma]$. As can be seen from the different distributions made with the data, the left side of these is very poorly fitted by a Gaussian. Hence, the choice of an asymmetric interval, which serves to avoid biasing the Gaussian parameters because of the residual low energy tail in the distributions. These are due to radiation losses and losses due to positron interactions with inhomogeneous material along the beam axis upstream of the calorimeter.

The mean μ and standard deviation σ of the Gaussian fit are taken as the mean energy response $\langle E \rangle$ and the resolution σ_E of the active part of the detector at a given beam energy. On the left side of Figure 4.2, the energy linearity is shown in black for the data and in red for the simulation. Linearity is defined here as the relationship between the reconstructed positron energy and the beam energy. To reconstruct the positron energies, the measured energies were scaled by a α slope factor determined from a linear fit, in which the slope and intercept were allowed to float. The residuals from the fitted straight line are less than 1% for the data and 0.5% for the MC.

The measured energy resolution $\sigma_E / \langle E \rangle$, is shown in the right part of Figure 4.2, and like for the linearity plot, the colour code to differentiate data and simulation is the same. The resolution measurements are fitted as a function of E_0 using a modified form of the resolution function introduced in Chapter 3:

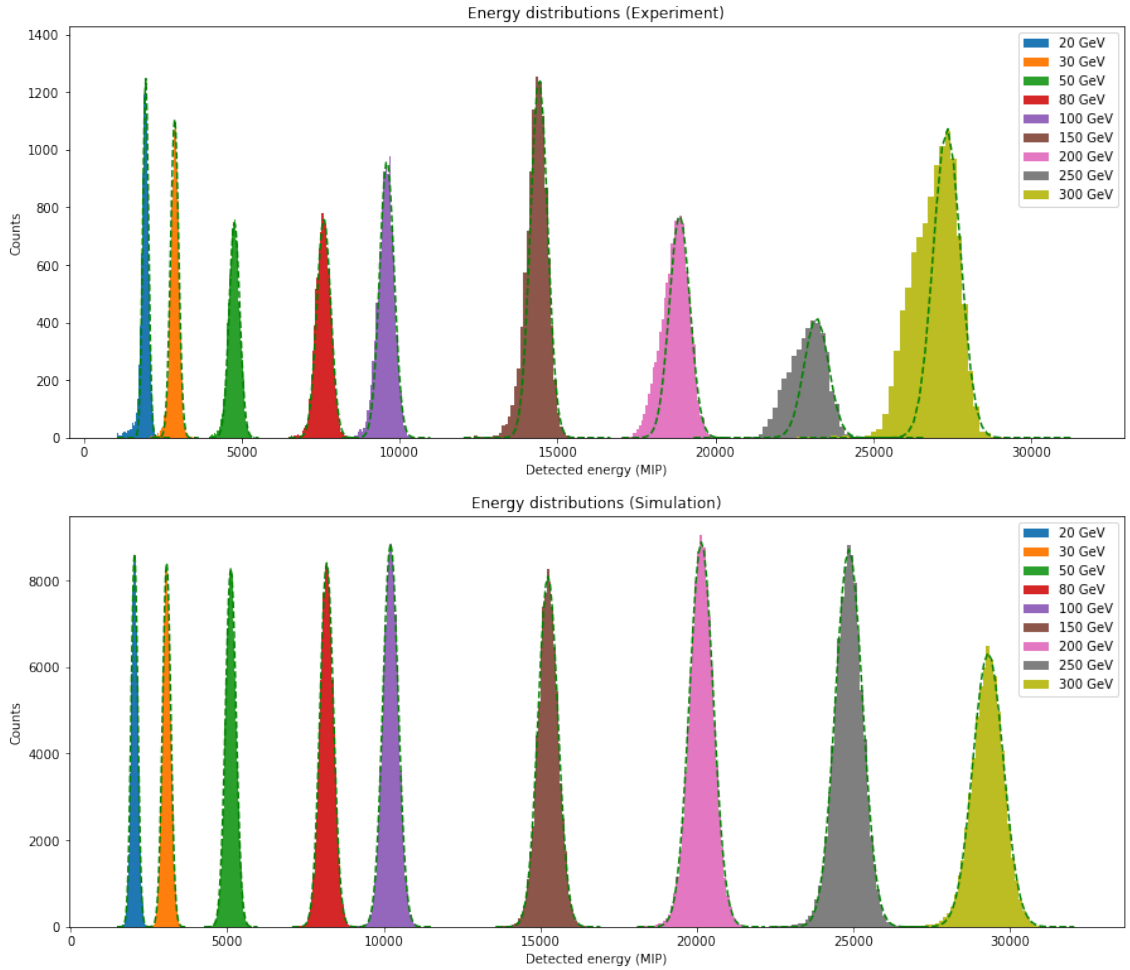

Figure 4.1: Positron shower energy distribution for different beam energy. Data are represented on the top plot and MC simulation on the bottom plot. Each distribution is fitted with a Gaussian function, shown in green dashed line, and for data the range is $[\mu - \sigma, \mu + 2.5\sigma]$.

$$\frac{\sigma_E}{\langle E \rangle} = \frac{b}{\sqrt{E_0}} \oplus c \tag{4.2}$$

The fitting function used does not include a noise term, as its residual contribution was found to be negligible after the pre-selection of hits chosen to reject noisy channels. Good agreement between the data and the MC is observed for both the stochastic and constant terms. The fact that the constant term in the data is equal to 0.6% is close to that predicted by the simulation, showing that there is no significant non-uniformity of the energy response in the trust window defined by the DWC cut. Furthermore, in the HGCAL project specifications, an energy resolution of less than 1% was required, and this requirement is met with this prototype.

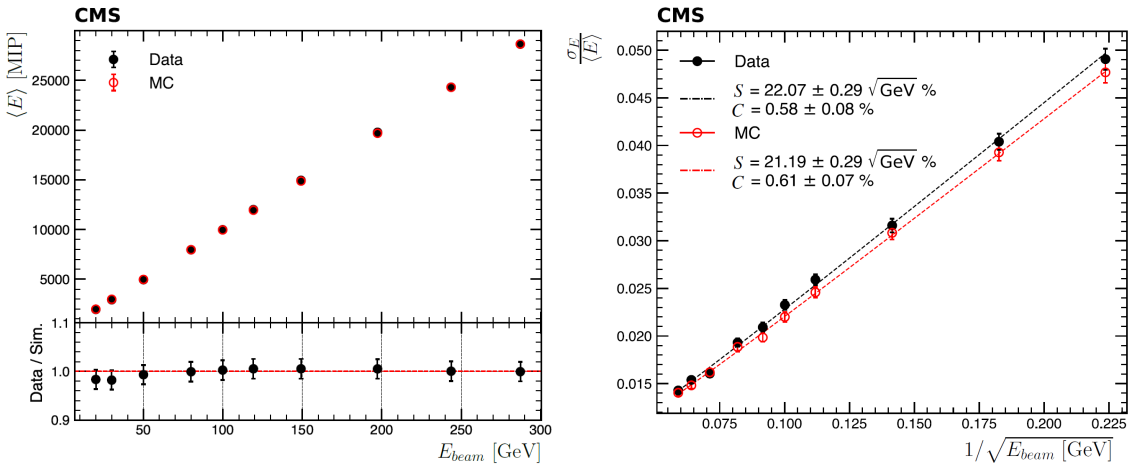

Figure 4.2: Mean measured energy as a function of the beam energy on the left. Measured energy resolution on the right [36]. Results obtained for data are represented in black, and in red for MC simulation.

4.1.3 Spatial reconstruction characteristics

After having seen that the prototype energy response and resolution are in agreement with the expected HGCAL energy performance, it remains to check the capability of the prototype to fully detect electromagnetic showers, meaning that its depth and transverse section are well dimensioned to contain the shower.

Longitudinal shape of electromagnetic showers

As described in the Chapter 3, one of the most important characteristics of a calorimeter is the shape of the electromagnetic sheaves in the longitudinal plane.

This longitudinal profile can be calculated in various ways. For example, it can be given by the mean number of occurrences or the median energy, both as a function of depth. In short, an estimator of the energy detected as a function of depth. Figure 4.3 shows the longitudinal profiles given by the mean number of occurrences and the median energy measured as a function of layer depth for nominal positron beam energies of 20, 100 and 300 GeV. In both cases, there is good agreement between data and simulation.

However, there is less measured energy in the data than in MC, giving about 3.5% less measured energy in the full detector in the data compared to MC. This percentage corresponds to the multiplicative factor of 1.035 introduced earlier. The average number of occurrences also shows fewer occurrences for the data than for MC in the middle layers. Despite the fact that, for absorbers, the average energy loss of almost one MIP in the even layers is close to twice the energy loss in the odd layers, the measured shower energy is higher in the odd layers than in the even layers. The greater energy deposited in the odd-numbered Si sensors is due to a greater number of soft electrons, dominated by delta rays produced in the material (especially the PCB) just in front of the sensors, and a greater amount of particles from backscattering due to the CuW plate just after the odd numbered sensors compared to the even numbered layers that are followed by the PCB.

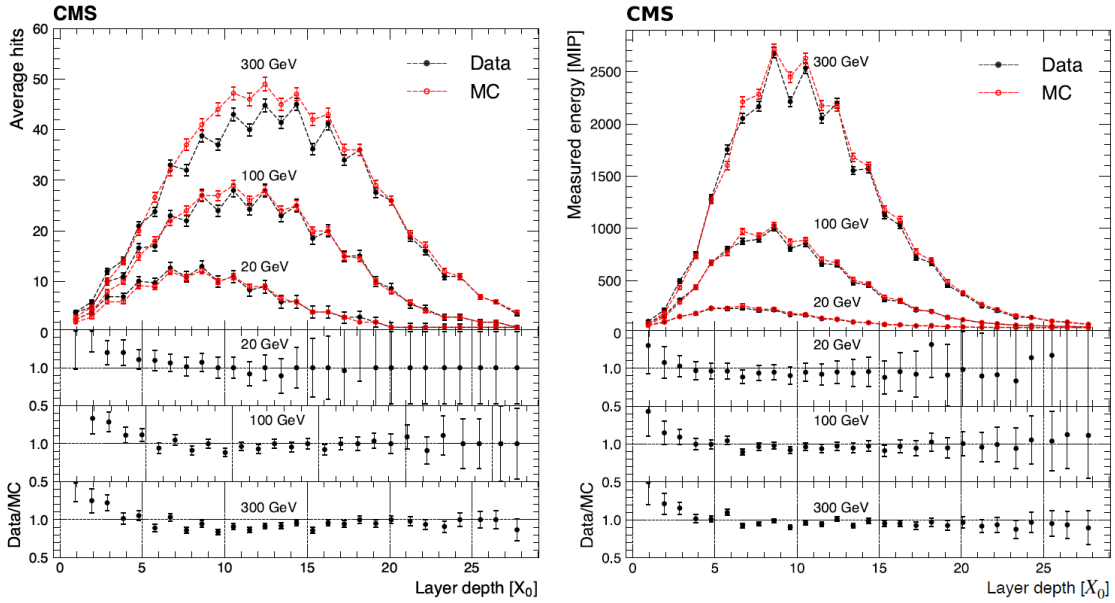

Figure 4.3: Longitudinal shower profiles for different nominal positron beam energies given by the average number of hits on the left, and the median measured energy on the right [36]. Results obtained for data are represented in black, and in red for MC simulation.

The measured energy longitudinal profiles are fitted with the function of Equation 3.7. From this fit, a parameter can be extracted and used with the formula given in Equation 3.8 to examine the expected logarithmic energy dependence of the position of the longitudinal shower maximum T expressed in radiation length X_0. Figure 4.4 gives the shower maximum as a function of the beam energy.

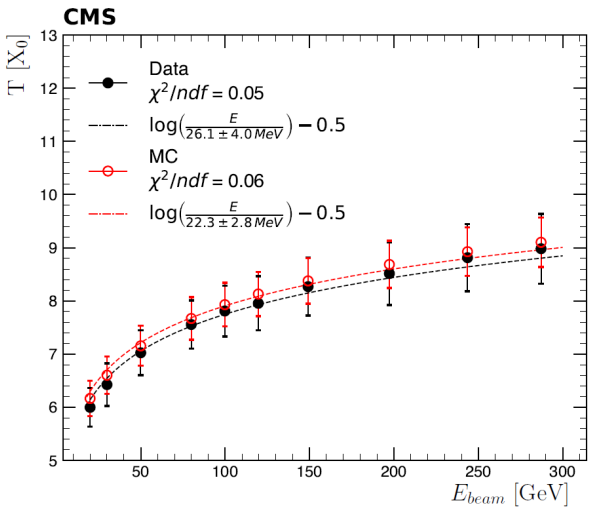

Figure 4.4: Shower maximum as a function of the beam energy. The shower maximum is determined from the longitudinal profile fit [36]. Results obtained for data are represented in black, and in red for MC simulation.

Similarly to the previous characteristics, there is a good agreement between data and MC simulation. Furthermore, the maximum depth of the shower determined from the longitudinal profiles is well fitted and shows its logarithmic dependency on the beam energy.

Transverse shape of electromagnetic showers

To study the lateral propagation of electromagnetic showers in the CE-E, we first define a central cell in each layer, the one with the maximum energy in the layer considered. The transverse shower profile of a layer is given by the energy deposited in a ring of cells per unit active area as a function of its radial distance r from the firing pad, normalized to the firing pad energy. This representation allows, in principle, to parameterize the lateral energy deposition as a function of the shower depth and the beam energy. In the left-hand side of Figure 4.5, the comparison of the transverse shower profiles between data and simulation is shown for 300 GeV positrons. As expected, the energy density is higher in the early layers. Once again, a reasonable agreement between data and simulation is observed, especially for the most energetic cells.

Figure 4.5 shows the average of $E(r)/E$ over all events, where E is the overall calorimeter energy per event and $E(r)$ is the energy contained in a cylinder of radius r. It can be seen that 90% of the energy is contained in a cylinder of radius of about 3 cm. More precisely, this corresponds to the central cell surrounded by two rings of cells, a total of 19 cells. A third and a fourth ring were also tested in order to be able to correctly parameterize $\langle E(r)/E \rangle$ for all values of r. The parameterization is performed by fitting the points obtained for each additional ring with the function of the equation 3.9.

In the right plot of Figure 4.5, the first points are not included in the fits because of the non-negligible variation of the energy deposited in the central cell is a strong function of the impact point. The contribution to the error on R from the choice of discrete values of r is much larger than that from the uncertainties of the fit. For energies between 20 GeV and 50 GeV, the increase in the value of R with decreasing positron energy, both for the data and for the simulation, is mainly due to the increase in scattering in the beam line upstream of the calorimeter. In the same energy range, the simulation predicts a lower value of R, which could be explained by the incomplete description of the beam line in the simulation, resulting in less upstream scattering. At high energies, the radial confinement is slightly larger than the calculated Molière radius of the HGCAL design: [32]. The largest contribution to the transverse propagation of electromagnetic showers in a sampling calorimeter comes from the air gaps, and as the air gaps in the final HGCAL are smaller compared to this prototype, the importance of what is presented lies in the comparison with the MC simulation.

Overall, the detection performance of electromagnetic showers fulfil the designed requirements, both for an energy point of view or for the spatial development of showers.

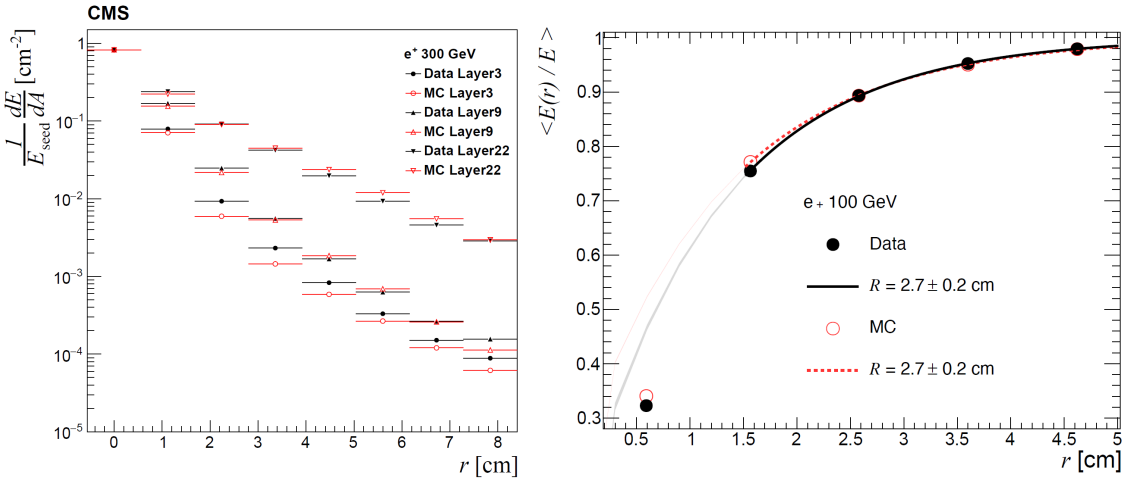

Figure 4.5: The transverse profile of electromagnetic showers from positron beams with a nominal energy of 300 GeV is represented on the left. Results are computed in layers 3, 9 and 22. The shapes correspond to the energy deposited in a ring of cells, depending on its radial distance r from the seed channel. The energy normalization of the seed pad is performed for the layer under consideration [36]. On the right, the ratio of the mean energy contained in a cylinder of radius r over the overall event energy. R is the Molière radius evaluated from the fit using Equation 3.9. For both, the results obtained for data are represented in black, and in red for MC simulation.

4.2 Energy and spatial performance of hadronic shower detection

The second preliminary study performed at the beginning of this thesis work was to determine the performance of the hadronic shower detection with the HGCAL prototype. Similarly to the studies presented in Section 4.1, the first step was to compute the energy resolution, and then the longitudinal and transverse characteristics of hadronic showers.

In this section, showers are induced by negative pions π^- with an energy ranging from 20 to 300 GeV. The nominal beam energies are the same as those presented in Table 3.2, except 150 GeV which was not used. Moreover, during the preliminary hadronic performance studies only the CE-E and CE-H parts were taken into account. The AHCAL data were not ready at the beginning of this work, and they were only added later for the final analysis.

Contrary to the previous section, the MC simulation uses two physics lists: FTFP_BERT_EMN which was already presented and QGSP_FTFP_BERT_EMN which is used to model the development of hadronic showers in the HGCAL prototype. The usage of both lists is explained by the will to compare the MC simulation performance with the data, thus a good model of hadronic showers is needed. The hadronic physics lists are a combination of models specified by the terms QGSP standing for Quark-Gluon String model, FTFP, and BERT, which dominate in different energy ranges. In the case of the QGSP_FTFP_BERT_EMN

physics list, the Bertini cascade model is used for energies lower than 12 GeV for pions and less than 6 GeV for all other particles, the QGSP for energies above 12 GeV for all particles, and the FTFP model is used between energies of 3 to 25 GeV. In the overlapping ranges of particle energies, the models are combined using predefined rates.

4.2.1 Information selection

A set of criteria was used to select pion events with high purity and hence a high quality dataset. The selection starts at the calorimeter hit level, and then at the event level. It is applied to ensure a reliable determination of the physics performance of the HGCAL prototype in terms of energy response and resolution and longitudinal and transverse shower profiles. It is applied to data as well as simulation. Concerning the hits' selection, it is composed of the two same requirements used for positrons:

1. Hits need to have their corresponding energy higher than 0.5 MIP.
2. Hits need to come from valid channels. Indeed, 3.2% of channels are abnormally noisy when considering both CE-E and CE-H. All the hits coming from these problematic channels are just discarded.

After the hits' selection, the next step consists of the full selection happening at the event level. This final selection requires three criteria, which are defined as:

1. Events need to have a single track reconstructed in all the DWC installed just the calorimeter prototype. This requirement allows rejecting the events with a shower start happening upstream to the prototype.
2. Events need to have an extrapolated track from DWC at the entrance of the CE-E compartment, containing in an acceptance window with a size of 2×2 cm^2 to select pion events for beam energies above 200 GeV. The window is extended to 4×4 cm^2 for pion beam energies below 120 GeV. This selection rejects particles which are too distant from the beam axis, and to ensure comparable beam profiles in both data and simulation.
3. Events need to have a total reconstructed energy $E > 100$ MIP in CE-E, $E > 60$ MIP in CE-H, and $E_{max}/E_{25} < 0.8$ in AHCAL. In this case, E_{max} and E_{25} correspond respectively to the sum of energy of the highest energy cell of each AHCAL layer, and the energy sum of its 25 nearest cells. These three energy criteria are used to avoid muon contamination.

Due to the high complexity of the processes implied in a hadronic shower, data are much affected by the noise instead of the simulation. Pions fulfilling these selection criteria across all beam energies are approximatively 75% for data and going up to 85% for MC simulation. The only exception is with a beam of 20 GeV in data for which selection efficiency is $\sim$65%.

For the events passing all the selection criteria, energies measured in the individual silicon cells and scintillator tiles in units of MIP are summed up for the CE-E, CE-H, and AHCAL prototype sections, and are compared to simulation. Energy distribution is composed of two main contributions: one detected in CE-E and purely electromagnetic E_e, and a second which is hadronic E_h, starting in the CE-H. The final energy requires weights corresponding to the contribution of each compartment, α_e (for the electromagnetic part) and α_h (for the hadronic part). Thus, the energy is equal to $E_f = \alpha_e \times E_e + \alpha_h \times E_h$.

4.2.2 Energy resolution

In the case of hadronic showers, it is not relevant to determine a linearity relation between detected energy per event and pion beam energy. Indeed, due to the non compensating nature of calorimeters and the fact that the π^0 component produced in hadronic showers depends on the incident beam energy, a nonlinearity in response is expected. Although, it is still possible to define the energy response as the average of the measured energy, taken as the Gaussian function used to fit the energy distribution. By construction, the response in data is equal to 1 when the beam energy is at 50 GeV

For all the other pion energies in the range from 20 to 300 GeV, the response shows a non linearity of the order of ∼10% with respect to the reference fixed at 50 GeV. The simulated response is consistently over-predicted by ∼10% for all energies in hadronic compartments. However, the nonlinearity of the response is reproduced by the simulation. The response is shown in the left part of Figure 4.6.

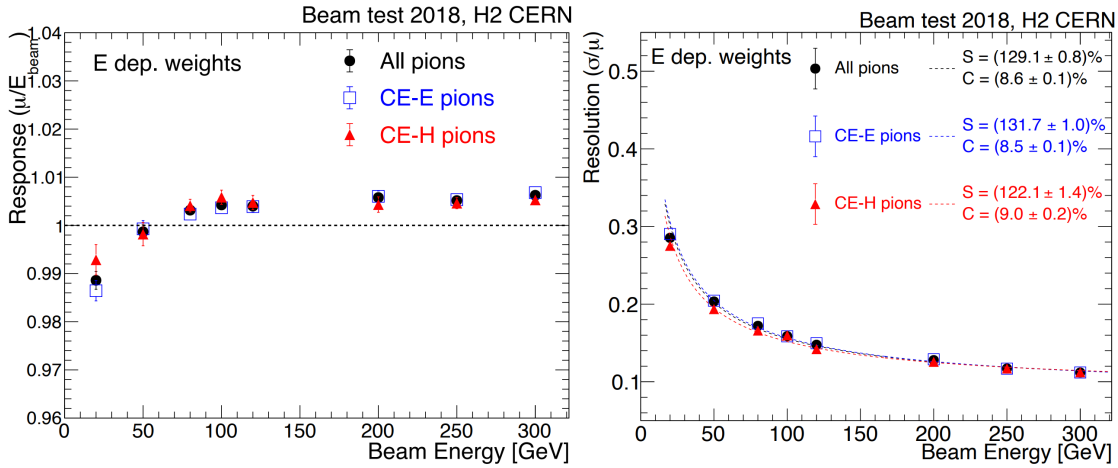

Figure 4.6: Energy response of hadronic showers on the left and energy resolution on the right, both depending on the beam energy [37]. All pions are represented in black, only CE-E pions in blue, and only CE-H pions in red.

The response of CE-E pions from simulation is higher than that measured from data by ∼5% across all beam energies. The simulation reproduces the observed nonlinearity for CE-E pions. The response is lower than one because the CE-E is calibrated to 50 GeV positrons and e/h for our calorimeter setup is less than one. According to this first result, a correction of the energy scale can be applied. In

simulation, it is done by 9.5% for CE-H and AHCAL based on 50 GeV π^- response, and by 3.5% for CE-E based on e^+ response.

The resolution as a function of beam energy is shown in Figure 4.6 for all pions in data, and only CE-H or CE-E pions. The resolution is fitted using the function 3.6. The noise term of the resolution is found to be negligible and is removed from the formula, like in the EM study. The resolution is observed to scale inversely with p E. We obtain a stochastic term of ∼123% and a constant term of 9.0% for CE-H.

4.2.3 Spatial reconstruction characteristics

Longitudinal shape of hadronic showers

The simulation describes quite well the longitudinal sheaves measured for the pions that have their first hadronic interaction in the second section of the CE-H prototype, as shown in figure 4.7. The profiles show a broad shower maximum, which is also consistent with the fact that the X_0/λ_n ratio is higher in steel than in lead absorbers. As expected, the shower develops deep in the AHCAL prototype section, and a substantial fraction of the energy is measured here.

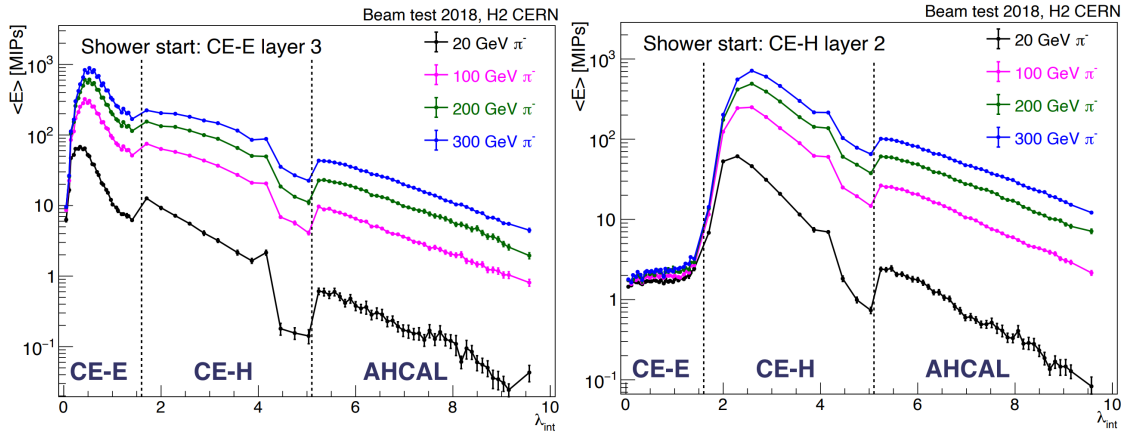

Figure 4.7: Longitudinal profiles of hadronic showers induced by pions with different energy [37]. The vertical dashed lines separate the different parts of the prototype. On the left, the shower is initiated in the CE-E, while on the right it starts in the CE-H.

As the last three layers of the CE-H consist of a single hexagonal module, there is a mismatch between the data and the simulation. This may indicate differences in the beam profile of the particle or in the angle of their propagation in the detectors.

Since the hadronic showers could start at different depths, hence it is impossible to fit their profiles with the function described in Equation 3.7. The difference between the two shapes is even more marked when one corresponds to a shower starting in CE-E and with the second starting in CE-H. In the same way, it does not make sense to consider the depth where occurs the shower maximum because this is very dependent on the depth of the shower start.

Transverse shape of hadronic showers

The modelling of the transverse propagation of pion induced showers as they move in the transverse plane must be well simulated by the hadronic physics lists of Genat4. This is necessary for a correct allocation of energy deposits in the presence of multiple incident particles, which will be the case with the high pile up rate expected during HL-LHC. As the longitudinal and transverse segmentation of the calorimeter sections is very important, this allows the comparison of the lateral profiles of the energy deposited in the different layers, and the study of the details of the shower modelling.

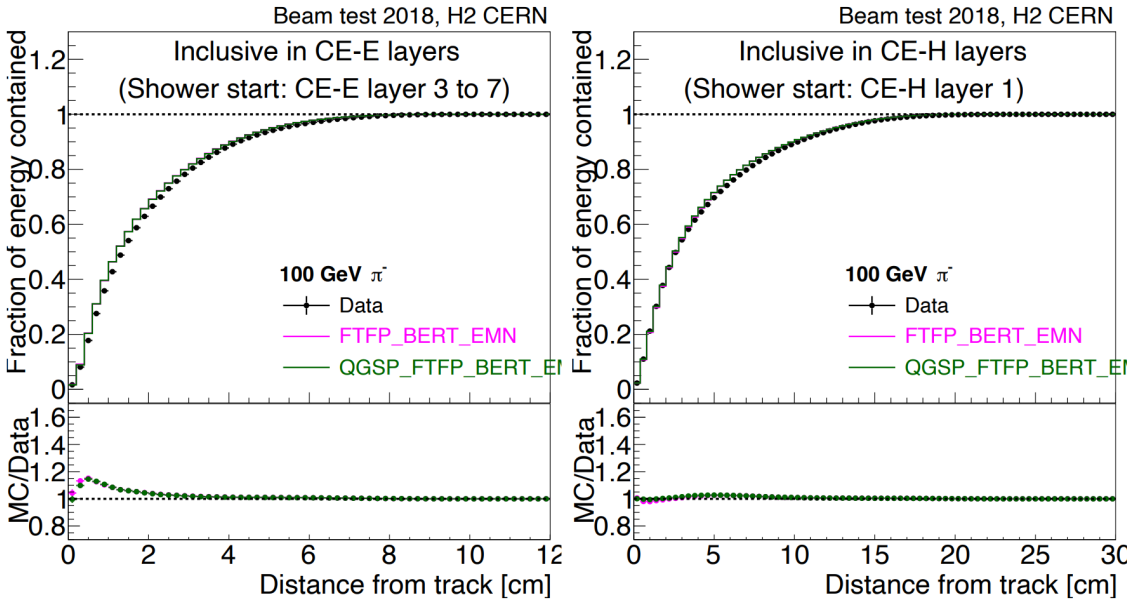

Figure 4.8: Fraction of energy contained in a cylinder with a varying radius [37]. Data and both MC simulation samples are presented. On the left, the shower is initiated in the CE-E, while on the right it starts in the CE-H.

The fraction of energy deposited in cylinders of varying radii around the beam axis is, according to the calorimeter sections, the starting point of the shower. This amount is shown in Figure 4.8 for pions with a beam energy of 100 GeV. The energy fraction measured here is normalized to the total energy measured in the respective calorimeter section, and does not take into account potential transverse leakage. Figure 4.8 shows the pion energy ratio as a function of the radius of the confining cylinder. On the left, it is measured in the CE-E section using pions that start to shower in the layers between the 3^{rd} and 7^{th} of the CE-E, and on the right, the shower starts in the first layer of the CE-H. The Geant4 physics lists predict the profiles well at higher energies, but show discrepancies near the shower axis. In both cases, there is a good match between the data and the simulation.

4.3 Timing performance

The study of the timing performance is one of the principal work completed about HGCAL in the context of this thesis. It has also a decisive importance in the validation of the prototype, since HGCAL should be a 5D calorimeter able to do fast timing measurement. This specific point is needed to mitigate the higher pile up rate and to discriminate more efficiently some background events, among which it is possible to cite the decay of π^0 into two photons very collimated. A precise timing measurement of such an event can determine that both particles were emitted at the same time, and then π^0 can be more easily identified and discarded. The main idea with the timing of the photons is to know if their time of flight is compatible with an emission from the primary vertex of the collision or from a vertex coming from the pile up.

4.3.1 Reconstruction of the timing information and selection

In this section, the procedure of the timing information is described, as well as the basic selection used for the following studies.

Concerning the reconstruction of the timing information, it starts with the *ToA* reconstruction operated in the Skiroc2-CMS ASIC and detailed in Section 3.4.4. In this model, the signal time is generated with the same effective approach used in [32], where simulated hits from Geant4 are exploited to record the generator-level time of the energy deposited in a detector cell. The model does not include the response of electronics components or the digitization, and thus any response non-linearities or similar effects are not simulated.

To obtain a realistic time resolution in the simulation, the time of the signal was convoluted with a Gaussian that had a width determined empirically for each channel. It consists in applying a smearing to the simulated time to take into account the detector effects.

Signal time reconstruction

The sequence of the time measurement in the ASIC is shown schematically in Figure 4.9. When the signal goes above a fixed threshold, the TDC ramp and the TDC clock are started and, after skipping the first clock edge, the TDC counter is latched twice: once on the rising, and again on the falling edge of the clock. This yields two time measurements, ToA_{rise} and ToA_{fall}, from which two separate signal times are estimated, T_{rise} and T_{fall}. These times are referenced to the system clock after corrections for the non-linearity of the TDC ramp, the time-walk that depends on the hit energy, and the deposited energy in the full module. These are the time of the energy deposition in a readout channel without any correction for time-of-flight between the layers or for variations due to angle of incidence. Thus, irrespective of a readout channel's location, they have a negligible impact on performance results.

First, candidate channels with reasonably high statistics of correct *ToA* readings and high hit energies are identified for the subsequent calibration. The criteria

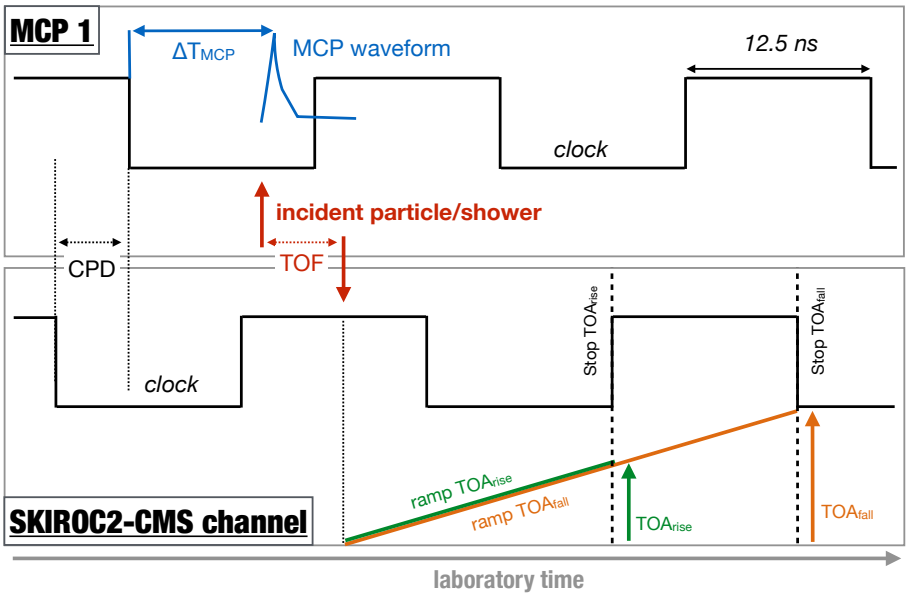

Figure 4.9: Timing measurements used in the calibration of the calorimeter hit timestamps. *CPD* denotes an arbitrary, but constant, clock-phase-difference between a given readout channel and the reference clock.

are presented in Section 4.1. Afterwards, the calibration procedure is discussed in detail in Section 4.3.1. Not all calibrated channels are accepted for the computation of shower timestamps. Instead, only good calibration results are selected for this purpose. The underlying validation strategy of good calibration outcomes is elaborated, before a representative evaluation of the per-channel timing resolution and accuracy.

Apart from the general selection criteria described in Section 4.1, there need to be at least 20 events with reconstructed hit energies above 200 MIP for a given channel to be subject to the subsequent calibration procedure.

In total, 310 channels in the electromagnetic section fulfil this requirement. For those, the calibration is run subsequently. Their location in the 2018 HGCAL prototype are depicted in yellow in Figure 4.10.

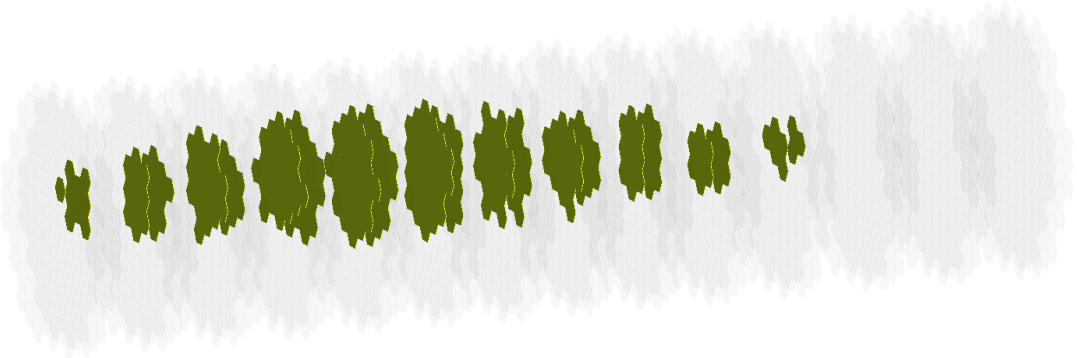

Figure 4.10: Location of the calibrated channel of the HGCAL prototype.

It is necessary to subtract the time of flight (ToF) in order to consider all the layers together. The ToF is estimated as the distance between the point of impact on the MCP of the incident particle and its impact on the HGCAL prototype plus the distance from the beginning of the calorimeter to the channel, all divided by the speed of light c:

$$ToF \;=\; \frac{\Delta X}{c} = \frac{1}{c} \cdot \left(z_0 \cdot \sqrt{1 + \tan^2 \alpha_x + \tan^2 \alpha_y} + \sqrt{(\Delta x)^2 + (\Delta y)^2 + (\Delta z)^2} \right) \tag{4.3}$$

In Equation 4.3, α_x and α_y denote the angles of the particle trajectory with respect to the beam line as measured by the delay wire chambers, $z_0 \;= 20$ cm symbolizes the distance between the MCP and the beginning of the HGCAL prototype, and Δz denotes the longitudinal depth of the respective channel within the calorimeter. Δx and Δy are both defined as the difference between the particle incidence coordinates as inferred from the DWC extrapolation and the channel position within the calorimeter.

Since the delay wire chambers (DWC) are an integral part of the ToF assessment, only events with a DWC reference are selected throughout this study. In addition, the computation of Δx and Δy relies on both the prototype module and the DWC coordinate systems to be aligned: First, the orientation of the DWC coordinate system does not agree with the calorimeter's and all transverse quantities reconstructed from the DWCs need to be inverted. Secondly, translational alignment constants δx and δx have to be inferred for each calorimeter layer.

As the timestamp reconstructed from the MCP waveform plus the digitized clock has a period of $\sim$25 ns, the relation of $ToA - (\Delta T_{\mathrm{MCP}} + ToF)$ exhibits discontinuities which need to be corrected for. The addition of the ToF to ΔT_{MCP} is not explicitly mentioned any more in the following. Subsequently, the MCP timestamp of the identified clusters are shifted by 0, +25 ns, or -25 ns respectively, to obtain a continuous distribution of the normalized $ToA - \Delta T_{\mathrm{MCP}}$.

To estimate the signal time, T, the procedure for both ToA measurements was as follows:

1. The ToA of all the channels are first corrected for the non-linearity of the ramp (f_{ToA}).

2. Then, an amplitude-dependent time walk correction (f_{TW}) was applied. The dependence of the ToA measurement on the reconstructed hit energy (E_{hit}), used as proxy for the signal amplitude, that is induced by the fixed-threshold discrimination. This effect is known as time walk and is denoted as f_{TW} in this work.

3. Finally, a correction for small signals (f_{R}) that depends on the total energy deposited in the module containing the channel (E_{module}) was applied.

Accordingly, the signal time, T, for each channel has three contributions, shown in Equation 4.4.

$$T \;=\; f_{\mathrm{ToA}}(ToA_{\mathrm{rise/fall}}) \;+\; f_{\mathrm{TW}}(E_{\mathrm{hit}}) \;+\; f_{\mathrm{R}}(E_{\mathrm{module}}, E_{\mathrm{hit}}) \tag{4.4}$$

The signal time T in any given channel is estimated for both ToA_{rise} and ToA_{fall}. The calibration procedure described in the following subsections is the same for both ToA_{rise} and ToA_{fall} measurements, and in the following section no distinction is made between them.

As the beam was asynchronous with the 40 MHz system clock, the signal arrival times were uniformly distributed within the 25 ns clock period. As the time difference between particle time and the ToA is independent of its location in a clock period and only depends on the time-of-flight and signal propagation differences, which are constant, the uniformity of the signal arrival time was used to derive corrections to the ToA values.

The time calibration of a readout channel is obtained by fitting with the formula of Equation 4.5. For each channel and for the rise and fall variants separately, the expression in Equation 4.4 is fitted to the sum of the two terms in Equation 4.5: the time of the signal in the MCP (ΔT_{MCP}) and the time-of-flight (ToF) from the MCP to the readout channel's location. The ToF is estimated from the beam particle trajectory (ΔX), reconstructed with wire chambers placed upstream of the MCP, and assuming that the shower particles proceed through the detector prototype at the speed of light (c).

$$T \;\leftrightarrow\; \Delta T_{\text{MCP}} + ToF = \Delta T_{\text{MCP}} + \frac{\Delta X}{c} \tag{4.5}$$

The time of the signal from MCP1 was required to have an amplitude greater than 100 ADC counts, where the resolution was better than 100 ps, as shown in 3.25. The times computed from MCP1 were aligned with the ToA readings in a given channel by correcting for the 25 ns periodicity of the digital clock [152]. Also, only readout channels with more than 1000 hits with $E_{\text{dep}} \geq 250$ MIP and with 30,000 or more hits in total were considered. The first requirement ensures that a large sample of measurements where the energy is estimated from the time-over-threshold measurement, not the ADC. As the beam was focused on the centre of the calorimeter, only 116 readout channels, or 3% of all channels, met these requirements.

Time of arrival non linearity correction

For each channel, the response was modelled using:

$$\hat{f}(x|\vec{\Theta}) = \Theta_1 \cdot x + \Theta_2 + \frac{\Theta_3}{x - \Theta_4} \tag{4.6}$$

Where $\vec{\Theta}$ are parameters derived from the fit to the distribution of signal times in a clock period, with the Θ_2 corresponding to an offset constant, denoted as CPD in Figure 4.9.

This transformation is used in order to get a single distribution of ToA. Indeed, as it is highlighted in Figure 4.12, the clock period induces a separation of the distribution because part of it is reconstructed on another clock signal. After this correction, the ToA distribution can be considered as a single block.

Variations in the TDC pedestals (ToA_{min}) were corrected for, and then the values were scaled by the full range (ΔToA) to yield ToA_{norm}, which ranged from

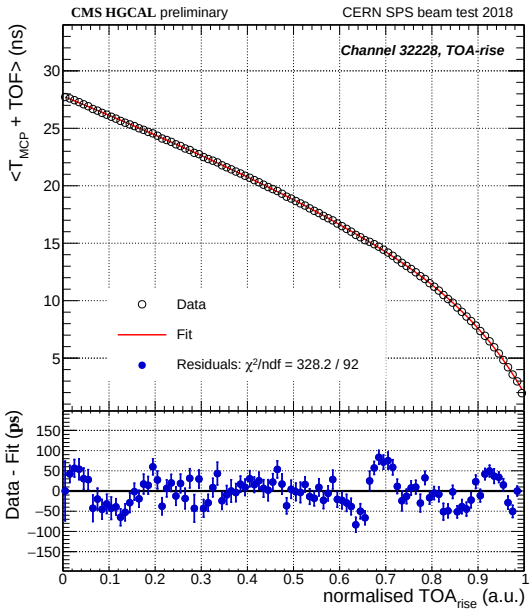

(a) TOA linearisation

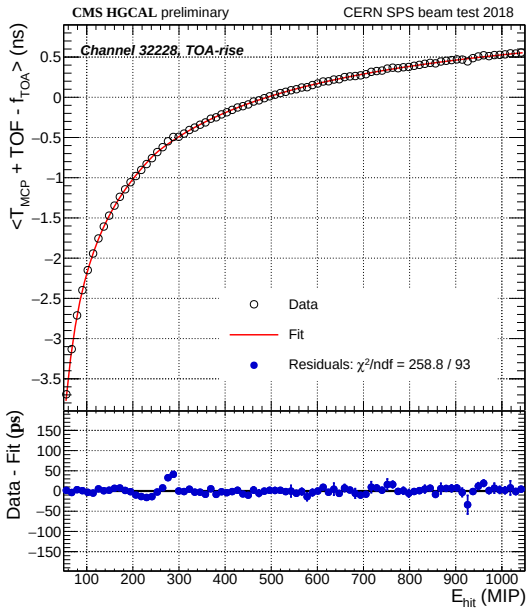

(b) Time-walk correction

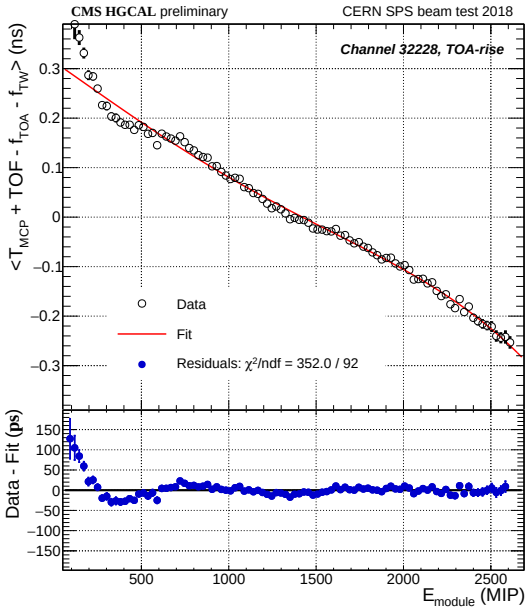

(c) Residual correction

Figure 4.11: The three *ToA* calibration steps (*ToA*-rise in this case) of a representative channel, centrally located inside the HGCAL prototype: (a) Linearization of the normalised *ToA*, (b) assessment of the signal-induced time-walk correction, and (c) assessment of the residual correction, a smaller time-walk that depends on the total energy in the module of the given channel. The magnitude of the time-walk corrections is about one and two orders of magnitude smaller than the calibrated time range, respectively.

zero to one and corresponded to the relative location of the TDC value in the clock period:

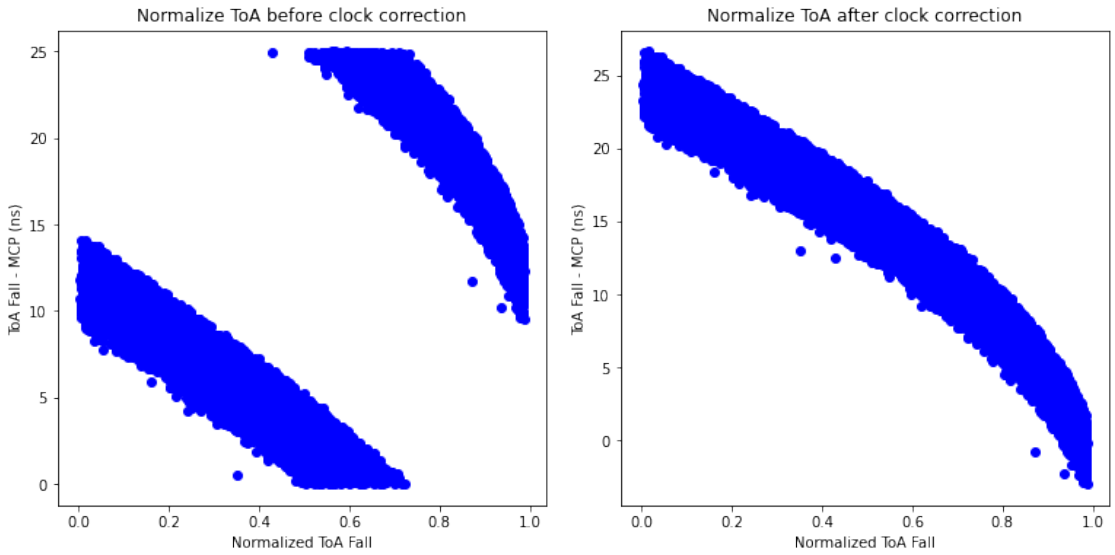

Figure 4.12: ToA_{fall} - MCP distribution depending on the normalized ToA. On the left, the clock correction is not applied, but it is the case on the right.

$$ToA_{\text{norm}} = \frac{ToA - ToA_{\text{min}}}{\Delta ToA} \tag{4.7}$$

After this normalization, Equation 4.6 was fitted to the average of the MCP signal times as a function of ToA_{norm}. The ToA_{norm} is calculated for ToA_{rise} as well as ToA_{fall}, and their distributions are given in the left part of Figure 4.13.

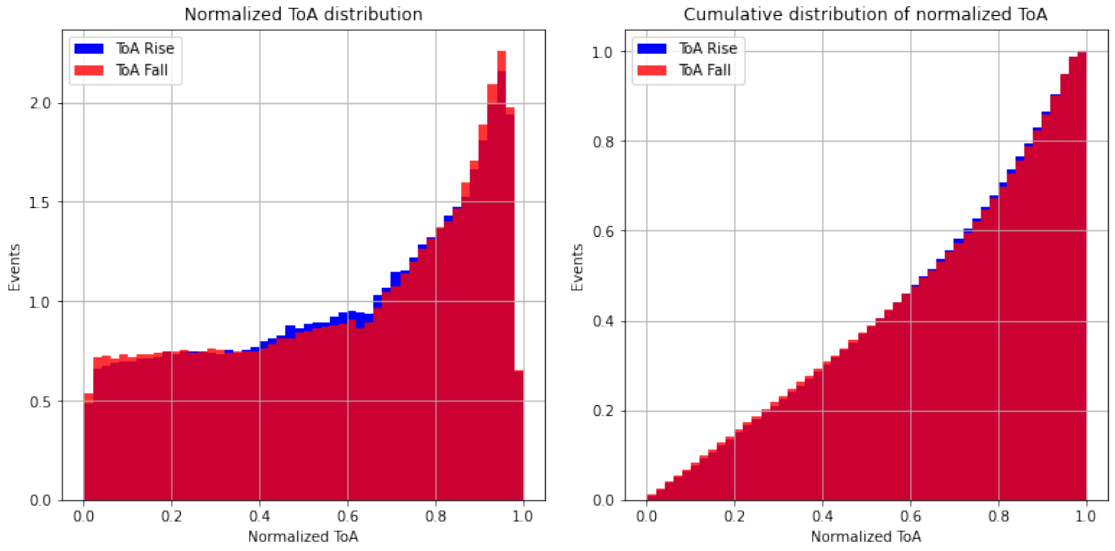

Figure 4.13: Normalized ToA distribution. ToA_{rise} is represented in blue and ToA_{fall} in red. The standard ToA distributions are on the left, and the cumulative ones on the right.

In the case of linearity, the ToA distribution should have been described by a uniform distribution, but in reality it is not the case. Then, the ToA cumulative

distribution represented in the right part of Figure 4.13 is taken into account in order to consider the derivative of the *ToA*.

Once the cumulative distribution is obtained, the next step consists of inverting it in order to get the non linearity correction function. This study was performed over different layers as shown in Figure 4.14.

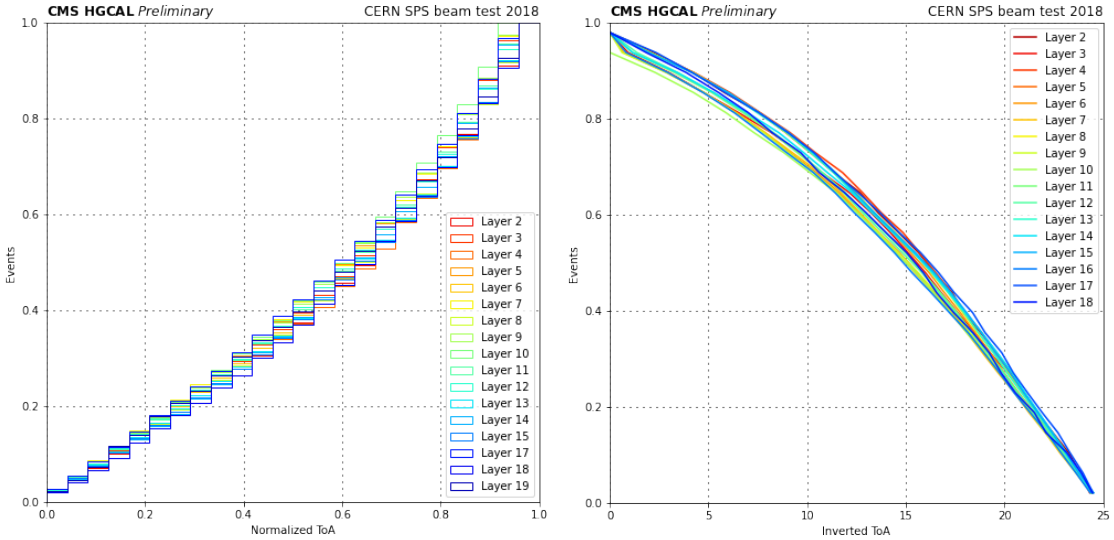

Figure 4.14: Normalized *ToA* cumulative distribution for different layers on the left, and their associated inverted curves on the left.

The *ToA* non linearity functions of all the channels are combined. The average value of this combination is fitted to have a generic correction function. This function is represented in Figure 4.15. This combination was used to validate the fit function, but then the calibration is done per channel and only the channel information will be taken into account for the fit.

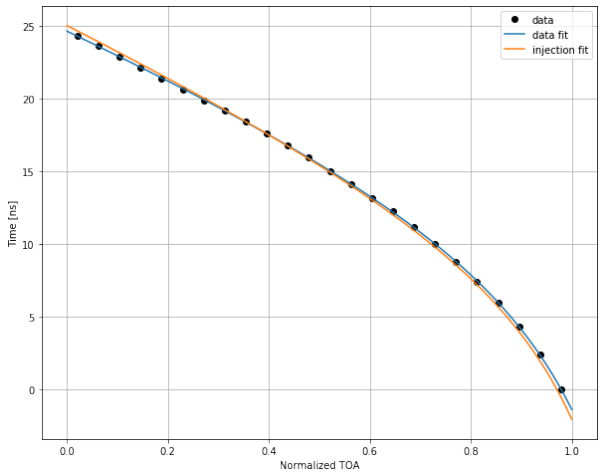

Figure 4.15: *ToA* non linearity correction function. Black points correspond to the average non linearity over all the channels. The blue and orange curves are the fits.

The accuracy of the linearization is improved by allowing separate parameter values in the linear ($ToA_{\text{norm}} < 0.65$) and non-linear regions ($ToA_{\text{norm}} \geq 0.65$):

$$f_{\text{ToA}}(ToA_{\text{norm}}) = \begin{cases} \hat{f}(ToA_{\text{norm}}|\vec{\Theta}_1^{ToA}) & \text{for } ToA_{\text{norm}} < 0.65. \\ \hat{f}(ToA_{\text{norm}}|\vec{\Theta}_2^{ToA}) & \text{for } ToA_{\text{norm}} \geq 0.65. \end{cases} \tag{4.8}$$

The final result of the linearization step is shown in Figure 4.11a for the ToA_{rise} of a representative channel, where the full 25 ns range is apparent. It is found that the parametrizations thus derived are consistent with the results from the first calibration results, based on the asynchronous nature of the beam particles [35].

Time walk correction

After the f_{ToA} linearization corrections were applied, an amplitude dependent correction for time-walk was applied. When having a look at the TW as a function of the normalized ToA, there is a TW spread which is related to the channel energy, as highlighted in Figure 4.16.

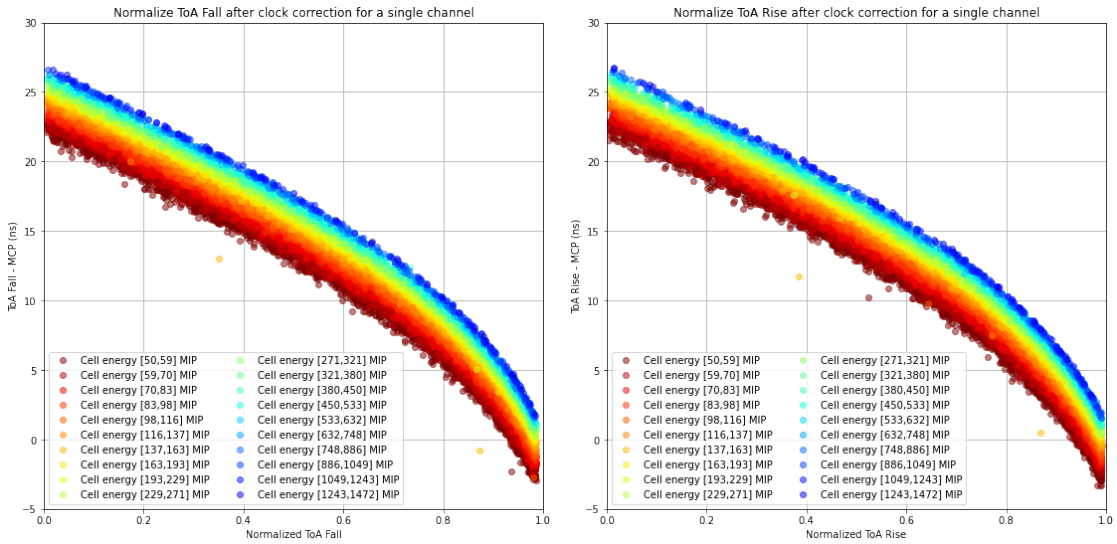

Figure 4.16: TW depending on the normalized ToA. Each colour corresponds to a specific cell energy range. The ToA_{fall} is on the left, and the ToA_{rise} is on the right.

Then, since the TW also depends on the cell energy, the correction function should depend on this energy. In order to get this parametrization, the average of the TW is computed for each energy range. The average TW depending on the normalized ToA is represented in Figure 4.17.

One of the energy range is taken as a reference, and its corresponding average TW is subtracted to the others. As it is illustrated in Figure 4.18, the average TW difference does not show any statistically significant dependency on the ToA_{norm}.

Thus, for each energy range, the mean of $TW - TW_{ref}$ is calculated and then represented as a function of the cell energy. The Figure 4.19 represents this for a TW computed from ToA_{fall}, as well as ToA_{rise}.

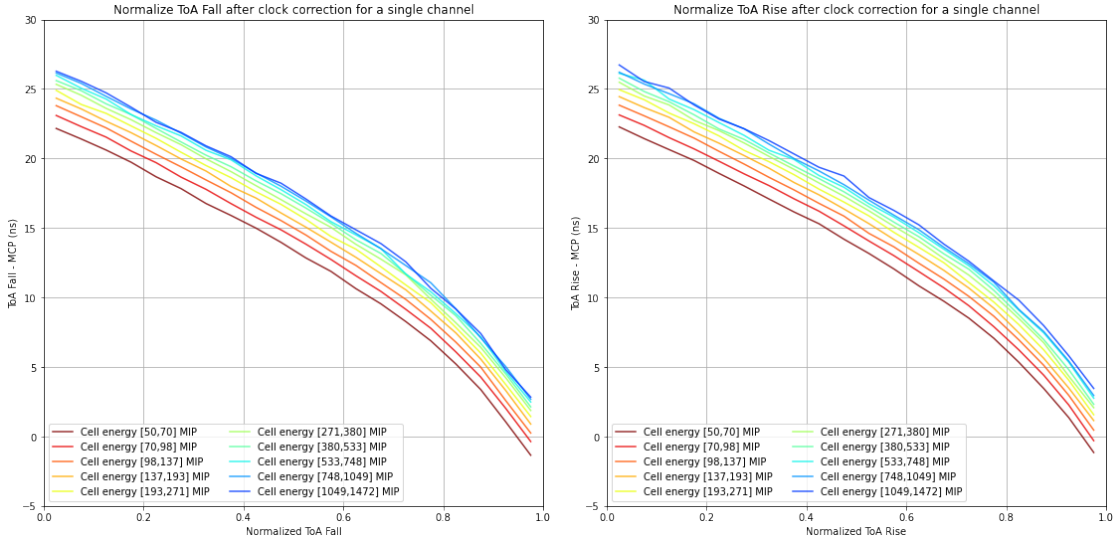

Figure 4.17: Average of the TW depending on the normalized ToA and represented for different cell energy ranges, each colour corresponds to an energy range. ToA_{rise} is represented on the right and ToA_{fall} on the left.

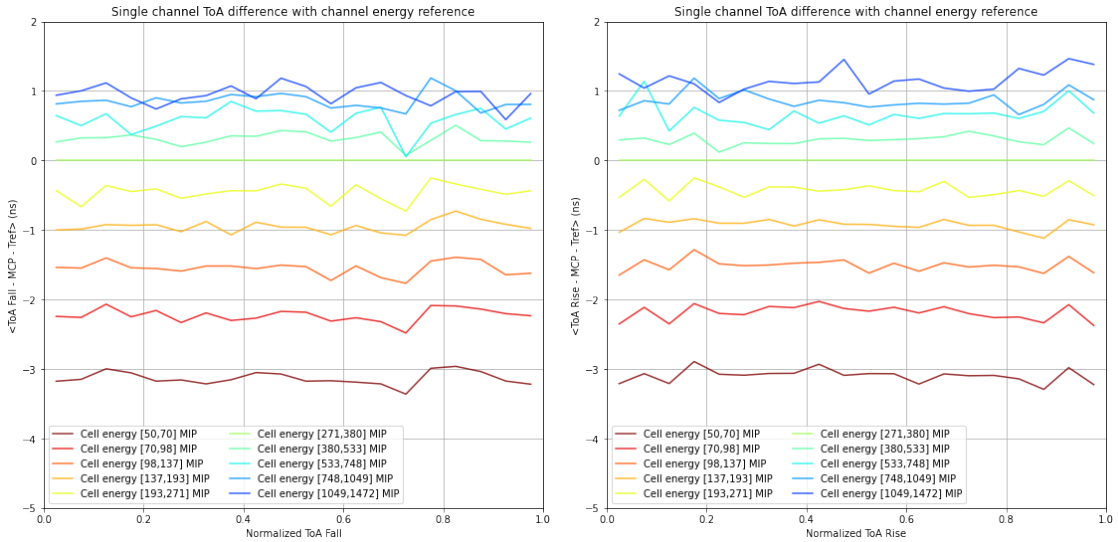

Figure 4.18: Average of the $TW - TW_{ref}$ depending on the normalized ToA, where TW_{ref} is the TW for specific energy range taken as a reference. Each colour corresponds to a specific cell energy range. The ToA_{fall} is on the left, and the ToA_{rise} is on the right.

To derive this correction, a fit of Equation 4.6 to the data as a function of the reconstructed signal amplitude, E_{hit} that is used as a proxy for the signal magnitude.

Therefore, the model is fit to the average of the reference timestamps corrected by f_{ToA}, as a function of E_{hit}.

It was also found that the fit was improved by separately fitting two regions of the signal amplitude, depending on whether the ADC ($E_{\text{hit}} < E_{\text{ToT}}$) or ToT is used

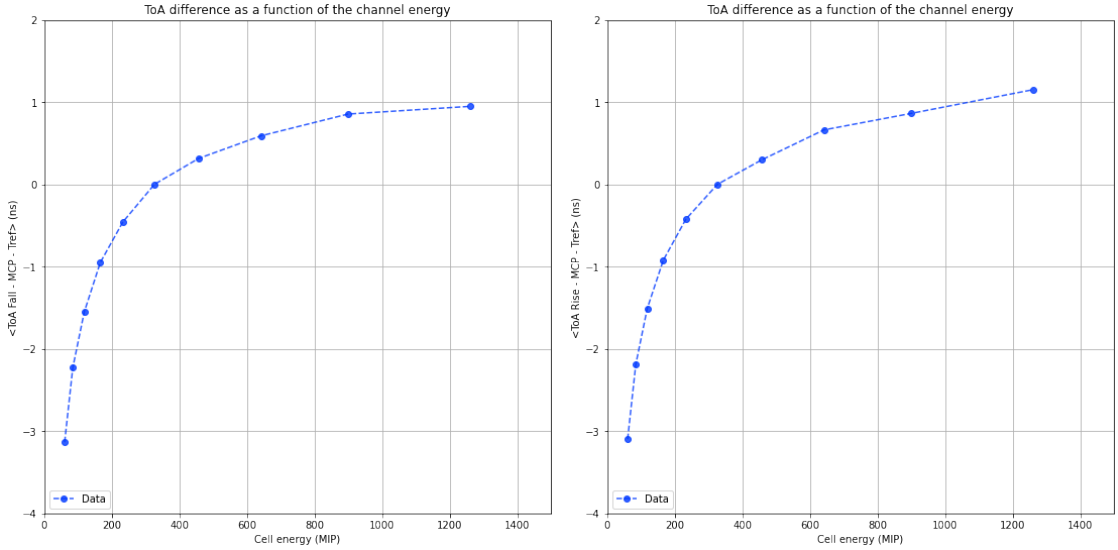

Figure 4.19: Average of the $TW - TW_{ref}$ depending on the normalized cell energy, where TW_{ref} is the TW for specific energy range taken as a reference. The ToA_{fall} is on the left, and the ToA_{rise} is on the right.

($E_{\text{hit}} \geq E_{\text{ToT}}$) to estimate the hit energy.

$$f_{\text{TW}}(E_{\text{hit}}) = \begin{cases} \hat{f}(E_{\text{hit}}|\vec{\Theta}_1^{TW}) & \text{for } E_{\text{hit}} < E_{\text{ToT}}. \\ \hat{f}(E_{\text{hit}}|\vec{\Theta}_2^{TW}) & \text{for } E_{\text{hit}} \geq E_{\text{ToT}}. \end{cases} \tag{4.9}$$

As can be seen in Figure 4.11b, the time-walk is found to reach $\mathcal{O}(1\text{ ns})$ for hit energies below a few 100 MIP.

Residual time walk correction depending on module energy

After the linearization and time-walk correction, timing corrections of the order of 100 ps were found to be needed for small hit energies when the energy deposited in the full module that contained the channel was wide. The parametrization of the residual time walk correction was done following the same procedure as for the time walk correction. First, the corrected TW was considered for different ranges of energy, but this time the all the energy of a layer, written E_{module}, was taken into account. Then, the average corrected TW depending on the normalized ToA was fitted with the Equation 4.8, and it is done per energy range. One taken as a reference, and the difference between it and the others is considered as a function of E_{module}.

This effect is probably due to the common-mode noise subtraction [34] being incomplete, as it applies only to small (ADC) signals, not large (ToT) ones. It was found that this residual correction can be well modelled by:

$$f_{\text{R}}(E_{\text{module}}, E_{\text{hit}}) = \begin{cases} \mathcal{P}_4(E_{\text{module}}) & \text{for } E_{\text{hit}} < E_{\text{ToT}}. \\ 0 & \text{for } E_{\text{hit}} \geq E_{\text{ToT}}. \end{cases} \tag{4.10}$$

Where $\mathcal{P}_4$ represents a fourth-degree polynomial whose parameters are determined from a fit to the average of the reference timestamps corrected by $f_{\text{ToA}} + f_{\text{TW}}$, as a function of the energy deposited in the module, E_{module}. Figure 4.11c shows the residual correction determined for a representative channel.

This residual correction may in principle be due to the procedure used to estimate and subtract common-mode fluctuations [34] that coherently affect many channels in the same module. This procedure only applies to ADC data and, therefore, to small signals.

For larger signals, namely when $E_{\text{hit}} > E_{\text{ToT}}$, it is observed that the residual correction is negligible, as directly reflected in Equation 4.10. For these hits, measured with the *ToT*, the common-mode correction does not apply, lending support to the hypothesis that the common-mode subtraction procedure may be at the root of the need for the residual correction.

While identifying the cause for this effect is beyond the scope of this work, it is suspected that the need for this residual correction is specific to the reconstruction of signals in the Skiroc2-CMS ASIC and does not necessarily generalize to other ASIC.

Full timing calibration

After these corrections were applied, the estimated precision of the time measurement for a single channel is ∼50 ps.

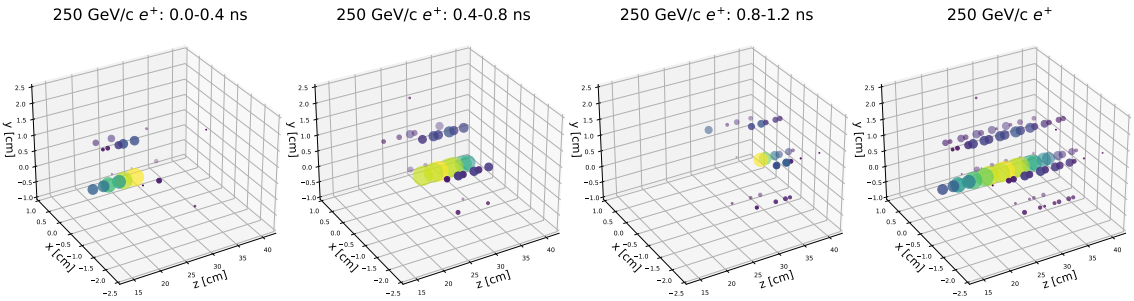

(a) $0 \leq T \leq 0.4$ (b) $0.4 < T \leq 0.8$ (c) $0.8 < T \leq 1.2$ (d) Full shower

Figure 4.20: Time-evolution (a–c) of a 250 GeV electron-induced shower (d) in the HGCAL prototype. Data are shown for 81 hits with reconstructed timestamps. If both *ToA* variants are within their linear region, timestamps are computed from an average of both. Otherwise, the variant in or closest to its linear region is taken. The size and colour of the markers both correspond to the reconstructed hit energy.

Fitted parameter values for the example illustrated in 4.11 are provided in Table 4.1. Among the 116 channels for which the time calibration procedure was possible, the parameter values vary by $\mathcal{O}(10\%)$. Thus, the analysis of the timing performance of the detector discussed below is restricted to only those channels. These channels are located centrally in the prototype, as can be seen in Figure 4.20, where a 250 GeV electron showering in the calorimeter is shown.

Table 4.1: Example of fitted calibration constants from Equations 4.8, 4.9, and 4.10 shown respectively in Figures 4.11a, 4.11b, and 4.11c. Numbers are rounded to their least significant digits.

Parameter	Value	Parameter	Value	Parameter	Value
$\Theta^{\mathrm{ToA}}_{1,1}$	-14.21 ns	$\Theta^{\mathrm{TW}}_{1,1}$	2.97 ps MIP^{-1}	p_0	314 ps
$\Theta^{\mathrm{ToA}}_{1,2}$	30.70 ns	$\Theta^{\mathrm{TW}}_{1,2}$	-0.73 ns	p_1	-0.24 ps MIP^{-1}
$\Theta^{\mathrm{ToA}}_{1,3}$	3.62 ns	$\Theta^{\mathrm{TW}}_{1,3}$	-177 ns MIP	p_2	-2×10^{-5} ps MIP^{-2}
$\Theta^{\mathrm{ToA}}_{1,4}$	1.253	$\Theta^{\mathrm{TW}}_{1,4}$	-0.8 MIP	p_3	4×10^{-8} ps MIP^{-3}
$\Theta^{\mathrm{ToA}}_{2,1}$	-10.00 ns	$\Theta^{\mathrm{TW}}_{2,1}$	0.05 ps MIP^{-1}	p_4	-1.2×10^{-11} ps MIP^{-4}
$\Theta^{\mathrm{ToA}}_{2,2}$	$\hat{f}\left(0.65 \middle\vert \vec{\Theta}_1^{ToA}\right)$	$\Theta^{\mathrm{TW}}_{2,2}$	$\hat{f}\left(E_{\mathrm{ToT}} \middle\vert \vec{\Theta}_1^{TW}\right)$		
$\Theta^{\mathrm{ToA}}_{2,3}$	5.53 ns	$\Theta^{\mathrm{TW}}_{2,3}$	-730 ns MIP		
$\Theta^{\mathrm{ToA}}_{2,4}$	1.298	$\Theta^{\mathrm{TW}}_{2,4}$	-150 MIP		

4.3.2 Impact of the geometry on the timing performance

One of the first steps in the comprehension of the timing properties of shower in the HGCAL prototype consists in studying the *ToA* distribution and its spatial characteristics. This preliminary study was performed using only simulated data.

An example of *ToA* distribution is given on the left plot of Figure 4.21. It is composed of a main peak and a second one less important and coming from a particle originating from back scattering interaction. This second peak is mostly present in the even layers, which are placed after a layer of absorber material.

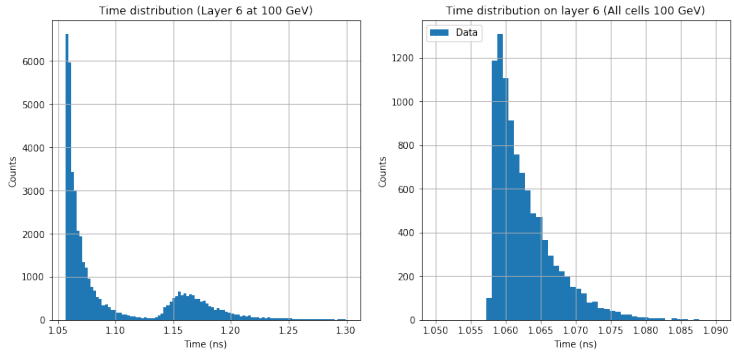

Figure 4.21: *ToA* distribution of layer 6 from 100 GeV positron beam. On the left, the raw distribution is shown, while on the right only the smallest interval with 68% of the *ToA* per event is kept.

The solution of not taking into consideration this parasitic hits is to keep only the smallest interval with 68% of the *ToA* per event. Once this operation is done, the second peak is removed. The right part of Figure 4.21 represents the new distribution.

Then, after a *ToF* correction, all the layers can be considered simultaneously. Raw timing information from the MC simulation has to be smeared in order to

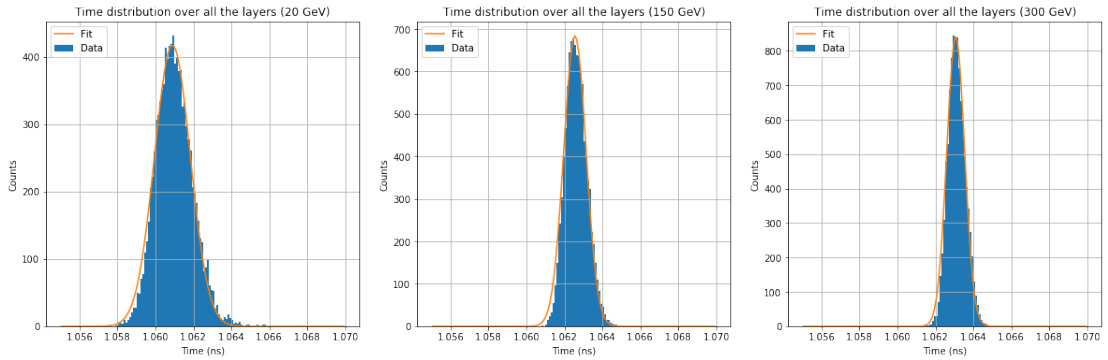

Figure 4.22: ToA distribution over all the layers for 20, 150, and 300 GeV. A Gaussian fit is performed and illustrated in orange.

reflect the impact of the electronic chip. Smeared time is defined as $t_{smeared} = t + \alpha$, where t is the time when the energy deposit per cell reaches a 15 MIP threshold and α is a random value from $\mathcal{N}(0, \sigma(E))$. And with $\sigma(E) = \sqrt{(\frac{b}{E})^2 + c^2}$, which corresponds to the resolution formula for a single cell. Parameters are estimated from data in order to add effects which were not modelled in the simulation. This gives a stochastic term equal to 10.42 ns$\times$MIP and a constant term equal to 50 ps. Plots of Figure 4.22 show the ToA distributions before applying the smearing, while Figure 4.23 shows them after smearing. In the following, the smeared ToA corresponds to the one from MC simulation only.

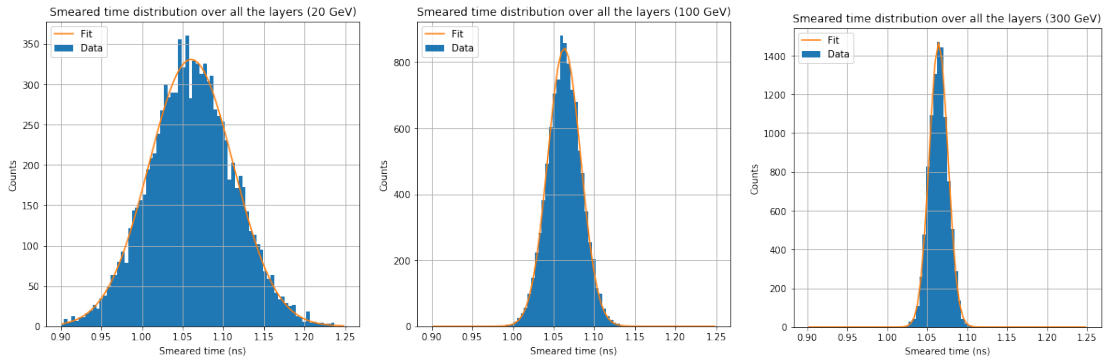

Figure 4.23: Smeared ToA distribution over all the layers for 20, 150, and 300 GeV. A Gaussian fit is performed and illustrated in orange.

As expected, the smeared ToA distributions are wider than the previous one. Since the random component is taken from a normal distribution, it is still possible to use a Gaussian function to fit it. The plots in Figure 4.23 are presented as a sanitary check in order to see if the smearing is working correctly.

Furthermore, the purpose of this preliminary study is to have a look at the timing performance depending on the spatial dimension. First, when looking at the performance as a function of the depth or the layer position. The ToA distribution for a single layer and for a single beam energy are presented in Figure 4.24.

Secondly, it is necessary to check if the transverse dimension has an impact on

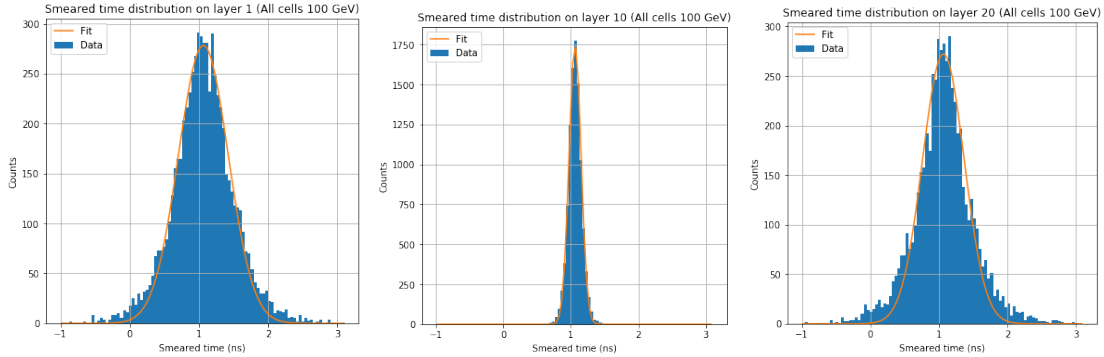

Figure 4.24: Smeared *ToA* distribution over all the cells of a single layer for 100 GeV. From left to right, layers 1, 10, and 20 are shown. A Gaussian fit is performed and illustrated in orange.

the performance. For that, three scenarios are considered: all the cells, then the most energetic cell and the first ring of its closest neighbours (meaning 7 cells), and finally the most energetic cell with two rings (meaning 19 cells). If there is a real impact, this can lead to the definition of a new selection cut.

Just about the distributions from Figure 4.23, the standard deviation of the distribution is strictly decreasing when the beam energy increases. Although, considering the distributions from Figure 4.24, it is clear that the sharpest distributions correspond to those computing with hits from the central layers (around the 10^{th} layer), also corresponding to the layers containing the highest hits density and thus the highest energy deposit. This comparison highlights the fact that the statistics play a role in order to get the best performance possible.

For the following, the smeared *ToA* distribution will be considered per layer and per transverse scenario. These distributions are then fitted with a Gaussian function and from the fits, parameters μ and σ are taken to plot respectively the mean time depending on the layer represented in Figure 4.25, and the standard deviation depending on the layer shown in Figure 4.26.

Standard deviation increases with the layer and decreases with the beam energy. It is minimal at the shower maximum. There are more fluctuations in the last layers because there is less energy. Once again, there is no significant difference between the three methods.

The mean time seems constant over the layers and for the different beam energies. There are more fluctuations for the last layers because there is less detected energy. Once again, there is no significant difference between the three methods.

These results show first that there is a very small impact of the transverse position of the cells on the performance, and the best resolution occurs in the layers where there is the maximum energy deposit. The higher the beam energy is, the better is the timing performance. Indeed, the timing resolution is lower for the 300 GeV positron beam, and its level stays almost the same for more layers.

Then, to be sure about the impact of the cell's transverse location, all the layers are considered all together. The timing resolution is computed, as well as the shower mean time. Both are shown in Figure 4.27.

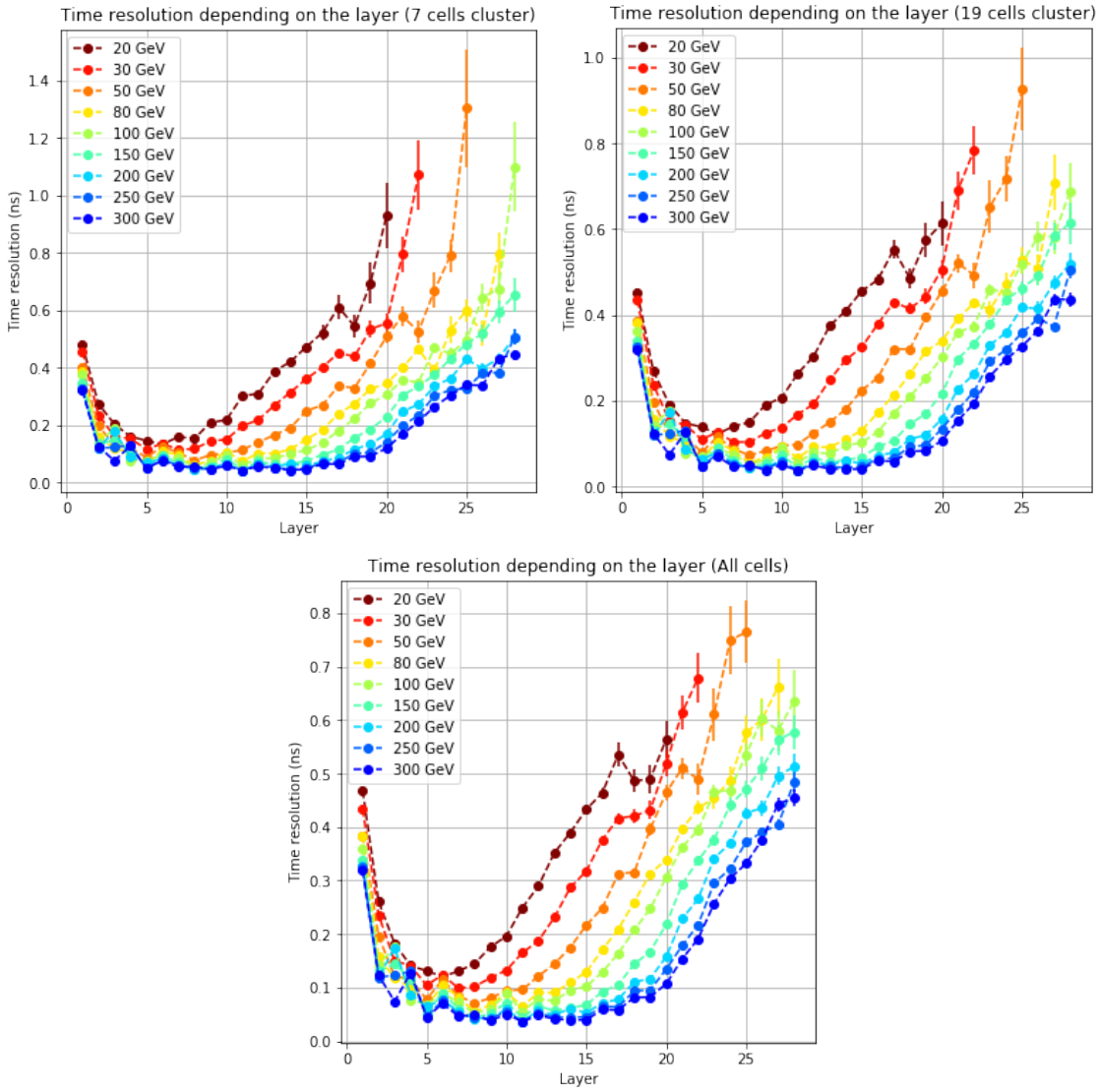

Figure 4.25: Standard deviation of the Gaussian fit done on *ToA* distribution for each beam energy and as a function of the layer. On the left, 7 cells are used, then 19 cells in the middle, and all the cells on the right.

In definitive, the best performance is obtained when considering all the cells or with at least 19 cells. Hence, this set of preliminary analyses prove the fact that there is no need to define additional selection criteria on the longitudinal or transverse location of the cells.

4.3.3 Single channel timing performance

This section describes the timing performance evaluation from the level of a single channel. The time resolution is determined for individual channels using the MCP as an external reference.

Before moving to the timing resolution calculation, a first selection is applied, consisting in keeping only the smallest interval containing 68% of the *ToA*, as it is

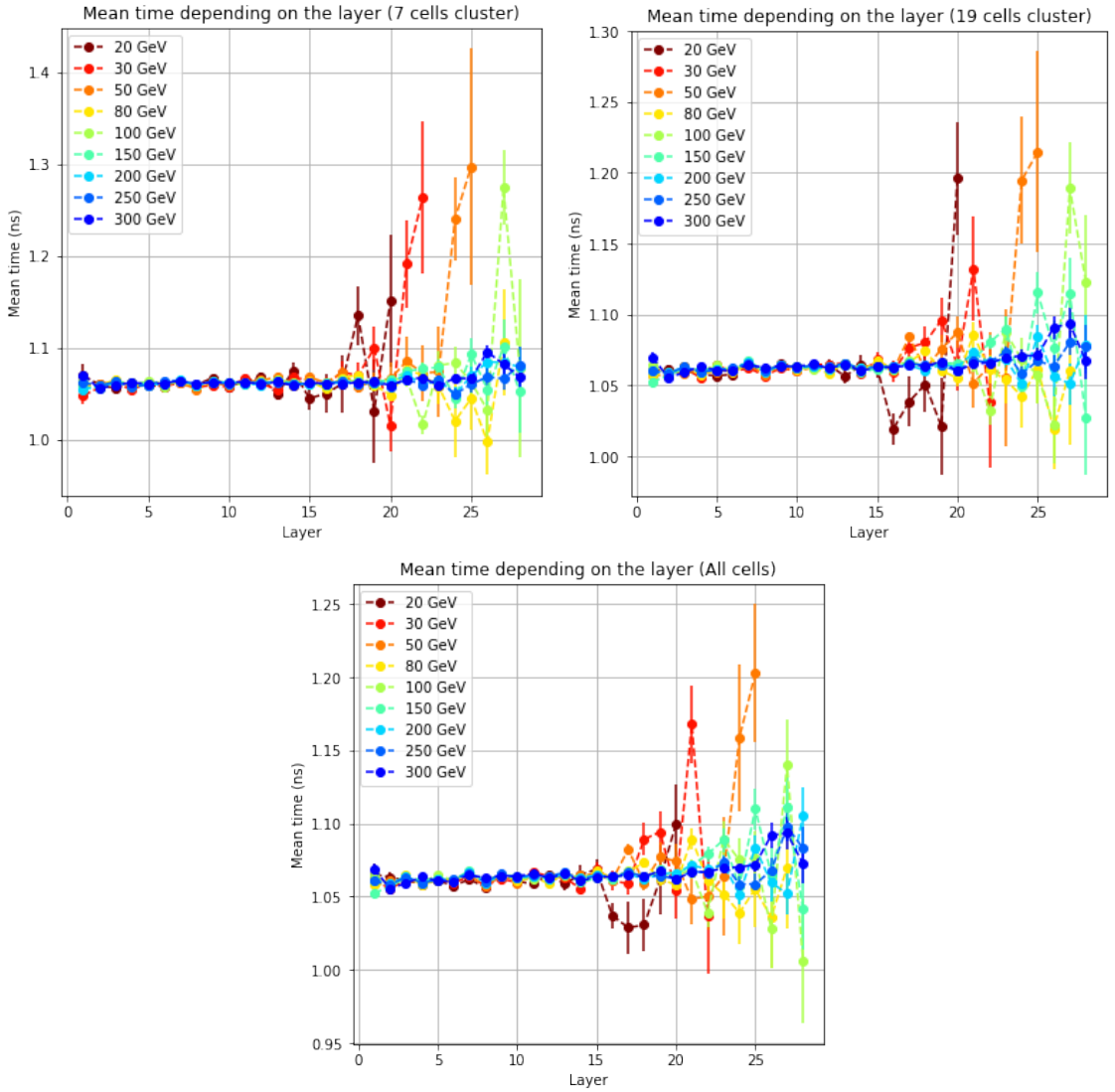

Figure 4.26: Mean time of the Gaussian fit done on *ToA* distribution for each beam energy and as a function of the layer. On the left, 7 cells are used, then 19 cells in the middle, and all the cells on the right.

shown in Figure 4.28.

In this section, only the data is studied. Indeed, the information from MC simulation must be smeared in order to be compared with data, and the smearing parameters are calculated from the experimental single channel resolution.

The average per-cell timing performance of the calibrated *ToA* values is quantified as a function of the corresponding energy deposit. For this purpose, the *ToA* values are compared to a reference time measurement in bins. Three *ToA* distributions are given for different cell energy ranges in Figure 4.29.

The binning of the cell energy follows a logarithmic law. It is used to have bins containing a similar amount of information. Indeed, there are fewer events with high energy than with low energy. Then a Gaussian fit is performed for each bin. The average time and the standard deviation of the fits are then extracted. The last

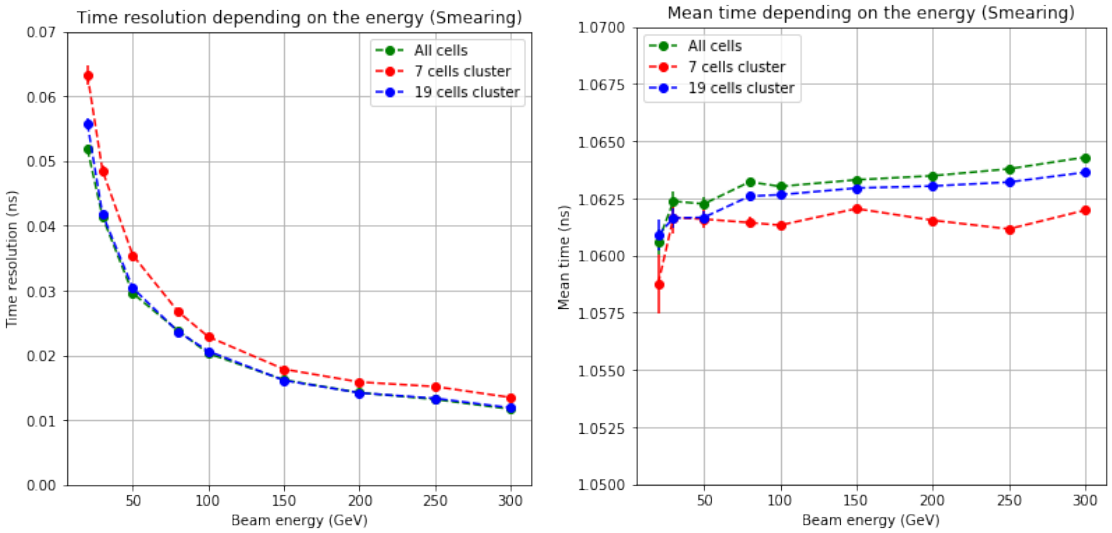

Figure 4.27: Standard deviation (on the left) and mean time (on the right) of the Gaussian fit done on *ToA* distributions as a function of the beam energy. In red 7 cells are used, in blue 19 cells, and all the cells in green.

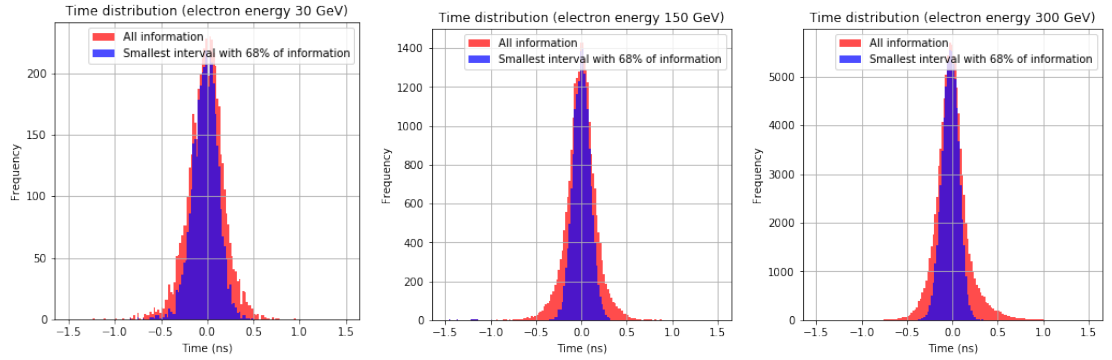

Figure 4.28: *ToA* distribution from data for a given positron beam energy. The blue distribution corresponds to the smallest interval containing 68% of the total *ToA* distribution represented in light red. From left to right, the positron beam energy is respectively equal to 30, 150, and 300 GeV.

one corresponds to the timing resolution.

The measured average time is found to be rather constant as a function of the beam energy, with deviations up to about 20 ps in the very low energy region (below 300 MIP), that are consistent with the outcome of the calibration procedure described in Section 4.3.1.

The measured resolution as a function of the deposited energy is done for two different choices of reference time measurement: in Figure 4.30 (black) this is provided by the MCP system, while in Figure 4.31 it is provided by one silicon cell within the HGCAL prototype itself, for pairs of cells from different modules (orange) and in the same. In each pair, different chips read out the considered cells. For both plots the timing resolution is fitted with $\sigma^2(E) = (a/E)^2 + c^2$, where E represents the energy, a is a term that decreases with signal amplitude, and energy,

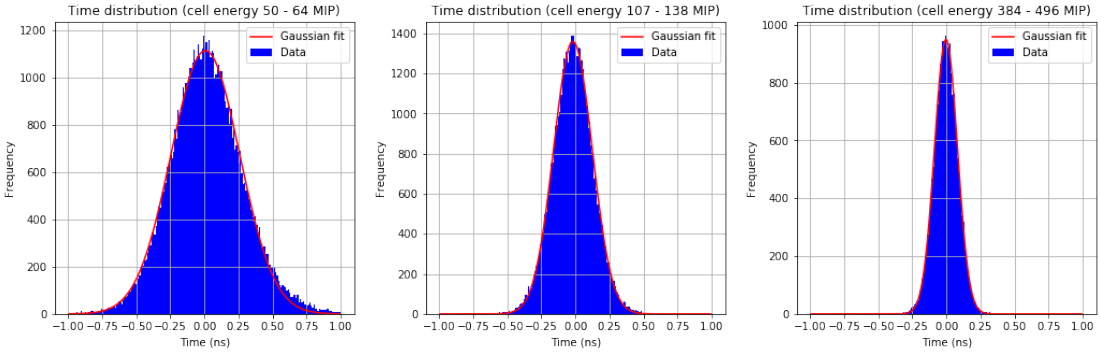

Figure 4.29: Experimental *ToA* distribution for a given range of cell energy. These distributions are fitted with a Gaussian function represented by the red line. From left to right, the cell energy range is respectively equal to [50,64] MIP, [107,138] MIP, and [384,496] MIP.

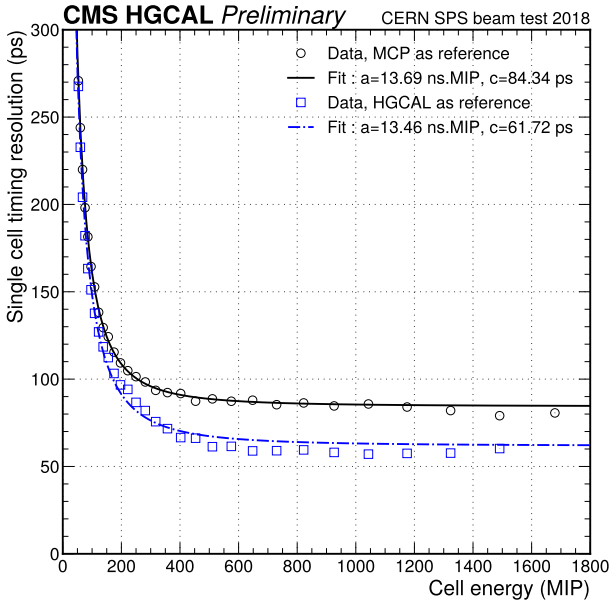

Figure 4.30: Comparison of the HGCAL prototype timing resolution for electron showers in data and simulated samples. For data, the resolution is measured for all layers using the MCP as a reference (black squares) as well as using only half the layers with respect to the other half and assuming they have identical resolution (purple triangles). Other measurements in the plot allow cross-checking and confirm the hypothesis that a global jitter between the MCP and HGCAL systems was present in the data.

and c is an irreducible, constant, term.

The constant term in Figure 4.30 includes the contribution of $\sim$25 ps due to the intrinsic timing resolution of the MCP system used as reference in Figure 3.25, providing a measurement of the average per-cell asymptotic timing resolution of $\sim$80 ps.

In Figure 4.31, the difference between the constant terms inferred from the same-module and different-module pairs clearly indicates the presence of timing correlations within the calorimeter prototype. Assuming the same timing resolution for all silicon cells, and a simple correlation model. One single correlation coefficient, independent of the cell energy or its position within the module. The constant term for uncorrelated cells is measured to be $\sim$60 ps, and a correlation coefficient $\rho \simeq 0.80$ can be inferred for cells in the same module.

The difference between the per-cell constant terms, when measured with the MCP and a with a silicon cell reference, indicates the presence of an additional smearing of about 50 ps between the HGCAL prototype and the MCP system. Although the source of this extra jitter could not be identified, and the setup no longer being available, we believe that it is constant and fully random, and thereby does not affect the performance of the calibration procedure of Section 4.3.1. The observed correlation has a negligible impact on the quoted results, as discussed in Section 4.3.4.

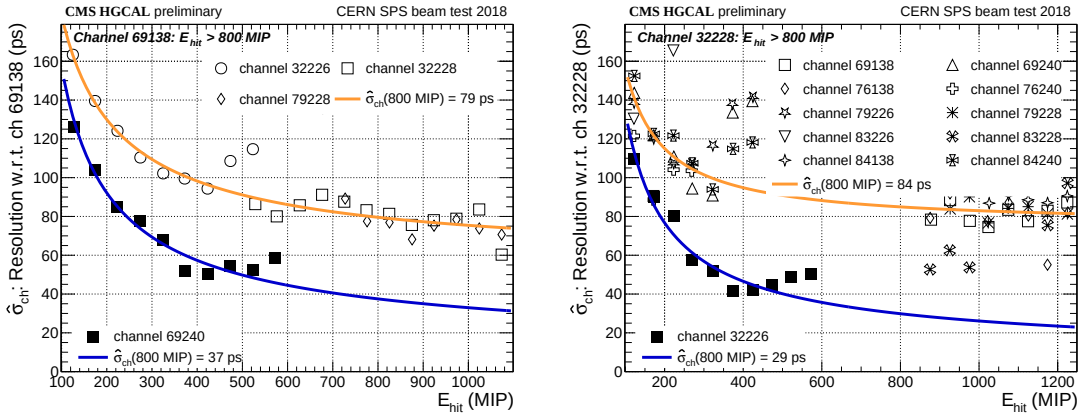

Figure 4.31: Single channel resolution as a function of the channel energy, using an other channel as timing reference chosen to be in a different module modules (orange) or on the same module (blue).

To measure the intrinsic timing performance of the HGCAL prototype, the calibrated *ToA* values are compared to an internal timing reference provided by the average time of the shower measured with the calorimeter prototype, as described in 4.30. Such a quantity is independent of any offset between the HGCAL prototype and the MCP system and is dominated by the per-cell timing resolution. The corresponding result is shown in 4.30 (blue squares) and fitted with the same resolution function. The resulting energy dependent term is identical to the one from the fit when using the MCP as the reference, while the difference between the two constant terms is consistent with the intrinsic timing resolution of the MCP system plus the inferred extra global event jitter.

As a summary, the timing resolution representative of the average per-channel performance, measured with the full readout chain, can be expressed as a function of the deposited energy as:

$$\sigma^2(E) \simeq \frac{(13.46\,\mathrm{ps})^2}{E^2} + (61.72\,\mathrm{ps})^2 \tag{4.11}$$

This resolution is in overall agreement with the electronics specifications of the Skiroc2-CMS ASIC and is used for the smearing of the Geant4 simulated hit timestamps for the analysis presented in the following sections.

4.3.4 Full shower performance

This section describes the timing performance evaluation from the level of a full shower. This resolution model is injected into the simulation and compared to the shower timing as measured in the actual data. Further studies of only HGCAL full shower timing resolution conclude this section.

The timing performance measured for full showers in data is compared to the Geant4 simulation. The same procedure mentioned in Section 4.3.2 was applied. First, only the smallest interval containing 68% of the *ToA* is taken into account, as it is shown in Figure 4.32.

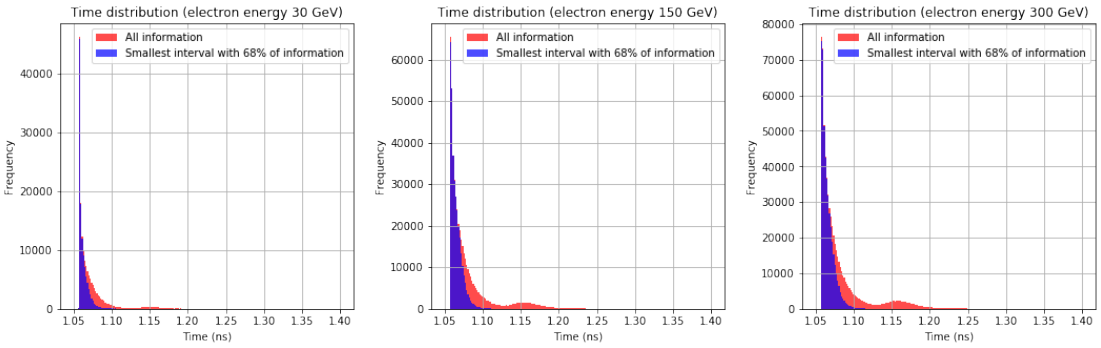

Figure 4.32: *ToA* distribution from simulation for a given positron beam energy. Blue distribution correspond to the smallest interval containing 68% of the total *ToA* distribution represented in light red. From left to right, the positron beam energy is respectively equal to 30, 150, and 300 GeV.

This first step is used to efficiently reject contribution from back scattering events. This outlier removal works correctly because the second peak of the light red distribution is no longer present in the blue one.In order to be able to do the comparison, realistic timing values are needed for the simulation, for this purpose, a smearing is applied on the *ToA* values from Geant4 with the average per-cell time resolution and given in Equation 4.11, including a term dependent on the energy deposited in the cell that is uncorrelated among the cells, and a constant term of ∼62 ps. This constant term includes a contribution from the MCP measurement of ∼25 ps and an additional jitter, discussed in Section 4.3.3, of ∼50 ps. Both contributions to the constant term are correlated over all the cells. The changes bring b the smearing on the *ToA* distributions are represented in Figure 4.33.

Since the smearing contribution is randomly taken from a normal distribution, the shape of the smeared *ToA* distribution is also Gaussian. This Gaussian feature is conserved with the energy. The Figure 4.34 proposes a better representation of the smearing effect on *ToA* for different cell energies. In this case, the constant part of the *ToF* was not removed, since this plot has just an illustration purpose

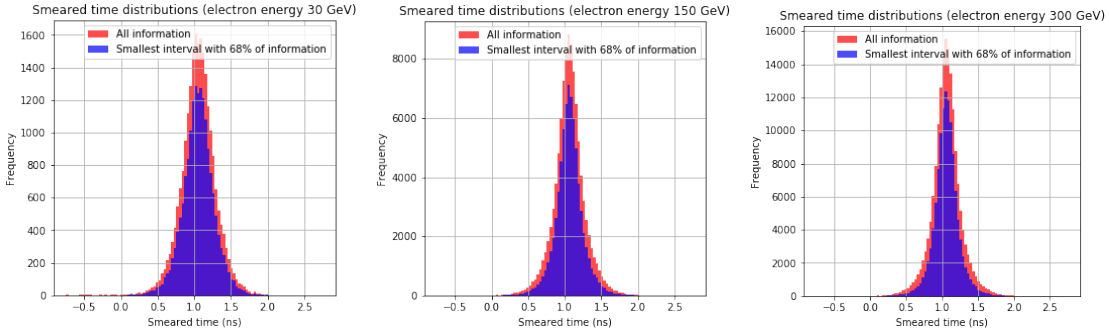

Figure 4.33: Smeared *ToA* distribution from simulation for a given positron beam energy. The blue distribution corresponds to the smallest interval containing 68% of the total smeared *ToA* distribution represented in light red. From left to right, the positron beam energy is respectively equal to 30, 150, and 300 GeV.

and this offset does not impact the standard deviation of the Gaussian fit. But, in the following it is removed.

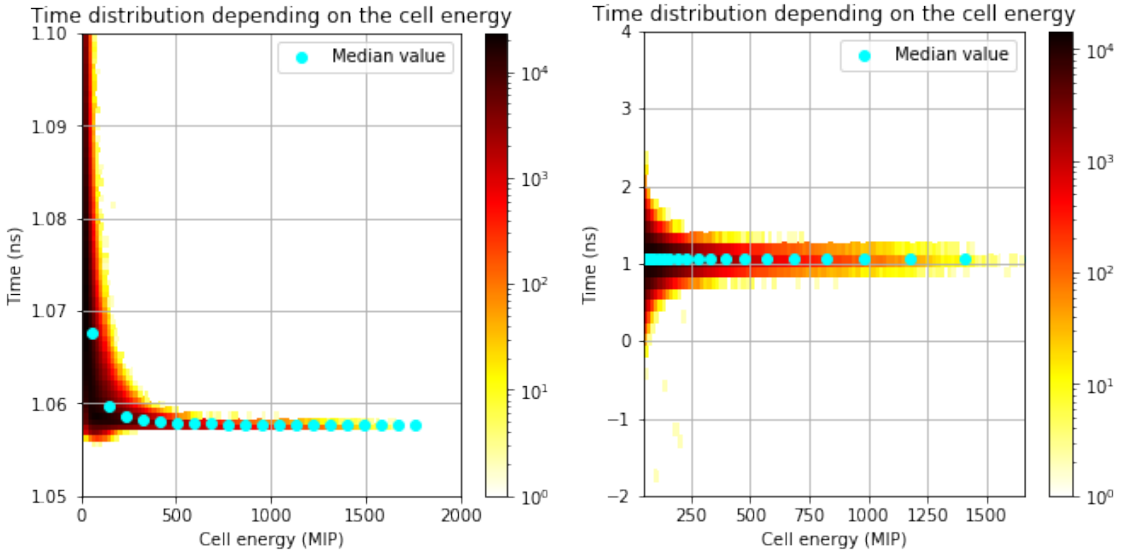

Figure 4.34: 2D *ToA* distribution as a function of the cell energy. Blue points correspond to the median value of each energy bin. The *ToA* distribution is on the left, and the smeared *ToA* distribution is on the right.

A study was performed in order to understand if the selection of events can impact the timing resolution. As it is shown in Figure 4.35, the selection is done with the same parameters as before and with the addition of different thresholds applied to the shower energy. Then, the timing resolution is computed for each energy threshold, and the computation is done using the MCP reference as well as the intrinsic resolution. In both cases, the resolution constant term increases with the value of the minimum energy required per event. This comforts the choice to not select only the most energetic showers.

The average time of a shower, $\bar{t}$, is estimated as the weighted average over the times, t_i, of the (n) contributing cells:

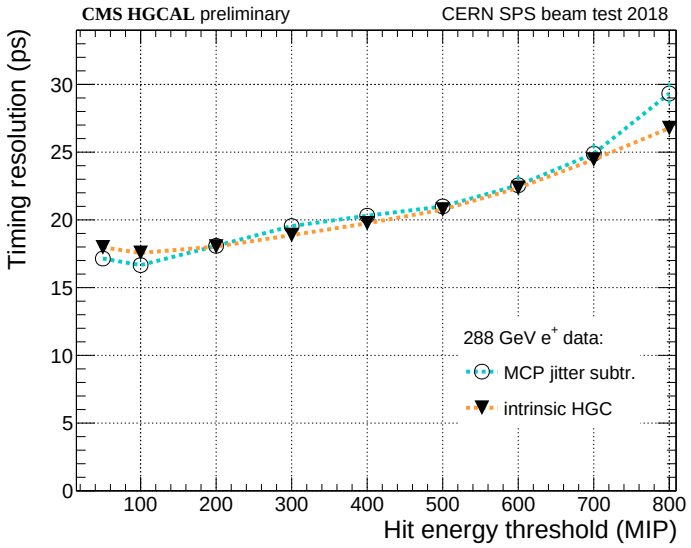

Figure 4.35: Time resolution constant term as a function of the hit energy threshold, only a single electron energy is considered. The resolution is measured for full layers, firstly using the MCP as reference and with a jitter subtraction (black circles linked with blue dashed lines), and secondly the intrinsic HGCAL resolution (black triangles linked with orange dashed lines).

$$\bar{t} = \frac{\Sigma_{i=1}^{n} w_i t_i}{\Sigma_{i=1}^{n} w_i}, \text{ where } w_i = \frac{1}{\sigma^2\left(E_{hit}\right)} \tag{4.12}$$

These shower time values are then fitted with a Gaussian function in bins of the particle beam energy. This allows to extract the average time and its standard deviation as a function of the impinging particle energy. The standard deviation from this fit is referred to in the following as the fitted resolution. The resolution weighted *ToA* distributions are represented in Figure 4.36, where the Gaussian fits are shown with the red lines.

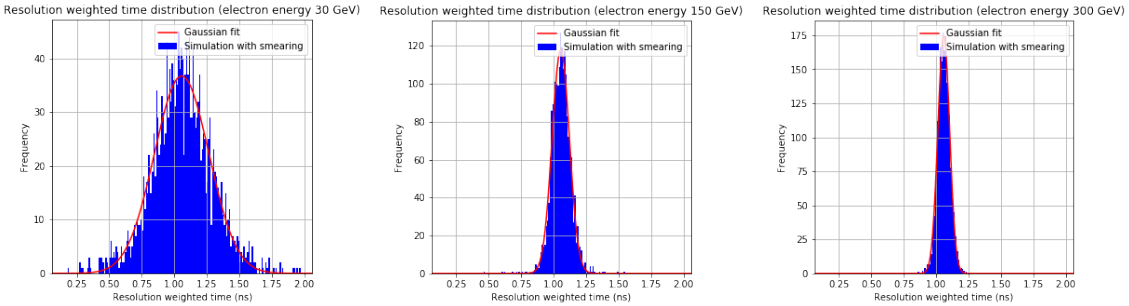

Figure 4.36: Smeared *ToA* distribution from simulation for a given positron beam energy. These distributions are fitted with a Gaussian function represented by the red line. From left to right, the positron beam energy is respectively equal to 30, 150, and 300 GeV.

To consolidate the characterization of the dataset, the average of the per-event

uncertainty is also computed using uncertainty propagation rules. This is referred to as expected resolution, $\sigma_{\bar{t}}$, in the following:

$$\sigma_{\bar{t}} = \frac{1}{\sqrt{\Sigma_{i=1}^{n} w_i}} \tag{4.13}$$

Figure 4.38 shows the results for the average time and the resolutions, as well as a good agreement between data and simulation, when including all previously-discussed smearing terms. The presence of the additional jitter between the calorimeter prototype and the MCP detectors clearly deteriorates the observed timing resolution performance for full showers, with a constant term of $\sim$56 ps, compared to $\sim$62 ps for single cells.

Correlation effects

To evaluate the impact of the timing correlation discussed previously, the full shower performance is re-evaluated by replacing the Equations 4.12 and 4.13 with the more general:

$$\bar{t} = \sigma_{\bar{t}}^2 \left(J^T W X \right) \text{ and } \sigma_{\bar{t}}^2 = \left(J^T W J \right)^{-1} \tag{4.14}$$

Where $X = [t_1, ..., t_n]$, $J = [1, ..., 1]^T$, and $W = C^{-1}$, where C is the covariance matrix among the t_i measurements:

$$C = \begin{pmatrix} \sigma_1^2 & \dots & \sigma_{ij} \\ \vdots & \ddots & \vdots \\ \sigma_{ij} & \dots & \sigma_n^2 \end{pmatrix} \text{ , where } \sigma_{ij} = \rho \cdot \sigma_i \sigma_i = 0.8 \cdot \sigma_i^2 \text{ for off-diagonal terms.} \tag{4.15}$$

An example of covariance matrices between channels is given in Figure 4.37. The correlations of the mean value as well as the resolution are represented, the only difference with the formula of Equation 4.15 consists in the fact that the matrices are filled bottom up, and not the inverse way, which causes the flip of the diagonals.

The analysis was repeated following the same procedure described above, and the obtained results differ from those shown in Figure 4.38 by only a few picoseconds.

Thus, the observed correlation has a small impact on the quoted performance, in particular, much smaller than the $\sim$50 ps additional jitter encountered. For simplicity, the reminder of the results reported in this thesis does not include the correlation model discussed in this section.

The constant term, on the other hand, is almost twice smaller than when using the MCP as reference, due to the absence of the jitter between the MCP and the HGCAL prototype.

The green markers in Figure 4.38 further illustrate the estimated performance when using all layers for the shower timing determination, meaning that it is dividing by $\sqrt{2}$ the resolution observed in half-shower data.

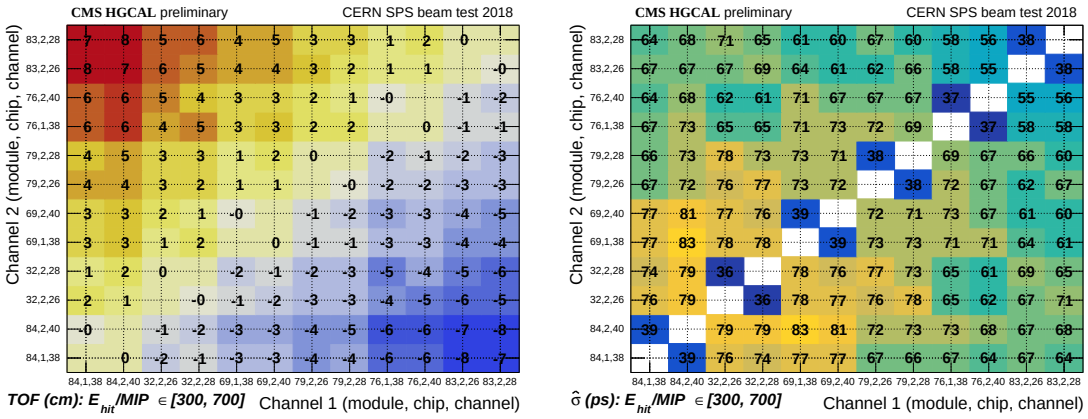

Figure 4.37: Correlation matrices between two channels, where they can be from different modules and connected to different chips. Correlation of the mean value on the left, and the resolution on the right.

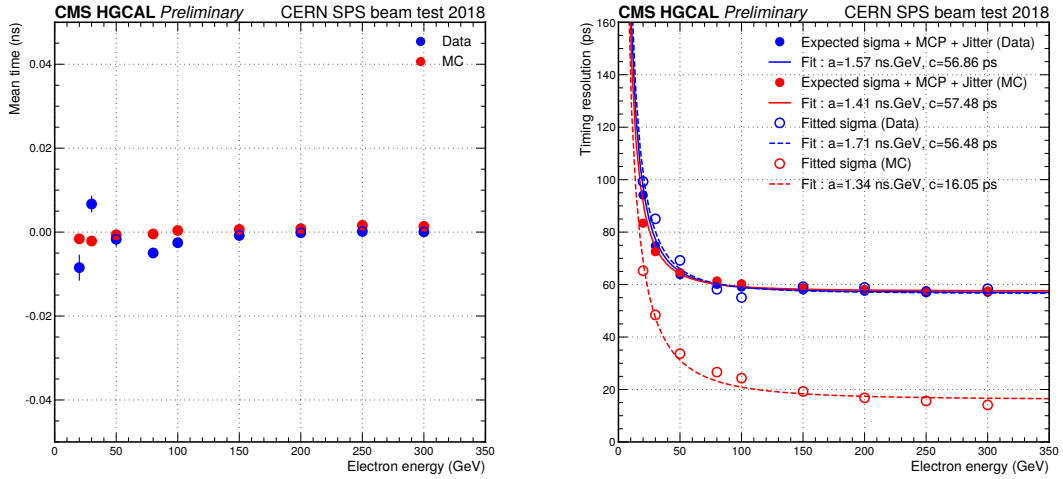

Figure 4.38: For electron showers contained in the HGCAL prototype, their average time on the left, and their timing resolution as a function of the beam energy on the right, for both beam data and simulated MC data.

The constant term of ∼16 ps for the full calorimeter prototype estimate in Figure 4.38 is consistent with the constant term for simulated data that does not include the ∼50 ps correlated jitter that is shown in the right plot of the figure.

Concerning the hadronic showers, the constant term of ∼39 ps for the electromagnetic calorimeter prototype estimate in Figure 4.39 is consistent with the constant term for simulated data that does not include the ∼100 ps correlated jitter. Moreover, the resolution difference between the two types of showers is first due to their nature because hadronic showers are much more complex, and also because part of the information is not taken into account because hadronic showers will have part of their hits contained in the CE-H or in AHCAL.

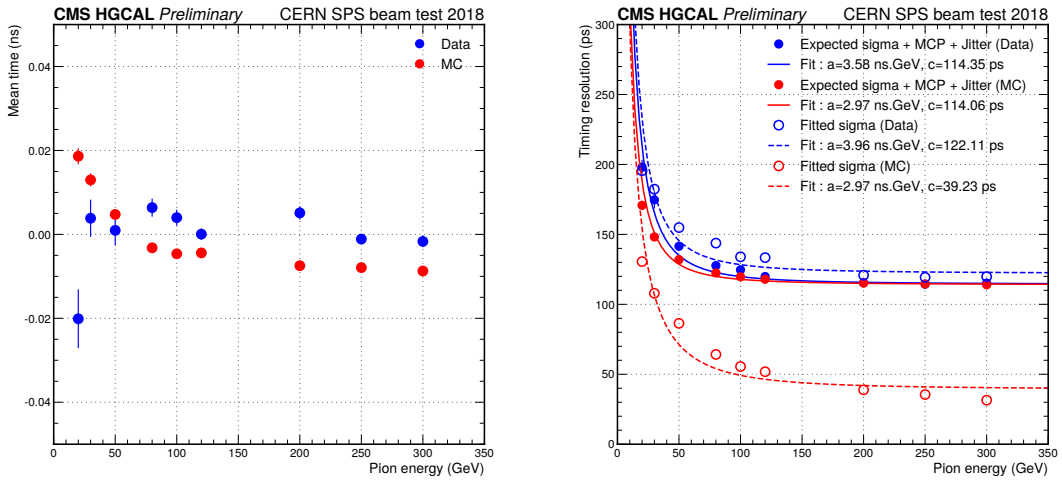

Figure 4.39: For pion showers contained in the HGCAL prototype, their average time on the left, and their timing resolution as a function of the beam energy on the right, for both beam data and simulated MC data.

Intrinsic timing resolution of the HGCAL prototype

The intrinsic timing performance of the HGCAL prototype can be characterized in spite of the experimental jitter observed between the calorimeter and the MCP devices. This is achieved by splitting the calorimeter into two equivalent halves for analysis purposes, each half acting as a reference and a target timing measurement, respectively. Even and odd layers are considered separately, and the time difference between the two half-showers reconstructed in each of the halves of the calorimeter is considered on an event-by-event basis.

The intrinsic time resolution is then determined under the assumption of similar time resolution of both halves, by taking the standard deviation of the time difference between the halves divided by $\sqrt{2}$.

Timing properties of electromagnetic showers

The timing resolution of the reconstructed electromagnetic showers using all layers in beam data is shown in Figure 4.41 as a function of the energy sum of hits in the shower and as a function of the number of contributing hits.

The resolution is observed to scale according to the expectation, with a continuous trend across different beam particle energies and hit multiplicities, that also have different beam profiles. This agreement shows that the shower time determination is stable with respect to varying beam conditions, including different beam profiles.

The differential measurements obtained with pion data again show that only a part of the full shower is probed, and the few points corresponding to large values of the x axis are affected by important statistical fluctuations.

The time distribution of the fraction of hits that were calibrated and used in

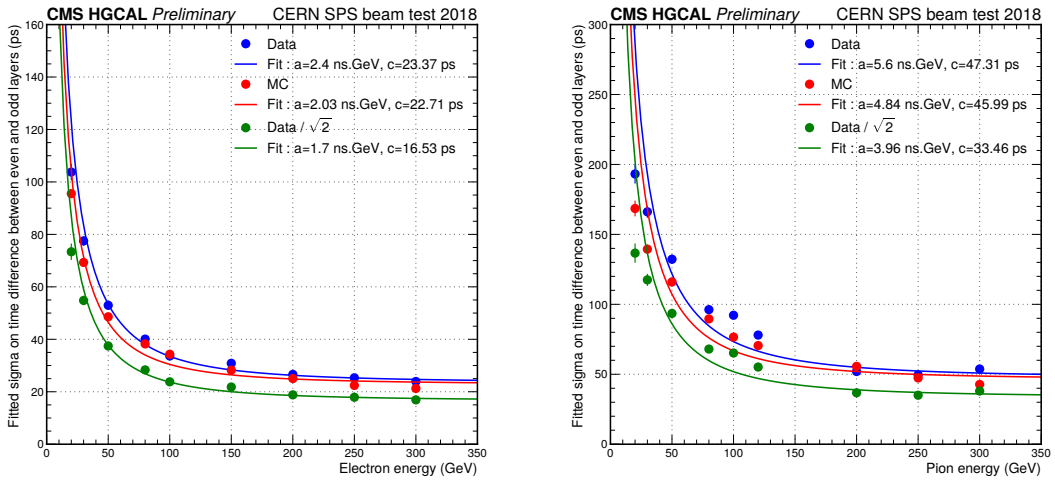

Figure 4.40: Resolution of the event-by-event difference between the time of electron half-showers computed with only even layers and only odd layers separately, as obtained for beam data (blue) and simulated Monte Carlo data (red). Results using positron beams are given on the left, and with pion beams on the right. The green markers correspond to beam data resolutions divided by $\sqrt{2}$, and are an estimate of the performance expected if all the layers were used for the shower time estimation. These measurements are not affected by the jitter between MCP and HGCAL.

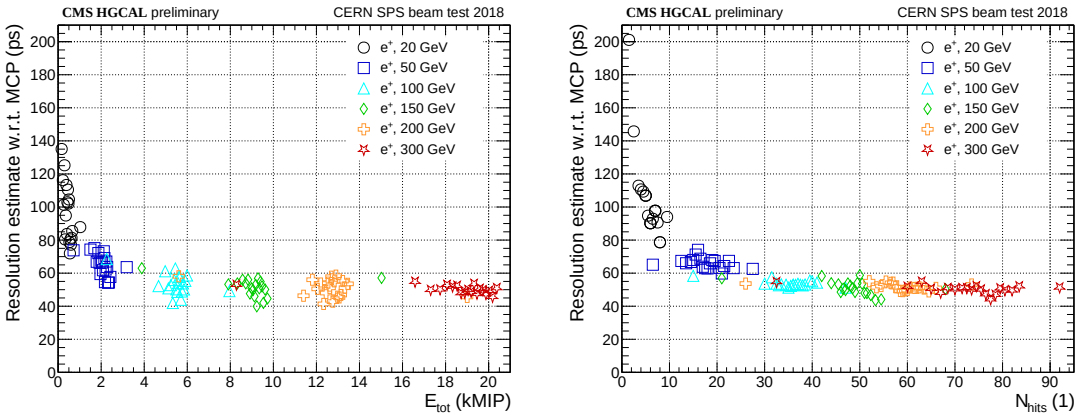

Figure 4.41: Time resolution of the reconstructed electron showers as a function of the energy sum on the left, and of the number of hits on the right.

the reconstruction of 300 GeV electron showers is displayed in Figure 4.42a for both beam data and simulated data, showing a good agreement between the two. For the same showers, Figure 4.42b shows the energy distribution of the hits as a function of their calibrated time. One can see that the most energetic component of the shower is deposited at times around zero by construction of the calibration. Also, in this case a reasonable agreement is found between beam data and simulated data.

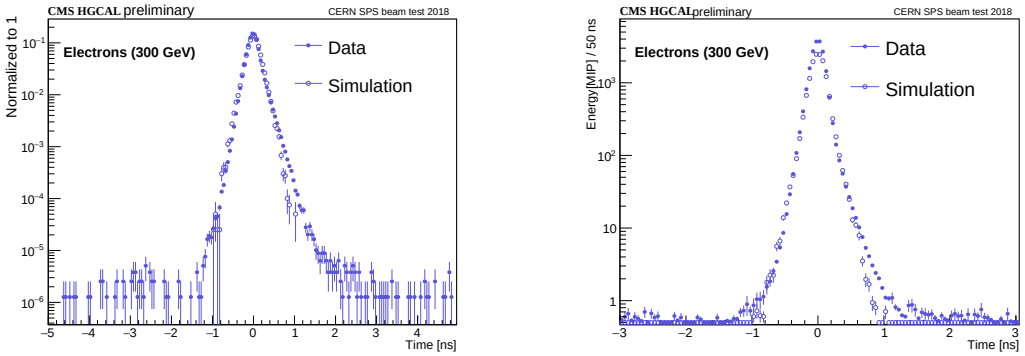

(a) Time distribution of hits.

(b) Time distribution of hit energy.

Figure 4.42: For the hits used in the reconstruction of the same 300 GeV electron showers, the time distribution of the fraction of hits on the left, and the energy distribution of the hits as a function of their calibrated time on the right. Beam data in full markers and simulated data in empty markers.

Timing properties of hadronic showers

The timing performance of the HGCAL prototype has also been checked by using the available pion data. Since the calorimeter prototype consists of the only electromagnetic section, when dealing with pions only a part of the full shower is detected and considered in the analysis.

Moreover, as explained in Section 3.4 the MCP detectors contribute with $\sim$100 ps timing resolution dominating the total resolution term.

The measured and expected sigma, for data and the Geant4 based simulation, are shown in Figure 4.39 as a function of the pion beam energy. Compared to electron data, this analysis of hits from pion showers shows timing performance limited by the different phase space, in terms of total energy deposits and number of hits with a lack of high energy hits. Nevertheless, the observed ballpark agreement between data and simulation, also in comparison with results from electrons, indicates consistent results.

In the same way, the timing resolution of hadronic showers depending on the number of hits or the energy sum, shown in Figure 4.43, does not show a good separation of the different beam energies as it was the case for positron beam. This limitation is mainly driven by the use of only the electromagnetic section of the HGCAL prototype to perform this study.

4.4 Conclusion on the HGCAL prototype performance

In this chapter, the three analyses presented were about the performance measurement of the first HGCAL prototype in a beam test.

The first one concerns the performances related to the detection of electromagnetic shower. The work performed as part of this thesis corresponds to preliminary studies where all the performances presented were obtained and which were presented inside the CMS HGCAL working group. For reasons of consistency, the

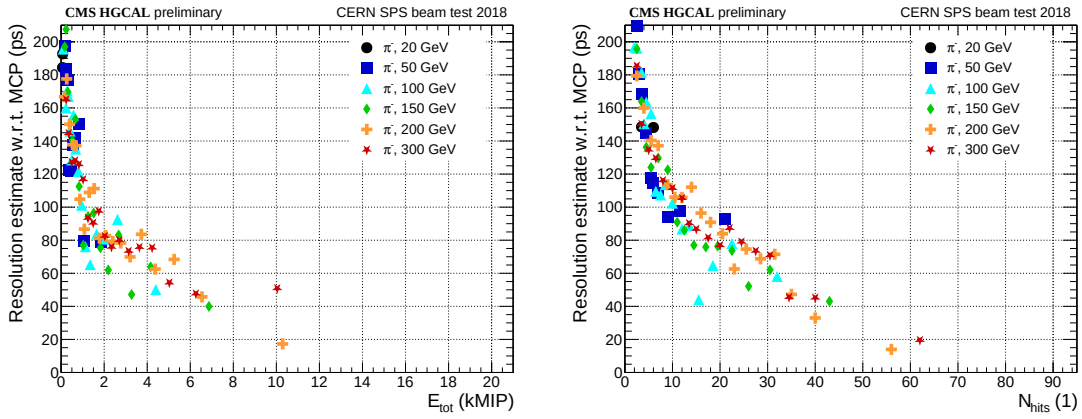

Figure 4.43: Time resolution of the reconstructed hadronic showers induced by pions as a function of the energy sum on the left, and of the number of hits on the right.

results shown in the different plots are those using the latest version of the calibration which was also used to perform the timing analysis. Indeed, the energy calibration applied on the data used for this last analysis was derived from the work carried out on the electromagnetic showers.

In this first part, the energy resolution and linearity were calculated and show results validating the designed specifications. In the same way, the study of longitudinal and transverse profiles of the showers allows getting a precise spatial parametrization of them, as well as the validation of the geometry of the detector since the EM showers were fully contained in the prototype.

The second part was about the performances related to the detection of hadronic showers and the work performed during this thesis consisted also to preliminary studying where the performances were calculated. Thus, exactly the same comments made for the first part can be made for this one. Similarly to what was said for the EM showers, the energy resolution and linearity computed from the hadronic shower show also results corresponding to the technical specifications. Furthermore, the study of the geometric characteristics of the showers, both longitudinally and transverse, made possible to validate the design of the prototype.

Moreover, both of these analyses show a good agreement between the data collected during the test beam and the MC simulation. And even if the HGCAL prototype that was used during the beam tests does not fully reflect the final version of the detector that will be installed in the CMS experiment, the analysis of its characteristics nevertheless allows us to validate its design in terms of expected performance.

The third analysis presented in this chapter was about the measurement of the timing performance of electron showers in the beam test with the first HGCAL prototype based on precise timing information. All this part corresponds to an original work carried out during this thesis and with the collaboration of other members of the CMS HGCAL timing working group. The focus of the analysis was to characterize the timing performance for single channels and full

showers in comparison with the designers' specifications, including the tuning and comparison to a Geant4 simulation.

After a detailed calibration of the *ToA* response, 116 readout channels in the central electromagnetic section could be fully calibrated, with an average asymptotic per-channel timing resolution of ∼62 ps, which is consistent with the electronics specifications. The time measurement provided by the MCP system was exploited as a reference throughout the calibration process and the MCP detector itself was measured to have a time resolution of the order of 25 ps. An additional ∼50 ps jitter between the MCP and HGCAL systems was found from the analysis of the data: although the original setup used during the data taking was no longer available and the origin of this additional jitter cannot be identified, this jitter is expected to be constant and fully random, such that its presence does not compromise the completed calibration performance. Due to limited amounts of data, only channels in the central electromagnetic section of the HGCAL prototype were calibrated. The timing performance of full electron showers was measured on data and compared with a simulation, where the ideal timing information was smeared according to the single-channel resolution model derived from data.

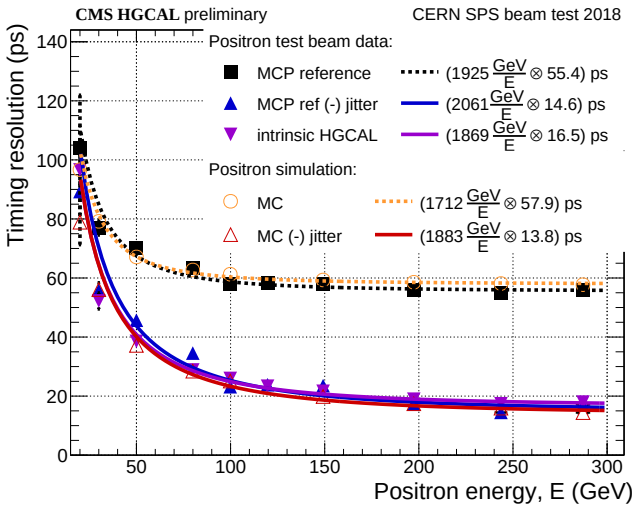

Figure 4.44: Comparison of the HGCAL prototype timing resolution for electron showers in data and simulated samples. For data, the resolution is measured for all layers using the MCP as a reference (black squares) as well as using only half the layers with respect to the other half and assuming they have identical resolution (purple triangles). Other measurements in the plot allow cross-checking and confirm the hypothesis that a global jitter between the MCP and HGCAL systems was present in the data.

The intrinsic performance of the HGCAL setup was tested by splitting the calorimeter prototype in two equivalent halves and taking the time difference between the two halves in reconstructing the same shower. The measured time resolution was found to be in agreement with simulation results and had a constant term of about 23 ps that corresponded to the time performance of a detector with equivalent total depth and only half the layers.

Figure 4.44 summarizes the measured resolution in data and simulation for

electromagnetic showers induced by positron, showing good agreement after taking into consideration the overall HGCAL-MCP system jitter that was observed. The results also show the intrinsic HGCAL prototype resolution having a constant term distinctly under 20 ps.

This work represents the first measurement of timing performance for calorimeter showers with a precision of tens of picoseconds and demonstrates the stability of the clock distribution tree used in this HGCAL prototype. The presented results can be understood as first experimental evidence of the possibility to complete $\mathcal{O}$(10 ps) timing resolutions with the new CMS high-granularity endcap calorimeter. This supreme timing performance will enable effective separation of pile-up interactions and, with it, contribute towards a successful operation of the CMS detector at the HL-LHC.

Chapter 5

The Golden Channel for the search of high mass resonance

Table of contents

5.1 Object selection . . . 156
5.1.1 Electrons . . . 156
5.1.2 Muons . . . 162
5.1.3 Photons . . . 167
5.1.4 Jets . . . 168
5.1.5 Summary of the object selection . . . 171
5.2 Event selection . . . 172
5.2.1 Trigger selection . . . 172
5.2.2 Z boson reconstruction . . . 173
5.2.3 ZZ candidate selection . . . 175
5.2.4 Optimization of the selection . . . 176
5.3 Event categorization . . . 188
5.3.1 Observables and discriminants . . . 188
5.3.2 Categories at high mass . . . 191

The second part of this thesis deals with the search for high mass resonance of the form $X \rightarrow ZZ \rightarrow 4l$ and this analysis is based on what was done for $H \rightarrow ZZ \rightarrow 4l$, as mentioned in Section 1.4.

Thus, in order to carry out this analysis, it is first necessary to be able to reconstruct the events of the Golden Channel and this starts with the reconstruction of the various primary objects which compose them, presented in Section 2.3. Then, to have the best leptons' purity while reducing the background, it is necessary to apply a selection on the various objects which is described in Section 5.1. In addition to this, energy calibration and corrections are applied so that the experimental and simulated data can be matched. To go further, the selection efficiency is studied to know the impact of the selection on the number of objects finally kept.

Once all these steps have been performed for each of the particle types, it is possible to reconstruct and select the events with $4l$, as explained in Section 5.2. Since this analysis is based on what was done for a H boson study, the mass range studied is around 125 GeV, and therefore the selection is optimized for this region. It is consequently relevant to check the behaviour of this selection at high mass in order to see its relevance and to adapt it if necessary.

The main goal of the selection consists of discarding the background events in order to have the best event purity. In this analysis, two signals are studied the gluon fusion $gg \to X \to 4l$ and the vector boson fusion $q\bar{q} \to X \to 4l$. Their main corresponding backgrounds are direct processes with the same final state, in which there is no X particle involved, such as $gg \to 4l$, but also electroweak (EW) processes of vector boson scattering and $Z + X$ standing for a set of processes made of a Z boson and something else, which is for instance composed of $Z+$ jets, $Z\gamma+$ jets, $t\bar{t}+$ jets, $WZ+$ jets, or $WW+$ jets.

The final step in processing the events is to distinguish from which mode of production each event originated. For this purpose, they are classified into mutually exclusive categories, each representing a mode of production. The categorization is done with the help of the different observables specific to the objects considered and also of the kinematic discriminants which are presented in more detail in Section 5.3.

5.1 Object selection

The first step of all the physics analyses performed with the CMS experiment consists of reconstructing the objects, allowing to build the events of interest. Since this step is performed, it is necessary to select them with appropriate criteria in order to be able to get only those coming from the decay of the event of interest. In the case of the Golden Channel, the two principal ingredients are the electrons and the muons. First, the different steps of the electrons selection and correction are described in Section 5.1.1. Then, the same presentation is made for muons in Section 5.1.2. In addition, photons radiated by both kinds of leptons must be taken into account to enhance the energy reconstruction as detailed in Section 5.1.3, and hadronic jets often produced during a VBF process are used to enhance this process identification as explained in Section 5.1.4. Most of the work presented in this section corresponds to the object selection studies performed in the context of the properties measurements of the Higgs boson in the $4l$ final state using the full Run-2 data [5].

5.1.1 Electrons

Once the electrons have been reconstructed as detailed in Section 2.3.2, they must be carefully selected in order to have candidates suitable for the study of the $H \to ZZ \to 4l$ decay. The selection starts with the first set of criteria used to get PF electrons. Then, additional criteria, based on the isolation and identification of electrons, are applied to reject non-prompt electrons which are not produced by a

Z boson decay. Moreover, these criteria allow increasing the purity of the selected H boson candidates.

Electrons selection

Firstly, the selection of electrons will consist of setting loose requirements on the transverse momentum and speed of the PF electron candidates. This is done with the objective of preserving as much as possible the efficiency of the reconstruction while rejecting part of the QCD background contribution. For this purpose, the primary vertex from the tracks is used to introduce additional cuts. These are composed of geometric requirements with $|\eta_e| < 2.5$, $d_{xy} < 0.5$ cm, and $d_z < 1$ cm. But also an energy criterion with $p_T^e > 7$ GeV. Where d_{xy} and d_z are respectively the absolute values of the electron impact parameter with respect to the primary collision vertex in the transverse plane and in the longitudinal direction.

Once these criteria are applied, the electrons that satisfy them are called loose electrons. Furthermore, an additional requirement concerning the significance of the impact parameter (SIP) with respect to the primary vertex is imposed:

$$\mathrm{SIP}_{3D} = \frac{|\mathrm{IP}_{3D}|}{\sigma_{\mathrm{IP}_{3D}}} \tag{5.1}$$

Where IP_{3D} is the impact parameter of the lepton track in three dimensions with respect to the primary vertex position and $\sigma_{\mathrm{IP}_{3D}}$ is its uncertainty. This parameter is used to ensure that the electrons are coherent with a common primary vertex, thus eliminating the presence of false electrons from photon conversion. To achieve this objective, it was chosen to have $\mathrm{SIP} < 4$.

The identification (ID) and isolation (ISO) of electrons are carried out jointly using a multivariate discriminant implementing the eXtreme Gradient Boosting (XGBoost) algorithm [153]. This algorithm defines a series of boosted decision trees (BDT) that are specifically trained to discriminate between prompt and isolated electrons from Z boson decays on the one hand and jets or products of hadronic decays that are considered as false leptons on the other. In order for the BDT to carry out their mission, they are trained on simulated Drell-Yan samples with jets. The training is carried out separately for each of the three data collection periods considered in the analysis, meaning 2016, 2017 and 2018. In the end, a total of 25 observables sensitive to the properties of electron candidates are used. All these observables are summarized in the Table 5.1. In addition, the BDT are trained to distinguish between prompt and non-prompt electrons. This recognition is based on parameters linked to the shape of the ECAL cluster, the correspondence between the cluster and the associated track, the information about the track quality, the PF isolation sums, and the average energy density. This last parameter is calculated from events introduced in the BDT training in order to ensure good PU resilience of the algorithm.

At the end, the best set of hyperparameters for the XGBoost model is determined with a grid search algorithm based on a Bayesian optimization procedure. More details and explanations are given in [154].

Table 5.1: List of observables used as inputs in the BDT employed for both the identification and the isolation of electrons.

Observable category	Observable	Definition
Cluster shape	$\sigma_{i\eta i\eta}$	RMS of the energy of crystal number i spectrum along η
	$\sigma_{i\phi i\phi}$	RMS of the energy of crystal number i spectrum along ϕ
	η width	Width of the ECAL SC along η
	ϕ width	Width of the ECAL SC along ϕ
	H/E	Ratio of hadronic energy behind the electron SC to the SC energy
	$(E_{5\times5} - E_{5\times1})/E_{5\times5}$	Circularity defined with the energy of 5×5 block of crystal centered in the highest energy crystal of the cluster seed $(E_{5\times5})$ and the energy from the strip of the crystals $(E_{5\times1})$
	$R_9 = E_{3\times3}/E_{SC}$	Sum of the seed and the adjacent 3×3 crystals centered in the high energy crystal $(E_{3\times3})$ divided by the SC energy (E_{SC})
	E_{PS}/E_{raw}	Fraction of energy in the pre-shower subdetector
Track-cluster matching	E_{tot}/p_{in}	Ratio of the supercluster energy to the inner track momentum
	E_{ele}/p_{out}	Ratio of the energy of the PF cluster to the associated outer track momentum
	$1/E_{tot} - 1/p_{in}$	Energy-momentum agreement
	$\Delta\eta_{in} = \lvert\eta_{tot} - \eta_{in}\rvert$	Position matching in η between the SC energy and inner track extrapolation
	$\Delta\phi_{in} = \lvert\phi_{tot} - \phi_{in}\rvert$	Position matching in ϕ between the SC energy and inner track extrapolation
	$\Delta\eta_{seed} = \lvert\eta_{seed} - \eta_{out}\rvert$	Position matching between the cluster seed and the outer track extrapolation to the ECAL
Track information	$f_{brem} = 1 - p_{ou}/p_{in}$	Fractional momentum loss between inner and outer tracks
	N_{KF}	Number of hits of the KF tracks
	N_{GSF}	Number of hits of the GSF tracks
	χ^2_{KF}	Reduced χ^2 of the KF tracks
	χ^2_{GSF}	Reduced χ^2 of the GSF tracks
	N_{miss}	Number of expected but missing hits
	P_{conv}	Probability of the conversion vertex fit χ^2
Isolation	$\mathcal{I}_{\gamma}$	PF photon isolation p_T sum
	$\mathcal{I}_{\text{charged hadrons}}$	PF charged hadrons isolation p_T sum
	$\mathcal{I}_{\text{neutral hadrons}}$	PF neutral hadrons isolation p_T sum
PU resilience	ρ	Mean energy density in the event

The BDT training is performed in six independent slices of p_T^e and η_e, with a particular focus on low energy electrons. Two p_T^e regions with a bin limit at 10 GeV are defined, each comprising three η_e regions with a lower limit at 0.8 and the upper one at 1.479. The performance of the model is assessed by examining the corresponding receiver operating characteristic (ROC) curves in each training bin and quantified by measuring the area under the curve (AUC). The ROC curves for the 2018 training in the $|\eta_e| > 1.479$ region for the $p_T^e < 10$ GeV and $p_T^e > 10$ GeV classes are presented in Figure 5.1.

The selection of the electron candidates is operated if their associated BDT score is sufficiently large. Then, the distributions for signal and background electrons are normalized. They are derived from the training on the 2018 dataset, which is

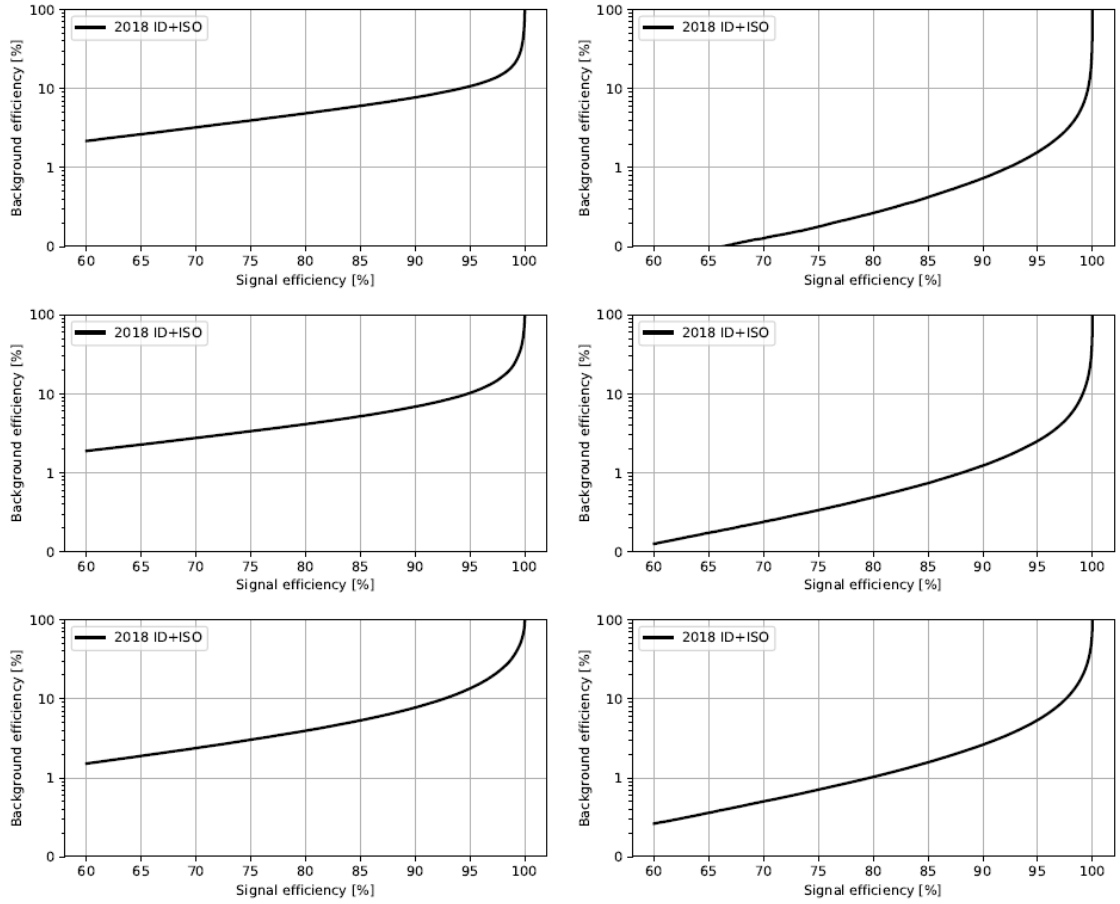

Figure 5.1: The ROC curves of the MVA developed for the electron identification in 2018 data. The training was performed on the 2018 MC simulation samples. Performance are shown for electrons with $5 < p_T^e < 10$ GeV on the left, and $p_T^e > 10$ GeV on the right. Both are done for three different η_e regions: $|\eta_e| < 0.8$ on the top, $0.8 < |\eta_e| < 1.479$ in the middle, and $|\eta_e| > 1.479$ on the bottom.

shown in Figure 5.2.

The operative working points of the BDT models are chosen separately for each data acquisition period. Moreover, they are specifically chosen to match the isolation and identification efficiencies obtained in the Run-1 analyses, and this even in cases where the performance is superior to the one from the approach using only kinematic observables. The operating point values are presented in Table 5.2, and correspond to an overall signal efficiency in the barrel of 95% for high p_T^e electrons and about 80% for low p_T^e electrons. For both kinds of electrons, it is of the order of 70% in the endcap region.

Electron energy calibration and correction

Once the isolation and identification has been optimized for electron selection, it is necessary to calibrate their energy. This calibration consists of a set of corrections, starting with the energy of the PF electrons. This is extracted by combining the information from the tracker and the electromagnetic calorimeter. For high

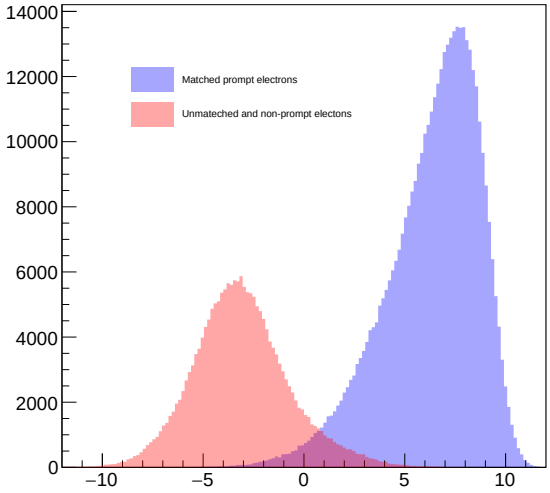

Figure 5.2: The BDT score distribution for the signal is re presented in blue, and for the background in red. BDT scores for electrons are obtained from the training on the 2018 dataset in the high p_T^e and $|\eta_e|$ bin, corresponding to the region $5 < p_T^e < 10$ GeV and $|\eta_e| > 1.479$.

Table 5.2: Minimum BDT scores required for the electron isolation and identification. Scores are computed for the six p_T^e and $|\eta_e|$ bins, and for the three different data taking years: 2016, 2017, and 2018.

2016			
	$\|\eta_e\| < 0.8$	$0.8 < \|\eta_e\| < 1.479$	$\|\eta_e\| > 1.479$
$5 < p_T^e < 10$ GeV	0.9503	0.9462	0.9387
$p_T^e > 10$ GeV	0.3782	0.3587	-0.5745
2017			
	$\|\eta_e\| < 0.8$	$0.8 < \|\eta_e\| < 1.479$	$\|\eta_e\| > 1.479$
$5 < p_T^e < 10$ GeV	0.8521	0.8268	0.8694
$p_T^e > 10$ GeV	0.9825	0.9692	0.7935
2018			
	$\|\eta_e\| < 0.8$	$0.8 < \|\eta_e\| < 1.479$	$\|\eta_e\| > 1.479$
$5 < p_T^e < 10$ GeV	0.8956	0.9111	0.9401
$p_T^e > 10$ GeV	0.0424	0.0047	-0.6042

transverse momentum electrons, the use of ECAL information is predominant over the tracker. The photon pairs from the π^0 decays ensure the accurate calibration of all ECAL crystals, thus guaranteeing a good reconstruction of the electrons and photons. Following this, specific corrections are calculated using a simulated sample of $Z \to e^+e^-$ and applied in p_T^e, $|\eta_e|$ slices of data. These are used to correct the residual misalignment between the data and the MC energy scales and to reduce the width of the e^+e^- mass spectrum. This is validated by matching the mass

resolutions $Z \to e^+e^-$ in the data and in the simulation is obtained by applying a pseudo-random Gaussian spread to the MC electron energies as a function of p_T^e and $|\eta_e|$. Once this step is complete, the energy scale of the electrons in the data from a Double Crystal Ball (DCB) fit to the $m_{e^+e^-}$ spectrum around the Z boson mass peak must be measured. The invariant mass e^+e^- and the corresponding energy scale and resolution are plotted in Figure 5.3 for the three data periods considered in this analysis treated in this thesis.

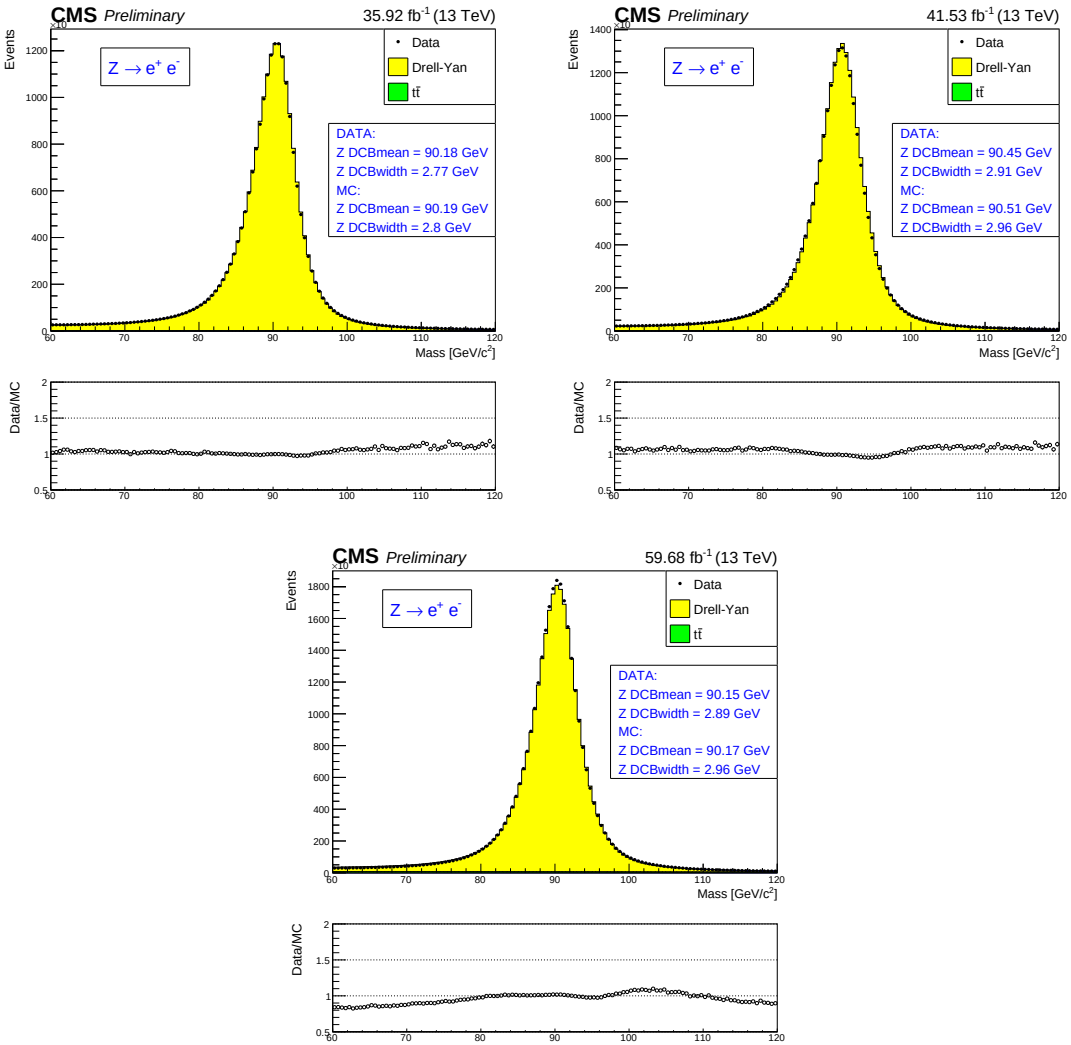

Figure 5.3: Electron pair energy distribution using $Z \to e^+e^-$ events. Data are represented with black points, while Drell-Yan background is represented in yellow and $t\bar{t}$ in green. Data corresponding to the 2016 period is shown on the top left, 2017 on the top right, and 2018 on the bottom. Electron energy scale correspond to the Double Crystal Ball fit mean and the resolution to the standard deviation.

These show that the agreement between the data and the modelling is globally satisfactory, although for large $m_{e^+e^-}$ values ($m_{e^+e^-} > 95$ GeV), a mismatch between the data and the MC energy scales is observed, in particular in the 2018 data

set. This effect is a possible consequence of a calibration problem of some crystals. But it may also be due to the loss of their response due to ageing. Ultimately, this effect has a marginal impact on the different analyses, as it is covered by the systematic uncertainties associated with lepton identification and energy scales.

Electron efficiency measurements

After applying the electron selection, it is necessary to know its impact on the number of events that are retained. To do this, it is necessary to study the electron selection efficiency, which is measured using a tag and probe technique applied on $Z \to e^+e^-$ events.

In order to perform the efficiency measurements, a model fit is used. To this end, the shape of the signal distribution $m_{e^+e^-}$ is taken from an MC simulation and convolved with a Gaussian. This is done for both successful and unsuccessful probes. The data is then fitted with the convolved MC model and an error function with a one-sided exponential tail. For slices of low p_T^e, a Gaussian is added to the signal model for the failing probes. The electron selection efficiency is measured as a function of the probe electron p_T^e and η_e.

In a nutshell, the electron efficiencies have been measured at about 95% for electrons with $p_T > 30$ GeV and are similar for the three years studied. The uncertainties in the measurement of low p_T electrons are very large due to the small number of events available. The total uncertainty for the scale factors (SF) measurement is the quadratic sum of the statistical uncertainties from the adjustment and the systematic uncertainties mentioned above. In these measurements, the largest source of uncertainty is the uncertainty in the FS measurement. As mentioned above, it is mainly statistical and comes from the low p_T ranges where there are not enough events to perform the adjustment in the failed probes.

5.1.2 Muons

In the same way as for the selection of electrons, muons are identified from the global PF candidates created. The following sections present the different identification and isolation criteria applied to these objects. These were chosen in order to obtain a set of good quality muons for the following steps of the analysis. Next, the calibration of the muon energy will be discussed before turning to the selection efficiency.

Muons selection

When talking about muon selection, it is necessary to take first elements from their reconstruction. For this purpose, the tracks of candidate PF muons are classified according to the sub-detectors used to reconstruct them. Thus, we can have different categories of muons. First, there are global muons reconstructed with both tracker and muon chamber information, then there are tracker muons reconstructed only from the tracker, and finally autonomous muons from the muon chambers only. For the purpose of this analysis, only global and tracker muons are

considered. The primary vertex of the tracks is used to introduce additional pre-selection cuts on PF muon candidates with geometric criteria $|\eta_\mu| < 2.4$, $d_{xy} < 0.5$ cm, and $d_z < 1$ cm, but also with a momentum threshold $p_T^\mu > 5$ GeV.

Furthermore, similarly to what is done for electrons, an additional requirement on the SIP with respect to the primary vertex is imposed. These identification criteria aim at reducing contamination from fake muons originating from in-flight decay of hadrons and cosmic rays. Therefore, it allows enhancing the selection of muons coming from the primary vertex. Once again the requirement is the same as the one for electrons, namely SIP < 4 for muons

The second part of the selection consists of distinguishing between prompt muons originating from the decay of Z bosons and muons originating from QCD processes where hadrons decay in a jet via the electroweak interaction. For this to happen, the energy flux in their neighbourhood must be below a given threshold. Thus, the definition of the relative isolation $\mathcal{I}_\mu$ from the muon p_T is based on the PF isolation. It has been determined that the relative isolation must be less than 0.35 to have a good distinction between the two types of muons. Subsequently, the contribution of the pile-up to the muon isolation cone must be subtracted. Such a correction is justified by the fact that during Run-2, data were collected with an average of thirty interactions per packet crossing, so that a large contribution can potentially affect the energy flux used for muon isolation and may lead to a loss of signal efficiency. For this purpose a correction called $\Delta\beta$ is applied, where this factor is defined as follows:

$$\Delta\beta = \frac{1}{2} \sum_{\substack{\text{charged} \\ \text{hadrons}}} p_T^{\text{PU}} \tag{5.2}$$

This coefficient is used because it gives an estimate of the unwanted energy deposition of neutral particles, both photons and neutral hadrons, from the pile up vertex. In addition, the factor of 0.5 corrects for the different fraction of charged and neutral particles in the neighbourhood of the muon under consideration. Then the relative isolation is defined as follows:

$$\mathcal{I}_\mu = \frac{1}{p_T^\mu} \left(\sum_{\substack{\text{charged} \\ \text{hadrons}}} p_T + \max \left[\sum_{\substack{\text{neutral} \\ \text{hadrons}}} p_T + \sum_{\text{photons}} p_T - \Delta\beta \right] \right) \tag{5.3}$$

In this equation, the different quantities correspond respectively to the scalar sum of the transverse moments of the charged hadrons from the chosen primary vertex of the event, the sum of the neutral hadrons and the sum of the photons. These three sums are called isolation sums, and they are all restricted to a volume bounded by a cone of angular radius $\Delta R = 0.3$ around the direction of the muon at the primary vertex, where the angular distance between two particles i and j is given by the formula :

$$\Delta R(i,j) = \sqrt{(\eta_i - \eta_j)^2 + (\phi_i - \phi_j)^2} \tag{5.4}$$

Moreover, a specific selection is applied to high p_T muons. When a loose muon with a large transverse momentum satisfy the condition $p_T^{\mu} > 200$ GeV, it is selected if it passes the Tracker High-p_T muon ID which is detailed in Table 5.3.

Table 5.3: Requirements for Tracker High-p_T muon identification.

Identification condition	**Description**
Muon station matching	The tracker muon is matched to segments in at least two muon stations
Good p_T measurement	$p_T/\sigma_{p_T} < 0.3$
Vertex compatibility	$d_{xy} < 2$ mm and $d_z < 5$ mm
Pixel hits	At least one pixel hit
Tracker hits	At least hits in six tracker layers

This ID will be particularly important for the research of high mass resonance analysis resented in this thesis. In addition, another selection criteria is applied on muons, which intervenes in the cases where a single muon can be misidentified as two or more particles. This problem is dealt with using a procedure called the ghost muon cleaning and consisting in removing tracker muons that do not satisfy the global muon definition. Moreover, if two muons share 49.9% or more of their track segments with other objects, only the one with the best track quality is retained. In this section, the ghost muon cleaning is part of the selection and the different quantities presented in this section, such as the $m_{\mu^+\mu^-}$ distribution or the muon reconstruction efficiency, are calculated with it. Although, the optimization of the selection for high mass events, which is described in Section 5.2.4, shows that the module doing the ghost muon cleaning is at the root of an important efficiency loss at high mass and does not have a real impact on background. That is why, it is no longer used for the $ZZ \to 4l$ analyses.

Muon energy calibration and correction

After applying the muon selection, it is necessary to check that their resolution does not affect the invariant mass of a possible resonance. Indeed, the resolution can lead to a muon scaling bias that would manifest itself by shifts in the position of the invariant mass peak of a resonance. For this reason, it is essential to probe the scale and resolution of the p_T muon and to extract appropriate corrections.

First, this can be done by exploiting the invariant mass distributions J/Ψ and Z. For this purpose, there are several methods for measuring the scale and resolution of muons in order to cover the whole p_T spectrum of muons down to the 1 TeV scale. The first one is the so-called Rochester method [155] because it was developed by physicists at the University of Rochester. It concerns the low and intermediate p_T range, and was developed to correct biases in the muon momentum reconstruction due to poor modelling of the detector alignment, magnetic field and energy losses. In fact, its interest comes from its sensitivity to the tracker alignment because the measurement of p_T in the mentioned p_T range is entirely tracker driven. From its use, it derives calibration constants using Z and J/Ψ events with a $\mu^+\mu^-$ decay which will be used with a matching procedure to

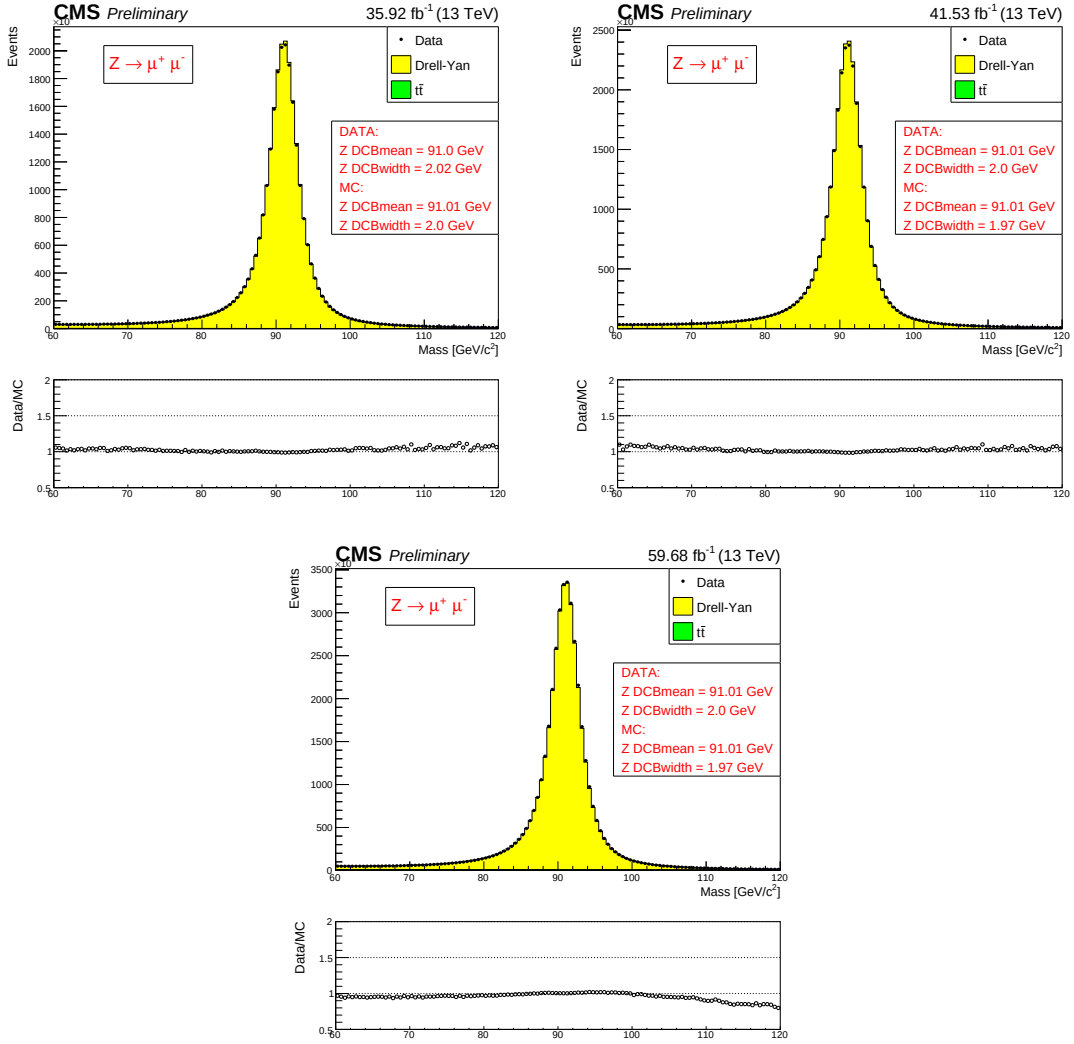

Figure 5.4: Muon pair energy distribution using $Z \rightarrow e^+e^-$ events. Data are represented with black points, while Drell-Yan background is represented in yellow and $t\bar{t}$ in green. Data corresponding to the 2016 period is shown on the top left, 2017 in the top right, and 2018 on the bottom. Muon energy scale correspond to the Double Crystal Ball fit mean and the resolution to the standard deviation.

obtain a configuration with a perfect match between the data and the simulated events. This procedure is carried out in several steps. For the muon scaling, the muons reconstructed from the MC data and simulation samples are corrected to match the generated muons from the simulation. In contrast, for the resolution, the simulated events are scaled to match the data.

The muon momentum scale is measured by fitting the mass spectrum $\mu^+\mu^-$ of the data using the Double Crystal Ball function. More precisely, the fit is made around the mass peak of the Z boson in the $Z \rightarrow \mu^+\mu^-$ control region. The energy scale and resolution are shown for the 2016, 2017 and 2018 data sets in Figure 5.4. This confirms that the fits made are in perfect correspondence with the data, and this for all three years as well.

Muon efficiency measurements

In the same way as for the electrons, the selection efficiency will be calculated to see the impact of the latter on the number of events retained. Even if the reconstruction of PF muons is simpler than that of electrons, there are still discrepancies between the data and the simulation. These discrepancies are found after the application of the selection criteria and in order to correct them, it is first necessary to measure the efficiency of the reconstruction and identification, both for the data and for the MC simulations. Then, appropriate SF must be derived to account for and correct for these effects, following the same strategy as for the electrons.

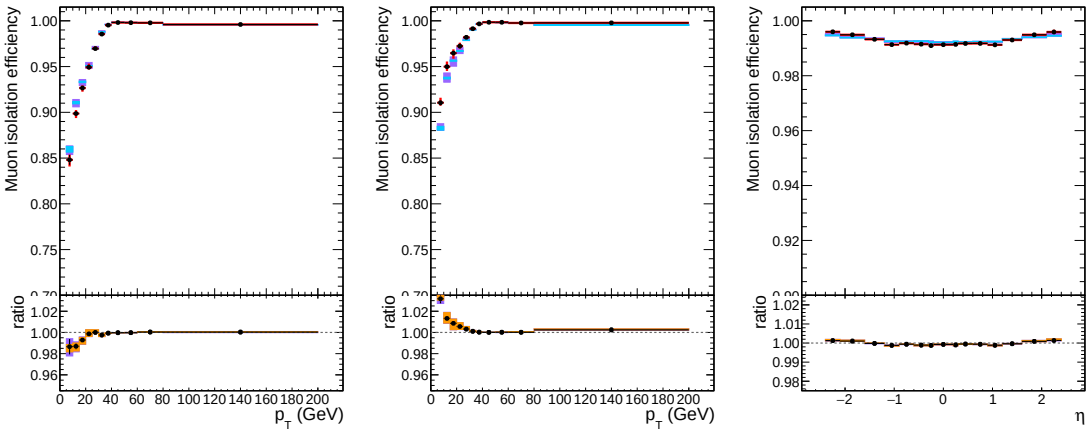

Figure 5.5: Muon reconstruction and identification efficiency at low p_T for the 2018 dataset using the tag and probe method.It is represented as a function of p_T in the barrel on the left and in the endcap regions in the middle, and as a function of η for $p_T > 5$ GeV on the right. Data and MC agreement is represented in the lower panel.

The same tag and probe technique used for electrons is applied to muons. The muon selection efficiencies are calculated in the different regions of the detector and are shown in Figure 5.5. Plots as a function of p_T^{μ} show that the efficiencies are greater than 99% in both the barrel and the endcaps. The calculation of the efficiency as a function of η_{μ} shows that this measure remains valid independently of the transverse momentum of the candidate muons.

Similarly, the Figure 5.6 shows the selection efficiencies only for loose muons in both regions of the detector. The efficiencies are above 98% in all regions of the detector, the accuracy of the measurement as well as the efficiency value is explained by the lower statistics of the loose muons.

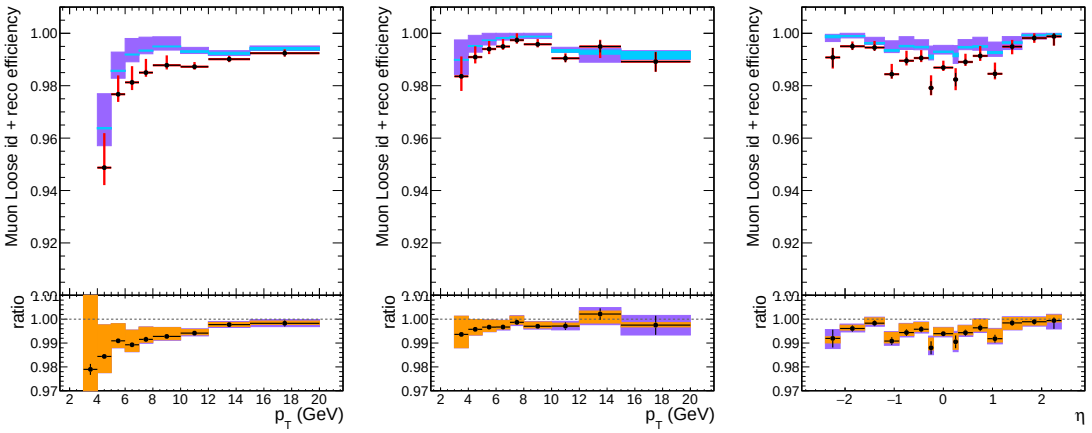

Figure 5.6: Loose muon reconstruction and identification efficiency at low p_T for the 2018 dataset using the tag and probe method.It is represented as a function of p_T in the barrel on the left and in the endcap regions in the middle, and as a function of η for $p_T > 5$ GeV on the right. Data and MC agreement is represented in the lower panel.

5.1.3 Photons

After presenting the selection of the two main elements of the analysis of this thesis, it is also necessary to focus on the reconstruction of the photons present in the events from the $H \to ZZ \to 4l$ decay. The processing of photons is necessary because of a phenomenon called final state radiation (FSR). Indeed, the probability that a photon with an energy higher than 2 GeV is radiated in a $Z \to l^+l^-$ decay is about 8% for $\mu^+\mu^-$ and 15% for e^+e^-. These proportions being far from negligible, this is why the photon energy must be included in the calculation of the invariant mass of the candidate boson H.

There are two categories of photons that need to be differentiated, firstly FSR photons and secondly all other photons from the initial state radiation (ISR). In order to make this distinction, a recovery algorithm for FSR photons is applied by exploiting their kinematics [156], The first part of the FSR photon selection consists in having $p_T^\gamma > 2$ GeV and $|\eta_\gamma| < 2.4$. In a second step, a criterion on relative isolation PF must be added, which must be lower than 1.8. For photons, this isolation is defined as :

$$\mathcal{I}_\gamma = \frac{1}{p_T^\gamma}\left(\sum_{\text{photons}} p_T + \sum_{\substack{\text{neutral}\\\text{hadrons}}} p_T + \sum_{\substack{\text{charged}\\\text{hadrons}}} p_T\right) \tag{5.5}$$

This isolation is only calculated from a cone of radius $R = 0.3$ and by applying a threshold of 0.2 GeV on charged hadrons and 0.5 GeV on neutral hadrons. Then, all leptons must pass the ID and SIP cuts, and they are grouped with the closest lepton. Finally, each selected FSR photon is excluded from the calculation of the isolation sum of all good muons in the event, considering photons that are within the isolation cone of radius $\Delta R < 0.4$ and outside the lepton muon isolation cone of radius $\Delta R > 0.01$.

5.1.4 Jets

The last type of object that remains to be discussed in the context of an analysis of the $H \to ZZ \to 4l$ channel are the jets. Once again, even if they are not part of the channel itself, they are sometimes found in the final state. For example, quarks in the initial state of a VBF event can continue their journey in the detector and generate jets. These form an additional signature to this type of production mode, which is why it is necessary to reconstruct and select them as well. Thus, an accurate reconstruction of the jets of the event is one of the keys to the discrimination of the different production mechanisms. Furthermore, the number of jets present in the event and their origin are used for event categorization, as described in Section 5.3. The analysis presented in this thesis exploits the reconstructed PF jets using an anti-k_T clustering algorithm with a radius $\Delta R = 0.4$ [124].

First, the calculation of the transverse momentum of the jets is based on the vector sum of the moments of all the particles that form them. A first selection of jets is applied and consists on the conditions $p_T^{jet} > 30$ GeV and $|\eta_{jet}| < 4.7$. These are cleaned from the presence of any tight lepton and any FSR photon requiring a radial separation of $\Delta R(jet, l/\gamma) > 0.4$.

Then a PU-derived jet identification algorithm is applied to jets with $p_T < 50$ GeV in order to mitigate the presence of extra traces and energy deposits in the calorimeters from the PU. The main reason for this choice is that the PU jet identification algorithm is trained with jets of $p_T < 50$ GeV, those with higher transverse momentum are the ones expected in the events of interest. This algorithm works with a BDT model that is trained with the following three features:

- The trajectories of the particles constituting the jet, this is to determine if the jet is compatible with the primary interaction vertex.
- The topology of the jet shape, which is used to discriminate true jets from PU-originated jets.
- The multiplicity of objects in the event.

From the BDT score, three work points are used for PU jet attenuation. The performance of the BDT for the free working point is shown in Figure 5.7 where an overall efficiency greater than 90% can be observed in all p_T and η regions. The BDT is trained on jet events from $Z \to \mu^+\mu^-+$ jets, and this model is applied on another tight working point and the three data taking periods are considered separately. Then, the geometry of the signal jets from the hard scattering is compared to that of a generator level jet. Furthermore, to be considered as signal jets, they must have $p_T > 8$ GeV, while all other jets are classified as pile up jets.

In order to analyse more precisely the sensitivity to different H boson production mechanisms, the analysis relies on a categorization of the events. This is based on kinematic discriminants and the number of jets in the events and their properties have a high discriminating power to distinguish the different production mechanisms.

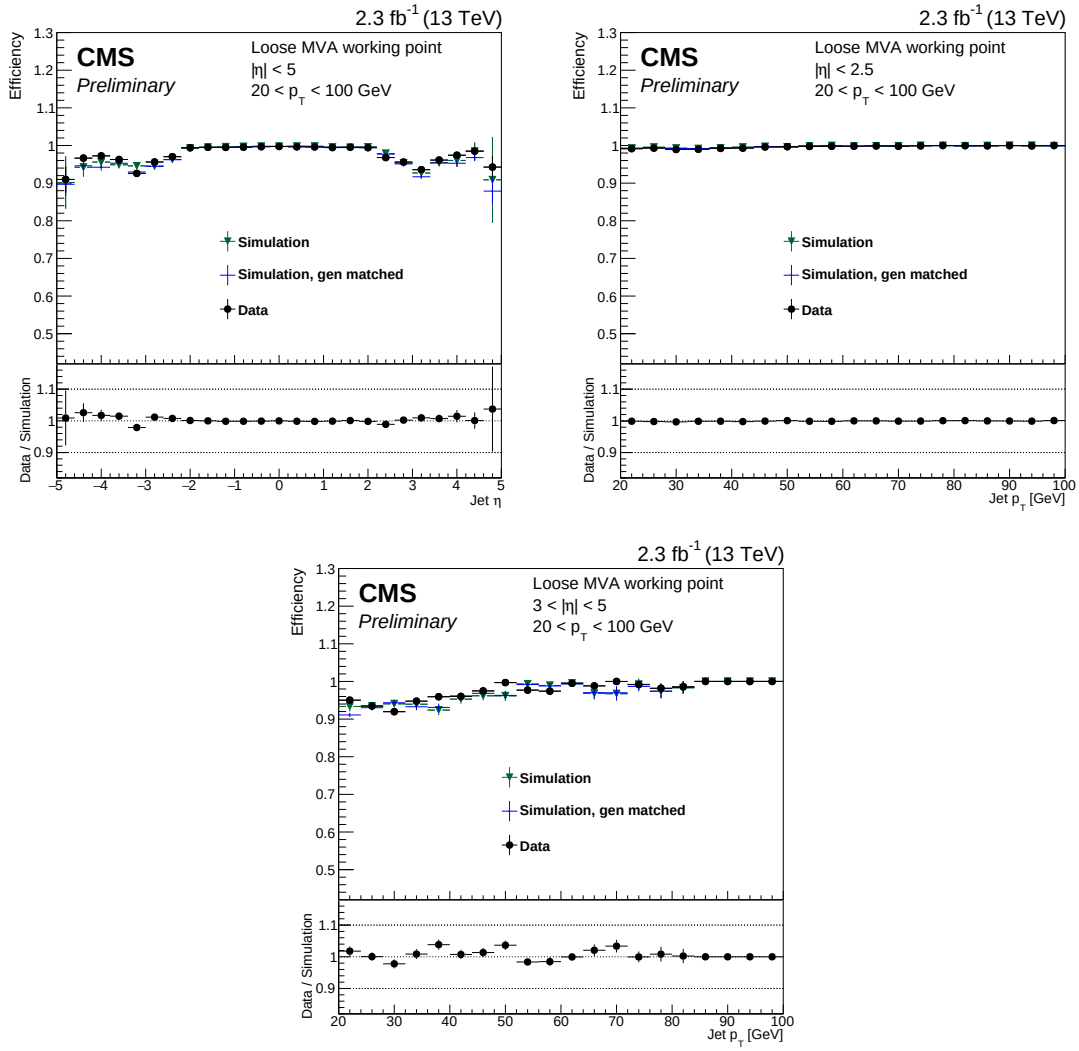

Figure 5.7: The PU jet ID efficiency on $Z \rightarrow \mu^+\mu^- +$ jets is shown for the loose working point of the BDT model. The efficiencies for data and MC simulation are shown as a function of the jet η on the upper left, as a function of p_T for central jets on the upper right, and forward jets on the bottom. The figures are taken from [38].

However, the precise characterization of the jets clashes with the performance of the trigger. Indeed, during the 2016 and 2017 data taking periods, a significant fraction of L1 trigger primitives were associated with the wrong packet crossing. This effect was due to the ECAL time lag not being properly propagated to the L1 trigger primitives.

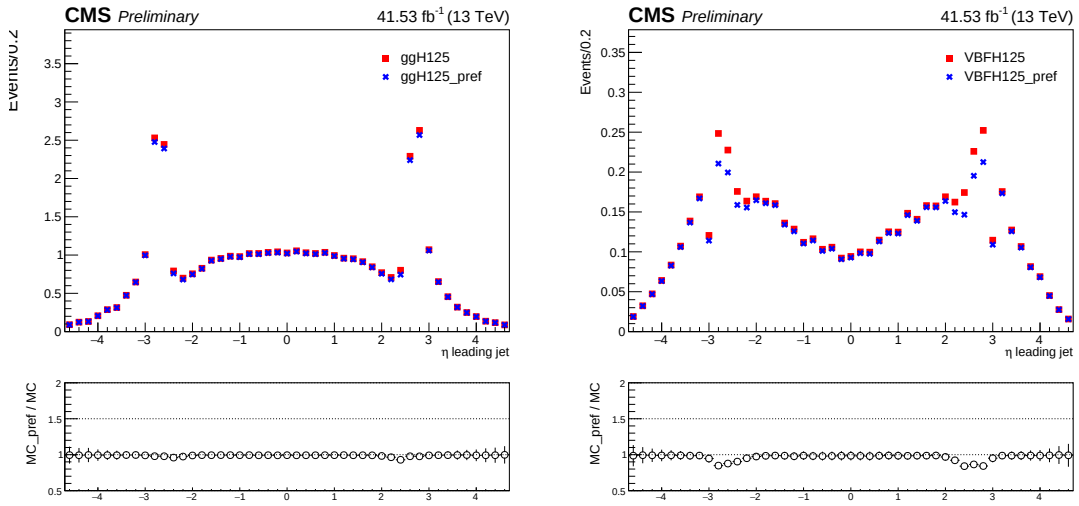

Figure 5.8: The effect of the L1 prefiring weights on 2017 MC samples for the ggH on the left, and VBF on the right. The samples without the L1 prefiring weight applied are depicted in the red histograms, while the blue histograms show the effect of the application of these weights. The plots are taken from [38].

The triggering principles of L1 prevent the triggering of two consecutive cluster crossings. Therefore, the events affected by this problem could cancel themselves when ECAL has already recorded a significant energy deposition in the $2.5 < |\eta_{jet}| < 3$ regions. This effect is observed in the data but is not modelled in the simulations. Therefore, weights had to be calculated to correct this problem, these were obtained as the product of the non-preference probability of all objects in the p_T^{jet} and η_{jet} bins. They were only applied to the simulated events of 2016 and 2017 to reproduce the behaviour observed in the data. The effect of the L1 prefix weights is illustrated in Figure 5.8 for the simulated signal samples ggH and VBF. While the effect is negligible for the former, the ratio between the two histograms shows a 2 or 3% deviation in the end regions for the VBF production mode.

The jet multiplicity was investigated in order to reduce the number of noisy jets, and it was found to be higher for the 2017 data. This anomaly is related to an increase in ECAL noise, which causes an anomalous peak-like structure in the η_{jet} distribution in the region defined by $2.5 < |\eta_{jet}| < 3$. This problem is only corrected from the second reprocessing of the data, also called Ultra-Legacy (UL) and including the latest calibrations and corrections applied to the various subdetectors.

5.1.5 Summary of the object selection

The first parts of this chapter introduced the selection criteria applied to the four types of objects that are used in the analysis of the $H \to ZZ \to 4l$ channel for the search of high mass resonance. Following this, corrections were applied to remedy undesirable detector effects and to have a good match between data and MC simulation. Finally, the analysis of the selection efficiency allows us to know the proportion of selected events and possibly to adapt the parameters.

In order to have a better visualization of the selection applied to the objects, and also to facilitate the understanding of the applied criteria, a summary is given in Table 5.4.

Table 5.4: Summary table of the selection requirements applied to the different kind of particles used to reconstruct $H \to ZZ \to 4l$ events.

Particle type	**Selection requirements**
Electrons	$p_T^e > 7$ GeV $\lvert\eta_e\rvert < 2.5$ $d_{xy} < 0.5$ cm $d_z < 1.0$ cm $\lvert\text{SIP}_{3D}\rvert < 4$ ID from BDT score Isolation from BDT score
Muons	Global or Tracker Muon Discard Standalone Muon tracks $p_T^\mu > 5$ GeV $\lvert\eta_\mu\rvert < 2.4$ $d_{xy} < 0.5$ cm $d_z < 1.0$ cm $\lvert\text{SIP}_{3D}\rvert < 4$ PF muon ID if $p_T^\mu < 200$ GeV Tracker High-p_T muon ID if $p_T^\mu > 200$ GeV $\mathcal{I}^\mu < 0.35$
Photons	$p_T^\gamma > 2$ GeV $\lvert\eta_\gamma\rvert < 2.4$ $\mathcal{I}^\gamma < 1.8$ $\Delta R(l,\gamma) < 0.5$ $\Delta R(l,\gamma)/(p_T)^2 < 0.012$ GeV^{-2}
Jets	$p_T^{jet} > 30$ GeV $\lvert\eta_{jet}\rvert < 4.7$ $\Delta R(l/\gamma, jet) > 0.4$ Cut-based ID Jet pile up ID

5.2 Event selection

The final object of the analysis is an event made up of several sub-objects, including the four leptons and possible jets and photons. The purpose of the physics analysis presented in this thesis is based on the study of a high-mass resonance decaying into a pair of Z bosons, themselves formed by a pair of leptons. This section will deal with the reconstruction and selection of the events, starting by mentioning the work done at the trigger level and the different trigger paths used. Then, explaining the selection of the leptons to form the Z boson candidates, and their matching to get the pair of bosons of interest. Finally, the whole selection discussed in this section will be analysed again in order to optimize it for the high mass resonance search.

5.2.1 Trigger selection

The first part of the event selection happens at the level of the triggering system. Indeed, as explained in Section 2.2.2, every second in CMS there are millions of collisions that are possible decays of a high mass resonance, which is why it is necessary to keep this data for offline analysis. The events are then collected in a dedicated collection of HLT triggers that are specially designed to have muon and electron candidates in the event. In addition, these objects must pass the identification and loose isolation requirements. It is worth noting that the minimum p_T required for leptons is different for the three years analysed in order to take into account the specificities of the detector during these periods.

The study of trigger efficiency was performed in order to know the proportion of events lost during the trigger phase. Since the efficiency measurement was covering a p_T range going up to 100 GeV, namely corresponding to the low mass region, this study is not optimized for the high mass events, although it is kept for the analysis presented in this thesis.

For the analysis in this thesis, the triggers used principally select two particles giving either a pair of muons or electrons, but also pairs of an electron and a muon. Also, triggers requiring only three leptons are used with relaxed p_T thresholds and no ISO requirement. The last type of trigger deals with isolated electrons or muons. Finally, collision events are stored if at least one of the considered HLT trajectories is triggered. In this thesis, six categories of primary datasets are used:

- **DoubleMuon** when the event has two or three muons.
- **DoubleEG** when the event has two or three electrons.
- **EGamma** when the event has one, two, or three electrons.
- **MuonEG** when the event has one muon with one or two electrons, or two muons with one electron.
- **SingleMuon** when the event has a single muon.
- **SingleElectron** when the event has a single electron.

Each of these primary datasets combines specific HLT paths, where additional requirements on the objects are applied, such as p_T or η thresholds. These triggers separate events according to the number of objects in their final state. For instance, for only one electron it will be done with *SingleEle* triggers, in the same way two muons with *DiMuon* triggers. In order to avoid having the same event collected by several primary datasets, events are assigned to a specific dataset following conditions on the triggers. At the end, an event will be collected by:

- **DoubleMuon** if it passes the *DiMuon* or *TriMuon* triggers and fails the *DiEle* and *TriEle* triggers.
- **DoubleEG** if it passes the *DiEle* or *TriEle* triggers and fails the *DiMuon* and *TriMuon* triggers.
- **EGamma** if it passes the *DiEle*, or *TriEle*, or *SingleEle* triggers.
- **MuEG** if they pass the *MuEle* or *MuDiEle* or *DiMuEle* triggers and fail the *DiEle* trigger.
- **SingleMuon** if they pass the *SingleMuon* trigger and fail all the other triggers.
- **SingleElectron** if they pass the *SingleEle* trigger and fail all the other triggers.

5.2.2 Z boson reconstruction

Once the leptons are selected, it is time to build the Z boson candidates in the event. In order to do that, the leptons are matched one by one in all the possible pairs respecting the opposite charge and the matching flavour conditions. For instance, the formed pairs are either e^+e^- or $\mu^+\mu^-$. Then, all the FSR photons are gathered with their associated leptons, and they are used for the computation of the invariant mass of the system. Moreover, each pair must satisfy a mass requirement corresponding to $12 < m_{l^+l^-} < 120$ GeV. After this step, numerous Z candidates could be reconstructed for a single event, the next thing to do is to select the best two candidates to build the event.

Both Z bosons from the same event are not treated in the same way. Indeed, the first one, noted Z_1, is composed of the best pair of leptons, meaning those with the clearest signature. And an additional mass threshold is imposed specifically for Z_1. It is selected if its invariant mass is $m_{Z_1} > 40$ GeV. By doing so, Z_1 is the candidate with the closest mass to the Z boson and this feature is observable in Figure 5.9 with the peak around 90 GeV. This figure represents the distribution of m_{Z_1} for the three final states and for all of them combined. Data are represented simultaneously with the H boson signal and the backgrounds. The H signal is composed of ggH and VBF, and the represented background are $gg \to ZZ$, $q\bar{q} \to ZZ$, EW, and $Z + X$. These backgrounds will be detailed later in Section 6.2.2.

Then, the second candidate Z_2 corresponds to the second-best pair of leptons. In this case there is no additional mass threshold only the standard $m_{Z_2} > 12$ GeV has to be taken account. The m_{Z_2} distribution is represented in Figure 5.10 for the

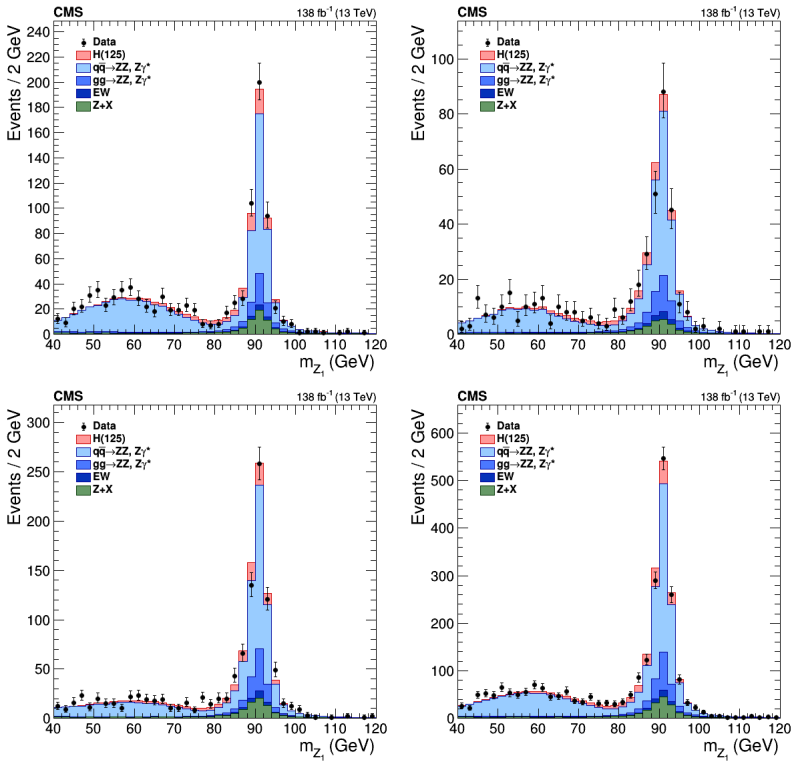

Figure 5.9: Distribution of m_{Z_1} using the full Run-2 statistic. Black points represent data, H signal in pink, and the backgrounds are $q\bar{q} \to ZZ$ in light blue, $gg \to ZZ$ in blue, EW in dark blue, and $Z + X$ in green. The plot on top left corresponds to 4μ, on top right to $4e$, on bottom left to $2\mu 2e$, and on bottom right to $4l$.

three final states and for all of them combined. The same signal and backgrounds shown for m_{Z_1} are also represented. With this observable, the Z boson mass peak is still visible even if it is wider, and there is now a low mass continuum due to the loose mass selection.

In the 4μ and $4e$ final states, an additional check on the pair matching must be performed. Indeed, with these final states, there is an alternative ZZ candidate that can be formed from the same four leptons. It is denoted $Z_a Z_b$, where Z_a is the closest to the nominal mass of the Z boson. Moreover, in this configuration, the $Z_a Z_b$ candidate is excluded if $m_{Z_b} < 12$ GeV. This condition rules out the 4μ and $4e$ events containing a Z on the shell and a low mass $\mu^+\mu^-$ resonance.

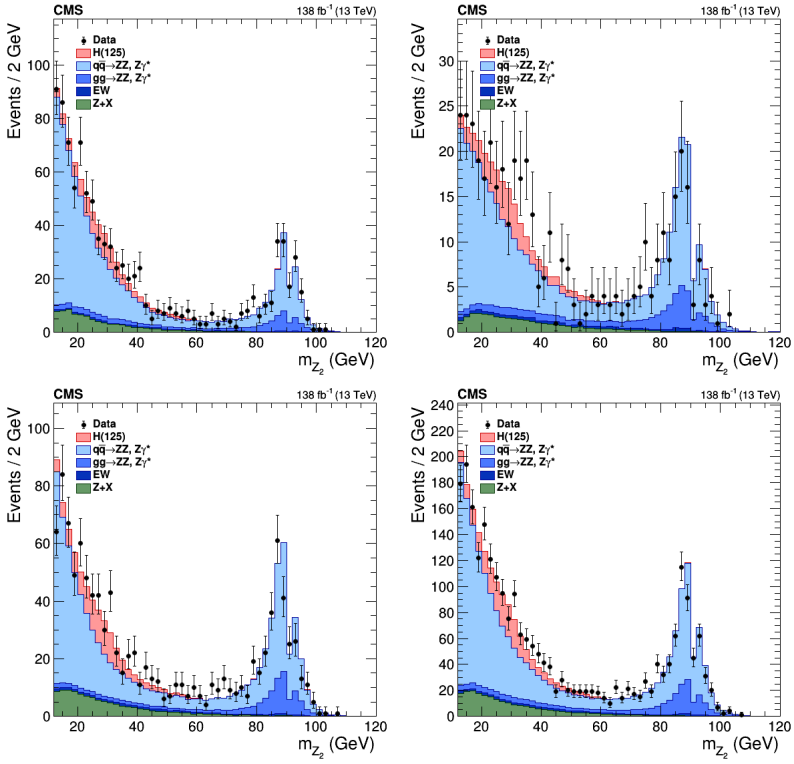

Figure 5.10: Distribution of m_{Z_2} using the full Run-2 statistic. Black points represent data, H signal in pink, and the backgrounds are $q\bar{q} \rightarrow ZZ$ in light blue, $gg \rightarrow ZZ$ in blue, EW in dark blue, and $Z + X$ in green. The plot on top left corresponds to 4μ, on top right to $4e$, on bottom left to $2\mu 2e$, and on bottom right to $4l$.

5.2.3 ZZ candidate selection

Once the Z boson candidates Z_1 and Z_2 formed, they are gathered into the ZZ candidate. Although, the work is not finished yet. Indeed, there are still other checks to pass in order to select the good ZZ candidates.

The first one consists in a suppression of QCD events which is realized by setting a requirement on the invariant mass of each pair of leptons. A new mass cut corresponding to $m_{l^+l^-} > 4$ GeV is applied regardless of the lepton flavour. The step has for objective the suppression of reducible background events made of leptons coming from the decay of a heavy flavour hadron or from the decay of low mass resonances. In this case, the lepton associated FSR photons are not used to compute the invariant mass because a QCD-induced low mass e^+e^- resonance coming from J/Ψ may have photons nearby originating from the decay of π^0.

The second step is to restrain the invariant mass of the four leptons to the mass range of $m_{4l} > 70$ GeV. This mass range is selected in order to consider only the phase space of interest for the further stages of the analysis.

The events that contain at least one selected ZZ candidate form the signal region. The Figure 5.11 presents the m_{4l} distribution for the three final states and for all of them combined. This time, the Z mass peak around 90 GeV is followed by the H mass peak centred around 125 GeV and represented in pink.

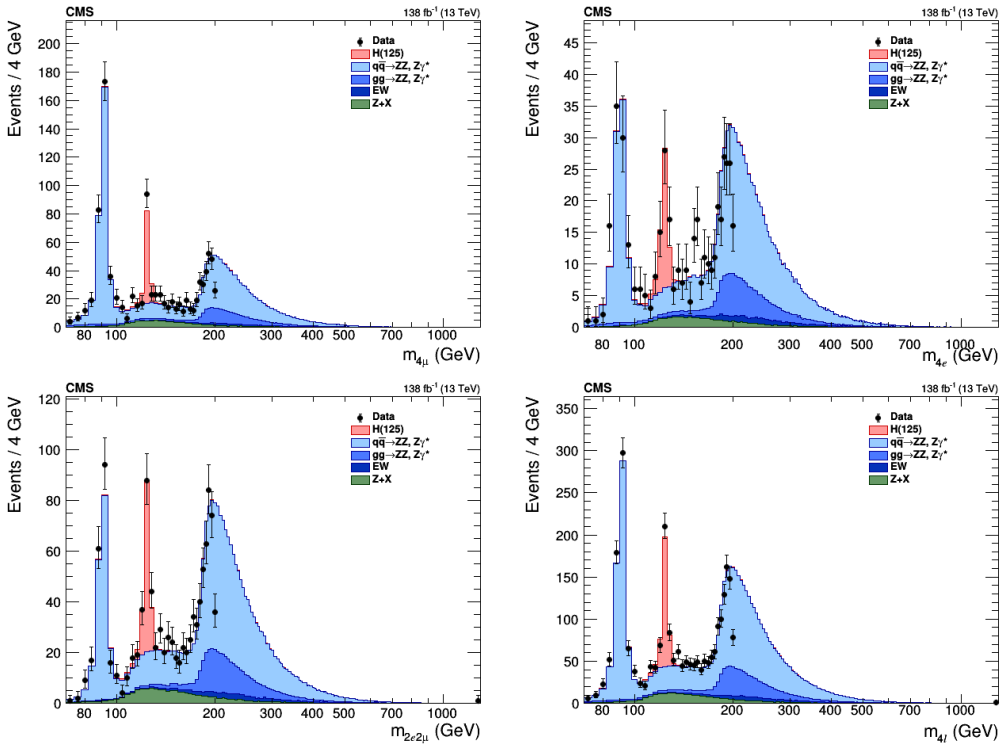

Figure 5.11: Distribution of m_{4l} using the full Run-2 statistic. Black points represent data, H signal in pink, and the backgrounds are $q\bar{q} \to ZZ$ in light blue, $gg \to ZZ$ in blue, EW in dark blue, and $Z + X$ in green. The plot on top left corresponds to 4μ, on top right to $4e$, on bottom left to $2\mu 2e$, and on bottom right to $4l$. Data are blinded after 200 GeV.

Finally, it is worth noting that if there is more than one ZZ candidate present in the event after the full selection procedure, the one retained will be the one with the highest value of the kinematic discriminant $\mathcal{D}^{kin}_{bkg}$, which will be defined in section 5.3.1. However, when different ZZ candidates involve the same four leptons, they have identical values of $\mathcal{D}^{kin}_{bkg}$: thus, the candidate whose mass m_{Z_1} is closest to the nominal mass of the Z boson is retained.

5.2.4 Optimization of the selection

So far, the selection of individual objects and events has been optimized for studies measuring the properties of the Higgs boson with a mass near 125 GeV. In the case of a high-mass analysis using this configuration, two problems arise. The first is physical and is reflected in the fact that there are very few high mass events. The second is related to the selection, which, not being optimized, risks losing signal events that are non-negligible due to the low statistics. In order to find out which parts of the selection could be removed or optimized, a study was carried out on the efficiency of event selection. This is detailed in this section, which uses mainly the 2018 samples.

Selection efficiency

In order to determine the relevance of the selection criteria, efficiency was used, as it allows us to know what proportion of events are selected in relation to those generated. This can be translated into the following equation:

$$\mathcal{E}_{\text{sel}} = \frac{N_{\text{sel}}}{N_{\text{gen}}} \tag{5.6}$$

Where N_{sel} is the number of reconstructed events passing the selection criteria and N_{gen} is the number of generated events. In the following, N_{gen} is defined as the number of generated events within the lepton acceptance. This acceptance corresponds to a set of criteria based on the leptons' reconstruction, with $|\eta_e| < 2.5$ and $p_T^e > 7$ GeV for electrons, and $|\eta_\mu| < 2.4$ and $p_T^\mu > 5$ GeV for muons.

The first thing that needs to be checked is the behaviour of the selection efficiency as a function of mass. For this, it was calculated for the different masses available, and this each time for the different production modes and decay channels. Figure 5.12 represents what was explained before using only 2018 samples.

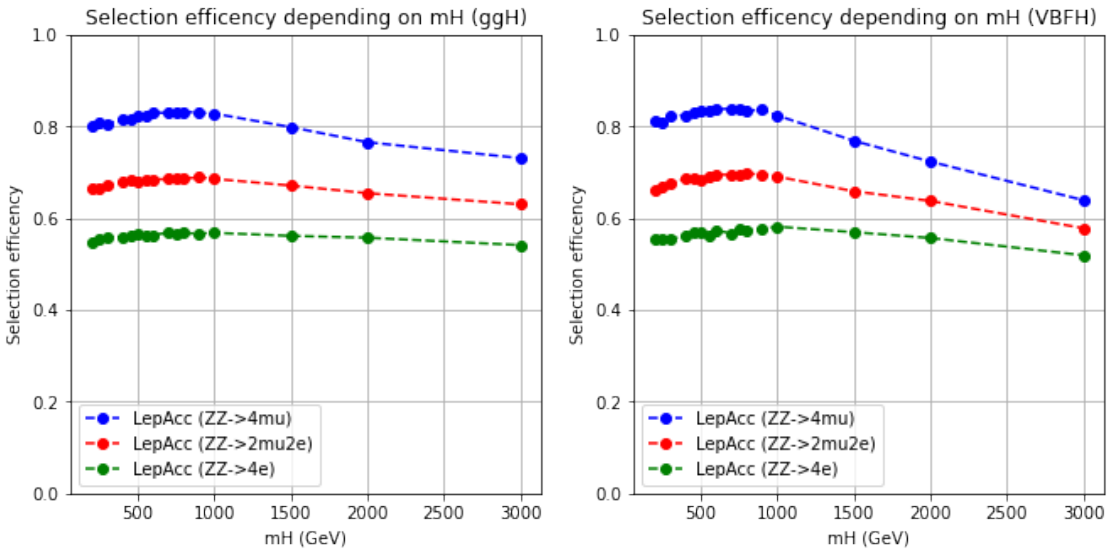

Figure 5.12: Selection efficiency depending on m_H from 2018 MC simulation. ggH is represented on the left, while VBF is represented on the right. 4μ channel is coloured in blue, $2\mu 2e$ in red, and $4e$ in green.

From this figure, it is easy to observe that the three decay channels doesn't have the same selection efficiency. Indeed, muons have a higher rate compared to electrons due to their clearer signature. Moreover, there is an efficiency loss at high mass starting from 1 TeV. This decrease is more important for channels with muons and in the worst case it corresponds to a loss of 20% of efficiency for 4μ from VBF.

Impact of the selection parameters on the efficiency

The next step is to understand the impact of the selection criteria on the selection efficiency. To do it, they will be relaxed or removed.

Firstly, selection criteria are considered individually, and then they are considered together as represented in Figure 5.13 and 5.14. Then, selection parameters were removed separately such as SIP corresponding to the red curves, the ISO in green, the ID in light blue, or the opposite charge (OC) requirement on leptons forming a pair shown in brown. The fact that we are interested in the OC requirement can be explained by the fact that it can also be a source of decreased efficiency at high mass. Indeed, the charge is estimated from the curvature of the trace, which becomes increasingly straight if the leptons have higher p_T at high mass. Foremost, in order to understand if the decrease at high mass comes from a correlation of different parameters, they were removed together. For instance, in yellow only the first three, and all of them in blue.

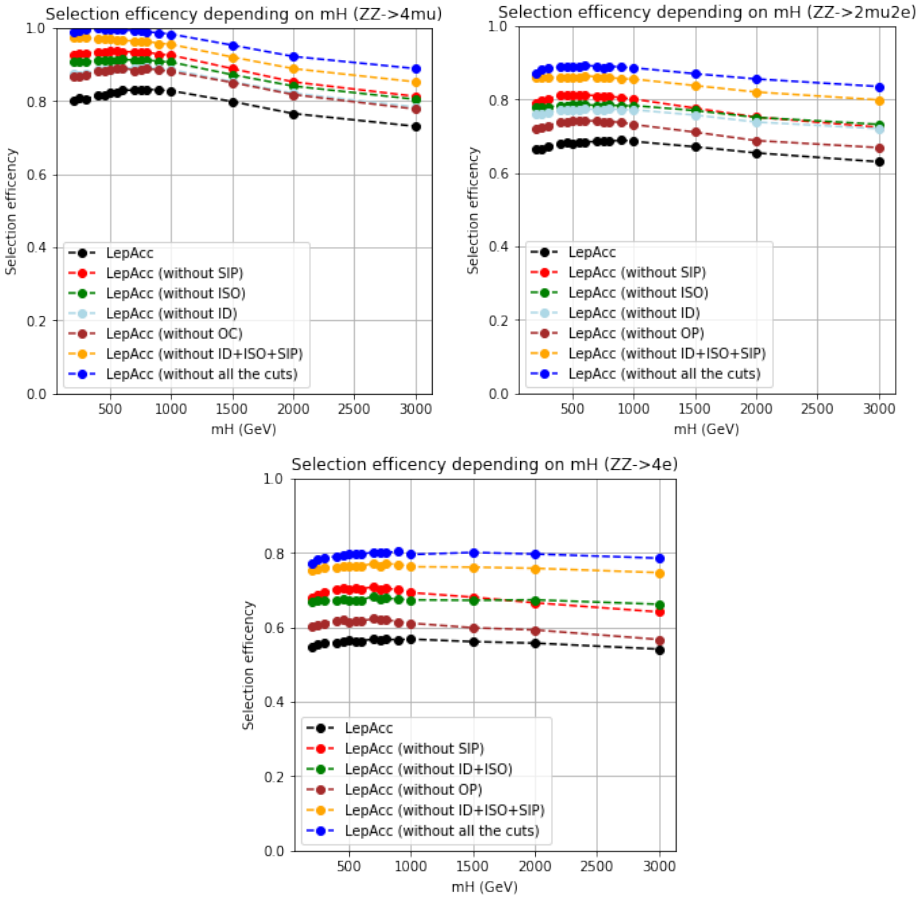

Figure 5.13: Selection efficiency depending on m_H from 2018 MC simulation of ggH. From left to right, 4μ channel is shown, followed by $2\mu 2e$, and then $4e$. In black all the cuts are applied, in red SIP is removed, in green ISO is removed, in light blue ID is removed, in brown the OC is removed, in yellow SIP + ISO + ID are removed, and in blue SIP + ISO + ID + OC are removed.

Since electron reconstruction is using a BDT to compute the ISO and the ID, both are considered together for the 4e decay channel.

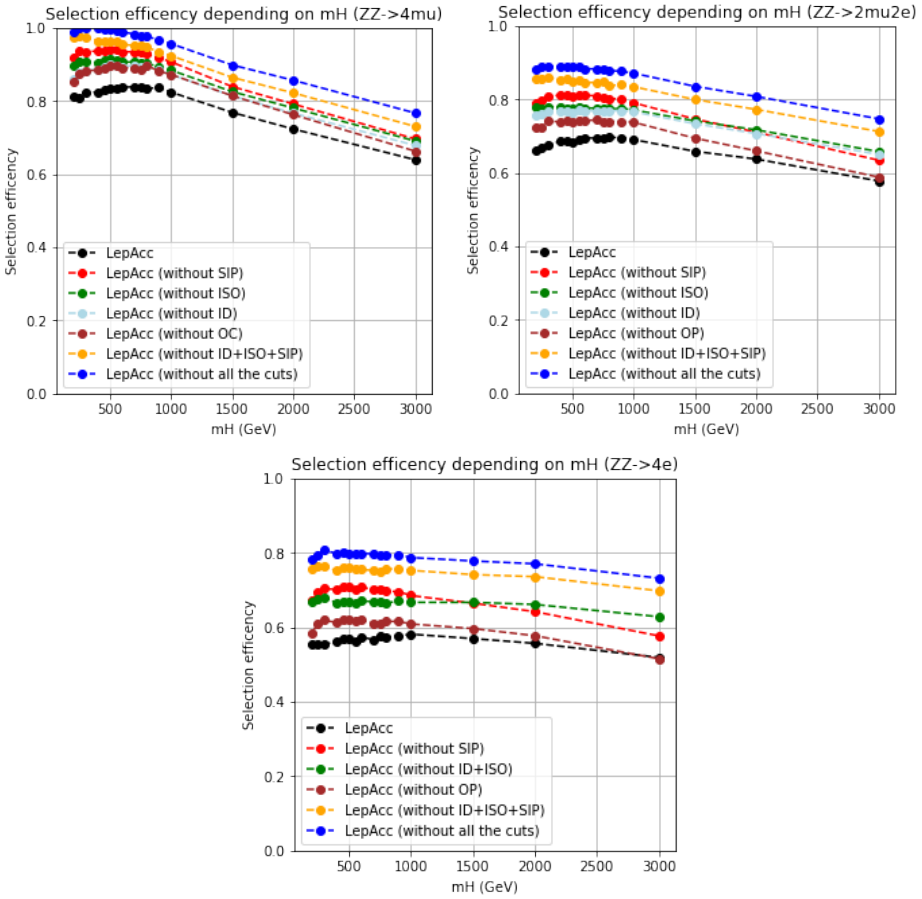

Figure 5.14: Selection efficiency depending on m_H from 2018 MC simulation of VBF. From left to right, 4μ channel is shown, followed by 2μ2e, and then 4e. In black all the cuts are applied, in red SIP is removed, in green ISO is removed, in light blue ID is removed, in brown the OC is removed, in yellow SIP + ISO + ID are removed, and in blue SIP + ISO + ID + OC are removed.

All the selection efficiency curves show the same important decrease after 1 TeV for channels having muons in their final states. Even after removing all the cuts, this feature remains and for VBF it represents a loss of almost 20% for 4μ and 15% for 2μ2e. For ggH, it is a bit lower, with 10% for 4μ and around 5% for 2μ2e.
Other checks will have to be performed in order to understand its origin.

Search for the cause of high mass efficiency loss

Since the study was using only 2018 MC simulation, the problem with the loss of muon selection efficiency could be from this specific year. The MC simulation samples were processed to see if the loss is year specific. Thus, the selection efficiency was calculated for the different production modes and decay channels. The comparison of the three years for VBF is represented in Figure 5.15. The choice

to show only VBF is motivated by the fact that the efficiency loss is more important with this production mode.

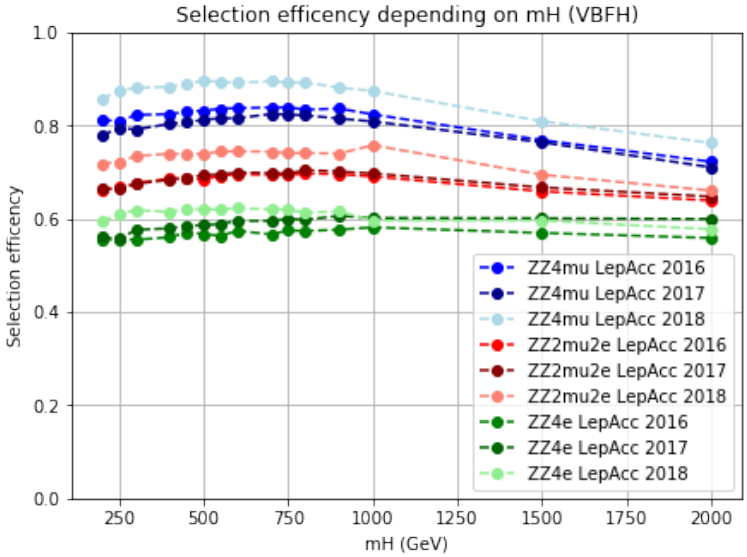

Figure 5.15: Selection efficiency depending on m_H from MC simulation of VBF. Curves coloured in blue are related to 4μ, those in red to $2\mu 2e$, and those in green to $4e$. Intermediate colours are related to 2016, dark ones to 2017, and light ones to 2018.

In order to calculate the $\mathcal{E}_{\text{sel}}$ the standard selection described earlier was applied. Moreover, this selection was applied in the same way on the three different years. As it is shown, $4e$ is almost constant over mass for the three years, and the efficiency loss is still happening for 4μ and $2\mu 2e$. Hence, the problem remains unresolved.

Since this problem is not related to the year of the data collection and does not apply to electrons, it seems to come from the selection of muons only. To know more precisely its origin, the characteristics of the muons that are not selected must be analysed. First, we will collect all events that do not pass the selection and with at least four muons in the final state. Then the first thing to do was to find out if there were any differences between the reconstructed muons and the generated muons. For the following, only a MC simulation sample of VBF at 3 TeV is used. The muons are studied in detail at high mass, because when they have a high p_T, the trace fit could not be good for some of them and therefore the muon trajectory measurement fails. Consequently, this changes the reconstructed value for m_{4l} and it does not pass the selection criteria or the reconstruction algorithm prefers to take another muon among the event leptons and the $4l$ candidate does not have the correct properties. Similarly, if the reconstructed p_T is very different from the generated p_T, because the calibration of high mass muons does not work well, this can lead to the same effects. Foremost, it is necessary to know if the muons have the same geometrical properties, meaning values of η and ϕ close to each other. For this, the study of the ΔR between generated and reconstructed muons is of great help. In this case, both indices of Equation 2.14 will refer respectively to the

reconstructed muon and the generated one. For each event, four pairs are formed using one generated muon and a reconstructed one. Muons already used in a pair cannot be part of another one, and the remaining pairs are those where ΔR is minimal. In the left part of Figure 5.16, there is the distribution of the minimal ΔR for each best pairs of generated and reconstructed muons. Then, in order to know if a reconstructed muon matches a generated one, both muon from a same pair must respect $\Delta R < 0.02$. For each event, the number of matched muons are computed and illustrated with its distribution in the right part of Figure 5.16.

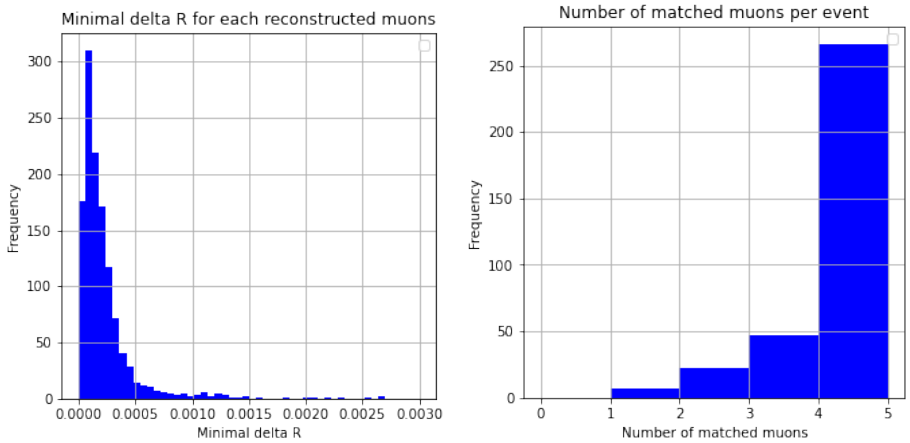

Figure 5.16: On the left, the distribution of the minimal ΔR between a generated and a reconstructed muon from events failing the selection. On the left, the number of matching muons per event.

This first study shows that almost 80% of the events have four matching muons. The 20% left cannot explain the efficiency loss observed after 1 TeV. Thus, the η and ϕ matching between generated and reconstructed muons are not the cause of the decrease. That is why other observables must be checked, such as p_T of muons.

For the following, only the events with at least four muons matching the ΔR condition are retained. The verification of the p_T matching is based on the comparison between the $p_{T_{\text{gen}}}$ of the generated muon and the $p_{T_{\text{reco}}}$ of reconstructed muon. The ratio of both is done for the four muons of each event, and the distributions of the ratios are shown in Figure 5.17.

The p_T ratio distributions are all the four peaked at 1, meaning that the generated and reconstructed muons have a close value of p_T. Then, for each event, different value of threshold for the p_T matching are considered. In this study, four values were used starting from 5%, then 10%, followed by 15%, and 20% to finish. For each of these thresholds, the distribution of matching muons per event is shown in Figure 5.18.

If considering a threshold of 5% only 15% of the events have four matching muons. When relaxing this condition to 10%, the number of events with four good muons goes up to 55%. This proportion increase until 80% when the limit is set to 20%. Since there is no selection criteria taking care of the p_T difference between generated and reconstructed muons, the efficiency loss has still no explanation.

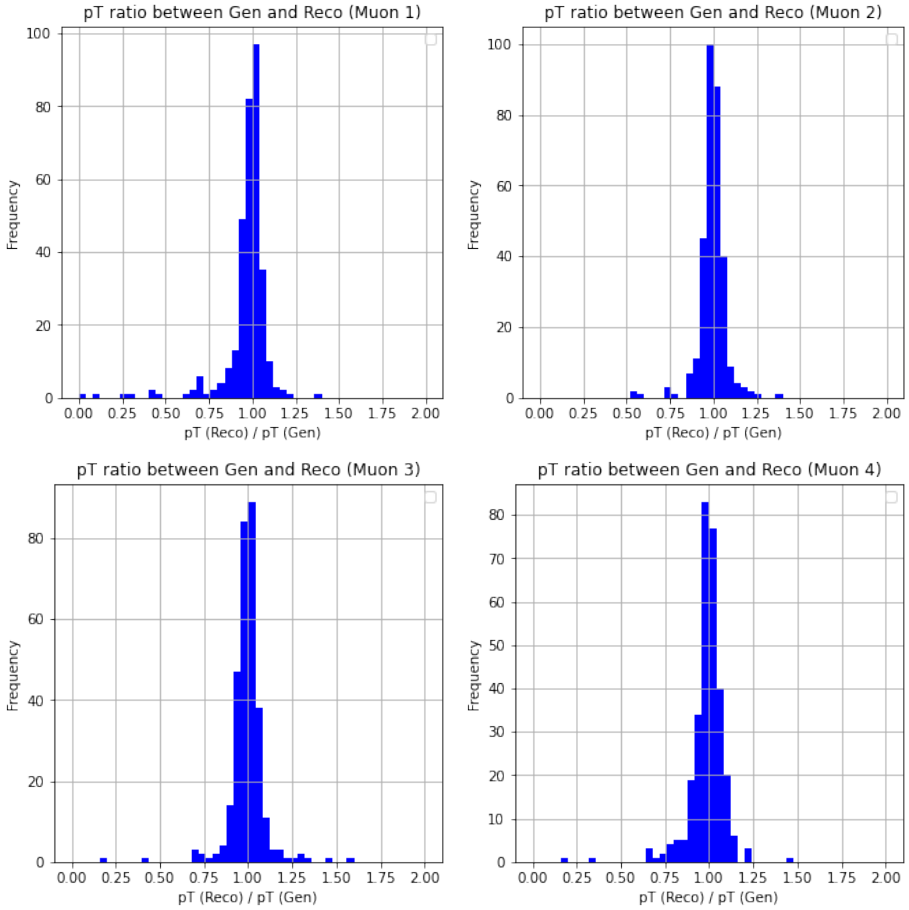

Figure 5.17: Distributions of the ratio of $p_{T_{\text{reco}}} / p_{T_{\text{gen}}}$. Each muon of an event is represented in a single plot.

Although, the p_T of muons does not seem to be problematic even if there is a non-negligible difference highlighted in Figure 5.19.

Until now, the checking studies were only using muon information, the next step will consist in adopting the same approach but for Z and ZZ candidates. However, since the events did not pass the selection, no reconstructed information from Z and ZZ were available. In order to perform this study, the different observables of interest were calculated with a standalone code using the same method as described in Section 5.2.2 and 5.2.3. Z_1 is composed of the best pair of muons and Z_2 the other one. In Figure 5.19, the generated p_T in blue is compared to the reconstructed one in red.

The reconstructed p_T are now calculated. The next step follows the same method used for muons, meaning that the ratio $p_{T_{\text{reco}}} / p_{T_{\text{gen}}}$ is computed. Distributions coming from the three objects are shown in Figure 5.20. And once again, the three distributions are peaked around one. Hence, there is no unexpected behaviour coming from the event reconstruction.

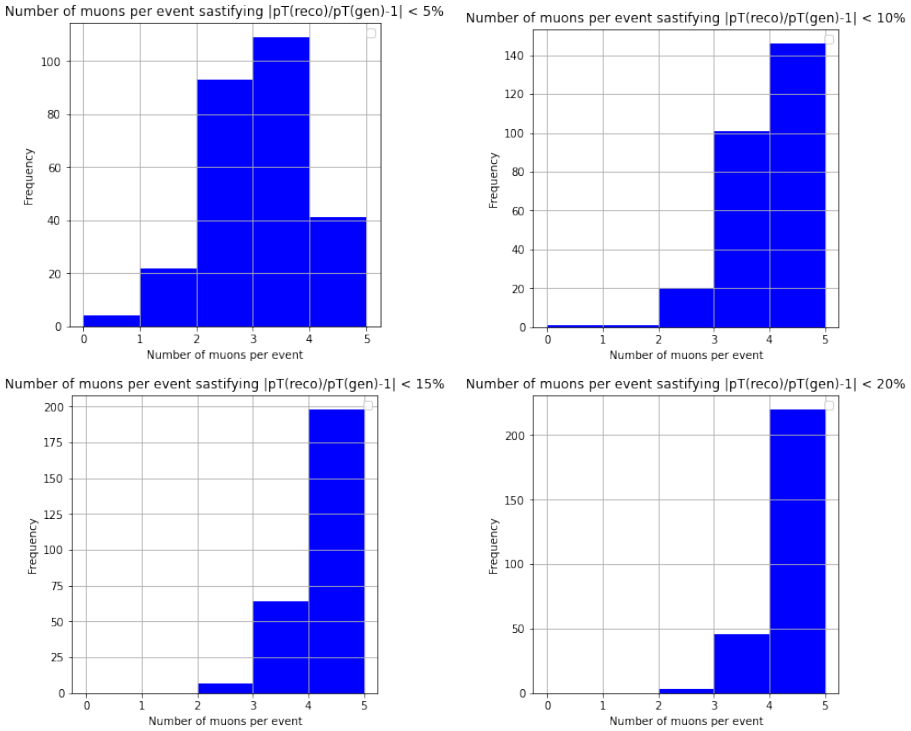

Figure 5.18: Distributions of the number of muons per event, respecting $|p_{T_{\text{reco}}}/p_{T_{\text{gen}}} - 1| < k$. From left to right, k is equal to 0.05, 0.10, 0.15, and 0.20.

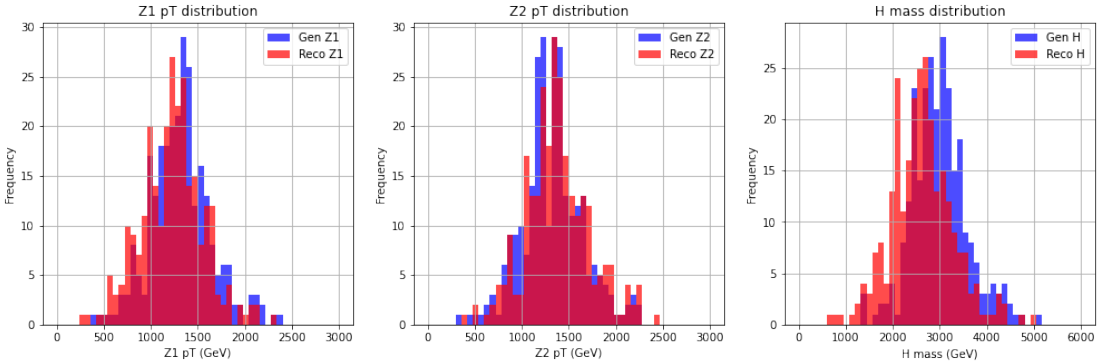

Figure 5.19: Distribution of $p_{T_{\text{gen}}}$ in blue and $p_{T_{\text{reco}}}$ in red. Z_1 is represented on the left, Z_2 in the middle, and ZZ on the right.

The reconstruction of the different objects for 4μ events does not give any clue concerning the efficiency loss at high mass. The final approach that remains to be addressed is the separation of muons and jets. Indeed, the VBF process is linked to the interaction of two quarks through the exchange of vector bosons. These quarks will remain in the system and will be at the origin of jets. Moreover, the reconstruction framework uses a module which discards the muons which would have a too important part of their trace in common with jets. If a muon shares more than 49.9% of its segments with jets, it is considered a ghost and is thus discarded. To find out if this module could be the cause of the problem, it will be deactivated. Then, the selection efficiency is calculated without the ghost muon

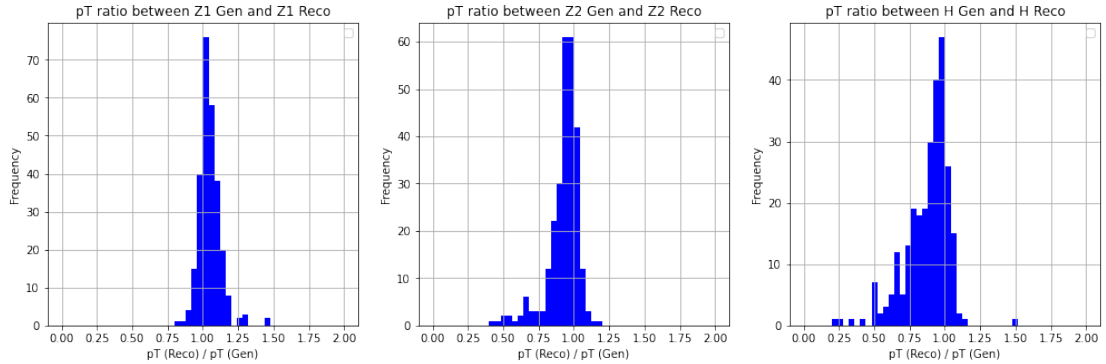

Figure 5.20: Distributions of the ratio of $p_{T_{\text{reco}}} / p_{T_{\text{gen}}}$. Z_1 is represented on the left, Z_2 in the middle, and ZZ on the right.

cleaner module and all the other cuts studied earlier. Only few mass points were used to see its impact, which is shown for VBF in Figure 5.21.

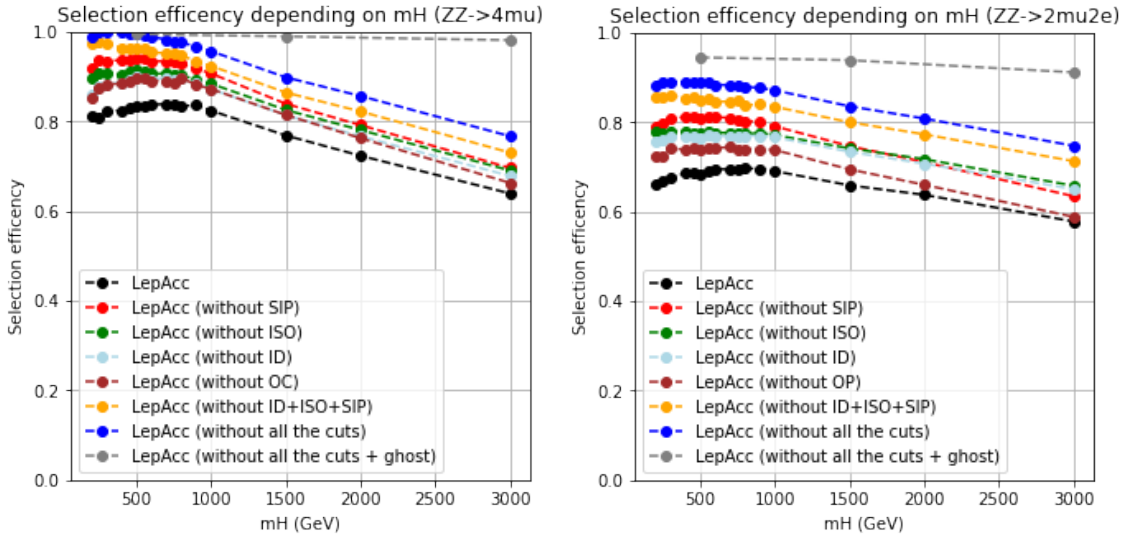

Figure 5.21: Selection efficiency depending on m_H from 2018 MC simulation of VBF. 4μ channel is on the left and $2\mu 2e$ on the right. In black all the cuts are applied, in red SIP is removed, in green ISO is removed, in light blue ID is removed, in brown the OC is removed, in yellow SIP + ISO + ID are removed, in blue SIP + ISO + ID + OC are removed, and in grey SIP + ISO + ID + OC + Ghost Cleaner are removed.

Thanks to this representation, it is clear that the ghost muon cleaner module is at the root of the decrease of efficiency at high mass. Indeed, when removing all the main cuts and the ghost muon cleaner module, the selection efficiency is close to 100% for VBF in 4μ, and it stays constant when the mass increases. This feature also concerns the $2l2q$ decay channel, even if the selection efficiency is lower. Now that the cause of the loss of efficiency is known, it remains to be seen whether the ghost muon cleaner module can be removed without causing further complications. To do this, its impact on the reconstruction of event observables,

as well as on the background noise, must be studied. In addition, to finalize this validation, it will be necessary to analyse its impact on low mass data, meaning outside our study area.

Concerning the verification on the impact of the ghost muon cleaner module on the signal, only the VBF production mode was used since it is more relevant since the impact is higher on it. Moreover, to have a clearer idea on what is happening with ghost muon cleaner module, different set ups are used. On a one hand, the module is activated only depending on different muon p_T thresholds. On the other hand, different requirement on the fraction of shared segment are used. This study is illustrated in Figure 5.22.

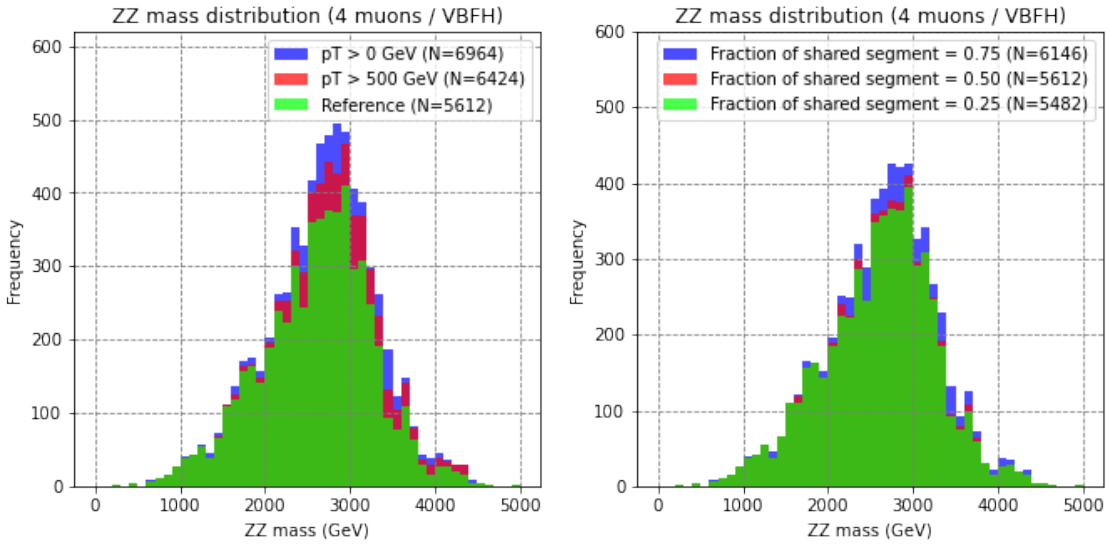

Figure 5.22: ZZ mass distribution from VBF in 4μ at 3 TeV. On the left, the green distribution correspond to the events passing the standard selection, in red only the ghost muon cleaner module is activated only for muon with $p_T < 500$ GeV, and in blue it is deactivated. On the right, in green the fraction of shared segment should be lower than 25%, in red it is 50%, and 75% in blue.

As it was expected by the increase of selection efficiency, the mass distribution has a higher statistic when relaxing the ghost muon cleaner module, with a pass-through condition on p_T as well as on the shared segment requirement. There is no unexpected behaviour observed, the distribution as the same shape, but with more events. When it is totally removed, there is an increase of $\sim$25%.

The most important to know before removing the module is its impact on background. Indeed, if the background increase a lot when it is deactivated, it does not make sense to remove it. In order to be sure of that, the same study performed on VBF is done on $qqZZ$. This background was chosen since it is the main background source for VBF and the two quarks can also be at the root of jets, which can make the module discarding good muons. The result of this study is represented in Figure 5.23.

When the ghost muon cleaner module is totally removed, there is an increase of background of the order of 0.5%. This gain takes place especially below 300 GeV, then the impact at high mass is very low. Comparatively, to the increase observed

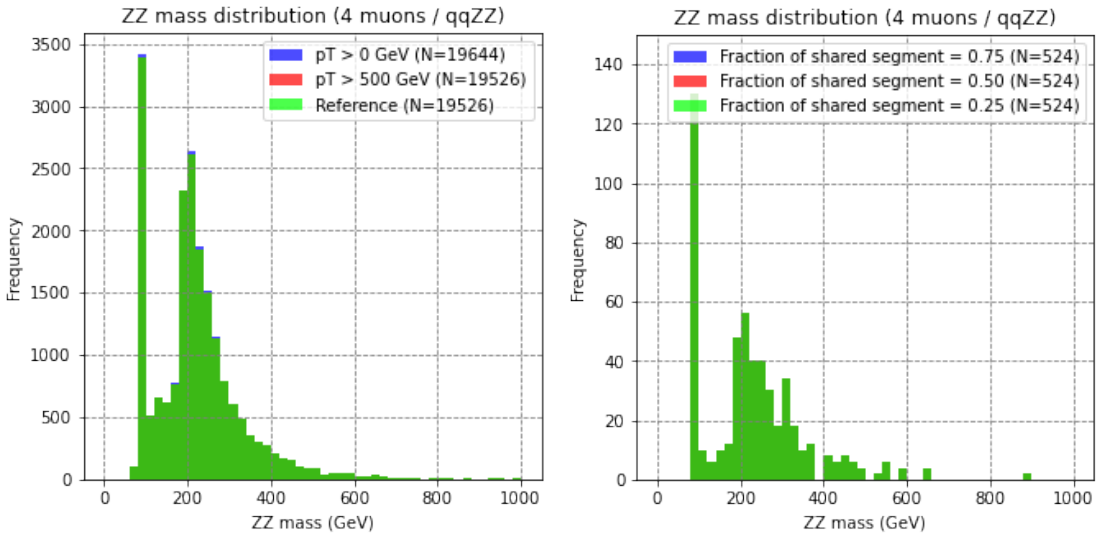

Figure 5.23: ZZ mass distribution from $qq \rightarrow ZZ \rightarrow 4\mu$. On the left, the green distribution correspond to the events passing the standard selection, in red only the ghost muon cleaner module is activated only for muon with $p_T < 500$ GeV, and in blue it is deactivated. On the right, in green the fraction of shared segment should be lower than 25%, in red it is 50%, and 75% in blue.

for VBF, this one is almost fifty times lower. If considering only the background, there is no objection to remove the module.

In addition, to be sure that there is no unexpected impact on data, a verification is done just by removing the module. At this time, the area of interest is kept blinded to avoid a human bias by looking at the data. In order to still perform this check, only the low mass region from 100 to 250 GeV was taken into consideration. The representation of the distribution with and without ghost muon cleaner is shown in Figure 5.24.

On the data low mass region, an increase of only 0.8% was observed. Such difference is not problematic since it is compatible to the increase observed for the background. Finally, the ghost muon cleaner module can be removed without any concern.

Optimized selection efficiency

The origin of the selection efficiency loss at high mass is now understood, and the selection was adapted to no longer taking it into account. The other selection criteria are kept like they are in the standard selection, since their impact is non-negligible on background. At the end, the selection efficiency is calculated without the ghost muon cleaner and the new representation depending on the mass is given in Figure 5.25.

This optimization of the selection for high mass allows avoiding the efficiency decrease at high mass. Moreover, there is also an increase of the selected events of around 20% for the 4μ decay channel and 10% for the $4e$. In the meantime, the background increases by only 0.5%.

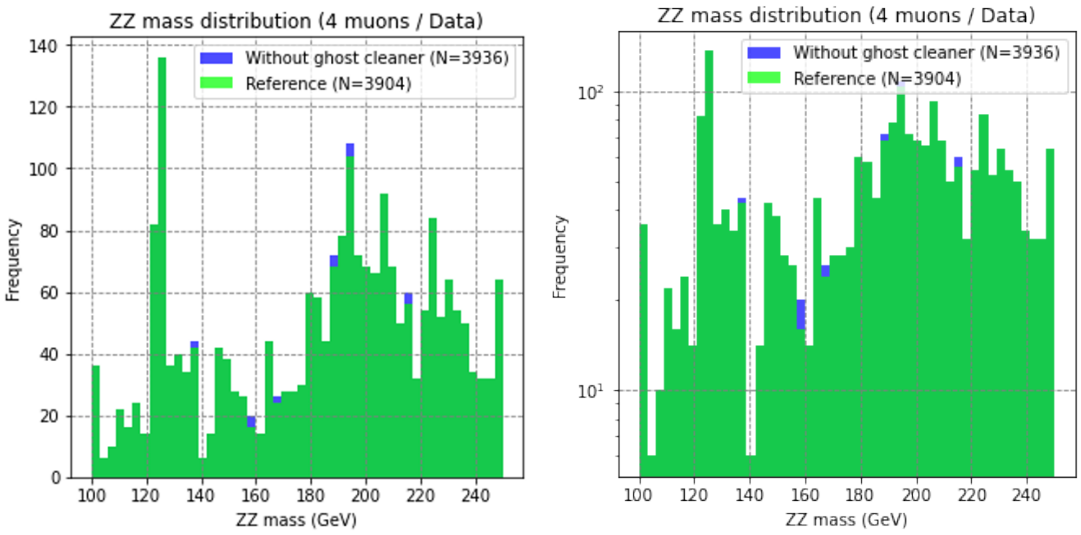

Figure 5.24: ZZ mass distribution from 4μ events taken from data. The green distributions correspond to the events passing the standard selection, and in blue the ghost muon cleaner module is deactivated. A linear scale is used on the left and a logarithmic on the right.

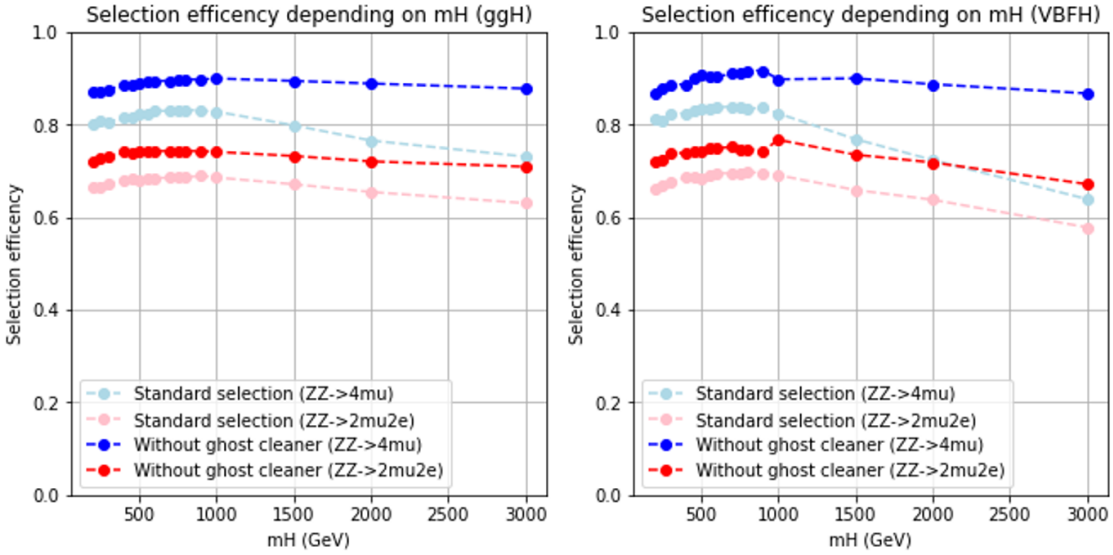

Figure 5.25: Selection efficiency depending on m_H from 2018 MC simulation. 4μ decay channel is represented in blue and $2\mu 2e$ in red. The light colours correspond to the efficiency calculated with the standard selection, while the ghost muon cleaner is removed for the more intense colours. ggH is represented on the left and VBF on the right.

This preliminary study shows encouraging results with a significant increase in selection efficiency which will be of great importance for the subsequent high mass study. Indeed, it has been observed that there are very few events reconstructed from the high mass data.

5.3 Event categorization

In order to carry out a physics analysis, whether it is for a precision measurement of a phenomenon or for the research of new physics, it can be carried out in two different ways. The first is called inclusive and consists of considering all events at the same time, so they are classified in a single category. The second is carried out on several categories, each corresponding to a particular type of event.

The interest of an analysis by category is to increase the sensitivity of the analyses by constructing categories with different associations of signals and noises, allowing to target different production modes. In fact, the signal events are classified in mutually exclusive categories, each sensitive to a production mode.

In the context of high mass resonance research, only two categories are used, and they correspond to the ggH and VBF production modes.

5.3.1 Observables and discriminants

Then the question arises of how to classify the events, on what criteria an event will go into such a category. For this purpose, a set of observables specific to the events is used for differentiation, as well as kinematic discriminants allowing the separation between the categories.

Observables of interest

The categorization of the $4l$ events requires the ability to differentiate them from each other in order to determine if they come from a ggH or a VBF process. For this purpose, a set of observables is used and corresponds to the following variable:

- m_{4l} the invariant mass of the $4l$ system
- m_{Z_1} and m_{Z_2} the invariant masses of the two Z boson candidates
- θ^* identified as the angle between the z axis and the Z_1 direction in the $4l$ rest frame
- Φ and Φ_1 the azimuthal angles between the planes containing the H boson and the decay products of the two Z bosons
- θ_1 and θ_2 the angles between the Z_1 and Z_2 flight directions and the planes containing the l^+l^- systems originating from the decay of these vector bosons

While the θ^*, Φ, and Φ_1 angles are defined in the H boson rest frame, θ_1 and θ_2 are defined with respect to the two Z bosons rest frames. A representation of ggH and VBF production modes is given in Figure 5.26. Besides, the set of angular variable as well as the mass of the Z bosons are hereafter referred to as $\vec{\Omega}^{H\to 4l}$.

Moreover, two other kind of observable are used for the categorization. The first one is the number of additional objects in the event. Among them, the one

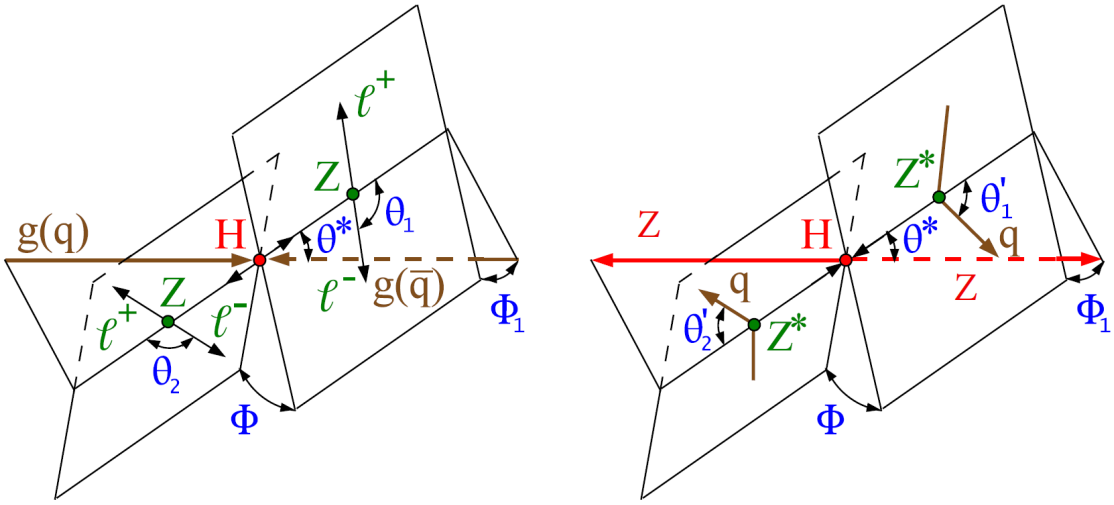

Figure 5.26: Illustrations of H boson production from ggH $gg \to H \to ZZ \to l^+l^-l^+l^-$ on the left, and from VBF $qq' \to qq'H \to qq'ZZ$ on the right. The five angles θ^*, θ_1, θ_2, Φ, and Φ_1 are shown in blue. The primary gluons and quarks are in brown. For ggH, the H boson is in red, while both Z bosons and the four leptons are in green. For VBF, in red are the H and Z bosons, in green are the two merging vector bosons.

interesting for a high mass resonance analysis is the number of selected jets in the event, which is a good tagger for the identification of VBF events. The other category corresponds to kinematic discriminant determined thanks to a matrix element method described in Section 5.3.1.

Matrix element technics

The categorization of the $H \to ZZ \to 4l$ events as well as the signal extraction presented in this thesis are carried out thanks to the Matrix Element Likelihood Approach (MELA). This method is implemented inside the MELA package, which relies on two generators: the Johns Hopkins University Generator (JHUGen) [157, 158, 159, 160, 161, 162, 163] studying spin-parity properties of new resonances, including the Higgs boson, and the Monte Carlo for FeMtobarn (MCFM) [164] is a program calculating cross-sections for various femtobarn-level processes occurring at hadron-hadron colliders. Both are used to compute matrix elements for signal and background events, respectively. The underlying assumption supporting the use of the MELA method is that the $H \to 4l$ decay can be completely characterized by means of eight independent degrees of freedom corresponding to the observables listed in the previous section.

Kinematic discriminant

For the purpose of this analysis, three kinematic discriminants are used, and they are dependent on the four lepton invariant mass m_{4l}.

The first one is the kinematic discriminant $\mathcal{D}^{kin}_{bkg}$, which is used to separate the

$gg \to H$ and $q\bar{q} \to H$ signals from the $gg \to 4l$ and $q\bar{q} \to 4l$ background. This discriminant is given by the following equation:

$$\mathcal{D}^{kin}_{bkg} = \left[1 + \frac{\mathcal{P}^{q\bar{q}}_{bkg}\left(\vec{\Omega}^{H\to 4l}|m_{4l}\right)}{\mathcal{P}^{gg}_{sig}\left(\vec{\Omega}^{H\to 4l}|m_{4l}\right)} \right]^{-1} \tag{5.7}$$

Where $\mathcal{P}^{q\bar{q}}_{bkg}$ corresponds to the probability to have a background event from the $q\bar{q} \to 4l$ process, which is dominant. Moreover, $\mathcal{P}^{gg}_{sig}$ defines the probability to have a signal event from the $gg \to H$ process. These probabilities are calculated with JHUGen or MCFM matrix elements within the MELA framework.

The distributions of $\mathcal{D}^{kin}_{bkg}$ for the main production modes and backgrounds are represented in Figure 5.27. This comparison shows the separation between signal and background, where the firsts one have their peaks around 0.8 while the seconds have theirs around 0.5. Moreover, signal $\mathcal{P}^{q\bar{q}}_{bkg}$ distribution are quite similar between ggH and VBF.

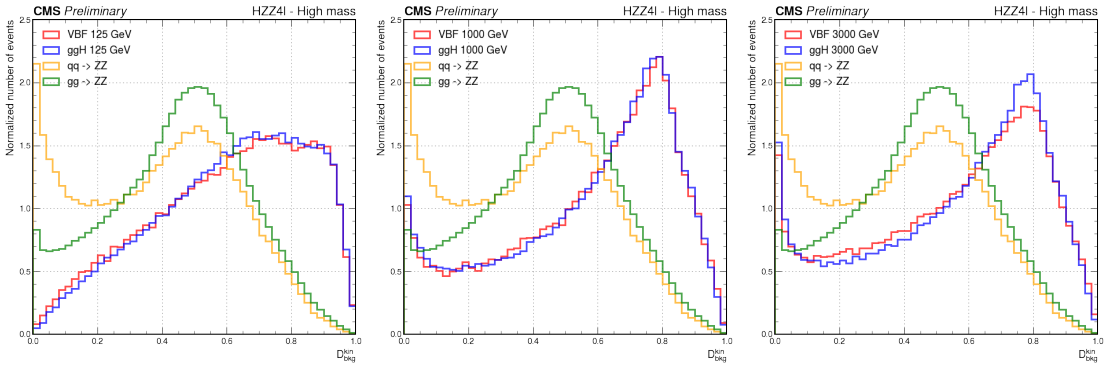

Figure 5.27: Distribution of $\mathcal{D}^{kin}_{bkg}$ using $4l$ events from 2018 MC simulation. VBF signal is represented in red and ggH in blue, $q\bar{q} \to ZZ$ and $gg \to ZZ$ backgrounds are coloured in yellow and green respectively. From left to right the signal mass is 125, 1000, and 3000 GeV.

In standard Golden Channel analyses, the distribution of this discriminant is studied only for a H boson at 125 GeV. But in a high mass analysis, different resonance masses can be considered, and it is good to know if the behaviour of the $\mathcal{D}^{kin}_{bkg}$ remains the same over mass. Then, the behaviour of this discriminant must be studied as a function of mass as shown in figure 5.27. Where three mass points are represented from 125 GeV to 3 TeV, and even when the mass increases the signal peaks are still well distinct from those of the background. Therefore, there is no reason to change the use of this discriminant for this analysis.

It may be added that the use of this discriminant is an essential element on which the analysis is based. More specifically, the likelihood calculation used in the statistical analysis is based on a model of the signal comprising a dependence of the invariant mass of the four leptons m_{4l} and a conditional probability calculated from a two-dimensional model of $\mathcal{D}^{kin}_{bkg}$ as a function of m_{4l}. In the same way, backgrounds are integrated into this likelihood and their templates are also used.

The Figure 5.28 represents the $\mathcal{D}_{bkg}^{kin}$ distribution for the three final states as well as for $4l$, results are obtained for Run-2 data and are plotted with the simulated signal and background.

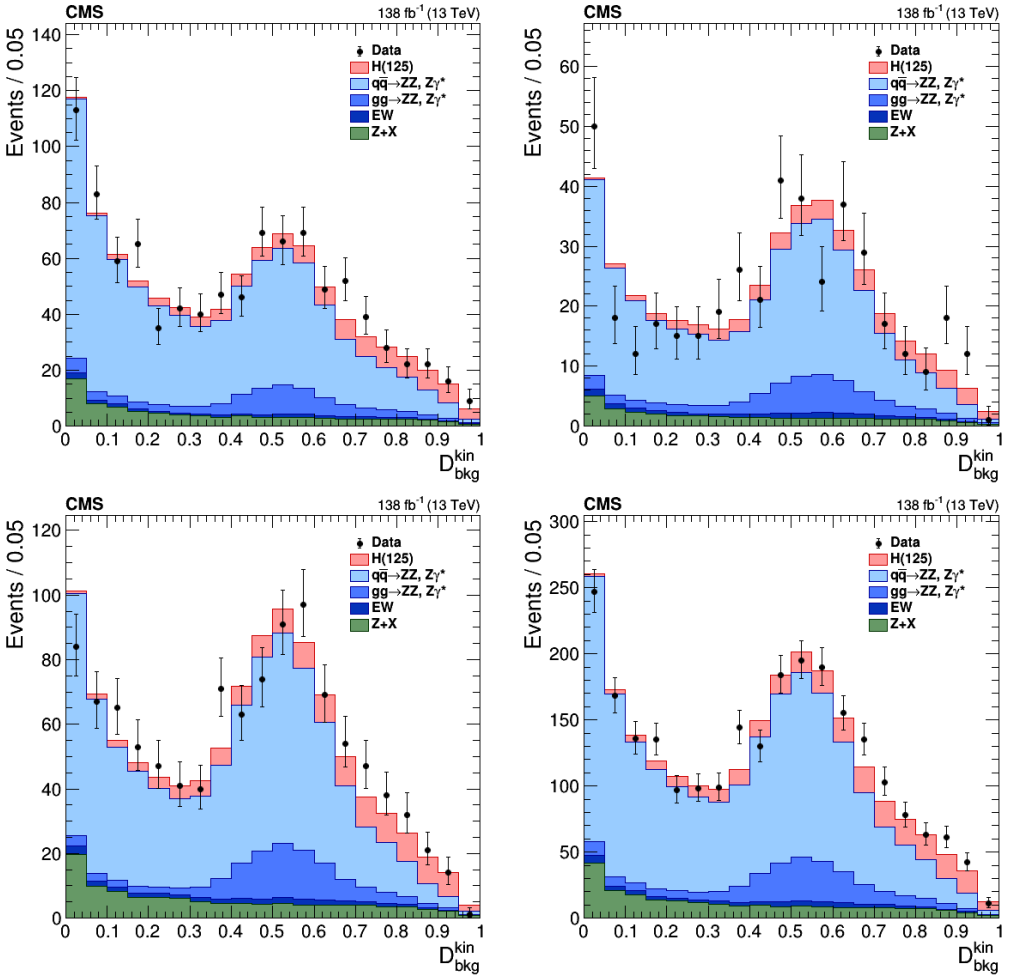

Figure 5.28: Distribution of $\mathcal{D}_{bkg}^{kin}$ using the full Run-2 statistic. Black points represent data, H signal in pink, and the backgrounds are $q\bar{q} \rightarrow ZZ$ in light blue, $gg \rightarrow ZZ$ in blue, EW in dark blue, and $Z + X$ in green. The plot on top left corresponds to 4μ, on top right to $4e$, on bottom left to $2\mu 2e$, and on bottom right to $4l$.

5.3.2 Categories at high mass

The first kinematic discriminant presented is used to separate signal and background. But, there are also kinematic discriminants allowing to distinguish the different production modes. The one used in this analysis is $\mathcal{D}_{2jets}^{VBF}$ and it allows the identification of the VBF signal topology associated with only two jets, it is defined as:

$$\mathcal{D}_{2jets}^{VBF} = \left[1 + \frac{\mathcal{P}_{HJJ}\left(\vec{\Omega}^{H+JJ}|m_{4l}\right)}{\mathcal{P}_{VBF}\left(\vec{\Omega}^{H+JJ}|m_{4l}\right)}\right]^{-1} \tag{5.8}$$

Where $\mathcal{P}_{HJJ}$ is the probability for an event to be produces via the ggH process in association with two jets. This probability is also calculated from JHUGen matrix elements. If taking the case of an event having four leptons and two jets, the discriminant can equally separate VBF from either $gg \to H + 2$ jets signals or both $gg \to 4l + 2$ jets and $q\bar{q} \to 4l + 2$ jets backgrounds.

Where $\mathcal{P}_{HJ}$ and $\mathcal{P}_{VBF}$ are respectively the probabilities for the ggH and for the VBF process, both in association with one jet. These probabilities are obtained from JHUGen matrix elements, and they are also calculated within the MELA framework. If taking the case of an event having four leptons and one jet, the discriminant can equally separate VBF from either $gg \to H+$ jet signals or both $gg \to 4l+$ jets and $q\bar{q} \to 4l+$ jets backgrounds. This separation is made possible because of the jet correlations in these processes which are distinct from the VBF process in the background, and they are a function of the mass of the four leptons.

The distributions of $\mathcal{D}_{2jets}^{VBF}$ for the two main processes considered for the search of high mass resonance are shown in Figure 5.29. The distributions are obtained from 2018 MC simulation of ggH and VBF, and this figure illustrates their evolution with the mass of the resonance.

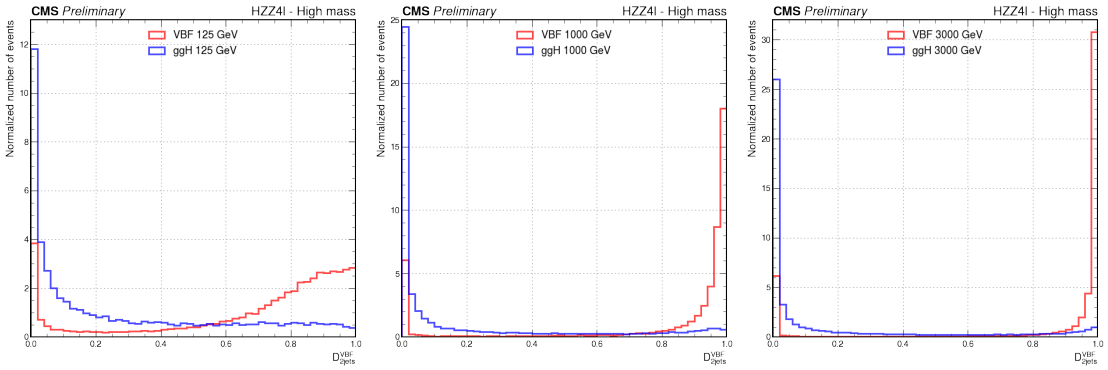

Figure 5.29: Distribution of $\mathcal{D}_{2jets}^{VBF}$ using $4l$ events from 2018 MC simulation. VBF signal is represented in red and ggH in blue. From left to right the signal mass is 125, 1000, and 3000 GeV.

On the left, the mass is equal to 125 GeV, and it corresponds to the distributions used in the Higgs boson analyses using the Golden Channel. In this case, it was determined that the optimal separation value is $\mathcal{D}_{2jets}^{VBF} = 0.5$. The separation between both processes is well visible because the 2 jets are a strong signature for VBF events, and when the mass increases the discrimination power is stronger due to the higher probability of having jets originating from the initial quarks of VBF events. Then, in the context of the search of high mass resonance, the idea was to have a cut for each mass that has the same efficiency in selecting VBF events with one jet as the one for 125 GeV. For this purpose, ROC curves of the identification

of VBF events versus ggH events have been studied for each mass points. The conclusion of this show that there is not a lot of change in the optimal cut. Indeed, the separation between both processes is clearer with the increase of energy, and there is not a strong interest in varying the discriminant cut.

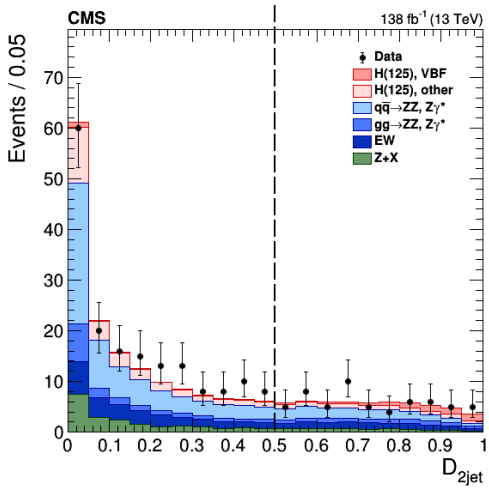

Figure 5.30: Distribution of $\mathcal{D}_{2jets}^{VBF}$ using $4l$ events from the full Run-2. Black points represent data, H signal in pink for VBF and in light pink for ggH. The backgrounds are $q\bar{q} \to ZZ$ in light blue, $gg \to ZZ$ in blue, EW in dark blue, and $Z + X$ in green. Dashed lines corresponds to the selection cut used in the high mass analysis.

Finally, the distribution of this was studied from the Run-2 data as it is presented in Figure 5.30. As it is only a preliminary study, the analysis is blinded to the mass range of interest for the high mass analysis, meaning that only the masses below 200 GeV were used for this plot. The main backgrounds are coloured in green for $Z + X$, or in the different shades of blue for $q\bar{q} \to ZZ$ and $gg \to ZZ$. The signal are illustrated in pink and are separated between VBF and ggH.

For the continuation of this analysis, the events' categorization will be made as such: the events passing the selection with the discriminant $\mathcal{D}_{2jets}^{VBF}$ will be classified in the category VBF and the others will be categorized as ggH. Moreover, an inclusive category is also considered and gathers all the events.

Chapter 6

Modelling of signal process and background

Table of contents

6.1 Signal and background simulation 196
6.1.1 Signal simulation samples 197
6.1.2 Background simulation samples 197
6.2 Background modelling 198
6.2.1 Irreducible background 198
6.2.2 Reducible background 202
6.2.3 Summary of the background modelling 210
6.3 Signal modelling 211
6.3.1 Analytical line shape of the signal 212
6.3.2 Signal efficiency 213
6.3.3 Signal resolution 216
6.3.4 Validation of the signal model 219

From the studies presented in the previous section, the events were selected to correspond to the $H \rightarrow ZZ \rightarrow 4l$ decay channel. Moreover, contrary to a classical analysis on the H boson, the selection made allows to consider high mass resonances $X \rightarrow ZZ \rightarrow 4l$. Now that the events have been correctly selected from the data, the next step is to check whether one can find signs of a new resonance in the high mass region.

The comparison between the data and the theoretical signal of the desired resonance cannot be done like that. Indeed, the theoretical model is ideal in the sense that it does not take into account the effects of the detector and the selection, contrary to the data. Therefore, a model must be built for the signal and also for the backgrounds. Both are determined in the first instance using MC simulation samples which are presented in Section 6.1. Then the backgrounds are estimated and modelled in Section 6.2 and finally the signal model is presented from Section 6.3.

At the moment of this thesis, only the 2018 data has been fully studied, thus

results presented in this chapter will only be about this specific data taking year. Data from both other years are partially analysed, and they should be fully treated in a near future.

6.1 Signal and background simulation

The simulation of events is an important aspect of an analysis since the theoretical prediction used to make the comparison with data are derived from MC simulation.

After the event generation performed by dedicated MC generators, and involving the different physical processes such as the shower development and the hadronization of dedicated MC generators, the simulated particles are propagated through a detailed simulation of the detector based on Geant4. However, some effects which are related to the detector cannot be observed in the simulation, but they are in data. In the same way, the simulation is imperfect because it is more ideal than the real detector, in fact it does not reproduce exactly all the effects of the detector. So to make the simulation more realistic, it must be corrected with scale factors so that it reproduces the real data as well as possible. In order to add artificially the impact of these effects to the simulation, the events are reweighted. One of the most important corrections concerns the pile up profile which uses projections based on simulations are used to estimate the expected PU profiles during each data taking period. These are based on a smooth PU profile which do not always match the ones recorded by the experiments because they are often the result of the convolution of different PU profiles. That is why, a dedicated weight is introduced to match the pileup profile in MC to the one observed in data.

Additional weights, noted w, are applied to the simulated events to take into account the actual number of events generated and the theoretical computations of the cross-section and branching fraction:

$$w = \frac{L_{int} \,.\, \sigma_X \,.\, BR_{4l} \,.\, w_{\mathrm{PU}} \,.\, SF_{4l} \,.\, w_{gen}}{\sum w_{gen}} \tag{6.1}$$

Where L_{int} refers to the integrated luminosity of the data taking period, $\sigma_X \,.\, BR_{4l}$ is the product between the best known theoretical prediction for the SM cross-section of the generated process and its branching ratio, w_{PU} is the pile up weight introduced at the beginning of this section, SF_{4l} is the per-event scale factor obtained from the product of the four leptons' efficiency scale factors, derived from the results presented in Section 2.3, and w_{gen} is the weight of the MC generator used. Ultimately, the product of these weights is rescaled by the sum of all the generation weights $\sum w_{gen}$ to get the expected yield for each process. For the samples related to the 2016 and 2017 data taking periods, the numerator is supplemented with an additional contribution correcting the issue on L1 trigger primitives mentioned in Section 5.1.4.

The specific MC generators used to simulate the different physical processes involved in the analysis are described in Section 6.1.1 for the signals and in Section 6.1.2 for the background processes.

6.1.1 Signal simulation samples

In this analysis, the MC simulation samples correspond only to two production modes: ggH and VBF. This choice is motivated by the fact that both processes are dominant at high mass as it was shown in Figure 1.5.

The POWHEG generator is used to produce these signal samples. Indeed, it is specially designed to describe the SM H boson production as well as BSM resonances associated with vector bosons, Z bosons in the case of this analysis. All the samples are generated at the next to leading order (NLO) in perturbative QCD with POWHEG [165, 166]. This generator is also used to produce ggH events [167, 168, 169], as well as events coming from VBF process with or without jet association [170, 171, 172, 173, 174].

All the signal samples used for this analysis are produced with a varying resonance mass and for the ggH and VBF processes. The different mass hypotheses are generated with m_X ranging from 200 GeV to 3000 GeV, and since the generation of MC samples is highly consuming in terms of computing resources, only a limited number of mass points was produced: one every 50 GeV in the range [200, 800] GeV, one every 100 GeV in the range [800, 1000] GeV, and one every 500 GeV in the range [1000, 3000] GeV. Moreover, the samples produced with the nominal H boson mass $m_H = 125$ GeV are also used in order to take into account the interference existing between the H boson resonance and the high mass one. These are used as a key feature for the signal modelling since they allow the calculation of the quantities representing the impact of the selection and the reconstruction such as the selection efficiency and the resolution.

Then, the decay simulation is obtained using the JHUGen generator, that properly takes into account the interference effects associated with permutations of identical leptons in the $4e$ and 4μ final states. Considering the $2e2\mu$ final state, there is no interference with an other final state in this case.

6.1.2 Background simulation samples

Concerning the background simulation, two categories must be distinguished. On one side, the backgrounds which are simulated in the same way as the signals and which could be used directly for the estimation of their contributions. On the other side, those which are also simulated but are only used to add correction factors to the estimation which is realized thanks to a data-driven approach.

Concerning the first category, the contribution from the $q\bar{q} \to ZZ$ background is generated with POWHEG at NLO with perturbative QCD and PYTHIA [175], using the same settings as for the H boson signal. Event simulation for the $gg \to ZZ$ process is done at LO with the generator MCFM. In order to match the distribution of the transverse momentum predicted by POWHEG at NLO, different PYTHIA settings are used for the showering in MCFM samples. Both simulated backgrounds require the application of dedicated factors to consider missing higher order corrections, as explained below.

Finally, the modelling of events containing Z bosons associated with jets, or vector bosons, or $t\bar{t}$ background are modelled using MadGraph [176]. They are not directly used to model data observations, because their contribution is actually

estimated using a data-driven technique and dedicated control regions defined in data. Nevertheless, they are necessary for the optimization and validation of the methods and for testing the data and MC simulation agreement in distributions of the object quantities and to ensure a good description of data in simulation. Moreover, Drell-Yan samples represent the source of signal and background leptons in lepton-level optimization studies and efficiency measurements. All of them are also generated using MadGraph.

6.2 Background modelling

The background contributions to the $X \to ZZ \to 4l$ analysis are divided into two groups presented previously irreducible and reducible ones, according to the signature of their final state.

On the first hand, the irreducible background category is composed of processes with four distinct leptons in their final states, they could originate from the decay of two Z bosons produced either via gluon fusion or quark-antiquark annihilation.

On the other hand, the reducible consists of processes implying decays of light mesons within jets, decays of heavy flavour hadrons, and charged hadrons misidentified as leptons because of overlaps with neutral pions. These backgrounds are dominated by processes in which a Z boson is accompanied by jets.

A precise modelling of the background is a key feature in the search for high-mass resonance where the statistics are very low. Indeed, in the mass region above 1 TeV very few events have been observed, and it is important to have a very accurate modelling of the background to know if these events can be part of a possible signal or not.

6.2.1 Irreducible background

In the context of the high mass analysis, only two irreducible backgrounds are considered: $gg \to ZZ \to 4l$ also referred as $ggZZ$, and $q\bar{q} \to ZZ \to 4l$ shorten in $qqZZ$. Both are quite similar to the ggH and VBF process detailed previously, but they differ since the couple of Z bosons is not produced via the decay of a H boson. Moreover, their final states are also composed of $4l$ and this similarity with the signal leads to a possible misidentification of the involved process.

These background processes are modelled via dedicated MC simulations presented in Section 6.1. One of the challenge of MC simulation production was coming from the $qqZZ$ background, matching well the theoretical modelling.

The shape parametrization of both considered irreducible backgrounds was done using a set of equations introduced in the search of standard model Higgs boson using the Golden Channel in 2012 [177]. For $ggZZ$, the shape is described with Equations 6.2 and 6.3, while $qqZZ$ shape is parametrized with Equations 6.2 and 6.4. These equations allow taking into consideration the high mass part of the background mass distribution as well as the lower mass part mostly located between 100 and 200 GeV.

$$
\begin{aligned}
f_1(m_{4l}, \vec{a}) &= \frac{1}{2}\left(1 + erf\left(\frac{m_{4l} - a_1}{a_2}\right)\right)\frac{a_3}{1 + e^{(m_{4l}-a_1)/a_4}} \\
f_2(m_{4l}, \vec{b}) &= \frac{1}{2}\left(1 + erf\left(\frac{m_{4l} - b_1}{b_2}\right)\right)\left(\frac{b_3}{1 + e^{(m_{4l}-b_1)/b_4}} + \frac{b_5}{1 + e^{(m_{4l}-b_1)/b_6}}\right) \\
f_3(m_{4l}, \vec{c}) &= \frac{1}{2}\left(1 + erf\left(\frac{m_{4l} - c_1}{c_2}\right)\right)\frac{c_3}{1 + e^{(m_{4l}-c_1)/c_4}}
\end{aligned}
\tag{6.2}
$$

These three equations are composed of two main terms, in the first one the mass dependency is contained in an error function, while the second is inversely proportional to an exponential function of the mass. The function f_1 and f_3 are the same but using different parameters as input, and f_2 has two exponential components.

$$
\mathcal{F}_{ggZZ}(m_{4l}, \vec{a}, \vec{b}) = f_1(m_{4l}, \vec{a}) + f_2(m_{4l}, \vec{b}) \tag{6.3}
$$

$$
\mathcal{F}_{qqZZ}(m_{4l}, \vec{a}, \vec{b}, \vec{c}) = f_1(m_{4l}, \vec{a}) + f_2(m_{4l}, \vec{b}) + f_3(m_{4l}, \vec{c}) \tag{6.4}
$$

Where the three vectors $\vec{a}$, $\vec{b}$, and $\vec{c}$ are quadruplets or sextuplets of variables, they are defined as $\vec{a} = (a_1, a_2, a_3, a_4)$, $\vec{b} = (b_1, b_2, b_3, b_4, b_5, b_6)$, and $\vec{c} = (c_1, c_2, c_3, c_4)$. Thus, the mass dependence of $ggZZ$ is described with 10 parameters while 14 parameters are used for $qqZZ$. Moreover, this parametrization is specifically designed to describe the distribution of these backgrounds after 100 GeV. Indeed, the functions do not model the Z boson peak at 90 GeV.

gg $\rightarrow$ ZZ $\rightarrow$ 4l background modelling

The $ggZZ$ background is one of the second most important background and its final state has a signature similar to signal events produced via gluon fusion. When the event categorization is done it becomes the main background in the ggH category.

The Figure 6.1 shows the m_{4l} distribution for $ggZZ$ for each of the three decay channels and obtained from the 2018 MC simulations. These distributions were fitted with Equation 6.3 in order to calculate the optimal parameters, which are given in Table 6.1, and the corresponding probability density function is represented with the blue curves.

This figure represents the fact that the high mass region is very poorly populated, only a few background events are expected with a mass higher than 500 GeV. In the $4e$ distribution, the low statistic leads to some values with a large uncertainty. Furthermore, the full mass range until 3 TeV is used in order to have a parametrization of this background even for the high mass region.

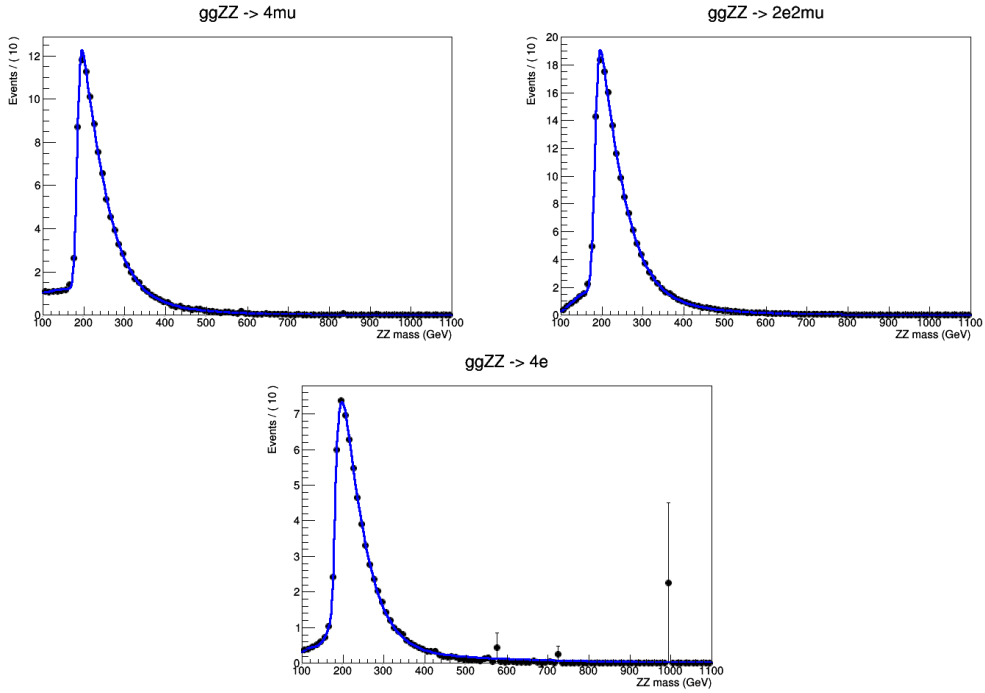

Figure 6.1: Distribution of $gg \to ZZ \to 4l$ background obtained from 2018 MC simulation. Black points represent the simulated data and the blue curve is the fit using Equation 6.3. On the upper left, the decay channel 4μ is represented, $2e2\mu$ on the upper right, and $4e$ on the bottom.

Table 6.1: Parameter values of the $\mathcal{F}_{ggZZ}$ function obtained from a fit performed for each year and for each decay channel. Only the data from 2018 are considered. The decay channels considered are 4μ, $4e$, and $2e2\mu$.

Year	**2018**		
Channel	4μ	$4e$	$2e2\mu$
a_1	102.2	94.0	133.2
a_2	121.6	27.7	40.1
a_3	129.6	247.2	141.6
a_4	0.06	0.03	0.03
b_1	183.8	177.5	183.1
b_2	9.1	22.8	10.5
b_3	41.9	44.7	44.7
b_4	0.6	0.7	0.5
b_5	36.1	3.3	43.7
b_6	-0.2	-0.3	-0.2

$q\bar{q} \to ZZ \to 4l$ background modelling

The $qqZZ$ background is one of the most important background of the Golden Channel and its final state has a signature similar to VBF events. After the categorization procedure it is the main background in the VBF categories.

The m_{4l} parametrization of the $qqZZ$ shape is a bit more complex than the one

of $ggZZ$. Even if their shapes are quite similar, the main difference lies in the mass region ranging from 100 to 200 GeV, where a small peak is visible in Figure 6.2. In order to take it into account, a third term is used in the fit function described in Equation 6.4.

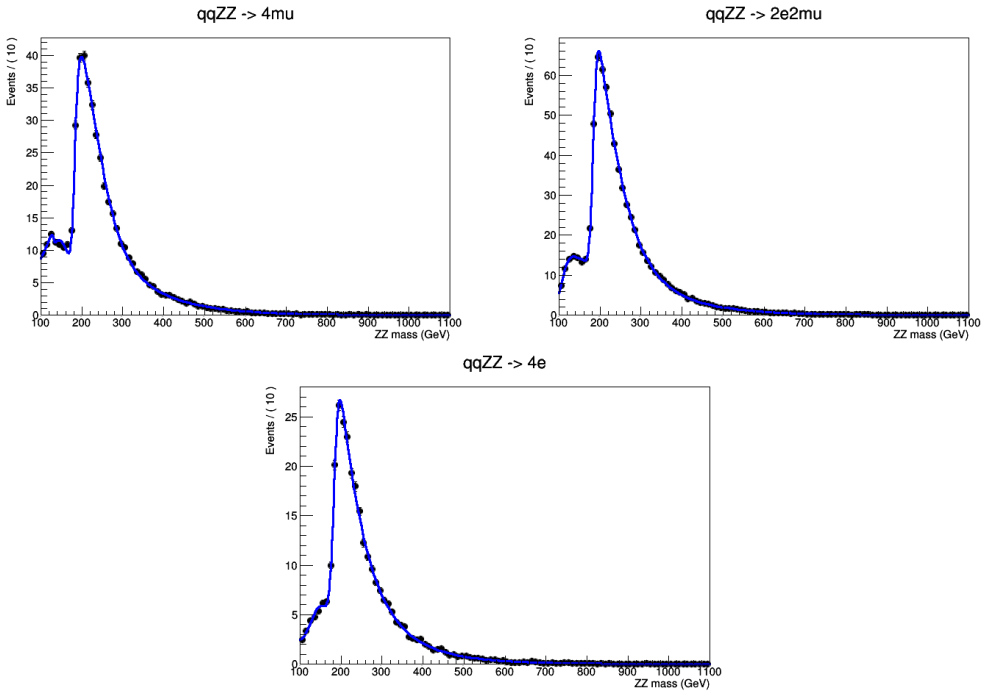

Figure 6.2: Distribution of $q\bar{q} \rightarrow ZZ \rightarrow 4l$ background obtained from 2018 MC simulation. Black points represent the simulated data and the blue curve is the fit using Equation 6.4. On the upper left, the decay channel 4μ is represented, $2e2\mu$ on the upper right, and $4e$ on the bottom.

In the Figure 6.2, the distributions of the background for the three final states are represented with their corresponding fits in blue. Once again, the fits were performed after 100 GeV in order to not taking into account the Z boson mass peak at 90 GeV. The values of the 14 parameters obtained after fitting are listed in Table 6.2.

Moreover, even if the search of high mass resonance is focused on the mass range starting from 200 GeV, it is important to consider lower energy to correctly parametrize the shapes. Indeed, if considering the main peak of the $qqZZ$ shape, it is required to consider events with an energy lower than 200 GeV in order to fully take it into account, and by extension to have the best fitting performance possible.

The plots showing the irreducible background distributions, as well as their corresponding fit, were only presenting a mass range from 100 GeV to 1100 GeV. This was done to put the focus on the most populated part of the mass distributions and also because there are only a few events with a higher mass. For the purpose of the analysis this range is extended to the full mass range up to 3 TeV, in order to have a parametrization of the backgrounds also for the high mass region.

Table 6.2: Parameter values of the $\mathcal{F}_{qqZZ}$ function obtained from a fit performed for each year and for each decay channel. Only the data from 2018 are considered. The decay channels considered are 4μ, $4e$, and $2e2\mu$.

Year	**2018**		
Channel	4μ	$4e$	$2e2\mu$
a_1	211.6	62.3	206.1
a_2	97.4	85.1	132.7
a_3	115.4	157.9	137.3
a_4	0.07	0.07	0.04
b_1	181.5	183.9	184.2
b_2	87.6	11.9	10.5
b_3	35.9	69.2	46.5
b_4	0.6	0.2	0.6
b_5	4.6	35.7	46.6
b_6	-0.3	0.3	-0.2
c_1	130.4	129.1	108.4
c_2	-2.7	20.0	20.0
c_3	105.9	88.1	89.8
c_4	0.01	0.07	0.08

6.2.2 Reducible background

Contrary to the irreducible backgrounds, the $Z + X$ background is obtained from a dedicated data-driven estimation. First, the $Z + X$ background stands for the set of processes made of a Z boson and something else, among which it is possible to cite $Z+$ jets, $Z\gamma+$ jets, $t\bar{t}+$ jets, $WZ+$ jets, or $WW+$ jets. The specificity of these processes is that their estimation from MC simulations is not optimal due to the lack of statistics in the corresponding samples. Indeed, the complex modelling of the jets associated with these processes makes the generation of simulation of events very difficult and this also leads to a poor modelling of the process in general. Therefore, the method used for irreducible background noise cannot be used in this case and therefore the estimation is made from the data.

Even though the estimation is data-based, there are nevertheless MC simulations of the different processes grouped in $Z + X$ and these are used to optimize the estimation methods and to check the agreement between the data and the MC simulation.

The data-based estimates exploit events from regions of the phase space orthogonal to the signal region (SR), and these are called control regions (CR). First, these CR are said to be orthogonal to the signal because they are based on events that do not correspond to the signal. Furthermore, they are used to extrapolate the expected yields and background shapes in the SR. The use of this approach is justified by two arguments, first, it allows the use of a much larger statistic, which reduces the uncertainty associated with the final estimate of the yields. In addition, it does not involve any bias that could be introduced by analysing SR events, which is not the case with CR events.

The first step to estimate the contribution of the $Z + X$ background in the SR consists in defining objects considered as fake leptons, more precisely they are leptons present in the final state that would have a topology similar to that of the leptons coming from the primary vertex. These false leptons are used to form CR, for example we can mention the $Z \rightarrow l^+l^- + l$ CR, where in this case l refers to the presence of an extra free lepton in the event. In this case, the extra lepton can either be a lepton passing (P) the selection criteria detailed in the table 5.4 or failing (F). In this CR, to be reconstructed the Z boson must be formed by leptons satisfying $p_T(l_1) > 20$ GeV and $p_T(l_2) > 10$ GeV. Moreover, there is another condition which concerns the pair formed with the extra lepton and the lepton of opposite sign of the Z boson, and this one must have a mass $m_{l^+l^-} > 4$ GeV.

Next, the CR must be corrected to take into account the amount of fake leptons, for this it is needed to determine the probability of unintentionally selecting a fake lepton, rephrasing, that a false lepton satisfies the selection criteria both those listed for the leptons in Table 5.4 and also those for the ZZ candidates. These probabilities are called fake rate (FR), and they are applied to the CR $Z + ll$ in order to derive the expected contribution of $Z + X$ in the SR.

In this analysis, two different methods are used and each has its own CR:

- **The opposite sign method** (OS) in which two control regions are used: the 2P2F and the 3P1F. They are characterized by a pair of passing leptons, and an other pair of opposite sign leptons which are respectively both failing or one failing and one passing the selection criteria.
- **The same sign method** (SS) in which the 2P2L control region is used, and it is composed of a Z candidate and two same sign leptons.

As presented in Section 5.1.3, the FSR photons are also recovered for events in the $Z + l$ and $Z + ll$ CR, and their addition is performed with the same algorithm applied to the SR. Even if the CR are constructed in such a way that they are completely orthogonal to the SR, the problem is that the selected events may both correspond to two different CR. In these cases, it is necessary to take into account and correct for these overlaps to avoid double counting and overestimation of events, as occurs for the 2P2F and 3P1F phase space regions used in the OS method.

The opposite sign method

In the OS method, the $Z + l$ CR includes all events with a reconstructed Z boson and an additional fake lepton. From this phase space, the FR are determined for electrons (f_e) and for muons (f_μ). In order to reduce contamination from asymmetric photon conversions and WZ and $t\bar{t}$ processes, additional requirements on $|m_{Z_1} - m_Z| < 7$ GeV and $p_T^{miss} < 25$ GeV are applied, .

In order to take into account the specificities due to the subdetectors and in particular the difference between barrel and endcaps, the two are studied separately for the calculation of the fake rates. Then, they are calculated for different bins of p_T of the free lepton, which correspond to the following intervals: [5,7], [7,10], [10,20], [20,30], [30,40], [40,50], [50,80], [80,120], and [120,200] GeV.

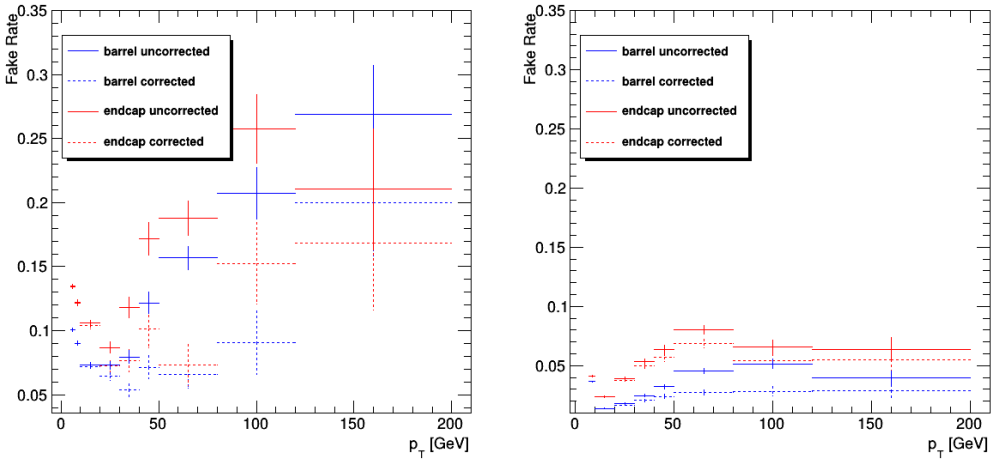

Figure 6.3: Fake rates from the OS method as a function of the probe p_T and using 2018 data. The barrel selection is represented in blue and the endcaps in red. The solid lines correspond to fake rates before the correction of WZ contribution from MC and after with the dashed lines. Muons are represented on the left and electrons on the right.

Compared to the previous analyses studying the Higgs boson properties with the Golden Channel, there are two additional bins after 80 GeV which are used to obtain a better estimation of the $Z + X$ background at higher mass. Although, no bin is used after 200 GeV due to the lack of statistic which does not allow the proposer calculation of the FR. Furthermore, in the case of electrons, the first bin is not taken into account because the low p_T electrons are not taken into account in the context of this analysis. Finally, the contribution of the background WZ estimated from the simulation is subtracted, in order to improve the quality of the measurement.

The FR are measured for each data taking period, separately for electrons and muons using the events $Z \to e^+e^-$ and $Z \to \mu^+\mu^-$. For instance, the measured FR for the 2018 data are presented in Figure 6.3 for muons on the left and electrons on the right. The muons FR are more important than those for electrons because of the higher probability of misidentifying a massive object, such as a jet or a heavy quark, as a muon. Besides, results are shown for barrel in blue and endcap in red, and the WZ correction is applied to the dashed plots. The FR are then applied to the CR $Z + ll$ to extrapolate the background contribution $Z + X$ in the SR.

Both 2P2F and 3P1F CR, are used to extract the final estimate of the $Z + X$ yields in the SR. By their definitions, these CR may have some overlap, in the sense that some events may occur in both, and therefore double counting in the determination of the $Z + X$ yields with the OS method should be avoided in order to not overestimate the importance of this background. All of this is presented in the Appendix 7.3, where all the ingredients used to calculate the final $Z + X$ yields for the OS method are presented.

The OS estimate of the $Z + X$ background in the SR, written $N_{\text{SR}}^{\text{OS}}$, is obtained by combining the contribution of 2P2F and 3P1F CR. For the first CR, the term

is similar to its former definition corresponding to Equation 6, while for 3P1F CR, two additional terms must be considered: the background $N^{\text{bkg}}_{\text{3P1F}}$ and the contribution extracted from the simulation N^{ZZ}_{3P1F} which is used to correct the absence of FSR photon contribution. The expression of the $Z + X$ estimate with the OS method is given by:

$$N^{\text{OS}}_{\text{SR}} = \left(N_{\text{3P1F}} - N^{\text{bkg}}_{\text{3P1F}} - N^{ZZ}_{\text{3P1F}}\right) \sum_i \left(\frac{f_i}{1-f_i}\right) + N_{\text{2P2F}} \sum_{i,j} \left(\frac{f_i f_j}{(1-f_i)(1-f_j)}\right) \tag{6.5}$$

Where N_{2P2F} and N_{3P1F} are respectively the yields computed from the 2P2F CR and from the 3P1F one. Then, the variables f_3 or f_4 are the FR of the third or fourth lepton.

When developing the $N^{\text{bkg}}_{\text{3P1F}}$ term in the previous equation, this one can be simplified in a more compact way which is given by:

$$N^{\text{OS}}_{\text{SR}} = \left(1 - \frac{N^{ZZ}_{\text{3P1F}}}{N_{\text{3P1F}}}\right) \sum_j^{N_{\text{3P1F}}} \left(\frac{f_4^j}{1-f_4^j}\right) - \sum_i^{N_{\text{2P2F}}} \left(\frac{f_3^i f_4^i}{(1-f_3^i)(1-f_4^i)}\right) \tag{6.6}$$

From this equation, the number of expected $Z + X$ events in the SR estimated with the OS method is calculated. This number is also called yield of the $Z + X$ background, and it is used in the analysis to scale the $Z + X$ contribution. The yields are computed for each category as presented in Table 6.3, and this for each data taking periods and for each final state considered in the analysis.

Table 6.3: $Z + X$ yields calculated for the four final states and for each category. Results are calculated only from 2018 data taking period, and they are obtained from OS method.

Year	**2018**			
Channel	4μ	$4e$	$2e2\mu$	$2\mu2e$
ggH	48.5 ± 15.2	24.2 ± 7.4	33.1 ± 10.5	31.9 ± 9.7
VBF + 2 jets	2.7 ± 1.1	1.3 ± 0.4	2.8 ± 1.1	1.5 ± 0.5
Inclusive	50.7 ± 15.8	25.3 ± 7.7	35.2 ± 11.1	33.0 ± 10.0

Finally, the mass distribution of the $Z + X$ background estimated with the OS method is represented in Figure 12 for an inclusive category and for each final state. Likewise to the comments enunciated for the 2P2F and 3P1F mass distributions, they can be repeated here.

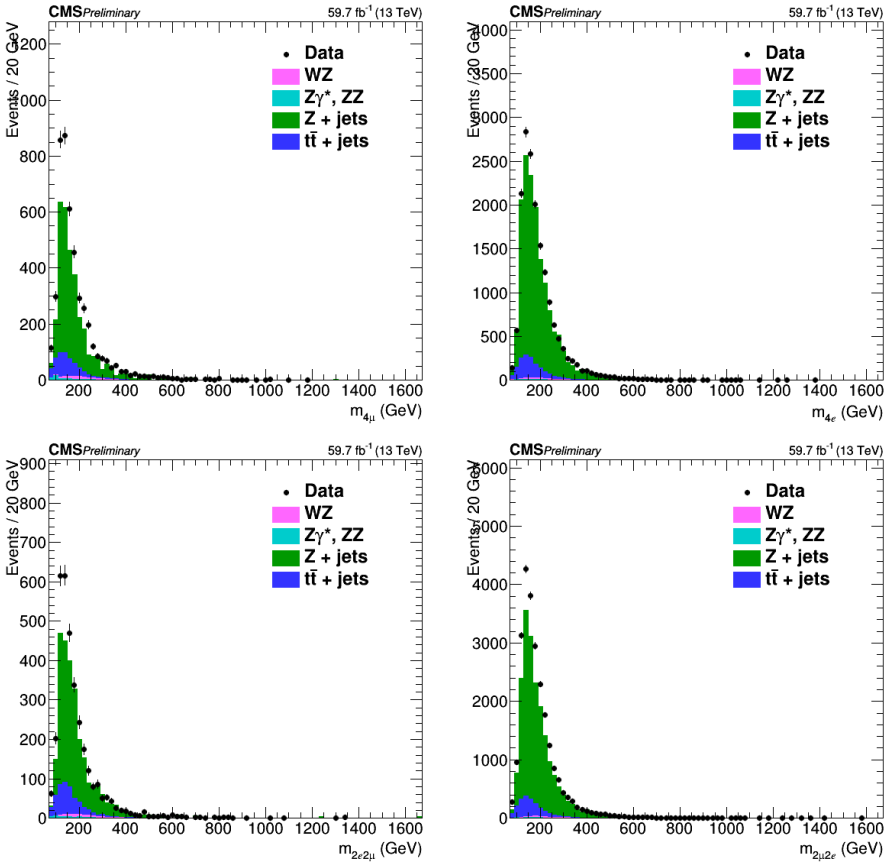

Figure 6.4: Distribution of the invariant mass of $Z + X$ background estimated with the OS method from 2018 samples. Data in black are compared to MC simulation of WZ in pink, $Z\gamma$ or ZZ in turquoise, $Z+$ jets in green, and $t\bar{t}+$ jets in blue. On top left, the 4μ final state is represented at the side of $4e$, and the bottom, the $2e2\mu$ and $2\mu2e$ are represented.

Now that the OS method has been used for the estimation of $Z + X$, it remains to see the SS method.

The same sign method

The SS method relies on the same strategy employed for the OS one, but having its own specificities. First, for the FR measurement, the only difference between both methods is the consideration of the mass range of $40 < m_{l^+l^-} < 120$ GeV which is extended compared to the previous one, in order to get a proper description of the SS topology. By extension, this leads to consider more events with asymmetric photon conversion entering in the $Z + l$ phase space. In particular in the $Z + e$ case where the FSR photon contribution was missing in the OS method because the $m_{l^+l^-} < 7$ GeV cut rejecting most of these events. Furthermore, the CR used in the SS method for the FR measurement does not correspond completely to the 2P2L CR, and because of that the $Z + e$ FR (f_e) must be corrected for this effect. The correction is performed by modifying the corresponding to modified ranges of the $|m_{l^+l^-} - m_Z|$ cut. The FR are also measured for all these samples in nine bins

of p_T for muons, or eight for electrons. There are also two η bins corresponding to the barrel and endcap.

More precisely, the electron fake rates f_e in the 2P2L CR are determined from the number of missing hits in each of the p_T bins considered in the analysis, extrapolating the correct fake rate from the linear relation described above. The resulting distribution of the FR obtained with 2018 data for electron and muons in the p_T bins considered for the analysis is shown in Figure 6.5.

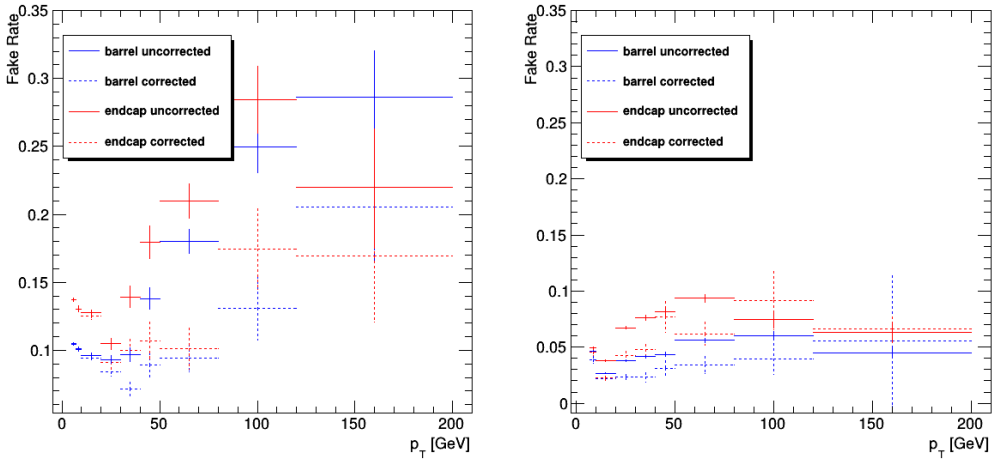

Figure 6.5: Fake rates from the SS method as a function of the probe p_T and using 2018 data. The barrel selection is represented in blue and the endcaps in red. The solid lines correspond to fake rates before the correction of WZ contribution from MC and after with the dashed lines. Muons are represented on the left and electrons on the right.

The estimate of the $Z + X$ background from the 2P2L control region is performed by weighing all the corresponding data events as follows:

$$N_{\mathrm{SR}}^{\mathrm{SS}} = \frac{N_{OS}}{N_{SS}} \sum_i (f_3^i \times f_4^i) \tag{6.7}$$

Where the sum runs over all the events in the 2P2L CR, f_3 and f_4 are the fake rates for the two loose leptons, and the correction factor N_{OS}/N_{SS} stands for the difference between the number of events in the OS and SS samples.

Table 6.4: Summary of the ratio N_{OS}/N_{SS} for the different decay channels and for the 2018 data taking period.

Channel	4μ	$4e$	$2e2\mu$	$2\mu2e$	$4l$
2018	1.03 ± 0.02	1.01 ± 0.01	1.03 ± 0.03	1.01 ± 0.01	1.01 ± 0.01

The values of this factor, obtained from data in the three data taking periods separately, are presented in Table 6.4. The four final states are taken separately as well as the general $4l$. All the ratios are close to one, even if the OS samples are always slightly higher.

The mass distribution of the $Z + X$ background estimated with the SS method is represented in Figure 6.6 for an inclusive category and for each final state. The estimation using the data-driven approach is compared to the MC simulation.

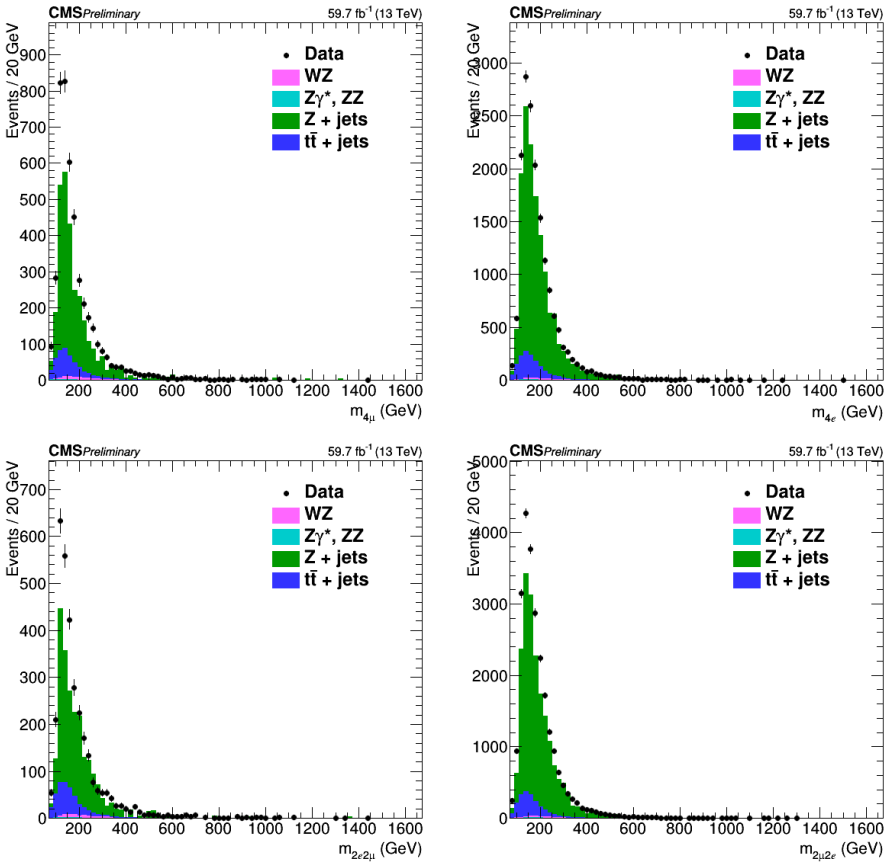

Figure 6.6: Distribution of the invariant mass of $Z + X$ background estimated with the SS method from 2018 samples. Data in black are compared to MC simulation of WZ in pink, $Z\gamma$ or ZZ in turquoise, $Z+$ jets in green, and $t\bar{t}+$ jets in blue. On top left, the 4μ final state is represented at the side of $4e$, and the bottom, the $2e2\mu$ and $2\mu2e$ are represented.

The number of expected $Z + X$ events in the SR estimated with the SS method is presented in Table 6.5, for all the data taking periods, for all the final states, and for all the categories considered in this analysis. The results are in agreement with the prediction obtained from the OS method, except for the $4e$ final state which shows a more important difference, due to the different selection applied on the additional electrons and from the treatment for the photon conversions between both methods.

From 2018 data, a total of 132.03 events are estimated for the $Z + X$ background, if considering all the decay channels at the same time and in an inclusive category.

Table 6.5: $Z + X$ yields calculated with the SS method for the four final states and for each category. Results are calculated only for 2018 data taking period.

Year	**2018**			
Channel	4μ	$4e$	$2e2\mu$	$2\mu2e$
ggH	50.6 ± 15.5	15.6 ± 5.7	36.5 ± 11.1	22.7 ± 8.3
VBF + 2 jets	3.1 ± 1.0	0.8 ± 0.3	2.0 ± 0.6	1.0 ± 0.4
Inclusive	53.7 ± 16.4	16.3 ± 6.0	38.5 ± 11.8	23.7 ± 8.6

The $Z + X$ estimate has three sources of uncertainty: the first one is composed of all the statistical uncertainties associated with the number of events in the $Z + l$ and $Z + ll$ CR, and with the number of missing hits used to calculate the FR in the SS method. The second source is the systematic uncertainty corresponding to the one σ shifts in each direction of the FR. And the third one comes from the systematic difference between the various processes constituting the $Z + X$ background, which corresponds to the difference between the FR and the ones obtained reweighing the individual FR according to the 2P2F CR. All of these contributions give to the overall $Z + X$ uncertainty, which is calculated to be 30.1%, 30.5%, and 36.6% in the 4μ, $2e2\mu$, and $4e$ decay channels respectively. These uncertainties on the $Z + X$ yield prediction are then included in the analysis as nuisance parameters in the calculation of the asymptotic limits.

Z+X background modelling

Now that the $Z + X$ background has been estimated, it is time to determine the shape of its distribution as a function of the invariant mass of the four leptons. To model this shape, a Landau function has been used

$$f_{Landau}(x, \mu, c) = \frac{1}{\pi c} \int_0^\infty e^{-t} cos\left(t\left(\frac{x-\mu}{c}\right) + \frac{2t}{\pi} log\left(\frac{t}{c}\right)\right) dt \qquad (6.8)$$

Where μ corresponds to the position of the maximum of the distribution and c is a shape parameter.

The use of such a function was motivated by the various works carried out on this decay channel, for example a source of inspiration to justify this choice is the last measurements of properties of the Higgs boson in the $4l$ final state [5].

The $Z + X$ distributions were fitted with the function from Equation 6.8 as it is illustrated in Figure 6.7. Here, the fit is performed for the three final states in an inclusive category. As it was already explained for $ggZZ$ and $qqZZ$ backgrounds, the fitting range is not going up to 3 TeV because of the lack of event after 1 TeV. But the background has a contribution at high mass thanks to its parametrization depending on m_{4l}.

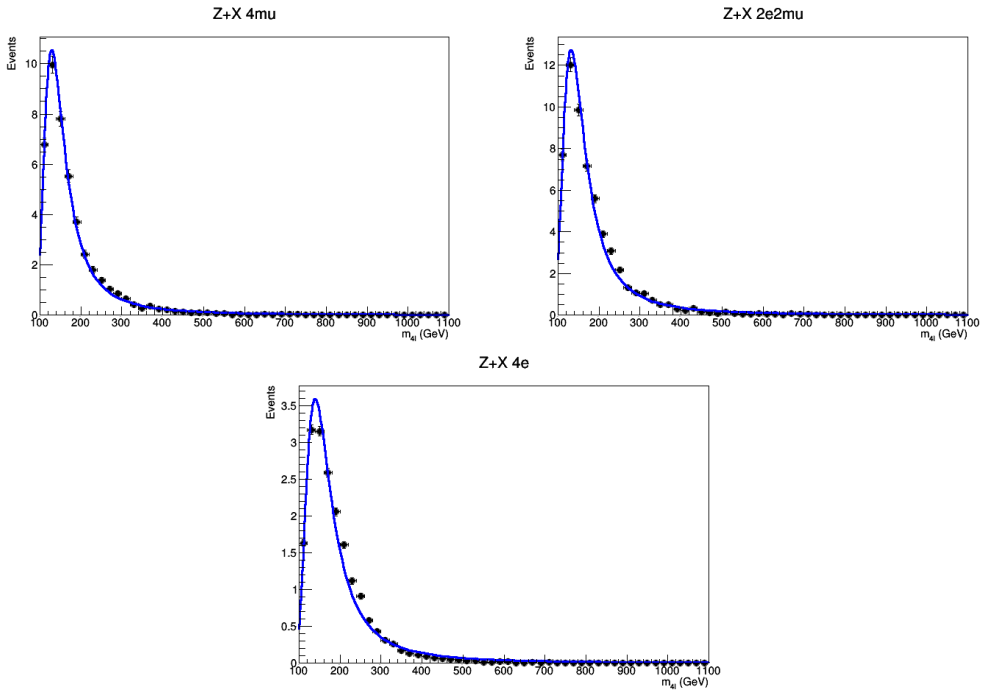

Figure 6.7: Distribution of $Z + X$ background obtained from 2018 data represented in black. The blue curve is the fit using Equation 6.8. On the upper left, the decay channel 4μ is represented, $2e2\mu$ on the upper right, and $4e$ on the bottom.

6.2.3 Summary of the background modelling

As a conclusion on the modelling of background, the Figure 6.8 summarizes very well all that has been done. Foremost, the estimation of the three main background noises, the two irreducible ones using MC simulations and the reducible one with a data-driven approach. Then, the weighting of the events is done directly in the case of the MC simulations with a factor taking into account the branching ratio of the process under study, and by the calculation of the yields for $Z + X$. Finally, a parametrization of the background as a function of the mass has been determined. This serves as an estimator of the impact of the background at a given mass, which is relevant in this analysis given that the mass of the resonance sought can vary.

And all this is shown in Figure 6.8. The points correspond to the distributions from the estimation of the three background, $qqZZ$ in blue, $ggZZ$ in red, and $Z + X$ in green. All distributions are scaled to correctly represent the weight of their contribution, and the mass parametrization corresponds to the fits.

The modelling of background processes is indeed a very important aspect for this analysis. However, the modelling of the signal that is presented in the next section has an equal importance if not more.

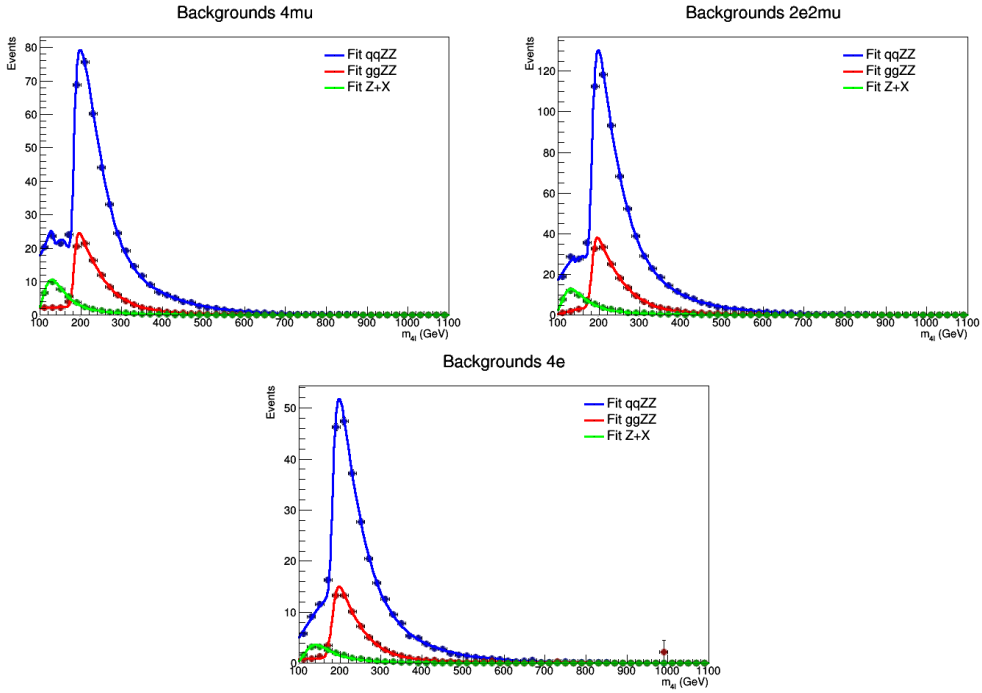

Figure 6.8: Distributions of the main backgrounds for $X \rightarrow ZZ \rightarrow 4l$. $qqZZ$ in blue and $ggZZ$ in red are obtained from 2018 MC simulation, while $Z + X$ in green is estimated from 2018 data. The fit performed on each background is represented in the same colour. On the upper left, the decay channel 4μ is represented, $2e2\mu$ on the upper right, and $4e$ on the bottom.

6.3 Signal modelling

Signal modelling, as well as background modelling, is required to estimate the expected signal for any mass of the four leptons between 200 and 3000 GeV. In addition, different combinations of resonance mass m_X and width Γ_X are considered in order to test the full range of possibilities for the nature of the resonance. The parametric approach used for this analysis was considered in order to test all possible signals, but also to avoid having to generate dedicated MC samples for each particular model. In this sense, the signal model that is used is much more generic than the theoretical models proposed by theorists. For this reason, the resonances that are sought in this analysis are initially modelled with an analytical shape expression that allows the desired mass and width to be varied for any value of m_{4l}, and this is detailed in Section 6.3.1. But this shape, being the result of a theoretical model, is ideal in the sense that it does not take into account the different effects that occur during detection, nor those of the selection. For these two reasons, other ingredients must be added to the signal model in order to make possible the comparison with the data collected by the CMS detector. The first of these ingredients, presented in Section 6.3.2, is the selection efficiency, which provides information on the effect of selection by giving the proportion of events selected as a function of invariant mass. The second ingredient is the signal resolution which adds to the model the effects of the detector as well as the

effects due to the reconstruction of the events, and this contribution is described in Section 6.3.3. From these elements, the model is built as follows:

$$\mathcal{P}(m_{4l}^{reco}) = \mathcal{E}(m_{4l}^{gen}) \times \left(\mathcal{P}(m_{4l}^{gen}|m_X, \Gamma_X) \otimes \mathcal{R}(m_{4l}^{reco}|m_{4l}^{gen})\right) \tag{6.9}$$

Where the signal model noted $\mathcal{P}(m_{4l}^{reco})$ is constituted by the convolution of the analytical shape $\mathcal{P}(m_{4l}^{gen}|m_X, \Gamma_X)$ and the resolution $\mathcal{R}(m_{4l}^{reco}|m_{4l}^{gen})$, and the product of this convolution is multiplied by the selection efficiency written $\mathcal{E}(m_{4l}^{gen})$. In this definition, m_{4l}^{reco} stands for the reconstructed mass of the four lepton, while m_{4l}^{gen} is the reconstructed one.

This final expression of the signal model will be built in this section and then used in the different steps of the statistical analysis presented in Chapter 7.

6.3.1 Analytical line shape of the signal

The first ingredient needed to build the signal model is the analytical shape of the resonance, ant it corresponds to the truth shape of the signal in the ideal case where no sources of smearing are applied. In order to cover all the phase space of the resonance mass and width, it is required to have a parametric model allowing the independence between the resonance mass and width variations. This means that there is no interdependence between m_X and Γ_X, if one is fixed the other parameter can vary freely.

In the analysis, the analytical shape of the signal is evaluated from the generated four lepton mass m_{4l}^{gen} and the model used is derived from works about the analytical line shape of the Higgs boson [178, 179]. This analytical model is defined as a function of the generated m_{4l}^{gen} has the advantage to take as argument m_X and Γ_X.

$$\mathcal{P}(m_{4l}^{gen}|m_X, \Gamma_X) = \frac{\sigma(m_{4l}^{gen})}{\pi} \frac{2m_{4l}^{gen} m_X \Gamma_X}{(m_{4l}^{gen\,2} - m_X^2)^2 + (m_X \Gamma_X)^2} \tag{6.10}$$

Where $\sigma(m_{4l}^{gen})$ is the multiplication of cross-section and branching ratio $\sigma.BR$ for a considered production mode and final state as a function of m_{4l}^{gen}. The values of $\sigma(m_{4l}^{gen})$ are taken from the work made by the LHC Higgs Cross-Section Working Group and presented in its fourth report [2], in which the cross-section is calculated as a function of the invariant mass of m_{4l}. Although, the $\sigma(m_{4l}^{gen})$ can be taken for another model and changed easily since it corresponds only to a scaling factor.

Moreover, this parametrization does not consider a complex pole scheme (CPS) correction, since they are not applicable for a non-SM resonance. For this reason, the Equation 6.10 is based on the expression of a Breit-Wigner distribution function. The other studies based on the Golden Channel for the search of high mass resonance [6, 10] use the same function.

An illustration of different resonances is given in Figure 6.9, where each resonance is represented by the function $\mathcal{P}(m_{4l}^{gen}|m_X, \Gamma_X)$ with a specific combination of m_X and Γ_X. These curves are shown as an example of what is the expected analytical line shape for the signal which is looked for.

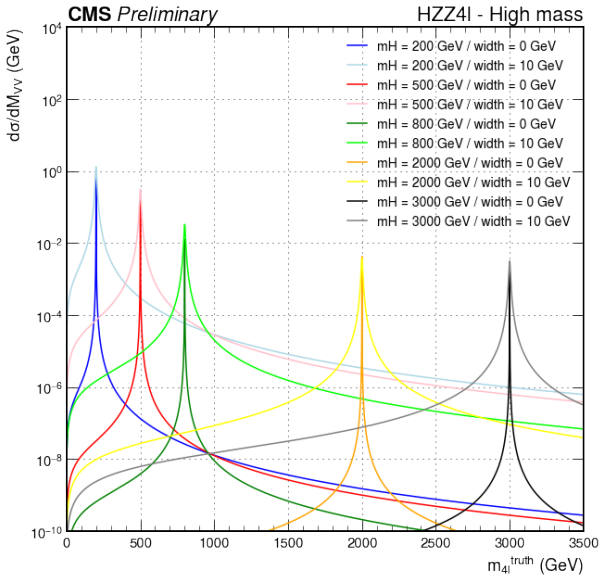

Figure 6.9: Examples of signal analytical line shapes as a function of the generated four lepton mass m_{4l}^{gen}. Each curve corresponds to a specific combination of resonance mass m_X and width Γ_X.

6.3.2 Signal efficiency

The second ingredient of the signal model is the selection efficiency computed within the lepton acceptance. This efficiency is calculated using the Equation 5.6 where both the generated and reconstructed events considered must respect the lepton acceptance. In terms of selection criteria, it corresponds to $p_T^e > 7$ GeV and $|\eta_e| < 2.5$ for electrons, $p_T^\mu > 5$ and $|\eta_\mu| < 2.4$ for muons. The interest of using the signal efficiency in the signal model is driven by the fact that the selection applied on the events has an impact on the number of events used in the analysis, and it is not constant over mass. In order to apply the correct efficiency value to the events, the efficiency must be defined as a function of the generated four lepton mass m_{4l}^{gen}.

The signal efficiency is calculated for each available mass samples starting from 115 GeV to 3 TeV. The extended range in the low mass region is used in order to get a good parametrization of the efficiency elbow occurring around 200 GeV. Moreover, ggH and VBF MC simulation samples were used to calculate the efficiency where both production modes were taken separately for the calculation, as well as the final states.

In order to have a signal efficiency value for each mass of the four leptons, a fit is performed on the efficiency points for each production mode and each final state. The function used for that is given by:

$$\mathcal{E}(m_{4l},\vec{a}) = a_0 + a_1.erf\left(\frac{m_{4l}-a_2}{a_3}\right)\left(a_4 + a_5.m_{4l} + a_6.m_{4l}^2 + a_7.m_{4l}^3\right) + \frac{a_8}{a_9\sqrt{2\pi}}e^{-\frac{1}{2}\left(\frac{m_{4l}-a_{10}}{a_9}\right)^2} \tag{6.11}$$

Where the vector $\vec{a} = (a_0, a_1, a_2, a_3, a_4, a_5, a_6, a_7, a_8, a_9, a_{10})$, it is used as a simplified notation of the eleven parameters of the equation.

This equation was used in the previous analysis on the high mass resonance carried out with CMS 2016 data [9], and it allows having a fitted curve matching the high mass region points as well as the low mass region, and especially the elbow around 200 GeV.

The signal efficiency described here is represented in Figure 6.10, where the two production modes and the three final states are taken separately. The fits are realized with Equation 6.11 for each of the six combination of decay channel.

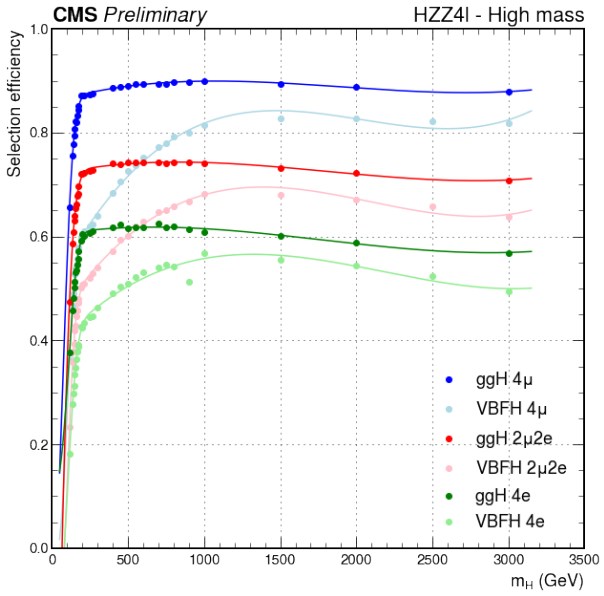

Figure 6.10: Selection efficiency $\mathcal{E}(m_{4l}^{gen})$ as a function of the generated mass of the four leptons m_{4l}^{gen}, and calculated from MC signal samples. Full colours corresponds to ggH, and light colours to VBF. The 4μ final state is represented in blue, $2\mu 2e$ in red, and $4e$ in green. The fit performed on the six different decay channels are represented in the same colour.

As a comment on the fits, the VBF curves show the limit of the function used because of the slight oscillation between 1 and 3 TeV. A way of improvement could be to use a spline using the function of Equation 6.11 before 1 TeV and then a simpler one like a first or second order polynomial function.

In the specific case of the selection efficiency it is very pertinent to also have an overview of the impact of the categorization, as it is shown on Figure 6.11. Here the two categories are represented with the inclusive one, and the results are

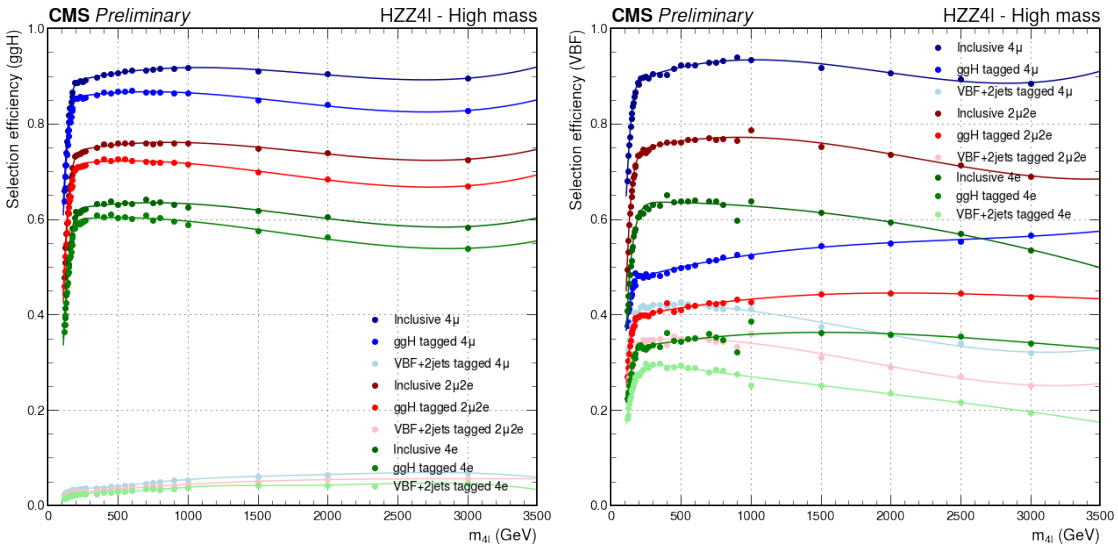

Figure 6.11: Selection efficiency $\mathcal{E}(m_{4l}^{gen})$ taking into account the lepton acceptance as a function of the generated mass of the four leptons m_{4l}^{gen}, calculated from ggF MC signal samples on the left, and from VBF on the right. Full colours corresponds to the ggH category, light colours to VBF + 2 jets, and dark colours to the inclusive category. The 4μ final state is represented in blue, $2\mu 2e$ in red, and $4e$ in green. The fit performed on the six different decay channels are represented in the same colour.

highly dependent on the production mode of the samples. Indeed, considering the selection efficiency calculated from the ggF samples, more than 90% of the events are tagged as ggH and less than 10% as VBF + 2 jets. On the other side, if considering the selection efficiency calculated from VBF samples, around 60% of the events are categorized as ggH and only 40% as VBF + 2 jets. Hence, VBF events are more often miscategorised, and because of that it is expected to have better results in terms of asymptotic limits on the cross-section for the ggH category.

6.3.3 Signal resolution

The third element of the signal model is the signal resolution defined as the mass difference between reconstructed and generated events. This quantity is used as an estimate of the impact of the reconstruction on the number of events expected for a given four leptons mass. Moreover, the signal model defined in Equation 6.9 is a function of m_{4l}^{reco}, and the signal efficiency and analytical line shape are both depending only on m_{4l}^{gen}, hence the mass parametrization of the model is mostly depending on the resolution as well as the correspondence between reconstructed and generated mass. Nevertheless, some detector effects affecting the invariant mass distribution are simulated with Geant4 and the resolution allows adding them to the signal model.

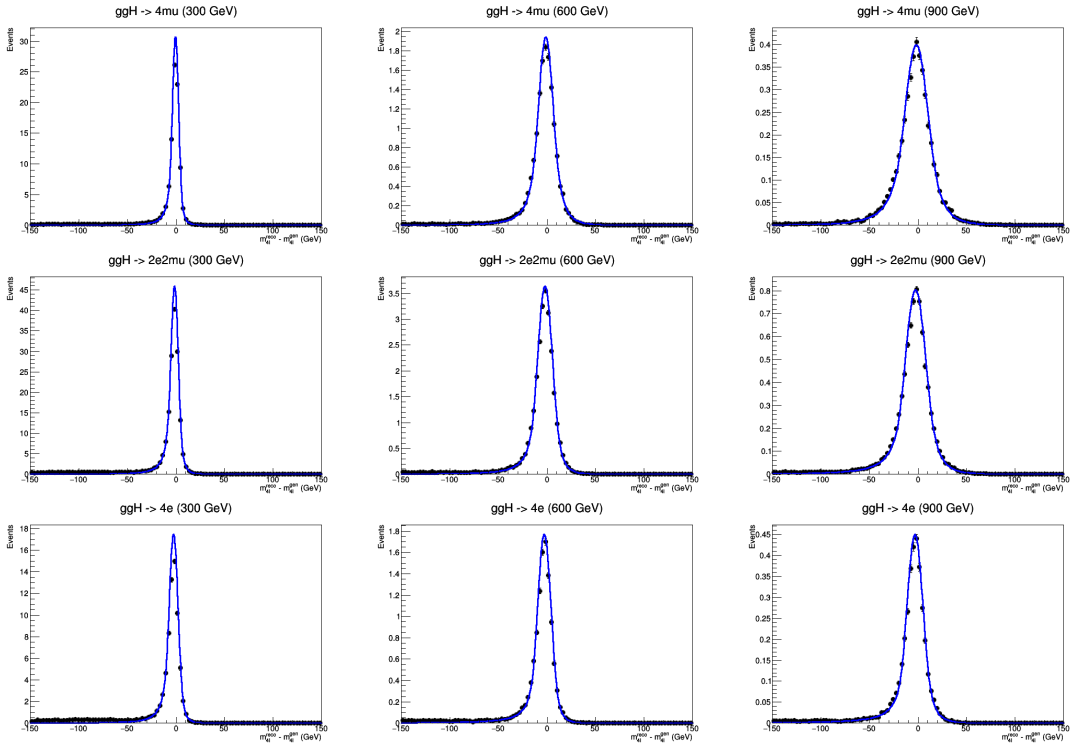

Figure 6.12: Distributions of $m_{4l}^{\text{reco}} - m_{4l}^{\text{gen}}$ coming from ggH events shown with the black points and the DCB fits performed simultaneously over all the mass points are drawn in blue. The top plots correspond to 4μ final state, those in the middle to $2e2\mu$, and those on the bottom to $4e$. From left to right, three mass points are represented for all the final states: 300, 600, and 900 GeV.

The signal resolution is obtained from the $m_{4l}^{reco} - m_{4l}^{gen}$ distribution, and in this analysis it is calculated for each mass point comprised between 200 GeV and 3000 GeV included. From each of the distribution a double Crystal Ball (DCB) function is used to perform a fit. The parameter values obtain from the fits are then used to have a resolution parametrization over all the mass range. The equation of the DCB function is given by:

$$\mathcal{R}(\xi, \vec{c}_L, \vec{c}_R) = \begin{cases} \left(\frac{n_L}{|\alpha_L|}\right)^{n_L} e^{-\frac{|\alpha_L|^2}{2}} \left(\frac{n_L}{|\alpha_L|} - |\alpha_L| - \xi\right)^{-n_L} & \text{if} \quad \xi \leq -\alpha_L \\ e^{-\frac{\xi^2}{2}} & \text{if} \quad -\alpha_L < \xi < \alpha_R \\ \left(\frac{n_R}{|\alpha_R|}\right)^{n_R} e^{-\frac{|\alpha_R|^2}{2}} \left(\frac{n_R}{|\alpha_R|} - |\alpha_R| - \xi\right)^{-n_R} & \text{if} \quad \xi \geq \alpha_R \end{cases} \tag{6.12}$$

The two vectors defined in the resolution function are doublets corresponding to $\vec{c}_L = (\alpha_L, n_L)$ and $\vec{c}_R = (\alpha_R, n_R)$. They are respectively composed of the parameters of the left and right parts of the DCB function. The last input of the function is defined as: $\xi = \frac{\Delta m_{4l} - \mu}{\sigma}$ with $\Delta m_{4l} = m_{4l}^{\text{reco}} - m_{4l}^{\text{gen}}$ the difference between the reconstruction four leptons mass and the generated one, μ is the mean mass of the Gaussian core of the double Crystal Ball, and σ is its standard deviation.

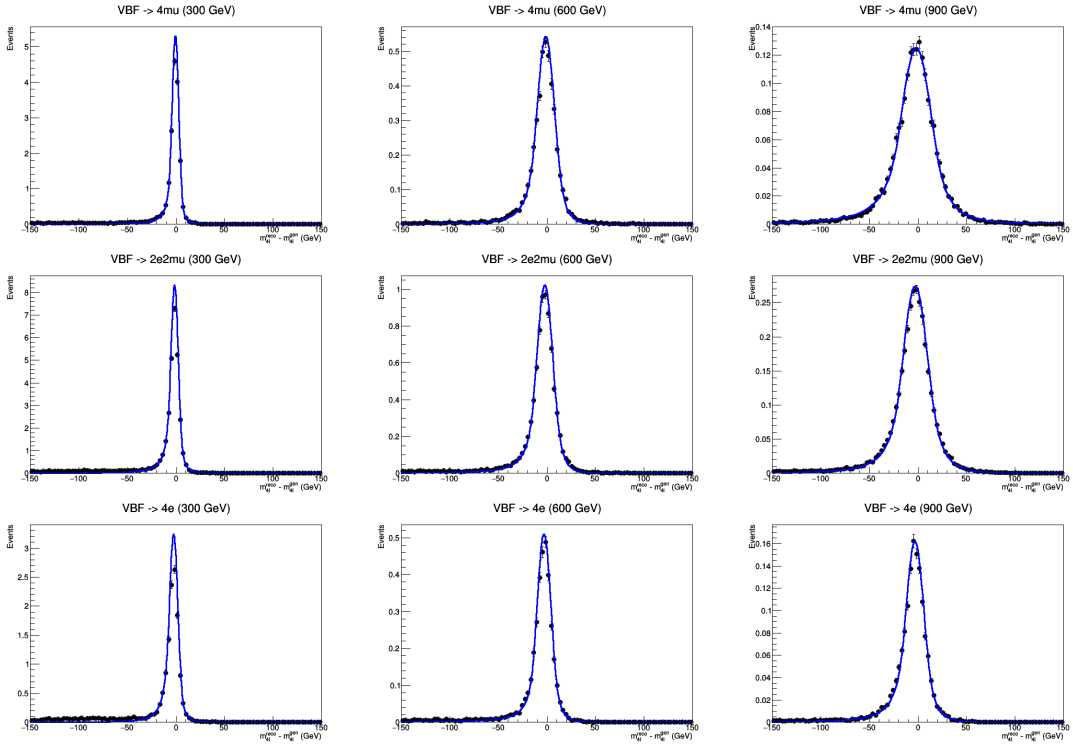

Figure 6.13: Distributions of $m_{4l}^{\text{reco}} - m_{4l}^{\text{gen}}$ coming from VBF events shown with the black points and the DCB fits performed simultaneously over all the mass points are drawn in blue. The top plots correspond to 4μ final state, those in the middle to $2e2\mu$, and those on the bottom to $4e$. From left to right, three mass points are represented for all the final states: 300, 600, and 900 GeV.

The mass difference distributions are shown for ggH in Figure 6.12 and for VBF in Figure 6.13, the fits in blue are performed simultaneously on all the available mass points. Such a technic was used in order to get a smoother distribution of

the parameters as a function of the mass. For a reason of optimization and for increasing the precision, the distributions were fitted separately in a first time to get an estimate of the DCB parameters. Then, the parameters collected from the fits were used as initial values in the simultaneous method.

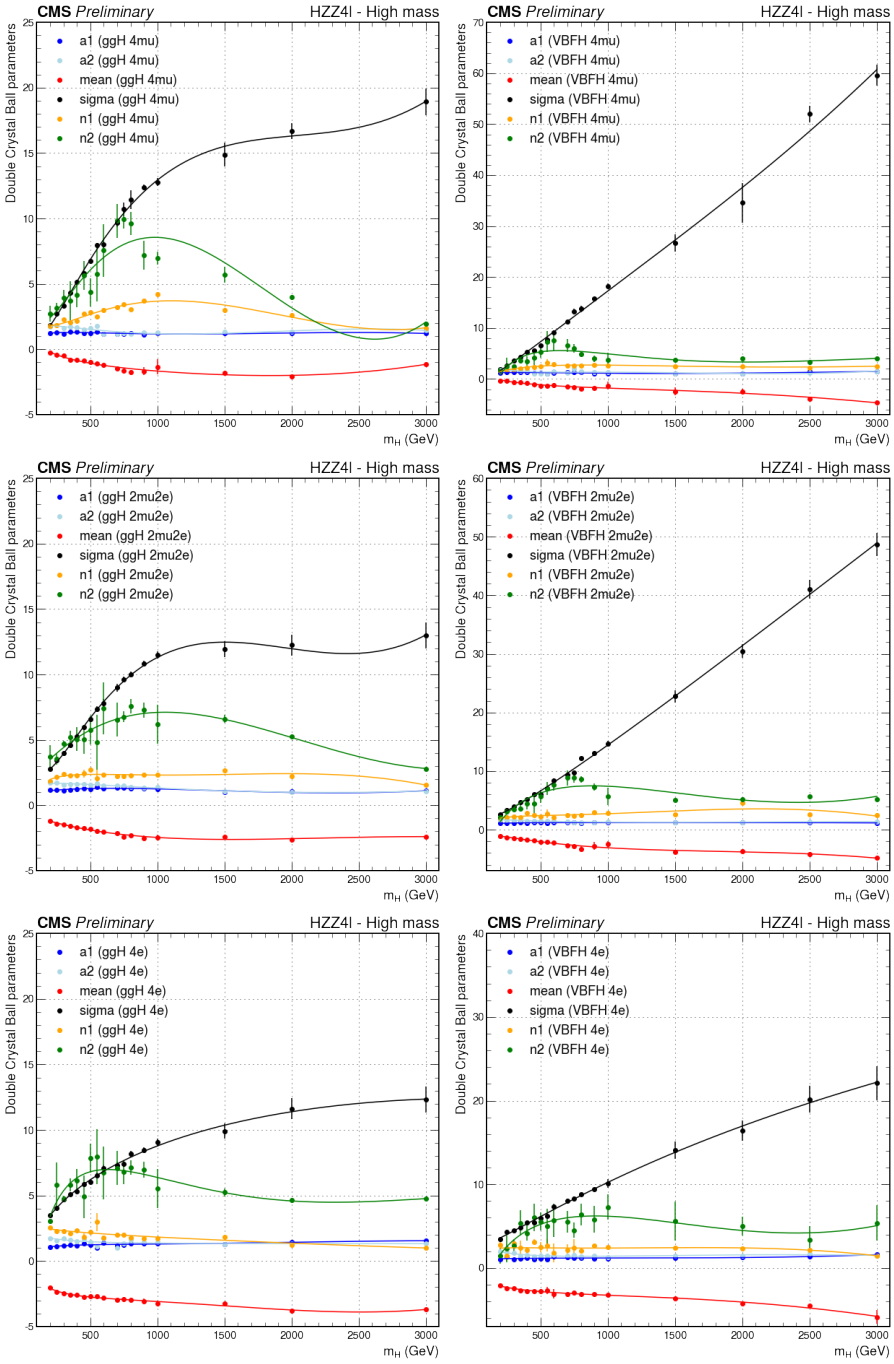

Figure 6.14: Double Crystal Ball parameters obtained from $m_{4l}^{\text{reco}} - m_{4l}^{\text{gen}}$ distribution fit as a function of m_{4l}^{reco}. The parameters and their corresponding fits are plotted in the same colour with α_L in blue, α_R in light blue, μ in red, σ in black, n_L in yellow, and n_R in green. On the left ggH events are considered, and VBF on the right. From top to bottom, the final states 4μ, $2\mu 2e$, and $4e$ are represented.

The DCB parameters are calculated for each mass points, production mode, and decay channel. Then, their mass parametrization is obtained by fitting them with a third order polynomial function as described in Figure 6.14. Here, each plot corresponds to a specific decay channel coming from ggH or VBF events.

In the same way as what was said about the signal efficiency fits, this figure shows some limitations of the third order polynomial function used to fit the DCB parameters over mass. For some parameters such as α_L, α_R, n_L or even μ the function chosen fit well their values over mass, but considering σ for ggH curves and n_R in general, it is clear that the fit can be improved. For both of these parameters, the problem also comes from the inflexion around 1 TeV and a spline using two polynomial functions one defined before the elbow and the other one after could be used.

6.3.4 Validation of the signal model

As a proof of concept and a validation of the model, closure tests are realized by comparing the reconstructed mass distributions obtained from the signal MC samples and the signal model $\mathcal{P}(m_{4l}^{reco})$.

Before doing the comparison, the signal model is build with the parametrization of its ingredients presented previously in this section, and they are combined inside Equation 6.9. In the Figure 6.15, the model is plotted for different combinations of m_X and Γ_X.

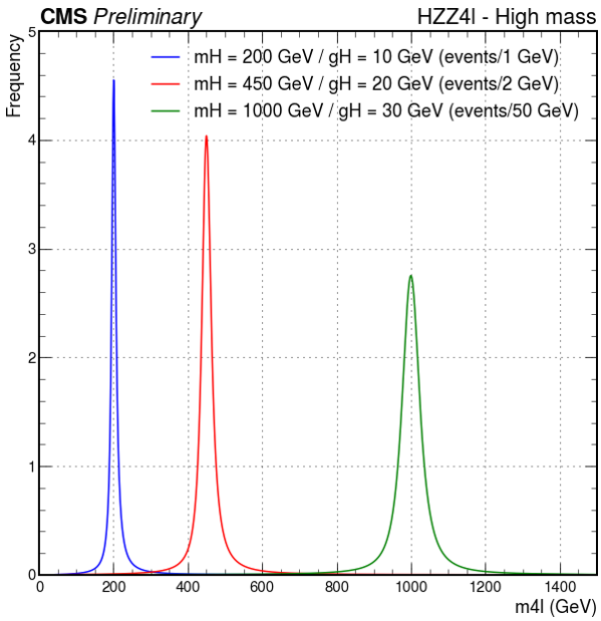

Figure 6.15: Illustration of the signal model as a function of m_{4l}^{reco}. In blue, the signal corresponds to a resonance with $m_X = 200$ GeV and $\Gamma_X = 10$ GeV. In red, the resonance is defined by $m_X = 450$ GeV and $\Gamma_X = 20$ GeV, and multiplied by a factor 2. In green, the resonance is defined by $m_X = 1000$ GeV and $\Gamma_X = 30$ GeV, and multiplied by a factor 50.

Moreover, for a better visualization of many signal shapes in a single figure, each of them have a specific scale. In theory, it is expected to have much smaller resonances at high mass, for instance the one in green corresponding to a resonance with $m_X = 1000$ GeV and $\Gamma_X = 30$ GeV should be 50 times smaller.

The analytical shape is based on a Breit-Wigner distribution function which does not include CPS correction at the opposite of the SM-like signals samples used. The comparison between both can be done only after a proper reweighting of the mass distribution in the MC signal samples. The new weights are calculating with the MELA approach in order to remove the CPS corrections, since they are no longer applicable for the high mass resonance which are not SM-like. Once obtained the weights are added to the weighting formula given by Equation 6.1.

For the closure tests the width value is taken from the mass parametrization presented in Figure 1.11, where the width of a SM-like resonance is defined as a function of its mass. For instance, the closure test realized with the 200 GeV signal samples is presented in Figure 6.16. In this case the signal model use the same resonance mass of 200 GeV and a width ∼1 GeV. The four leptons invariant mass distribution used for the comparison is the one using the reweighting mentioned in the previous paragraph. The signal models correspond to events with a $4l$ final state coming from ggH on the left and from VBF on the right.

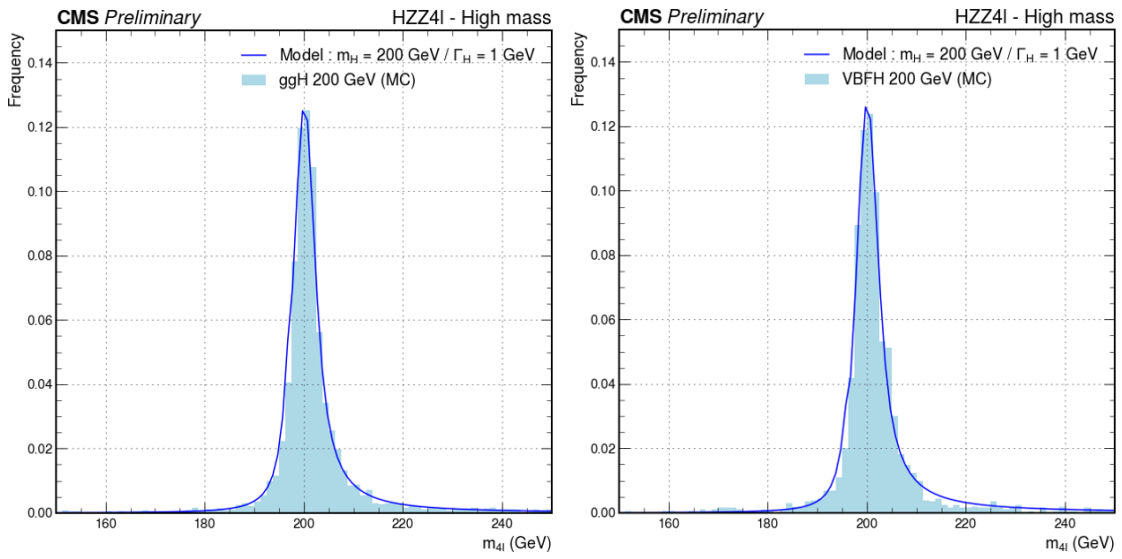

Figure 6.16: Closure test of the signal model on ggH at 200 GeV on the left and VBF at 200 GeV on the right. The model is compared to the reweighted four leptons invariant mass distribution from MC simulation samples.

As a conclusion of the closure tests, it was observed that the signal models built for this analysis are matching the m_{4l} distributions obtained from the MC signal samples after a proper reweighting removing the CPS corrections. This allows to validate the model built so far.

Chapter 7

Statistical analysis and results on the high mass resonance search

Table of contents

7.1 Statistical analysis strategy 222
7.1.1 Method of the maximum likelihood 222
7.1.2 The signal and background template parametrization 224
7.1.3 Interferences contribution to the model 226
7.2 Systematic uncertainties 227
7.2.1 Experimental uncertainties 228
7.2.2 Theoretical uncertainties 229
7.2.3 Summary on the uncertainties 230
7.3 Results on the search of high mass resonance 231

The main objective of the physics analysis presented in this thesis is to find out if there is a high mass resonance. To do this, it is necessary to check if the signal model that was constructed in the Chapter 6 can coincide with the experimental data, and this is operated by looking for an excess of data compared to the theoretical expectation and to quantify it. To find out if there is a statistically sufficient match between the two, a test consisting of maximizing a likelihood function, described in Section 7.1.1, is performed. Moreover, the likelihood function is estimated with a multidimensional fit on the four lepton invariant mass as well as the kinematic discriminant, to do so conditional templates are added to the model as explained in Section 7.1.2. The likelihood function takes into account all the ingredients presented above, such as the signal, background noise, but also interference phenomena which are explained in Section 7.1.3. Finally, the statistical test results also take into account the different sources of uncertainty on the different quantities used in the model or that may affect it.

At the end, to understand if the observed data can describe the resonance, it is necessary to get the confidence intervals on the product of the expected X boson cross-section and branching ratio, written $\sigma_X.BR_{4l}$. These intervals also called limits are computed from MC samples to get the expected ones, and from data for

the observed ones. Both are determined from profile likelihood scans for a given set of m_X and Γ_X, as well as the fraction of VBF events f_{VBF}. All these results are presented and discussed in Section 7.3.

Similarly to what was explained in Chapter 6, only the results obtained from 2018 data are presented in this chapter.

7.1 Statistical analysis strategy

At the beginning of Run-1, a statistical procedure was proposed by the LHC Higgs Combination Group for both ATLAS and CMS analyses [180]. It aims to have a common method used by both collaborations in order to coordinate the combination of the results for claiming the Higgs boson discovery. In this thesis the same procedure is used and detailed in this section.

As it was explained previously, the main goal for the physics analysis presented in this thesis is to search for a significant excess of events with respect to the SM expectation, and to build the expected and observed limits on the product of the cross-section for a new boson and the branching fraction for its decay into a pair of Z boson. Besides, this work is done for a wide range of resonance mass and width.

The statistical methods should gather together the selected events from the data, or the signal model, the background models, and the uncertainties which are discussed in Section 7.2. Moreover, this method must evaluate the presence or absence in the observed data of a signal following the model built. As suggested by the LHC Higgs Combination Working Group the method of the maximum likelihood should be used in this case.

7.1.1 Method of the maximum likelihood

The method of maximum likelihood is performed on parameter of interest (POI) and includes also the treatment of nuisance parameters (NP) which represent all the other parameters of the statistical model that are not POI. In this analysis, the POI are m_{4l}, $\mathcal{D}_{bkg}^{kin}$, m_X and Γ_X, while the NP are the uncertainties discussed in Section 7.2.

For measurements of continuous physics parameters, a maximum likelihood estimation is used. The method of maximum likelihood is based on the likelihood function $\mathcal{L}(\vec{x}|\theta)$, where θ denotes a POI on which depends the measured data written $\vec{x}$. For example, in this analysis, data can be measured values of the m_{4l}, while in that case the θ parameter would represent the expected value of the new boson mass m_X. The maximum likelihood method finds the values of the POI from a dataset, which maximize the likelihood function. In other words, this method allows obtaining the POI values that make the observed data the most probable.

The most general model used relies on one global signal strength parameter μ that multiply the expected cross-section of a high mass resonance such that $\mu = \sigma/\sigma_X$. All production modes are scaled by this factor, while branching fractions are assumed to be preserved. The systematic uncertainty is assigned in the model as a nuisance parameter β. The signal and the background yields

are functions of these parameters, and they can be written as $\mu \times \mathcal{S}(\theta)$ and $\mathcal{B}(\theta)$, respectively. In general, the systematic uncertainties reflect the possible deviations of a quantity from the input value $\tilde{\beta}$ provided by a separate measurement. On that basis, the likelihood can be defined for the data or for a pseudo-experiment, also called a toy. The generic form of the likelihood is described by:

$$\mathcal{L}(\vec{x}, \tilde{\theta}|\mu, \theta) = \prod_i (\mathcal{L}_i(\vec{x}|\mu \times \mathcal{S}(\theta) + \mathcal{B}(\theta)) \times \prod_j (p_j(\tilde{\beta}_j|\beta_j) \tag{7.1}$$

Where the first product runs over all the decay channels, and the second one over all possible nuisance parameters considered in the analysis.

The ultimate goal of this analysis is to determine if a set of X boson parameters m_X, Γ_X, and $\sigma_X.BR_{4l}$, where the latter is the signal production cross-section times the $X \to ZZ \to 4l$ branching ratio in each production mode are consistent with the data. In practice, the $\sigma_X.BR_{4l}$ must be considered with the fraction of event in the VBF category f_{VBF}, and the confidence intervals on $\sigma_X.BR_{4l}$ are determined from profile likelihood scans for a given set of (m_X, Γ_X, f_{VBF}). The likelihood defined in Equation 7.2 is maximized with respect to the nuisance parameters which include the constrained parameters describing the systematic uncertainties. The extended likelihood function is defined for candidate events as:

$$\mathcal{L} = exp\left(-\sum_i n_i^{4l} - \sum_i n_i^{\mathrm{bkg}}\right) \prod_k \prod_j \left(\sum_i n_i^{4l} \mathcal{P}_{i,k}^{4l}(\vec{x}_j, m_X, \Gamma_X) + \sum_i n_i^{\mathrm{bkg}} \mathcal{P}_{i,k}^{\mathrm{bkg}}(\vec{x}_j)\right) \tag{7.2}$$

Where $\vec{x}_j$ corresponds to the observables for the event j from the category k. In this analysis $\vec{x}_j$ is composed of m_{4l} and $\mathcal{D}_{bkg}^{kin}$. The indices i stand for the signal and background type defined for each production mechanism, and the number of events associated to both of them are respectively n_i^{4l} and n_i^{bkg}. The background processes considered here are those not interfering with the signal, and they are described by their PDF in $\mathcal{P}_{i,k}^{\mathrm{bkg}}(\vec{x}_j)$. The signal processes are in their case brought in the likelihood expression through $\mathcal{P}_{i,k}^{4l}(\vec{x}_j, m_X, \Gamma_X)$.

The profile likelihood ratio test is the most powerful statistical test according to the Neyman-Pearson lemma, and it implies the contribution of the signal strength modifier μ. In order to measure central values and uncertainty intervals, the strategy then consists in maximizing $\mathcal{L}$ with respect to μ and θ, to obtain the best fit values $\hat{\mu}$ for the POI, and $\hat{\theta}$ for the NP. One defines a negative log-likelihood function:

$$\tilde{q}_\mu = -2ln(\Delta\mathcal{L}) = -2ln\left(\frac{\mathcal{L}(\vec{x}|\mu, \hat{\theta}_\mu)}{\mathcal{L}(\vec{x}|\hat{\mu}, \hat{\theta})}\right) \tag{7.3}$$

and performs a maximum likelihood fit to data, where $\hat{\theta}_\mu$ maximizes the numerator for a fixed set of values μ of the parameters of interest. The determination of confidence intervals relies on the Wilks theorem, which states that for a model with n POI, the distribution of $-2ln(\Delta\mathcal{L})$ approaches a χ^2 with n degrees of freedom in the limit of a large data sample. For example, when measuring one single

parameter μ, the 68% and 95% CL intervals are deduced from the conditions $-2ln(\Delta\mathcal{L}) < 1$ and $-2ln(\Delta\mathcal{L}) < 3.84$, respectively. Expected results can also be provided or some nominal values of the parameters, which is very useful for estimating the sensitivity of a given measurement. In principle, this would require the generation of several pseudo-experiments, but a very good approximation is provided by the Asimov data set [181], corresponding to a single data set in which the observed rates and distributions coincide with the predictions under the nominal set of NP.

The likelihood fit is not directly performed on the signal model described in Section 6.3 because some background processes interfere with the signal, as well as the SM H boson for lower masses considered. Indeed, when looking at the data, the signal can not be observed as it was defined in the previous chapter, because the interferences directly impact it and modify its shape. Hence, the likelihood fit is done with an enhanced signal model $\mathcal{P}^{4l}_{i,k}$ considering also interference effects:

$$\mathcal{P}^{4l}_{i,k}(\vec{x}_j, m_X, \Gamma_X) = \mu_i \times \mathcal{P}^{\text{sig}}_{i,k}(\vec{x}_j, m_X, \Gamma_X) + \sqrt{\mu_i} \times \mathcal{P}^{\text{int}}_{i,k}(\vec{x}_j, m_X, \Gamma_X) + \mathcal{P}^{\text{bkg}}_{i,k}(\vec{x}_j) \tag{7.4}$$

Where μ_i corresponds to the relative signal strength for a production mode i and defined as the ratio of $\sigma_i.BR_{4l}$ over the expected cross-section of the resonance $\sigma_X.BR_{4l}$ for which the normalization is determined. This equation is composed of three terms, a first one using the signal model presented in Section 6.3, a second one corresponding to the interference contribution, and the last one is representing the contribution of the interfering backgrounds. The last two items will be discussed in Section 7.1.3.

7.1.2 The signal and background template parametrization

The signal model presented in Section 6.3 must be improved for the statistical analysis, indeed some detector effects are missing because they are not directly affecting m_{4l} but $\mathcal{D}^{kin}_{bkg}$. Since the desired parametrization must depend on m_{4l}, taking these effects into account will involve adding parametric templates of $\mathcal{D}^{kin}_{bkg}$ as a function of m_{4l}, which are written $\mathcal{T}(\mathcal{D}^{kin}_{bkg}|m^{reco}_{4l})$. Then, the overall signal model is at the same time a function of m^{reco}_{4l} and $\mathcal{D}^{kin}_{bkg}$, and it is expressed as:

$$\mathcal{P}(m^{reco}_{4l}, \mathcal{D}^{kin}_{bkg}) = \mathcal{P}(m^{reco}_{4l}) \times \mathcal{T}(\mathcal{D}^{kin}_{bkg}|m^{reco}_{4l}) \tag{7.5}$$

This final expression of the signal model will be used in the different steps of the statistical analysis presented in Section 7.3, and its four components are described in the following sections.

As it is written in Equation 7.5, the templates are included in the model by multiplying it to $\mathcal{P}(m^{reco}_{4l})$. As for the rest of the analysis, the templates are built for each production modes and final states as represented in Figure 7.1 for signal processes.

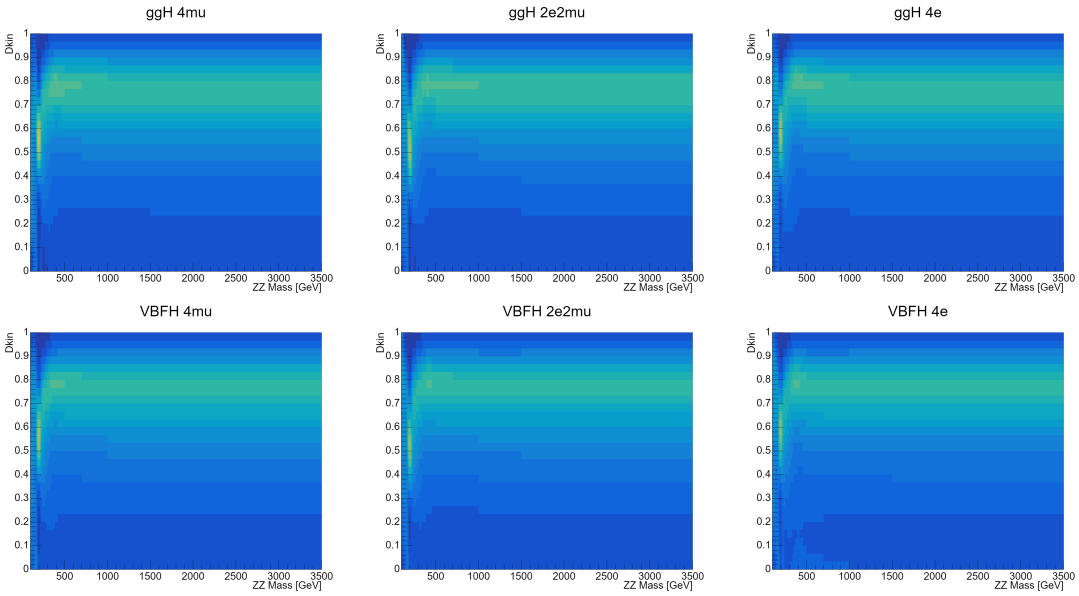

Figure 7.1: Conditional templates of $\mathcal{D}_{bkg}^{kin}$ depending on m_{4l}^{reco} calculated from MC signal samples. The upper row corresponds to ggH process and VBF is on the lower one. The first column corresponds to the 4μ channel, $2e2\mu$ for the second one, and $4e$ for the third one. On the colour scale, the more the bin is blue, the more the value is close to one. Inversely, the more the bin is yellow, the more the value is close to one. For each m_{4l} bin, the $\mathcal{D}_{bkg}^{kin}$ distribution is normalized to 1.

These 2D histograms are built by combining all the MC samples, and they are made in a such way to have the $\mathcal{D}_{bkg}^{kin}$ distribution normalized to 1 for each m_{4l} bin. Moreover, the binning follows a logarithmic distribution, meaning that the mass range per bin increases with the mass according to a logarithmic law, and such a binning is used to have a comparable number of events per bin because of the poorer event density at high mass.

Finally, the signal model used in the following statistical analysis corresponds to the one described in Equation 7.5, and it depends on m_{4l}^{reco} and $\mathcal{D}_{bkg}^{kin}$. In the same way, to what is done for the signal, the templates are also used for the background processes as it is shown in Figure 7.2. Here, the three main backgrounds are represented, $ggZZ$ on top, followed by $qqZZ$, and $Z + X$ on the bottom.

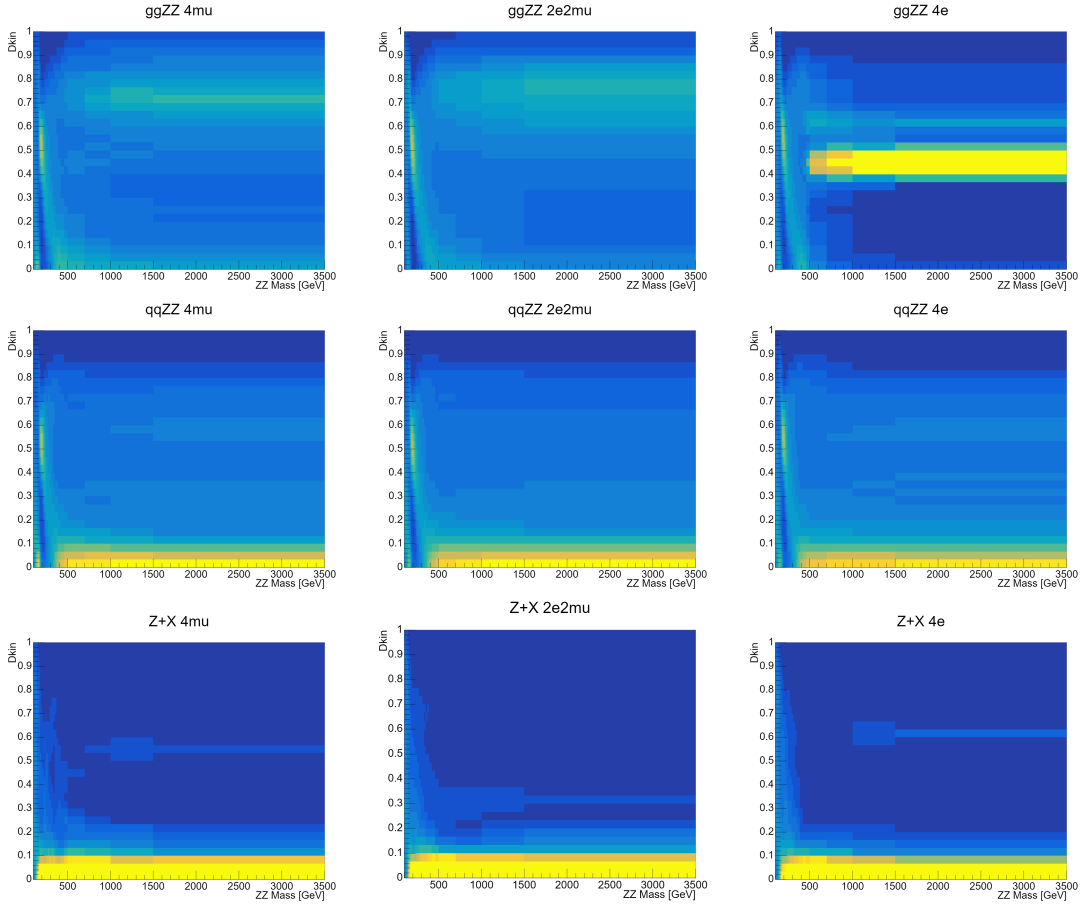

Figure 7.2: Conditional templates of $\mathcal{D}_{bkg}^{kin}$ depending on m_{4l}^{reco}. The upper row corresponds to $ggZZ$ process, $qqZZ$ in the middle, and $Z + X$ on the lower one. The first column corresponds to the 4μ channel, $2e2\mu$ for the second one, and $4e$ for the third one. On the colour scale, the more the bin is blue, the more the value is close to one. Inversely, the more the bin is yellow, the more the value is close to one. For each m_{4l} bin, the $\mathcal{D}_{bkg}^{kin}$ distribution is normalized to 1.

7.1.3 Interferences contribution to the model

In the experimental data, when the signal will be measured part of the resonance could be affected by the background or even by SM signals. In the mass region above 200 GeV there are parts of the background continuum as well as the off-shell tail of the SM H boson distribution. It is expected to have interferences of X boson with both of them, and this should account for an important effect when considering a resonance with a non-negligible width. This parameterization naturally scales the size of interference with the cross-section of the signal peak σ_X with a proper accounting for interference depending on the signal strength, as well as a parametric dependence on the mass distribution. All of this is described in Equation 7.4, where the signal is considered simultaneously with the interfering backgrounds and the interferences.

Two configurations associated to MC samples must be considered to reflect both production modes studied in this analysis. The first one is used for the ggH

category, and it stands as the sum of the contributions of ggH at 125 GeV, $ggZZ$ background, and their interference. The second one corresponds to the H boson coming from VBF at 125 GeV, EW $qqZZ$, and their interference. Both are not coming from the same generator because of the nature of the processes implied, MCFM is used for the first one while the second is generated with JHUGen. Then, these samples are not used like that, indeed, the desired interference does not afford for the background contribution. In order to extract only the interference contribution, the pure signal at 125 GeV and the pure background are subtracted to the samples. This operation is done after a proper reweighting and at the end only the interference remains. Although, at this stage the interferences obtained are just those between the H boson and the background, to get those involving the new X boson the m_{4l} and $\mathcal{D}^{kin}_{bkg}$ conditional templates are built in the same way as it was explained in the previous section. Moreover, the sample reweighting is performed with the MELA package in a such way to change the resonance signal hypothesis and thus to change the expected mass and width. Finally, the interferences are functions of m_{4l}, $\mathcal{D}^{kin}_{bkg}$, m_X, and Γ_X.

Actually, the final interference is composed of three contributions. A first one defined between the X boson signal and the background, a second between the H boson at 125 GeV and the background, and the third one between the H boson and the new X boson.

7.2 Systematic uncertainties

Uncertainties are an essential aspect of a physics analysis. Indeed, they are related to the accuracy of the measurements made by the experiments and can be separated into two different contributions. Firstly, statistical uncertainties arise mainly from the amount of data collected by the experiment. The larger the amount of data, the greater the precision of a measurement will be, and this also leads to a better significance of the research carried out. Since this source of uncertainty is a parameter that can be modified by new data, one of the objectives of successive improvements to the LHC is to collect as much data as possible. As already explained, the most prominent example is the HL-LHC during which the instantaneous luminosity will increase considerably. Moreover, this is linked to the rest of the uncertainties which can be divided into two groups. On one side, experimental uncertainties are related to imperfect knowledge of the detector, such as the luminosity, the different calibrations applied on the data, the efficiencies, and the resolutions. On the other side, the theoretical uncertainties are mainly related to the generators used for modelling the signal and background processes. For instance, the theoretical predictions of the processes that are studied are not ideal in the sense that they admit simplifications of physical phenomena that are either too complex to be implemented, or are not fully understood, and their modelling is imperfect.

All of these sources of uncertainty can influence the modelling of the signal and background processes that was detailed in Section 6. These will degrade the predictions made about the expected signal and background parameters. In the

context of statistical analysis, these systematic uncertainties are considered as NP that are profiled in the maximum likelihood fitting described in Section 7.1. Thus, to have the best comparison between experimental results and theoretical predictions, it is essential to have the best possible estimate of the uncertainties. This is all the more true when the statistical uncertainty is the least important. On the other hand, if we focus on the high mass region, the very small number of events means that the statistical uncertainty is dominant. However, the measurement of the others should not be neglected, as this analysis aims to have the best possible accuracy. Although, the impact of systematic uncertainties on the measurements will be discussed with the results of the analysis in Section 7.3.

7.2.1 Experimental uncertainties

The experimental uncertainties gather all those related to the detector and coming from the different phases of particles reconstruction and selection. As detailed in the following list, the dominant uncertainty sources originate from the luminosity measurement, the lepton reconstruction and identification, the selection efficiency, the lepton resolution, the jet scale, and the reducible background estimate. In this uncertainty category, the value of each of them are calculated for each data-taking period. Only the lepton and jet energy scale and resolution are calculated only once since they are uncorrelated to the year.

- **The integrated luminosity** measurement is performed with Van der Meer scans [182] on the different datasets. It is affected by a normalization uncertainty which ranges from 2.3% to 2.6% depending on the data-taking period [111, 112, 113] and affects all final states, both signal and background.

- **The lepton reconstruction and selection efficiency** represents the effects brought by the requirements from all steps from the trigger to the final selection. In this case, muons and electrons are taken separately since the selections of these objects are different. The uncertainty ranges from 1% to 2.3% in the 4μ channel and from 11% to 15.5% in the $4e$ channel. The gap between muons and electrons is mainly due to the low p_T^{μ} measurement which is done with the $\mu^+\mu^-$ resonances are used to measure the efficiency in the low p_T regions, while in the electron case the efficiency measurement relies only on the Z boson resonance, resulting in a higher uncertainty in the low p_T^e region.

- **The lepton momentum scale and resolution** impact the signal shape since they make the DCB function parameters varying. Their estimations are done with the study of the $Z \to l^+l^-$ invariant mass distribution in data as well as in simulation. Events are classified according to the p_T and η of one of the two leptons, determined randomly, and integrated over the other. Then, the distribution of the l^+l^- mass is fitted with a function close to the one used for the signal modelling, since the fit is done with the convolution of a Breit-Wigner function and a DCB function. For the 4μ channel the scale uncertainty is around 0.04% and 0.3% in the $4e$ channel. In the case of the resolution uncertainty, it was calculated at 20% for both channels.

- **The jet energy scale and resolution** do not have a direct impact on the signal selection efficiency. Indeed, jets are not part of the final state, but they are used in the categorization to separate ggH events to VBF ones which are associated with one or two jets. Moreover, they have an impact on the shape of the discriminants. In the context of a high mass analysis, the uncertainty on both jet energy scale and resolution are of the order of 1% when considering high p_T jets. The measurement of these uncertainties was part of the jet reconstruction performance with the CMS detector [126]. Their impact on the measurements are negligible when considering an inclusive category. However, their impact is much more significant in the measurements of the VBF categories, since they are related to the jet kinematics.

- **The reducible background estimate** represents one of the main source of systematic uncertainty in the analysis. As described in Section 6.2.2, this background is quite complex to simulate due to its composition, and the data driven method used to estimate it can lead to rate uncertainties. Those values are around 30% for the 4μ final state, between 30% and 35% for $2\mu 2e$, and between 37% to 41% for $4e$. These uncertainties are treated as uncorrelated between the different final states, indeed each of them corresponds to a separate measurement.

7.2.2 Theoretical uncertainties

The theoretical uncertainties are calculated for the three data-taking periods all together since they are neither correlation between them nor any detector related effect. Moreover, they are treated as correlated between each others. They affect both signal and background estimation and come from the theoretical computations, in particular the renormalization and factorization scale and the choice of the PDF set. The main contributions to the overall theoretical uncertainty considered in this analysis are presented as follows:

- **The uncertainty on the branching ratios** associated to the $X \to ZZ \to 4l$ decay is the first theoretical uncertainty. Since the resonance is search for different value of m_X, the BR is also taken for the expected mass and the uncertainty is calculated for each of the desired mass. In average this uncertainty is around 2%.

- **The QCD uncertainty** is applied on both irreducible background samples. This uncertainty corresponds to the PDF renormalization as well as the scale factor, and it is determined by varying these factors between 0.5 and 2 times their nominal value. Besides, their fraction values are kept between 0.5 and 2. Depending on the process, this uncertainty ranges from 3.1% to 4%.

- **The irreducible background modelling uncertainties** are coming from the k-factors which are used to rescale the irreducible background simulations to the most recent theoretical calculations. More precisely, when considering the $gg \to ZZ$ k-factors, they are of the order of 10%, while the uncertainty

affecting the k-factor for the electroweak corrections of the $q\bar{q} \to ZZ$ process is in average of the order of 0.1%.

7.2.3 Summary on the uncertainties

To summarize what has been said about the uncertainties, there is nothing better than a table with all the contributions and their values. This is done in Table 7.1, where the experimental uncertainties are first presented, some of them have a specific value for each data-taking year, and they are followed by the theoretical uncertainties. Hereafter, they are added as NP in the likelihood fit.

Table 7.1: Summary of the experimental and theoretical uncertainties used in the analysis. Some experimental uncertainties are calculated for each data taking years.

Experimental uncertainties			
Year	**2016**	**2017**	**2018**
Luminosity	2.6%	2.3%	2.5%
Reconstruction efficiency μ	1.2%	1.1%	0.7%
Reconstruction efficiency e	15.5%	12%	11%
$Z + X$ (4μ)	30%	30%	30%
$Z + X$ ($2\mu 2e$)	35%	33%	30%
$Z + X$ ($4e$)	41%	38%	37%
Energy scale μ	0.04%		
Energy scale e	0.3%		
Energy resolution μ and e	20%		
Jet energy scale	1%		
Jet energy resolution	1%		
Theoretical uncertainties			
Branching ratio ($X \to ZZ \to 4l$)	2%		
QCD scale ($q\bar{q} \to ZZ$)	3.2%		
QCD scale ($gg \to ZZ$)	4%		
PDF ($q\bar{q} \to ZZ$)	3.1%		
PDF ($gg \to ZZ$)	4%		
EW corrections ($q\bar{q} \to ZZ$)	0.1%		
k-factor corrections ($gg \to ZZ$)	10%		

7.3 Results on the search of high mass resonance

Once the signal and background models have been developed, and the uncertainties have been calculated, it is possible to perform the statistical test mentioned in the previous section. Thanks to this, the search for a scalar resonance $X \to ZZ \to 4l$ is performed for the mass range m_X between 200 and 3000 GeV. Furthermore, it is performed for a resonance width that can have any value, from the narrow width approximation (NWA), corresponding to $\Gamma_X < 0.5$ GeV, to a relatively large width compared to the mass, although this corresponds in this case to $\Gamma_X < m_X$. The production of the X resonance could be produced via gluon or vector boson fusion processes. As the relative importance of these production modes are unknown for X, it is necessary to introduce the VBF production fraction parameterized with f_{VBF}. This one corresponds to the number of events resulting from VBF on the sum of the events VBF and ggH.

Figure 7.3 shows the upper limits expected at 95% CL on the product of the boson cross-section X and the branching ratio $X \to ZZ$. The limits are obtained with the fit performed on two observables used in the superimposed signal and background expectations. A maximum likelihood fit, without binning, of m_{4l} and $\mathcal{D}_{bkg}^{kin}$ distributions is performed on the set of selected events between $100 < m_{4l} < 3500$ GeV. The constraints on the effective resonance production cross-section σ_X are reported for a scan of m_X and with a fixed value of Γ_X. Moreover, the value of f_{VBF} can be fixed at a certain value or left unconstrained in the fit. In this example the two extreme values $f_{VBF} = 0$ and 1 were chosen to cover the range of possible limits, in the first case only ggH events are considered, and only VBF in the second. In both cases, the upper limits expected at 95% CL on $\sigma_X.BR_{4l}$ have a similar trend as a function of m_X. These results look comparable to what was found with the study of 2016 data [9], where the main results were presented in Chapter 1.

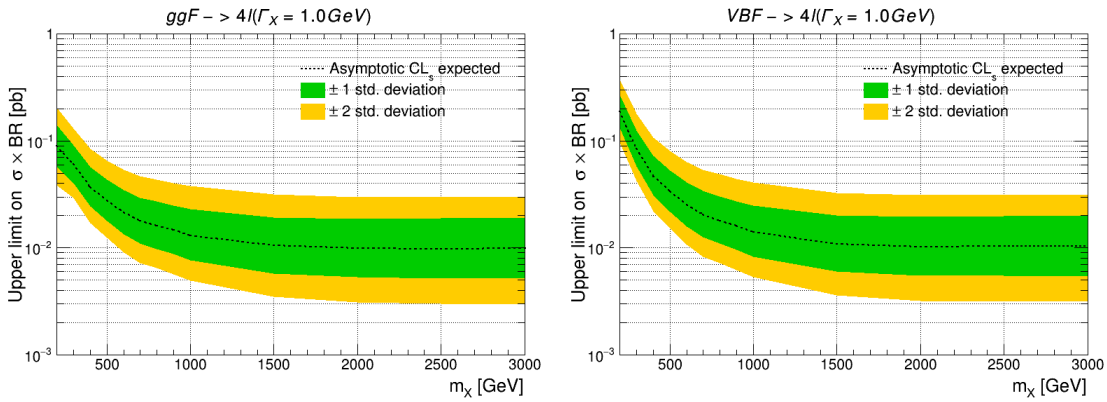

Figure 7.3: Expected upper limits at 95% CL on the product of the X boson cross-section and the $X \to ZZ$ branching ratio as a function of the resonance mass m_X and with a fixed width $\Gamma_X = 1$ GeV. The limits are calculated from 2018 samples only and with $4l$ events from an inclusive category. f_{VBF} is set to 0 on the left, and to 1 on the right.

Figure 7.4 shows the expected 95% CL limits with different width hypotheses, from 0.1 GeV on the left to 100 GeV on the right, and with $f_{VBF} = 0$. The lower width value respects the narrow width approximation and has a lower contribution coming from the interference. While, for a width of 100 GeV the interference effects are not at all negligible and this is even visible with the lower limit at low mass. Indeed, the low mass region is the one the most affected by interference since the backgrounds and the 125 GeV Higgs boson have almost no contribution at masses higher than 500 GeV.

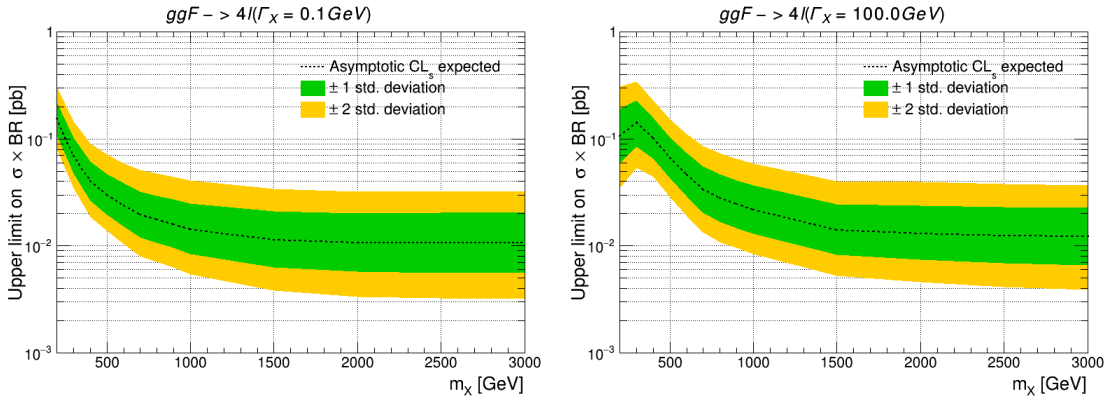

Figure 7.4: Expected upper limits at 95% CL on the product of the X boson cross-section and the $X \to ZZ$ branching ratio as a function of the resonance mass m_X. The resonance width is set to $\Gamma_X = 0.1$ GeV on the left and $\Gamma_X = 100$ GeV on the right. The limits are calculated with $4l$ events from 2018 samples, an inclusive category was used, and f_{VBF} is set to 0.

Since the interference affects the shape of the expected 95% CL limits over the resonance mass, a study of its impact was done and presented in Figure 7.5. In these four plots a comparison of the model with and without the interference is done on the limits for ggH signal for different width assumptions. As mentioned earlier, in the NWA the impact of the interference on the signal is negligible, which is confirmed by the case where $\Gamma_X = 0.1$ GeV and where both curves are similar. Then, when the width increase to 1 GeV the NWA is no longer valid and the differences start to appear, and then they are even amplified with higher values as pointed in the two lower plots of the figure. Thus, the expected behaviour of the interference on the model is verified.

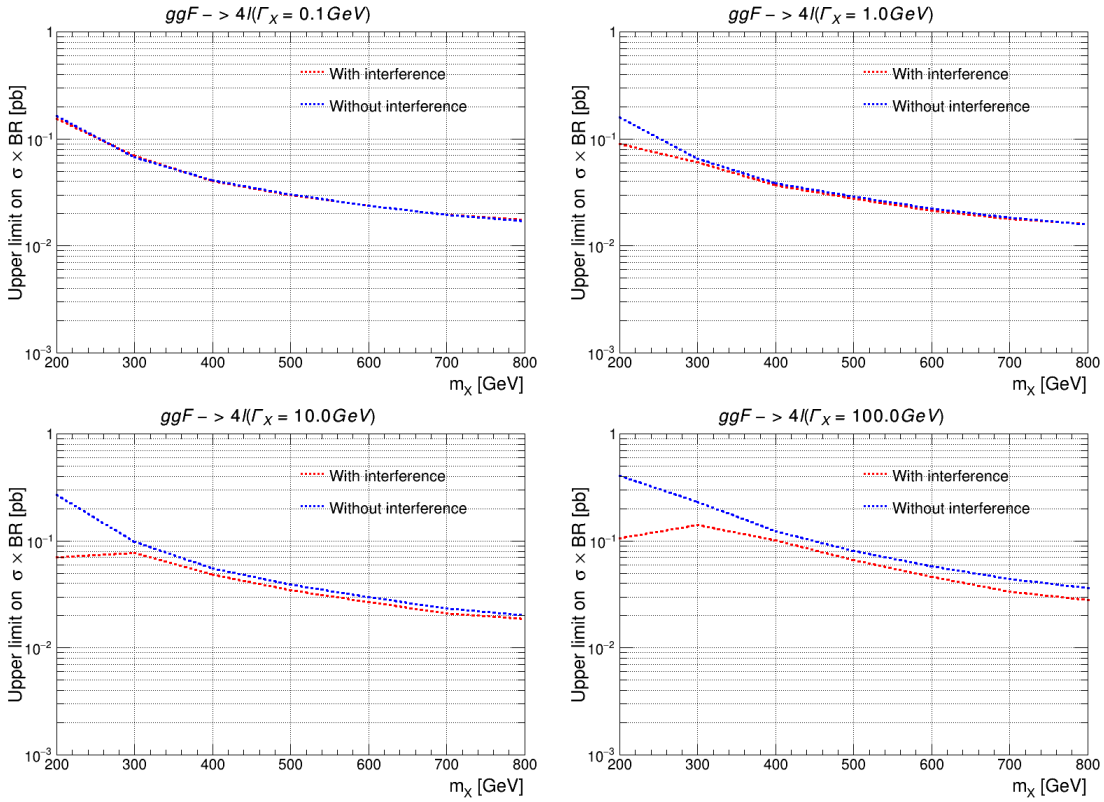

Figure 7.5: Expected upper limits at 95% CL on the product of the X boson cross-section and the $X \to ZZ$ branching ratio as a function of the resonance mass m_X. The four plots correspond to different resonance width $\Gamma_X = 0.1$, 1, 10, and 100 GeV. The limits are calculated from 2018 samples, with $4l$ events from an inclusive category, and f_{VBF} is set to 0. The blue curves represent the limits using a model without interference and with in red.

Another verification consists in understanding the contribution of each decay channel and to see if it matches the expected relative limits. For that, the limits are calculated for each channel separately, as shown on Figure 7.6.

If there is no problem it is obviously expected to have the $4l$ limits lower than all the others since it is the combination of all of them. Then, those from $4e$ are expected to have the worst limits because of its lower efficiency, and in this way 4μ should have better limits. Finally, concerning $2e2\mu$ even if the efficiency is lower than the one from 4μ, it has much higher statistics making it the decay channel with the best expected limits. To conclude, all of these suppositions are clearly confirmed by the limits shown on Figure 7.6.

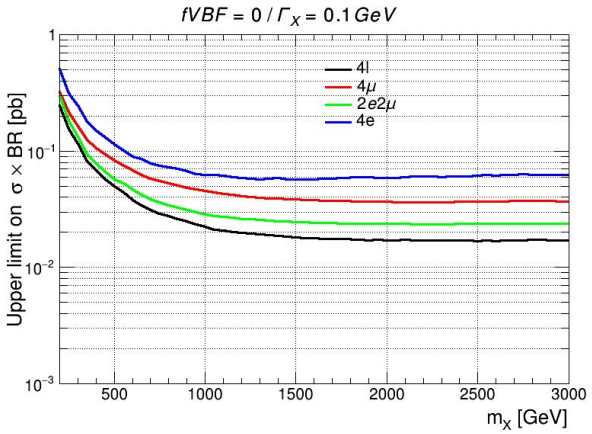

Figure 7.6: Expected upper limits at 95% CL on the product of the X boson cross-section and the $X \to ZZ$ branching ratio as a function of the resonance mass m_X. The limits are calculated from 2018 samples, with a resonance width $\Gamma_X = 0.1$ GeV, and f_{VBF} is set to 0. The black curve represents the limits of $4l$, 4μ in red, $2e2\mu$ in green, and $4e$ in blue.

After knowing that there is no unexpected behaviour or issue the expected limits, it is possible to unblind the data in the region of interest, meaning that all the events with a mass above 200 GeV are now available. If considering the m_{4l} unblinded distribution from Figure 5.11, but only in the high mass region, the Figure 7.7 is obtained. On this figure, all the high mass events are represented below 1300 GeV since there is no more event after this value.

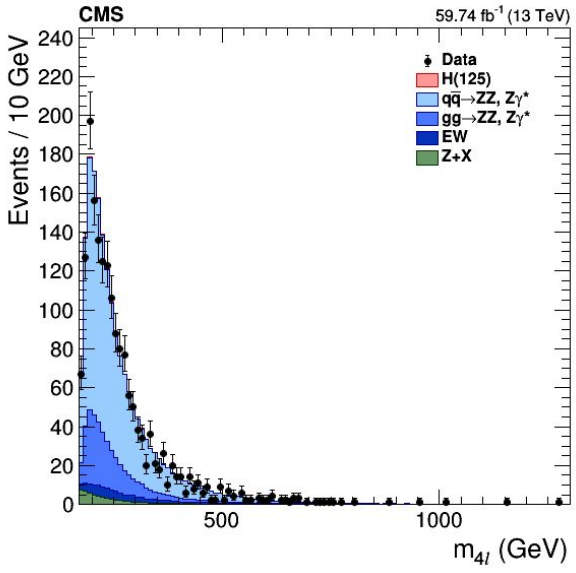

Figure 7.7: Distribution of m_{4l} from high mass events using the full Run-2 statistic. Black points represent data, H signal in pink, and the backgrounds are $q\bar{q} \to ZZ$ in light blue, $gg \to ZZ$ in blue, EW in dark blue, and $Z + X$ in green.

The unblinding can also be done on the limits, thus like that the observed limits can be calculated and then compared to the expected ones in order to know if

there is a sign of a new high mass particle.

In the same way as what was done for the expected limits, the comparison for different widths and for the different fraction of production mode. The first observed limits to be compared are those coming from pure ggF events, where f_{VBF} is set to 0 and shown in Figure 7.8.

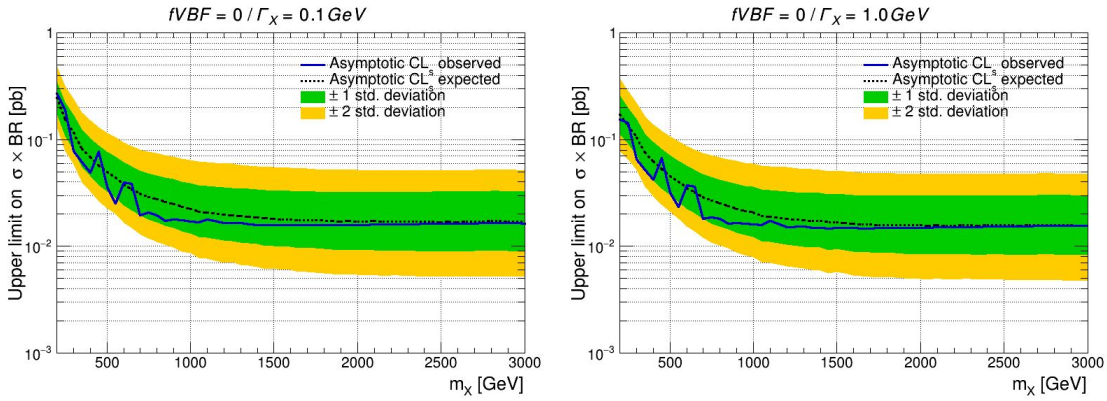

Figure 7.8: Observed and expected upper limits at 95% CL on the product of the X boson cross-section and the $X \to ZZ$ branching ratio as a function of the resonance mass m_X. The resonance width is set to $\Gamma_X = 0.1$ GeV on the left and $\Gamma_X = 1.0$ GeV on the right. The limits are calculated with $4l$ events from 2018 samples, the two categories were used, and f_{VBF} is set to 0.

From these plots, there is the same behaviour induced by the width changes, and in all the case the observed limits are contained in the $+2\sigma$ bands of the expected limits. Thus, there is no significative excess observed with pure ggF events.

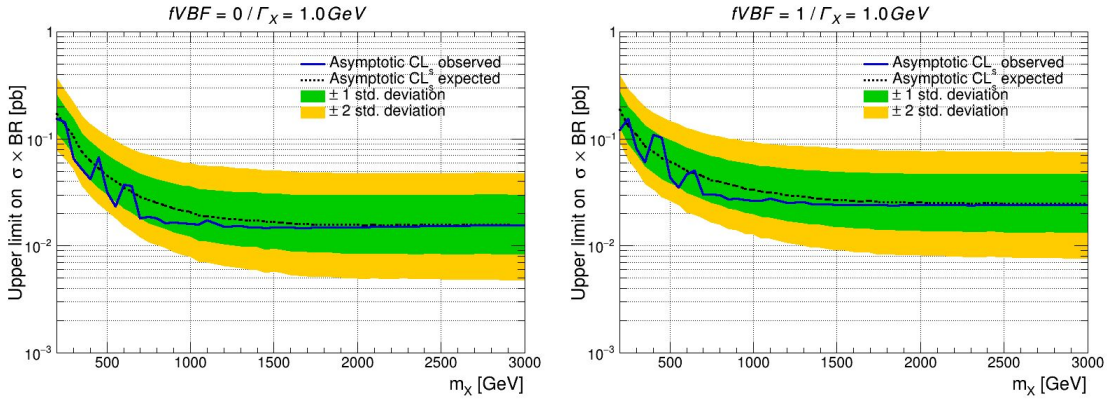

Figure 7.9: Observed and expected upper limits at 95% CL on the product of the X boson cross-section and the $X \to ZZ$ branching ratio as a function of the resonance mass m_X. The resonance width is set to $\Gamma_X = 1.0$ GeV. The limits are calculated with $4l$ events from 2018 samples, the two categories were used, f_{VBF} is set to 0 on the left and to 1 on the right.

In the same way, the same comparison was done with pure VBF events, and the results were the same. Figure 7.9 shows the comparison between the limits

calculated with only ggF events or only VBF, and one more time no significant excess was observed.

Finally, the fraction of VBF events is set as a floating parameter and the corresponding limits for different width values are represented in Figure 7.10. Once again, no significant excess was observed.

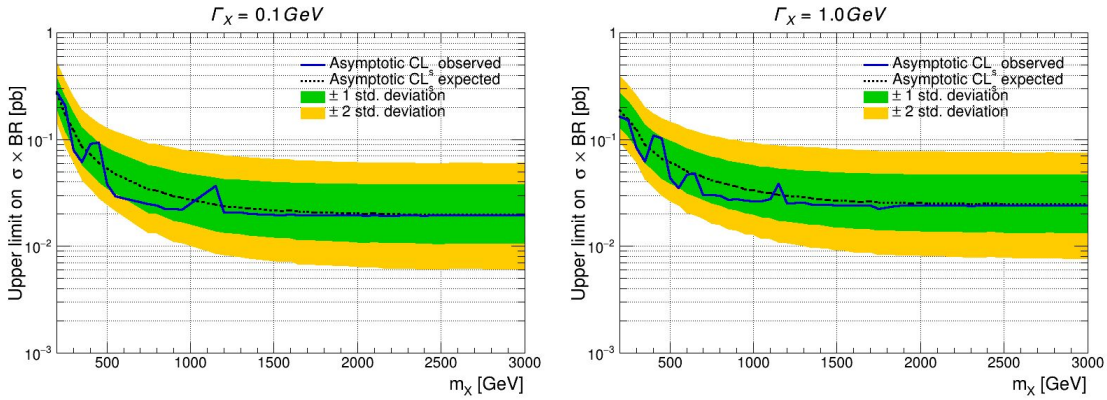

Figure 7.10: Observed and expected upper limits at 95% CL on the product of the X boson cross-section and the $X \to ZZ$ branching ratio as a function of the resonance mass m_X. The resonance width is set to $\Gamma_X = 0.1$ GeV on the left and $\Gamma_X = 1.0$ GeV on the right. The limits are calculated with $4l$ events from 2018 samples, the two categories were used, and f_{VBF} is floating.

To conclude on the high mass resonance search, a statistical test based on maximum likelihood method was used in order to calculate the observed and expected limits on the production cross-section and branching ratio of the resonance. Thus, the limits obtained are model independent, and can therefore be used by theorists to check whether their predictions can work. Nevertheless, the limits obtained show no significant excesses, so no sign of a new particle is visible.

However, analysis of the entire Run-2 is required before any conclusions can be drawn. The results obtained so far show an improvement of a factor $\sim$2 compared to the limits obtained with 2016 samples only. This increase is partially explained by the higher statistics available in 2018, but also but the optimization of high mass event selection and a better modelling of the different processes. Finally, these results are statistically limited by the fact that there are very few high mass events, and the Run-3 of the LHC as well as the HL-LHC could be of great benefit in overcoming this limitation. At the moment, only the data acquired in 2018 has been fully studied. Part of the work for both other years has already been started, and should soon provide results for the whole Run-2.

Conclusion

As already explained throughout this thesis, the latest resounding success in particle physics is the discovery of the Higgs boson by the ATLAS and CMS collaborations in 2012. This discovery was made possible by data collected during LHC Run-1. Following a two-year shutdown, LHC operations resumed with Run-2, where proton collisions reached unprecedented energies going up to $\sqrt{s} = 13$ TeV. These new data have enabled precise measurements of the properties of the Higgs boson, and searches to be carried out for possible signs of physics beyond the Standard Model, but so far without success.

The Standard Model limitations, as well as the desire of getting more precise measurements of certain constants, have required the need for more statistics to carry out such studies, some of which may lead to the discovery of potential new physics. To meet this goal, improvements are planned for the LHC and all its experiments. The HL-LHC is expected to generate ten times more data than during the entire Phase-1 of the collider, but will also result in higher pile-up rates and unprecedented radiation levels. A substantial upgrade of the LHC infrastructure and detectors is required to maintain current detection performance in such a harsh environment. The CMS collaboration will replace the current end calorimeters with the High Granularity Calorimeter, designed to improve discrimination power and radiation resistance in the highly active HL-LHC environment. The HGCAL will be the first large-scale silicon-based imaging calorimeter ever used in a high-energy physics experiment.

This thesis therefore comes at a time when all the Run-2 data is accessible and can be analysed, and when the future detectors for the HL-LHC are being prototyped or assembled. Because of this particular situation, this thesis presented two topics related to the search of new physics with the LHC. On one side, there is a physics analysis exploiting the Run-2 data collected by the CMS experiment in order to look for a new high mass scalar particle. On the other side, there is the development of the new detector to push further the frontier of physics, and consisting of measurements of the HGCAL prototype performance.

This thesis therefore comes at a time when all the Run-2 data is accessible and can be analysed, and when the future detectors for the HL-LHC are being prototyped or assembled. Because of this particular situation, this thesis presented two topics related to the search of new physics with the LHC. On one side, particle there is the development of the new detector to push further the frontier of physics, and consisting of measurements of the HGCAL prototype performance. On the other side, there is a physics analysis exploiting the Run-2 data collected by the CMS experiment in order to look for a new high mass scalar resonance.

The search for high mass scalar resonance presented in this thesis is based on the study of the golden channel, or more precisely in $X \to ZZ \to 4l$. The interest of this channel lies in its very clear experimental signature and very good signal over background ratio. For these reasons, many studies have used it to measure the Higgs boson properties, and in the case of my study this was particularly useful as events reconstruction methods from this decay channel already existed. The aim of the study carried out in this thesis is to establish asymptotic limits on the production cross-section of a high mass resonance for any value of signal mass and width. The first step in the analysis was to optimize the selection of high mass events, then to build a resonance model using information from both physics theories and MC simulation samples. The limits were obtained using a statistical test based on maximum likelihood method, and in order to perform this, the parameterization of background and the study of systematic uncertainties was carried out. Thus, the limits obtained are model independent, and can therefore be used by theorists to check whether their predictions can work.

At the moment, only the data acquired in 2018 has been fully studied. Part of the work for both other years has already been started, and should soon provide results for the whole Run-2. In addition, this analysis has been carried out in parallel with the high mass resonance study from the $X \to ZZ \to 2l2q$ channel, and a combination of these two channels is planned for publication in a peer-reviewed journal. The limits obtained show no significant excesses, so no sign of a new particle is visible. However, analysis of the entire Run-2 is required before any conclusions can be drawn. Finally, these results are statistically limited by the fact that there are very few high mass events, and the Run-3 of the LHC as well as the HL-LHC could be of great benefit in overcoming this limitation.

Regarding the work carried out on the HGCAL prototype, this thesis is based primarily on the study of timing performance, but also, to a lesser extent, on the energy and spatial reconstruction performance of the showers. The latter have shown that the energy response and resolution are in line with HGCAL's technical specifications, and that the longitudinal and transverse profiles of the showers are as expected. This has been done for both electromagnetic showers originating from positrons and hadronic showers originating from pions, and in both cases the showers are well contained within the prototype. These studies validate the design in terms of energy reconstruction and detector geometry.

Concerning the timing performance, after a detailed calibration of the ToA, the single cell timing resolution was found to be consistent with the electronics specifications and the work on the full shower timing performance represents the first measurement of timing performance for calorimeter showers with a precision of tens of picoseconds and shows experimental evidences of the possibility to complete $\mathcal{O}(10$ ps) timing resolutions with HGCAL. Ultimately, this study proves that the timing performance will enable effective separation of pile-up interactions and, with it, contribute towards a successful operation of the CMS detector at the HL-LHC.

HGCAL is currently being assembled and commissioned, and there are a few differences between the final version and the prototype described in this thesis. In particular, the Skiroc2-CMS electronic chips have been replaced by HGCROC,

which are an improved version of the old ones. Although, the final detector will retain most of the design of the prototype studied. Finally, HGCAL should be installed in the next few years, and enter service in 2029 with the start of HL-LHC operations.

Appendix: Z+X estimation in 2P2F and 3P1F control regions

In Section 6.2.2, two control regions are defined for the opposite sign method: 2P2F and 3P1F. Both CR are used to extract the final estimate of the $Z + X$ yields in the SR. By their definitions, these CR may have some overlap, in the sense that some events may occur in both, and therefore double counting in the determination of the $Z + X$ yields with the OS method should be avoided in order to not overestimate the importance of this background.

The contribution of both CR are presented in this appendix, first because the final $Z + X$ yields for the OS method are obtained from those of each of the CR, but also by taking into account the background of the 3P1F CR which corresponds to the overlap between both CR. This appendix has for goal to show all the ingredients allowing to calculate the yields calculated from the OS method.

Moreover, the fake rates used to compute the different $Z + X$ contributions are those presented in Section 6.2.2.

The 2P2F control region

The 2P2F CR describes events having signatures where only two leptons passing the selection are found in the event, such as those from $Z+$ jets and $t\bar{t}$ processes. Therefore, the final contribution to the SR ($N_{\text{SR}}^{\text{2P2F}}$) can be extrapolated by weighting each event in the 2P2F CR (N_{2P2F}) by the product of the FR of the third (f_3) and fourth (f_4) leptons, as it is described with the follow equation:

$$N_{\text{SR}}^{\text{2P2F}} = \sum_i N_{\text{2P2F}} \left(\frac{f_3^i f_4^i}{(1 - f_3^i)(1 - f_4^i)} \right) \tag{6}$$

The estimation of $Z + X$ in the 2P2F CR is also compared to some MC simulation samples of its components. The mass distribution of this background is represented in Figure 11 for an inclusive category and for each final state. It is relevant to notice that $2e2\mu$ and $2\mu2e$ are separated for the $Z + X$ estimation. This estimation was also performed per category in order to have the corresponding $Z + X$ contribution and to improve the sensibility of the analysis. Although, only the inclusive category is shown here, since it gathers all the others.

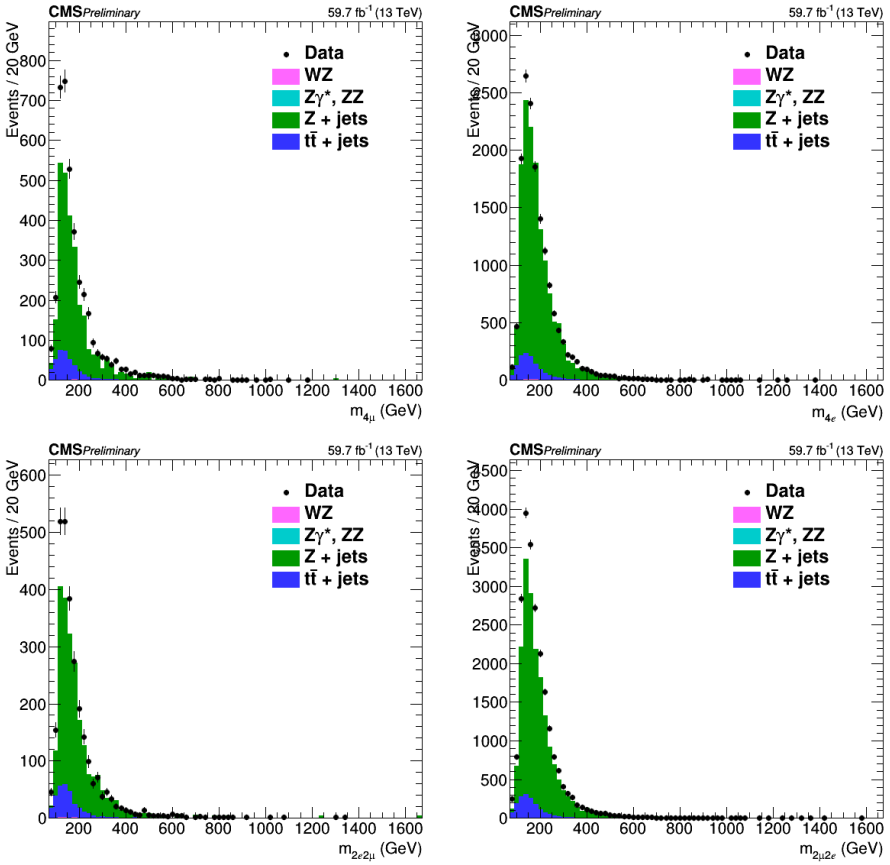

Figure 11: Distribution of the invariant mass of $Z + X$ background calculated in the 2P2F CR from 2018 samples. Data in black are compared to MC simulation of WZ in pink, $Z\gamma$ or ZZ in turquoise, $Z+$ jets in green, and $t\bar{t}+$ jets in blue. On top left, the 4μ final state is represented at the side of $4e$, and the bottom, the $2e2\mu$ and $2\mu2e$ are represented.

The 3P1F control region

In the same way as what was done for the 2P2F CR, the contribution of the additional loose lepton in the 3P1F CR ($N_{\text{SR}}^{\text{3P1F}}$) is taken into account by weighing each event by the corresponding FR. In this case, only f_4 is used and the following equation:

$$N_{\text{SR}}^{\text{3P1F}} = \sum_j N_{\text{3P1F}} \left(\frac{f_4^j}{1 - f_4^j} \right) \tag{7}$$

The mass distribution of the $Z + X$ background estimated from the 3P1F CR is represented in Figure 12 for an inclusive category and for each final state. Similarly to the 2P2F mass distributions, this figure shows the comparison with MC simulation samples and the same comments can be repeated here.

In addition, there is the expected mass distributions extrapolated from the 2P2F distributions. In the final states with lose electrons, meaning $4e$ and $2\mu2e$, the difference observed between the 3P1F distribution and the one extrapolated from

2P2F is due to the missing contribution of FSR photons, which is coherent with the fact that the difference happens in particular in the low mass region. Thus, the FR does not describe properly the background composition of the 2P2F CR.

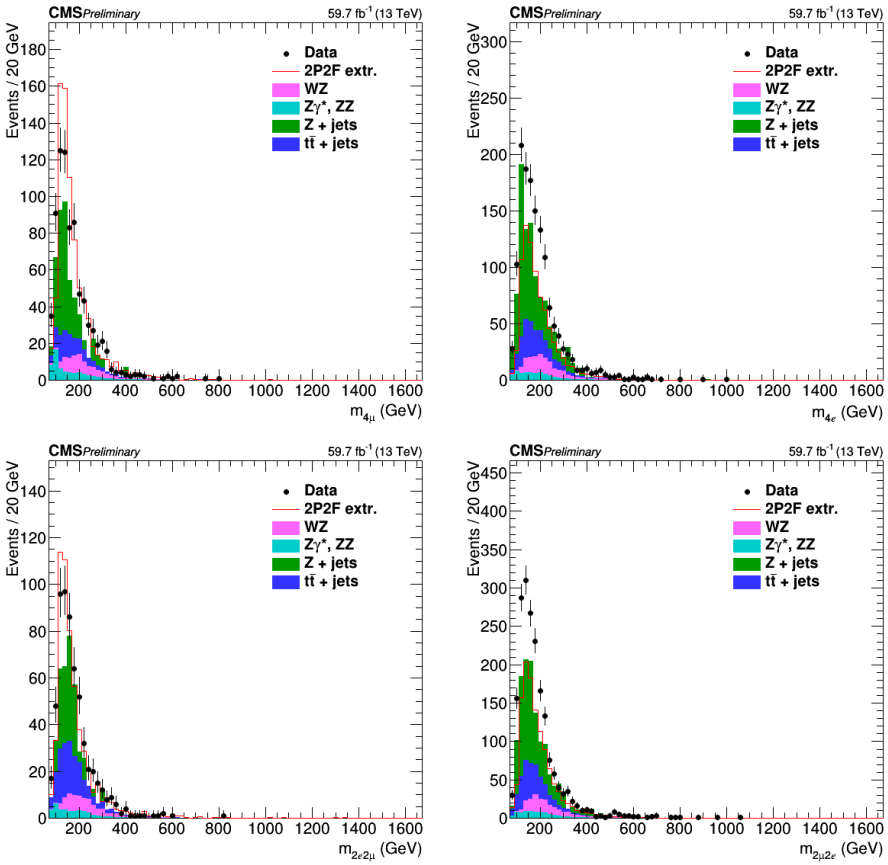

Figure 12: Distribution of the invariant mass of $Z + X$ background calculated in the 3P1F CR from 2018 samples. Data in black are compared to MC simulation of WZ in pink, $Z\gamma$ or ZZ in turquoise, $Z+$ jets in green, and $t\bar{t}+$ jets in blue. On top left, the 4μ final state is represented at the side of $4e$, and the bottom, the $2e2\mu$ and $2\mu2e$ are represented. 2P2F contribution is plotted with a red curve.

As it was already explained, both 2P2F and 3P1F are overlapping. In this way, the 2P2F CR could be considered as a background for the 3P1F CR. Thus, it is necessary to calculate the events in the 3P1F region. Thus, the double counting correction $N^{\text{bkg}}_{\text{3P1F}}$ is defined as:

$$N^{\text{bkg}}_{\text{3P1F}} = \sum_{i,j} N_{\text{2P2F}} \left(\frac{f_i}{1 - f_i} + \frac{f_j}{1 - f_j} \right) \tag{8}$$

The final OS estimate of the $Z + X$ background in the SR presented in Section 6.2.2.

Acronyms List

ADC Analogue to Digital Converter
ALICE A Large Ion Collider Experiment
ASIC Application Specific Integrated Circuits
ATLAS A Toroidal LHC Apparatus
AUC Area Under the Curve
BCM1F Beam Condition Monitor Fast
BCM1L Beam Condition for Losses
BDT Boosted Decision Trees
BEH Brout-Englert-Higgs
BR Branching Ratio
BSM Beyond Standard Model
CERN Conseil Européen pour la Recherche Nucléaire
CKM Cabibbo-Kobayashi-Maskawa
CL Confidence Level
CMS Compact Muon Solenoid
CP Charge and Parity
CPS Complex Pole Scheme
CPU Central Processing Unit
CR Control Region
CSC Cathode Strip Chambers
CTF Combinatorial Track Finder
DAQ Data Acquisition System
DCB Double Crystal Ball
DT Drift Tube
DWC Delay Wire Chamber
DY Drell-Yan
EB ECAL Barrel
ECAL Electromagnetic Calorimeter
EE ECAL Endcaps
EM Electromagnetic
ES Electromagnetic Preshower
EWSB Electroweak Symmetry Breaking
EW Electroweak
EWT Electroweak Theory
FASER Forward Search Experiment
FPGA Field Programmable Gate Arrays
GEM Gas Electron Multiplier

FR Fake rate
FSR Final State Radiation
FTF Fritiof
g.d.r Giant Dipole Resonance
ggF Gluon Fusion
GSF Gaussian-Sum Filter
HB HCAL Barrel
HCAL Hadronic Calorimeter
HGCAL High Granularity Calorimeter
HE HCAL Endcaps
HF HCAL Forward
HL-LHC High Luminosity Large Hadron Collider
HLT High Level Trigger
HO HCAL Outer
ID Identification
IP Interaction Point
ISO Isolation
JGUGen Johns Hopkins University Generator
L1 Level 1
LEP Large Electron Positron collider
LHC Large Hadron Collider
LHCb Large Hadron Collider beauty
LHCf Large Hadron Collider forward
LINAC Linear Accelerator
LO Leading Order
LUT Programmable Memory look up Table
MC Monte Carlo
MCFM Monte Carlo for FeMtobarn
MCP Microchannel Plate
MELA Matrix Element Likelihood Approach
MIP Minimum Ionizing Particle
MoEDAL Monopole and Exotics Detector At the LHC
MPI Multi-Parton Interaction
MS Modèle Standard
MSSM Minimal Supersymmetry Standard Model
MTD MIP Timing Detectors
NLO Next to Leading Order
NP Nuisance Parameter
NWA Narrow Width Approximation
OC Opposite Charge
OS Opposite Sign
PCB Printed Circuit Board
PDF Parton Density Function
PF Particle Flow
PLT Pixel Luminosity Telescopes
POI Parameter Of Interest

PS Proton Synchrotron
PU Pile-Up
QCD Quantum Chromodynamic
QED Quantum Electrodynamics
QFT Quantum Field Theory
RFQ Radio Frequency Quadrupole
RMS Root Mean Square
ROC Receiver Operating Characteristic
RPC Resistive Plate Chambers
SCA Switch Capacitor Array
SIP Significance of the Impact Parameter
SiPM Silicon Photomultiplier
SM Standard Model
SPS Super Proton Synchrotron
SR Signal Region
SS Same Sign
TAC Time-to-Amplitude Converter
TEC Tracker Endcaps
ToA Time of Arrival
TOB Tracker Outer Barrel
ToF Time of Flight
ToT Time over Threshold
TOTEM Total Elastic and diffractive cross-section Measurement
TriDAS Trigger and Data Acquisition System
TW Time Walk
UL Ultra Legacy
VBF Vector Boson Fusion
WIMP Weakly Interacting Massive Particle
XGBoost eXtreme Gradient Boosting

Bibliography

[1] Zyla PA, Barnett RM, Beringer J, Dahl O, Dwyer DA, Groom DE, et al. Review of Particle Physics, 2020-2021. RPP. PTEP. 2020;2020:083C01. 2093 p. Available from: `https://cds.cern.ch/record/2729066`. *(Cited on pages xiii, 7, 24, 88, and 91)*

[2] The LHC Higgs Cross Section Working Group. CERN Yellow Reports: Handbook of LHC Higgs cross sections: 4. Deciphering the nature of the Higgs sector. CERN; 2017. Available from: `https://e-publishing.cern.ch/index.php/CYRM/issue/view/32`. *(Cited on pages xiii, 21, 23, 25, and 212)*

[3] ATLAS Collaboration. A combination of measurements of Higgs boson production and decay using up to 139 fb^{-1} of proton-proton collision data at $\sqrt{s} = 13$ TeV collected with the ATLAS experiment. ATLAS CONF Note. 2020. *(Cited on pages xiii, 22, and 23)*

[4] ATLAS Collaboration. Higgs boson production cross-section measurements and their EFT interpretation in the 4ℓ decay channel at $\sqrt{s}$ =13 TeV with the ATLAS detector. Eur Phys J C. 2020;80(10):957. [Erratum: Eur.Phys.J.C 81, 29 (2021), Erratum: Eur.Phys.J.C 81, 398 (2021)]. *(Cited on pages xiii and 26)*

[5] CMS Collaboration. Measurements of production cross sections of the Higgs boson in the four-lepton final state in proton–proton collisions at $\sqrt{s} = 13\,\text{TeV}$. Eur Phys J C. 2021;81(6):488. *(Cited on pages xiii, 26, 156, and 209)*

[6] CMS Collaboration. A measurement of the Higgs boson mass in the diphoton decay channel. Phys Lett B. 2020;805:135425. *(Cited on pages xiii, 25, 26, 30, and 212)*

[7] The LHC Higgs Cross Section Working Group. CERN Yellow Reports: Handbook of LHC Higgs Cross Sections: 3. Higgs Properties. CERN; 2013. Available from: `http://cds.cern.ch/record/1559921`. *(Cited on pages xiv and 27)*

[8] CMS Collaboration. Combined measurements of the Higgs boson's couplings at $\sqrt{s} = 13$ TeV. 2018. *(Cited on pages xiv and 28)*

[9] CMS Collaboration. Search for a new scalar resonance decaying to a pair of Z bosons in proton-proton collisions at $\sqrt{s} = 13$ TeV. JHEP. 2018;06:127. [Erratum: JHEP 03, 128 (2019)]. *(Cited on pages xiv, 30, 31, 214, and 231)*

[10] ATLAS Collaboration. Search for heavy resonances decaying into a pair of Z bosons in the $\ell^+\ell^-\ell'^+\ell'^-$ and $\ell^+\ell^-\nu\bar{\nu}$ final states using 139 fb^{-1} of proton–proton collisions at $\sqrt{s} = 13$ TeV with the ATLAS detector. Eur Phys J C. 2021;81(4):332. *(Cited on pages xiv, 30, 32, and 212)*

[11] Lopienska E. The CERN accelerator complex, layout in 2022. Complexe des accélérateurs du CERN en janvier 2022. 2022 Feb. General Photo. Available from: `https://cds.cern.ch/record/2800984`. *(Cited on pages xiv and 36)*

[12] Deutsches Elektronen-Synchrotron DESY. The most precise picture of the proton. News from the DESY research centre. 2015 7. *(Cited on pages xiv and 38)*

[13] LHC Machine. JINST. 2008;3:S08001. *(Cited on pages xiv and 40)*

[14] High Luminosity LHC Project Collaboration. LHC / HL-LHC Plan . 2022 2. *(Cited on pages xiv and 45)*

[15] Public luminosity results. *(Cited on pages xiv, 46, and 47)*

[16] Sakuma T, McCauley T. Detector and Event Visualization with SketchUp at the CMS Experiment. J Phys Conf Ser. 2014;513:022032. *(Cited on pages xiv, 48, and 51)*

[17] CMS Collaboration. The CMS tracker system project: Technical Design Report. 1997. *(Cited on pages xiv, xv, 51, 52, and 54)*

[18] CMS Collaboration. CMS Technical Design Report for the Pixel Detector Upgrade. 2012 9. *(Cited on pages xv and 52)*

[19] CMS Collaboration. The CMS ECAL performance with examples. JINST. 2014;9:C02008. *(Cited on pages xv and 56)*

[20] CMS Collaboration. Laser monitoring system for the CMS lead tungstate crystal calorimeter. Nucl Instrum Meth A. 2008;594:292-320. *(Cited on pages xv and 57)*

[21] CMS Collaboration. Calibration of the CMS hadron calorimeters using proton-proton collision data at $\sqrt{s} = 13$ TeV. JINST. 2020;15(05):P05002. *(Cited on pages xv and 58)*

[22] CMS Collaboration. CMS, the magnet project: Technical design report. 1997 5. *(Cited on pages xv and 60)*

[23] CMS Collaboration. Performance of the CMS muon detector and muon reconstruction with proton-proton collisions at $\sqrt{s} = 13$ TeV. JINST. 2018;13(06):P06015. *(Cited on pages xv, 61, and 69)*

[24] CMS Collaboration. CMS Technical Design Report for the Level-1 Trigger Upgrade. 2013 6. *(Cited on pages xv and 64)*

[25] CMS Collaboration. Heavy Ion Physics Program in CMS Experiment. Nucl Phys A. 2009;830:97C-104C. *(Cited on pages xv and 66)*

[26] CMS Collaboration. Particle-flow reconstruction and global event description with the CMS detector. JINST. 2017;12(10):P10003. *(Cited on pages xv, xvi, 66, 68, 70, 72, 73, 75, and 76)*

[27] Rembser J. CMS Electron and Photon Performance at 13 TeV. J Phys Conf Ser. 2019;1162(1):012008. *(Cited on pages xv, 72, 73, and 74)*

[28] CMS Collaboration. Jet energy scale and resolution in the CMS experiment in pp collisions at 8 TeV. JINST. 2017;12(02):P02014. *(Cited on pages xv and 74)*

[29] CMS Collaboration. Technical Proposal for the Phase-II Upgrade of the CMS Detector. 2015 6. *(Cited on pages xvi, 78, 79, and 92)*

[30] Patrignani C, et al. Review of Particle Physics. Chin Phys C. 2016;40(10):100001. *(Cited on pages xvi, 82, 83, and 85)*

[31] Israeli Y. Energy Reconstruction of Hadrons in highly granular combined ECAL and HCAL systems. JINST. 2018;13(05):C05002. *(Cited on pages xvi, 86, and 87)*

[32] CMS Collaboration. The Phase-2 Upgrade of the CMS Endcap Calorimeter. 2017. *(Cited on pages xvi, xvii, xviii, 80, 92, 94, 95, 98, 104, 119, and 125)*

[33] Paulitsch P. The silicon sensors for the High Granularity Calorimeter of CMS. Nucl Instrum Meth A. 2020;978:164428. *(Cited on pages xvii and 93)*

[34] B Acar et al . Construction and commissioning of CMS CE prototype silicon modules. JINST. 2021;16:T04002. *(Cited on pages xviii, 104, 106, 134, and 135)*

[35] A Lobanov. Precision timing calorimetry with the CMS HGCAL. JINST. 2020;15(07):C07003. Available from: `https://doi.org/10.1088/1748-0221/15/07/c07003`. *(Cited on pages xviii, 107, 108, and 132)*

[36] Acar B, et al. Response of a CMS HGCAL silicon-pad electromagnetic calorimeter prototype to 20-300 GeV positrons. 2021 11. *(Cited on pages xviii, xix, 99, 101, 113, 117, 118, and 120)*

[37] CMS Collaboration. Performance of the CMS High Granularity Calorimeter prototype to charged pion beams of 20−300 GeV/c. 2022 11. *(Cited on pages xix, 113, 122, 123, and 124)*

[38] CMS Collaboration. Jet algorithms performance in 13 TeV data. 2017. *(Cited on pages xxiii, 169, and 170)*

[39] ATLAS Collaboration. Observation of a new particle in the search for the Standard Model Higgs boson with the ATLAS detector at the LHC. Physics Letters B. 2012 sep;716(1):1-29. Available from: `https://doi.org/10.1016%2Fj.physletb.2012.08.020`. *(Cited on pages 6 and 20)*

[40] CMS Collaboration. Observation of a new boson at a mass of 125 GeV with the CMS experiment at the LHC. Physics Letters B. 2012 sep;716(1):30-61. Available from: https://doi.org/10.1016%2Fj.physletb.2012.08.021. *(Cited on pages 6, 20, and 30)*

[41] Kobayashi M, Maskawa T. CP Violation in the Renormalizable Theory of Weak Interaction. Prog Theor Phys. 1973;49:652-7. *(Cited on page 8)*

[42] Maki Z, Nakagawa M, Sakata S. Remarks on the unified model of elementary particles. Prog Theor Phys. 1962;28:870-80. *(Cited on page 8)*

[43] S L Glashow. Partial-symmetries of weak interactions. Nuclear Physics. 1961;22(4):579-88. Available from: https://www.sciencedirect.com/science/article/pii/0029558261904692. *(Cited on page 9)*

[44] S Weinberg. A Model of Leptons. Phys Rev Lett. 1967 Nov;19:1264-6. Available from: https://link.aps.org/doi/10.1103/PhysRevLett.19.1264. *(Cited on page 9)*

[45] A Salam. Elementary Particle Physics: Relativistic Groups and Analyticity. Eighth Nobel Symposium: Almquvist and Wiksell. 1968. *(Cited on page 9)*

[46] Thomson M. Modern Particle Physics. Cambridge University Press; 2013. *(Cited on page 9)*

[47] M J Herrero. The Standard Model. arXiv; 1998. Available from: https://arxiv.org/abs/hep-ph/9812242. *(Cited on page 9)*

[48] Higgs PW. Broken Symmetries and the Masses of Gauge Bosons. Phys Rev Lett. 1964;13:508-9. *(Cited on page 14)*

[49] Englert F, Brout R. Broken Symmetry and the Mass of Gauge Vector Mesons. Phys Rev Lett. 1964;13:321-3. *(Cited on page 14)*

[50] Guralnik GS, Hagen CR, Kibble TWB. Global Conservation Laws and Massless Particles. Phys Rev Lett. 1964;13:585-7. *(Cited on page 14)*

[51] Goldstone J. Field Theories with Superconductor Solutions. Nuovo Cim. 1961;19:154-64. *(Cited on page 14)*

[52] Fukuda Y, et al. Evidence for oscillation of atmospheric neutrinos. Phys Rev Lett. 1998;81:1562-7. *(Cited on page 17)*

[53] Vogel WLZC P. Neutrino oscillation studies with reactors. Nature Communications. 2015;6. *(Cited on page 17)*

[54] Aker M, et al. First operation of the KATRIN experiment with tritium. Eur Phys J C. 2020;80(3):264. *(Cited on page 18)*

[55] Sakharov AD. Violation of CP Invariance, C asymmetry, and baryon asymmetry of the universe. Pisma Zh Eksp Teor Fiz. 1967;5:32-5. *(Cited on page 18)*

[56] Sofue Y, Rubin V. Rotation curves of spiral galaxies. Ann Rev Astron Astrophys. 2001;39:137-74. *(Cited on page 18)*

[57] Li M, Li XD, Wang S, Wang Y. Dark Energy. Commun Theor Phys. 2011;56:525-604. *(Cited on page 18)*

[58] Wells JD. Higgs naturalness and the scalar boson proliferation instability problem. Synthese. 2017;194(2):477-90. *(Cited on page 18)*

[59] Csaki C. The Minimal supersymmetric standard model (MSSM). Mod Phys Lett A. 1996;11:599. *(Cited on page 19)*

[60] CMS Collaboration. Search for higgsinos in channels with two Higgs bosons and missing transverse momentum in proton-proton collisions at $\sqrt{s} =$ 13 TeV. 2021. *(Cited on page 20)*

[61] ATLAS Collaboration. Search for pair production of higgsinos in final states with at least three b-tagged jets in $\sqrt{s} = 13$ TeV pp collisions using the ATLAS detector. Phys Rev D. 2018;98(9):092002. *(Cited on page 20)*

[62] Steffen FD. Dark Matter Candidates - Axions, Neutralinos, Gravitinos, and Axinos. Eur Phys J C. 2009;59:557-88. *(Cited on page 20)*

[63] ATLAS and CMS Collaborations. Combined Measurement of the Higgs Boson Mass in pp Collisions at $\sqrt{s} = 7$ and 8 TeV with the ATLAS and CMS Experiments. Phys Rev Lett. 2015;114:191803. *(Cited on pages 20 and 30)*

[64] CMS Collaboration. Measurements of the Higgs boson width and anomalous HVV couplings from on-shell and off-shell production in the four-lepton final state. Phys Rev D. 2019;99(11):112003. *(Cited on pages 27 and 30)*

[65] CMS Collaboration. Measurements of properties of the Higgs boson decaying to a W boson pair in pp collisions at $\sqrt{s} = 13$ TeV. Phys Lett B. 2019;791:96. *(Cited on page 27)*

[66] CMS Collaboration. Evidence for the direct decay of the 125 GeV Higgs boson to fermions. Nature Phys. 2014;10:557-60. *(Cited on page 27)*

[67] CMS Collaboration. Observation of Higgs boson decay to bottom quarks. Phys Rev Lett. 2018;121(12):121801. *(Cited on page 27)*

[68] CMS Collaboration. Observation of the Higgs boson decay to a pair of τ leptons with the CMS detector. Phys Lett B. 2018;779:283-316. *(Cited on page 27)*

[69] CMS Collaboration. Evidence for Higgs boson decay to a pair of muons. JHEP. 2021;01:148. *(Cited on page 27)*

[70] CMS Collaboration. Search for Higgs boson decay to a charm quark-antiquark pair in proton-proton collisions at $\sqrt{s}$ = 13 TeV. 2022 5. *(Cited on page 28)*

[71] Alasfar L, Corral Lopez R, Gröber R. Probing Higgs couplings to light quarks via Higgs pair production. JHEP. 2019;11:088. *(Cited on page 28)*

[72] CMS Collaboration. A portrait of the Higgs boson by the CMS experiment ten years after the discovery. Nature. 2022;607(7917):60-8. *(Cited on page 28)*

[73] ATLAS Collaboration. Constraints on the Higgs boson self-coupling from the combination of single-Higgs and double-Higgs production analyses performed with the ATLAS experiment. 2019 10. *(Cited on page 28)*

[74] Degrassi G, Giardino PP, Maltoni F, Pagani D. Probing the Higgs self coupling via single Higgs production at the LHC. JHEP. 2016;12:080. *(Cited on page 28)*

[75] Arnison G, et al. Experimental Observation of Isolated Large Transverse Energy Electrons with Associated Missing Energy at $\sqrt{s} = 540$ GeV. Phys Lett B. 1983;122:103-16. *(Cited on page 37)*

[76] Banner M, et al. Observation of Single Isolated Electrons of High Transverse Momentum in Events with Missing Transverse Energy at the CERN anti-p p Collider. Phys Lett B. 1983;122:476-85. *(Cited on page 37)*

[77] Bagnaia P, et al. Evidence for $Z^0 \to e^+e^-$ at the CERN $\bar{p}p$ Collider. Phys Lett B. 1983;129:130-40. *(Cited on page 37)*

[78] Fanti V, et al. A New measurement of direct CP violation in two pion decays of the neutral kaon. Phys Lett B. 1999;465:335-48. *(Cited on page 37)*

[79] LHC Design Report Vol.1: The LHC Main Ring. 2004 6. *(Cited on pages 37 and 41)*

[80] CMS Collaboration. Measurement of the inelastic proton-proton cross section at $\sqrt{s} = 13$ TeV. JHEP. 2018;07:161. *(Cited on page 42)*

[81] CMS Collaboration. Pileup measurement and mitigation techniques in CMS. J Phys Conf Ser. 2012;404:012045. *(Cited on page 42)*

[82] ATLAS Collaboration. ATLAS: Detector and physics performance technical design report. Volume 2. 1999 5. *(Cited on page 42)*

[83] CMS Collaboration. CMS Physics: Technical Design Report Volume 1: Detector Performance and Software. 2006. *(Cited on pages 43 and 50)*

[84] ALICE Collaboration. ALICE transition-radiation detector: Technical Design Report. 2001. *(Cited on page 43)*

[85] LHCb Collaboration. LHCb technical design report: Reoptimized detector design and performance. 2003 9. *(Cited on page 43)*

[86] Kucharczyk M. LHCb Results on Penta(tetra)-Quark Search. JPS Conf Proc. 2017;13:010006. *(Cited on page 43)*

[87] TOTEM Collaboration. TOTEM: Technical design report. Total cross section, elastic scattering and diffraction dissociation at the Large Hadron Collider at CERN. 2004 1. *(Cited on page 44)*

[88] LHCf Collaboration. Technical design report of the LHCf experiment: Measurement of photons and neutral pions in the very forward region of LHC. 2006 2. *(Cited on page 44)*

[89] MoEDAL Collaboration. Technical Design Report of the MoEDAL Experiment. 2009 6. *(Cited on page 44)*

[90] Preskill J. MAGNETIC MONOPOLES. Ann Rev Nucl Part Sci. 1984;34:461-530. *(Cited on page 44)*

[91] FASER Collaboration. Technical Proposal for FASER: ForwArd Search ExpeRiment at the LHC. 2018 12. *(Cited on page 44)*

[92] CMS Collaboration. CMS Technical Design Report for the Muon Endcap GEM Upgrade. 2015 6. *(Cited on pages 46 and 62)*

[93] CMS Collaboration. The CMS electromagnetic calorimeter project: Technical Design Report. 1997. *(Cited on page 55)*

[94] CMS Preshower Collaboration. Performance of CMS ECAL preshower in 2007 test beam. J Phys Conf Ser. 2009;160:012052. *(Cited on page 55)*

[95] CMS Collaboration. The CMS hadron calorimeter project: Technical Design Report. 1997. *(Cited on page 57)*

[96] CMS Collaboration. Upgrade of the CMS Hadron Outer Calorimeter with SiPM sensors. J Phys Conf Ser. 2012;404:012018. *(Cited on page 59)*

[97] CMS Collaboration. The CMS barrel calorimeter response to particle beams from 2-GeV/c to 350-GeV/c. Eur Phys J C. 2009;60:359-73. [Erratum: Eur.Phys.J.C 61, 353–356 (2009)]. *(Cited on page 59)*

[98] CMS Collaboration. CMS Technical Design Report for the Phase 1 Upgrade of the Hadron Calorimeter. 2012 9. *(Cited on page 59)*

[99] Klyukhin VI, et al. The CMS Magnetic Field Map Performance. IEEE Trans Appl Supercond. 2010;20(3):152-5. *(Cited on page 60)*

[100] CMS Collaboration. The CMS muon project: Technical Design Report. 1997. *(Cited on page 60)*

[101] CMS Collaboration. Performance of the CMS drift tube chambers with cosmic rays. Journal of Instrumentation. 2010 mar;5(03):T03015-5. Available from: `https://doi.org/10.1088/1748-0221/5/03/t03015`. *(Cited on page 60)*

[102] CMS Collaboration. Performance of the CMS cathode strip chambers with cosmic rays. Journal of Instrumentation. 2010 mar;5(03):T03018-8. Available from: https://doi.org/10.1088/1748-0221/5/03/t03018. *(Cited on page 61)*

[103] CMS Collaboration. Performance of the Resistive Plate Chambers in the CMS experiment. Journal of Instrumentation. 2012 jan;7(01):C01104-4. Available from: https://doi.org/10.1088/1748-0221/7/01/c01104. *(Cited on page 61)*

[104] CMS Collaboration. CMS RPC Background – Studies and Measurements. 2020 05. *(Cited on page 62)*

[105] CMS Collaboration. CMS. The TriDAS project. Technical design report, vol. 1: The trigger systems. 2000 12. *(Cited on page 63)*

[106] CMS Collaboration. CMS: The TriDAS project. Technical design report, Vol. 2: Data acquisition and high-level trigger. 2002 12. *(Cited on pages 63 and 65)*

[107] The CMS BRIL Collaboration. The Pixel Luminosity Telescope: A detector for luminosity measurement at CMS using silicon pixel sensors. 2022 Jun. Available from: https://cds.cern.ch/record/2812782. *(Cited on page 65)*

[108] The CMS BRIL Collaboration. A new on-line luminometer and beam conditions monitor using single crystal diamond sensors. 2015 Jun. Available from: https://cds.cern.ch/record/2039907. *(Cited on page 65)*

[109] The CMS BRIL Collaboration. First BHM performance plots. 2015 Jun. Available from: https://cds.cern.ch/record/2039942. *(Cited on page 65)*

[110] The CMS BRIL Collaboration. Pixel Luminosity Telescope (PLT) calibration and first measurements. 2015 Jun. Available from: https://cds.cern.ch/record/2039909. *(Cited on page 65)*

[111] CMS Collaboration. CMS Luminosity Measurements for the 2016 Data Taking Period. 2017. *(Cited on pages 65 and 228)*

[112] CMS Collaboration. CMS luminosity measurement for the 2017 data-taking period at $\sqrt{s} = 13$ TeV. 2018. *(Cited on pages 65 and 228)*

[113] CMS Collaboration. CMS luminosity measurement for the 2018 data-taking period at $\sqrt{s} = 13$ TeV. 2019. *(Cited on pages 65 and 228)*

[114] CMS Collaboration. Particle-flow reconstruction and global event description with the CMS detector. JINST. 2017;12(10):P10003. *(Cited on page 67)*

[115] Billoir P. Progressive track recognition with a Kalman like fitting procedure. Comput Phys Commun. 1989;57:390-4. *(Cited on pages 67 and 69)*

[116] Billoir P, Qian S. Simultaneous pattern recognition and track fitting by the Kalman filtering method. Nucl Instrum Meth A. 1990;294:219-28. *(Cited on page 67)*

[117] Billoir P, Qian S. Further test for the simultaneous pattern recognition and track fitting by the Kalman filtering method. Nucl Instrum Meth A. 1990;295:492-500. *(Cited on page 67)*

[118] Azzurri P. Track Reconstruction Performance in CMS. Nucl Phys B Proc Suppl. 2009;197:275-8. *(Cited on pages 67 and 69)*

[119] CMS Collaboration. Description and performance of track and primary-vertex reconstruction with the CMS tracker. JINST. 2014;9(10):P10009. *(Cited on page 67)*

[120] CMS Collaboration. Muon Reconstruction and Identification Performance with Run-2 data. 2020. Available from: `https://cds.cern.ch/record/2727091`. *(Cited on page 71)*

[121] CMS Collaboration. Electron reconstruction in CMS. Eur Phys J C. 2007;49:1099-116. *(Cited on page 71)*

[122] CMS Collaboration. Reconstruction of Electrons with the Gaussian-Sum Filter in the CMS Tracker at the LHC. 2005 1. *(Cited on page 71)*

[123] CMS Collaboration. Performance of Electron Reconstruction and Selection with the CMS Detector in Proton-Proton Collisions at $\sqrt{s}$ = 8 TeV. JINST. 2015;10(06):P06005. *(Cited on page 72)*

[124] Cacciari M, Salam GP, Soyez G. The anti-k_t jet clustering algorithm. JHEP. 2008;04:063. *(Cited on pages 74 and 168)*

[125] CMS Collaboration. Determination of Jet Energy Calibration and Transverse Momentum Resolution in CMS. JINST. 2011;6:P11002. *(Cited on page 75)*

[126] Strologas J. Performance of Jet reconstruction in CMS at 13 TeV. PoS. 2016;ICHEP2016:736. *(Cited on pages 75 and 229)*

[127] CMS Collaboration. Quark-gluon Jet Discrimination At CMS. 2014 9. *(Cited on page 75)*

[128] CMS Collaboration. The Phase-2 Upgrade of the CMS Tracker. 2017 6. *(Cited on page 79)*

[129] CMS Collaboration. The Phase 2 Upgrade of the CMS Inner Tracker. Nucl Instrum Meth A. 2020;980:164396. *(Cited on page 79)*

[130] CMS Collaboration. The Phase-2 Upgrade of the CMS Outer Tracker. Nucl Instrum Meth A. 2020;979:164432. *(Cited on page 79)*

[131] CMS Collaboration. CMS ECAL electronics developments for HL-LHC. JINST. 2015;10(03):C03028. *(Cited on page 80)*

[132] CMS Collaboration. A MIP Timing Detector for the CMS Phase-2 Upgrade. 2019. *(Cited on page 80)*

[133] CMS Collaboration. CMS ECAL upgrade for precision timing and energy measurements at the High-Luminosity LHC. Nucl Instrum Meth A. 2022;1038:166949. *(Cited on page 80)*

[134] CMS Collaboration. The Phase-2 Upgrade of the CMS Barrel Calorimeters. 2017. This is the final version, approved by the LHCC. Available from: `https://cds.cern.ch/record/2283187`. *(Cited on page 80)*

[135] CMS Collaboration. The Phase-2 Upgrade of the CMS Muon Detectors. 2017 9. *(Cited on page 80)*

[136] CMS Collaboration. The Phase-2 Upgrade of the CMS Data Acquisition and High Level Trigger. 2021. This is the final version of the document, approved by the LHCC. Available from: `https://cds.cern.ch/record/2759072`. *(Cited on page 80)*

[137] Longo E, Sestili I. Monte Carlo Calculation of Photon Initiated Electromagnetic Showers in Lead Glass. Nucl Instrum Meth. 1975;128:283. [Erratum: Nucl.Instrum.Meth. 135, 587 (1976)]. *(Cited on page 90)*

[138] Lobanov A. Electronics and triggering challenges for the CMS High Granularity Calorimeter. JINST. 2018;13(02):C02056. *(Cited on page 98)*

[139] Borg J, Callier S, Coko D, Dulucq F, de La Taille C, Raux L, et al. SKIROC2_CMS an ASIC for testing CMS HGCAL. JINST. 2017;12(02):C02019. *(Cited on pages 98 and 102)*

[140] Callier S, Dulucq F, de La Taille C, Martin-Chassard G, Seguin-Moreau N. SKIROC2, front end chip designed to readout the Electromagnetic CALorimeter at the ILC. JINST. 2011;6:C12040. *(Cited on page 98)*

[141] N Charitonidis and B Rae. H2 beam line. 2017. Available from: `http://sba.web.cern.ch/sba/BeamsAndAreas/h2/H2manual.html`. *(Cited on page 99)*

[142] Ambrosini G, et al. Measurement of charged particle production from 450-GeV/c protons on beryllium. Eur Phys J C. 1999;10:605-27. *(Cited on page 100)*

[143] Unger M. Results from NA61/SHINE. EPJ Web Conf. 2013;52:01009. *(Cited on page 102)*

[144] Acar B, et al. The DAQ system of the 12,000 channel CMS high granularity calorimeter prototype. JINST. 2021;16(04):T04001. *(Cited on page 103)*

[145] Acar B, et al. Construction and commissioning of CMS CE prototype silicon modules. JINST. 2021;16(04):T04002. *(Cited on pages 104 and 114)*

[146] Brianza L, et al. Response of microchannel plates to single particles and to electromagnetic showers. Nucl Instrum Meth A. 2015;797:216-21. *(Cited on pages 109 and 110)*

[147] Agostinelli S, et al. GEANT4–a simulation toolkit. Nucl Instrum Meth A. 2003;506:250-303. *(Cited on page 111)*

[148] Banerjee, Sunanda, Ivanchenko, Vladimir, on behalf of the CMS Collaboration. Validation of Physics Models of Geant4 Versions 10.4.p03, 10.6.p02 and 10.7.p01 using Data from the CMS Experiment. EPJ Web Conf. 2021;251:03010. Available from: `https://doi.org/10.1051/epjconf/202125103010`. *(Cited on page 111)*

[149] Wright DH, Kelsey MH. The Geant4 Bertini Cascade. Nucl Instrum Meth A. 2015;804:175-88. *(Cited on page 111)*

[150] Folger G, Wellisch JP. String parton models in GEANT4. eConf. 2003;C0303241:MOMT007. *(Cited on page 112)*

[151] Incerti S, Ivanchenko V, Novak M. Recent progress of Geant4 electromagnetic physics for calorimeter simulation. JINST. 2018;13(02):C02054. *(Cited on page 112)*

[152] T Quast. Qualification, Performance Validation and Fast Generative Modelling of Beam Test Calorimeter Prototypes for the CMS Calorimeter Endcap Upgrade. RWTH Aachen, Germany; 2020. Available from: `http://doi.org/10.18154/RWTH-2020-06473`. *(Cited on page 128)*

[153] Chen T, Guestrin C. XGBoost: A Scalable Tree Boosting System. 2016 3. *(Cited on page 157)*

[154] Rembser J. Measurement of triboson production in the multilepton final state and electron studies with the CMS experiment at the LHC. Institut Polytechnique de Paris; 2020. Available from: `https://theses.hal.science/tel-03720899`. *(Cited on page 157)*

[155] Bodek A, Van Dyne A, Han JY, Sakumoto W, Strelnikov A. Extracting Muon Momentum Scale Corrections for Hadron Collider Experiments. Eur Phys J C. 2012;72:2194. *(Cited on page 164)*

[156] CMS Collaboration. Performance of Photon Reconstruction and Identification with the CMS Detector in Proton-Proton Collisions at sqrt(s) = 8 TeV. JINST. 2015;10(08):P08010. *(Cited on page 167)*

[157] Gao Y, Gritsan AV, Guo Z, Melnikov K, Schulze M, Tran NV. Spin Determination of Single-Produced Resonances at Hadron Colliders. Phys Rev D. 2010;81:075022. *(Cited on page 189)*

[158] Bolognesi S, Gao Y, Gritsan AV, Melnikov K, Schulze M, Tran NV, et al. On the spin and parity of a single-produced resonance at the LHC. Phys Rev D. 2012;86:095031. *(Cited on page 189)*

[159] Anderson I, et al. Constraining Anomalous HVV Interactions at Proton and Lepton Colliders. Phys Rev D. 2014;89(3):035007. *(Cited on page 189)*

[160] Gritsan AV, Röntsch R, Schulze M, Xiao M. Constraining anomalous Higgs boson couplings to the heavy flavor fermions using matrix element techniques. Phys Rev D. 2016;94(5):055023. *(Cited on page 189)*

[161] Gritsan AV, Roskes J, Sarica U, Schulze M, Xiao M, Zhou Y. New features in the JHU generator framework: constraining Higgs boson properties from on-shell and off-shell production. Phys Rev D. 2020;102(5):056022. *(Cited on page 189)*

[162] Martini T, Pan RQ, Schulze M, Xiao M. Probing the CP structure of the top quark Yukawa coupling: Loop sensitivity versus on-shell sensitivity. Phys Rev D. 2021;104(5):055045. *(Cited on page 189)*

[163] Davis J, Gritsan AV, Guerra LSM, Kyriacou S, Roskes J, Schulze M. Constraining anomalous Higgs boson couplings to virtual photons. Phys Rev D. 2022;105(9):096027. *(Cited on page 189)*

[164] Campbell JM, Ellis RK. MCFM for the Tevatron and the LHC. Nucl Phys B Proc Suppl. 2010;205-206:10-5. *(Cited on page 189)*

[165] Nason P. A New method for combining NLO QCD with shower Monte Carlo algorithms. JHEP. 2004;11:040. *(Cited on page 197)*

[166] Frixione S, Nason P, Oleari C. Matching NLO QCD computations with Parton Shower simulations: the POWHEG method. JHEP. 2007;11:070. *(Cited on page 197)*

[167] Alioli S, Nason P, Oleari C, Re E. NLO Higgs boson production via gluon fusion matched with shower in POWHEG. JHEP. 2009;04:002. *(Cited on page 197)*

[168] Bagnaschi E, Degrassi G, Slavich P, Vicini A. Higgs production via gluon fusion in the POWHEG approach in the SM and in the MSSM. JHEP. 2012;02:088. *(Cited on page 197)*

[169] Anastasiou C, Duhr C, Dulat F, Herzog F, Mistlberger B. Higgs Boson Gluon-Fusion Production in QCD at Three Loops. Phys Rev Lett. 2015;114:212001. *(Cited on page 197)*

[170] Nason P, Oleari C. NLO Higgs boson production via vector-boson fusion matched with shower in POWHEG. JHEP. 2010;02:037. *(Cited on page 197)*

[171] Ciccolini M, Denner A, Dittmaier S. Electroweak and QCD corrections to Higgs production via vector-boson fusion at the LHC. Phys Rev D. 2008;77:013002. *(Cited on page 197)*

[172] Bolzoni P, Maltoni F, Moch SO, Zaro M. Higgs production via vector-boson fusion at NNLO in QCD. Phys Rev Lett. 2010;105:011801. *(Cited on page 197)*

[173] Bolzoni P, Maltoni F, Moch SO, Zaro M. Vector boson fusion at NNLO in QCD: SM Higgs and beyond. Phys Rev D. 2012;85:035002. *(Cited on page 197)*

[174] Ciccolini M, Denner A, Dittmaier S. Strong and electroweak corrections to the production of Higgs + 2jets via weak interactions at the LHC. Phys Rev Lett. 2007;99:161803. *(Cited on page 197)*

[175] Bierlich C, et al. A comprehensive guide to the physics and usage of PYTHIA 8.3. 2022 3. *(Cited on page 197)*

[176] Alwall J, Frederix R, Frixione S, Hirschi V, Maltoni F, Mattelaer O, et al. The automated computation of tree-level and next-to-leading order differential cross sections, and their matching to parton shower simulations. JHEP. 2014;07:079. *(Cited on page 197)*

[177] CMS Collaboration. Search for the standard model Higgs boson in the decay channel H to ZZ to 4 leptons in pp collisions at $\sqrt{s} = 7$ TeV. Phys Rev Lett. 2012;108:111804. *(Cited on page 198)*

[178] Kauer N, Passarino G. Inadequacy of zero-width approximation for a light Higgs boson signal. JHEP. 2012;08:116. *(Cited on page 212)*

[179] Goria S, Passarino G, Rosco D. The Higgs Boson Lineshape. Nucl Phys B. 2012;864:530-79. *(Cited on page 212)*

[180] Procedure for the LHC Higgs boson search combination in Summer 2011. 2011 8. *(Cited on page 222)*

[181] Cowan G, Cranmer K, Gross E, Vitells O. Asymptotic formulae for likelihood-based tests of new physics. Eur Phys J C. 2011;71:1554. [Erratum: Eur.Phys.J.C 73, 2501 (2013)]. *(Cited on page 224)*

[182] Van der Meer S. Calibration of the Effective Beam Height in the ISR. 1968 6. *(Cited on page 228)*

ECOLE DOCTORALE

Titre : Recherche de résonances à haute masse avec les canaux multi-leptons et étude des performances temporelles du High Granular Calorimeter de CMS

Mots clés : CMS ; LHC ; Higgs ; Particle Flow ; Calorimètre ; Nouvelle Physique

Résumé :
Cette thèse prend place à un moment charnière où l'ensemble des données collectées par l'expérience CMS lors du Run-2 du LHC (2015 à 2018) sont disponibles et où la nouvelle génération de détecteurs visant à sonder encore plus loin nos connaissances de la physique sont en train d'être élaborés.
Dans cet esprit, cette thèse s'articule autour de deux problématiques, dont la première porte sur l'étude des performances d'un prototype du High Granular Calorimeter (HGCAL) de CMS. Celui-ci s'inscrit dans une vaste campagne d'améliorations à l'horizon de la future phase de vie du LHC, aussi appelée High-Luminosity LHC (HL-LHC) et qui devrait être mise en place en 2029. Son objectif est de générer dix fois plus de données que pendant l'ensemble de la première phase du LHC, et ceci dans le but de mesurer encore plus précisément les prédictions du Modèle Standard (MS) de la physique des particules, ainsi que d'étudier des phénomènes rares qui ne sont pas observables à l'heure actuelle. L'augmentation de la luminosité sera aussi associée à une importante hausse du nombre d'événements simultanés et de la dose de radiation que vont recevoir les détecteurs. Ceux actuellement en place ne sont pas prévus pour fonctionner dans un tel environnement, et c'est pourquoi les actuels calorimètres aux extrémités seront remplacés par HGCAL Celui-ci sera le tout premier calorimètre imageur à base de capteurs en silicium à être utilisé. Pour déterminer sa faisabilité, un premier prototype a été construit et utilisé lors de tests sous faisceaux utilisant des positons et des pions ayant une énergie allant de 20 à 300 GeV. Dans cette thèse, l'accent sera mis sur l'étude des performances temporelles du prototype, en passant par les différentes étapes de la calibration et jusqu'au calcul de la résolution temporelle pour une unique cellule de HGCAL et pour l'ensemble d'une gerbe électromagnétique ou hadronique. Les résultats obtenus lors de cette thèse sont comparés à ceux issus de simulations Monte Carlo et le très bon accord entre les deux confirme la conception finale de HGCAL.
La seconde problématique sur laquelle se penche cette thèse est la recherche de résonances à haute masse en utilisant les canaux de désintégration multi-leptoniques. Une telle recherche s'explique par le fait que le MS ne permet pas de décrire certains phénomènes, mais d'autres théories leur proposent une explication avec notamment l'ajout de nouveaux bosons. L'objectif de cette analyse est de regarder s'il existe une résonance ayant une masse comprise entre 200 GeV et 3 TeV pouvant correspondre à un nouveau type de boson scalaire. Pour cela, les 138 fb^{-1} de données collectées par l'expérience CMS lors du Run-2 sont utilisées dans le canal de désintégration $H \rightarrow ZZ \rightarrow 4l$. L'intérêt d'utiliser ce canal en particulier est qu'il correspond à l'un des modes de production dominant à haute masse et qu'il possède un état final pleinement reconstruit avec une excellente résolution et un bon rapport signal sur bruit. Cette thèse va tout d'abord présenter comment les différents objets constituants les événements d'intérêts sont reconstruits et sélectionnés. Ensuite, la construction d'un modèle de signal est faite de telle sorte que n'importe laquelle des combinaisons de paramètres de la résonance puissent être comparées aux données. Pour cela, cette modélisation comprend une partie décrivant le signal théorique et une autre qui prend en considération tous les effets du détecteur. Afin de savoir si les données expérimentales peuvent être décrites par le signal construit dans cette thèse, un test statistique est réalisé en maximisant une fonction de vraisemblance prenant en compte le signal, ainsi que les bruits de fond et les interférences entre les deux. En guise de résultats sur cette recherche, les limites sur la vraisemblance du signal attendu sont présentées et permettent d'exclure ou non une région de masse dans laquelle peut se trouver une résonance de haute masse.

Title : Search for high mass resonances with multi-lepton channels and study of timing performance of the CMS High Granularity Calorimeter

Keywords : CMS ; LHC ; Higgs ; Particle Flow ; Calorimeter ; New Physics

Abstract :
This thesis takes place at a critical moment when all the data collected by the CMS experiment during the LHC Run-2 are available and when the new generation of detectors aiming to probe even further our knowledge of physics are being developed.
In this context, this thesis is structured around two problematics, the first one concerns the study of the performance of a prototype of the CMS High Granular Calorimeter (HGCAL). It is part of a vast campaign of upgrades for the future life phase of the LHC, also known as the High-Luminosity LHC, which should be in service by 2029. Its aim is to generate ten times more data than during the entire first phase of the LHC, in order to measure even more accurately the predictions of the Standard Model (SM) of particle physics, as well as to study rare phenomena that are not observable at present. The increase in luminosity will also be associated with a significant increase in the number of simultaneous events and the radiation dose that the detectors will receive. The current detectors are not designed to operate in such an environment, so the endcap calorimeters of CMS will be replaced by HGCAL. It will be the first imaging calorimeter based on silicon sensors to be used. To determine its feasibility, a first prototype has been built and used in beam tests using positrons and pions with energies ranging from 20 to 300 GeV. In this thesis, the focus will be on the study of the temporal performance of the prototype, through the various stages of calibration and up to the calculation of the temporal resolution for a single HGCAL cell and for the whole electromagnetic or hadronic showers. The results obtained in this thesis are compared with those obtained from Monte Carlo simulations and the very good agreement between both confirms the final design of HGCAL.
The second problematic addressed in this thesis is about the search for high mass resonances using the multi-leptonic decay channel. Such a search is explained by the fact that the SM does not describe some phenomena, but other theories propose an explanation with the addition of new bosons. The aim of such an analysis is to see if there is a resonance with a mass between 200 GeV and 3 TeV that could correspond to a new type of scalar boson. For this purpose, the 138 fb^{-1} of data collected by the CMS experiment during Run-2 are used in the $H \rightarrow ZZ \rightarrow 4l$ decay channel. The interest in using this particular channel is that it corresponds to one of the dominant high-mass production modes and has a fully reconstructed final state with excellent resolution and good signal-to-noise ratio. Firstly, this thesis presents how the different objects constituting the events of interest are reconstructed and selected. Secondly, the construction of a signal model is done in such a way that any combination of the resonance parameters can be compared to the data. For this purpose, this modelling consists of a part describing the theoretical signal and another part that takes into account all the effects of the detector. In order to find out whether the experimental data can be described by the signal constructed in this thesis, a statistical test is performed by maximizing a likelihood function taking into account the signal, as well as the background and interference between both. As a result, limits on the expected signal cross-section are calculated and allow excluding or not a region of mass in which a high mass resonance can be found.

Institut Polytechnique de Paris
91120 Palaiseau, France